

**Project Report  
STK-235  
Volume I**



**Proceedings of the 1995  
Space Surveillance Workshop**  
(Title UNCLASSIFIED)

**K.P. Schwan  
Editor**

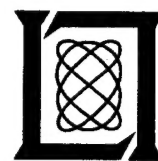
**28 – 30 March 1995**

---

**Lincoln Laboratory**

MASSACHUSETTS INSTITUTE OF TECHNOLOGY

LEXINGTON, MASSACHUSETTS



Prepared with partial support of the Department of the Air Force  
under Contract F19628-95-C-0002.

Approved for public release; distribution is unlimited.

DTIC QUALITY INSPECTED 5

19950515 083

Prepared with partial support of the Department of the Air Force under Contract F19628-95-C-0002.

This report may be reproduced to satisfy needs of U.S. Government agencies.

The ESC Public Affairs Office has reviewed this report, and it is releasable to the National Technical Information Service, where it will be available to the general public, including foreign nationals.

This technical report has been reviewed and is approved for publication.

FOR THE COMMANDER



Gary Tutungian  
Administrative Contracting Officer  
Contracted Support Management

Non-Lincoln Recipients

PLEASE DO NOT RETURN

Permission is given to destroy this document  
when it is no longer needed.

# **Unclassified**

29 March 1995

## **ERRATA**

Document: STK-235, Volume 1  
Proceedings of the 1995 Space  
Surveillance Workshop (Title UNCLASSIFIED)  
28–30 March 1995

A page from the Wallner et al. text was inadvertently omitted.  
Please incorporate page 215(a), which is attached.

*Publications Office*  
MIT Lincoln Laboratory  
244 Wood Street  
Lexington, MA 02173-9108

# **Unclassified**

- 3) the magnitude and general consistency of the abutment errors (position discontinuities that arose from piecing together individual fits into one RO);
- 4) the extent to which the ROs agreed with external precision ephemerides (when available).

The significance of these four measures is discussed below.

First, in the case where the model error is an order of magnitude smaller than the observation error, and provided that the observations have been sufficiently sampled, the position RMS does not provide a good measure of the amount of absolute error in the orbit resulting from a weighted OD. In this case, the position RMS is largely a reflection of the noise in the observations, as opposed to a reflection of the error in the orbit resulting from the OD (which is the error of interest). This was particularly relevant to the RO generation process because 1) high accuracy SP models were used over relatively short fit spans and 2) there were a large number of observations available. In particular, an analysis using the precise ephemerides on two satellites in orbit categories 2 and 3 showed that for the fit spans and SP models used in the RO generation, the model error was about 15 meters (RMS). In contrast, the inherent noise in the SSN observations translated into approximately one kilometer of position error for the near-Earth satellites we are studying.

The interpretation of the position RMS was further complicated by the fact that the ODs were performed weighted and by the fact that the range observations were generally an order of magnitude better than the azimuth and elevation observations (as measured by their contributions to the position RMS). Unweighted ODs, because of the observation rejection scheme they employ, tend to arrive at a position RMS that is reflective of the accuracy of the best observations. However, weighted ODs employ a rejection scheme that (provided the a priori weights are representative) tends to accept roughly equal percentages of all the observation types, regardless of their relative a priori accuracies. This results in a situation where the least accurate observations, though contributing little to the solution, have equal contributions to the position RMS; thereby "inflating" it.

Based on all these considerations, and upon examining the data, it was decided that little could be inferred from the position RMSs beyond the fact that they were always consistent with the noise in the SSN observations. Therefore, the position RMS was not used as a measure of merit in determining the accuracy of the ROs. A specific example involving an external precision ephemeris is presented shortly that illustrates and strengthens this decision.

The second measure of the quality of the ROs was the state error covariance matrix of each fit. The RO quality indicated by these matrices was optimistic, primarily because the error statistics implied by the matrices assume 1) that no model error is present, 2) that the observations are sampled from unbiased stationary Gaussian distributions, and 3) that the accuracy of the observations are uncorrelated with the state. For the conditions present in this study, none of these assumptions are valid, and the state error covariance matrix gave error estimates that were only one-quarter to one-half as large as the estimates resulting from the other measures. Therefore, the state error covariance matrices were not used as a measure of the quality of the ROs.

The third measure of the quality of the ROs was the magnitude and general consistency of the abutment errors arising across the many adjacent trajectories that constituted a single RO. We believe that these abutment errors, while clearly not providing an exhaustive measure, give a good general indication of both the self-consistency of the ROs as well as a reasonable but conservative

MASSACHUSETTS INSTITUTE OF TECHNOLOGY  
LINCOLN LABORATORY

PROCEEDINGS OF THE 1995  
SPACE SURVEILLANCE WORKSHOP

PROJECT REPORT STK-235  
VOLUME I

28 - 30 MARCH 1995

ISSUED 20 MARCH 1995

Accesion For	
NTIS	CRA&I <input checked="" type="checkbox"/>
DTIC	TAB <input type="checkbox"/>
Unannounced <input type="checkbox"/>	
Justification _____	
By _____	
Distribution / _____	
Availability Codes	
Dist	Avail and / or Special
A-1	

The thirteenth Annual Space Surveillance Workshop held on 28-30 March 1995 was hosted by MIT Lincoln Laboratory and provided a forum for space surveillance issues. This *Proceedings* documents most of the presentations, with minor changes where necessary.

Approved for public release; distribution is unlimited.

LEXINGTON

MASSACHUSETTS

## **PREFACE**

The thirteenth Annual Space Surveillance Workshop sponsored by ESC/MIT Lincoln Laboratory will be held on 28, 29 and 30 March 1995. The purpose of this series of workshops is to provide a forum for the presentation and discussion of space surveillance issues.

This *Proceedings* documents most of the presentations from this workshop. The papers contained were reproduced directly from copies supplied by their authors (with minor mechanical changes where necessary). It is hoped that this publication will enhance the utility of the workshop.

Mr. Kurt P. Schwan  
Editor

## TABLE OF CONTENTS

Joint Operations Planning for Space Surveillance Missions on the MSX Satellite <i>Grant H. Stokes - MIT Lincoln Laboratory</i> <i>Andrew Good - JHU Applied Physics Laboratory</i>	1
The MSX Operations Planning Center's Role in the Scheduling and Analysis of Space-Based Surveillance Experiments <i>Robert B. Dickey and James H. Polaha - JHU Applied Physics Laboratory</i>	9
The Space-Based Space Surveillance Experiment Simulator for the MSX Spacecraft <i>Andrew J. Wiseman - MIT Lincoln Laboratory</i>	19
Geosynchronous Surveillance with a Space Based Sensor <i>William F. Burnham and R. Sridharan - MIT Lincoln Laboratory</i>	33
MSX Spacecraft Sensor Demonstration of BMD Target Tracking Against Stressing Infrared Backgrounds Using Resident Space Objects <i>Bernie Klem, G.C. Light, J.M. Lyons, C.J. Rice, Nelson W. Schulenburg - The Aerospace Corporation</i> <i>Ed Zack - USAF/SMC</i>	45
A Metric Analysis of IRAS Resident Space Object Detections <i>Mark T. Lane, Joseph F. Baldassini and E. Michael Gaposchkin - MIT Lincoln Laboratory</i>	59
Orbital Debris Radar Calibration Spheres <i>Thomas J. Settecerri - Lockheed Engineering &amp; Sciences Co.</i> <i>Eugene G. Stansbery - NASA/Johnson Space Center</i>	71
The NASA/JSC Ionization Radar <i>Walter Marker - NASA/Johnson Space Center</i> <i>Herbert R.A. Schaeper - University of Houston/Cl</i> <i>Greg E. McCaskill and Sassan Yerushalmi - Lockheed Engineering &amp; Sciences Co.</i>	85
The Los Alamos Photon Counting Detector Space Object Detection Project: An Update <i>Cheng Ho, Bill Priedhorsky, Miles Baron and Don Casperson - Los Alamos National Laboratory</i>	93

1994 Space Debris Campaign - Preliminary Results <i>Taft DeVere - SenCom Corp.</i> <i>Tim Payne - SWC/AE</i> <i>Capt. Gary Wilson - AFSPC/DOYY</i>	101
Kwajalein Missile Range Contribution to the 1994 Debris Campaign <i>Andrew Gerber, Gary Duff and Dale Izatt - MIT Lincoln Laboratory</i>	111
Use of a NAVSPASUR-type Radar to Track and Catalog Orbital Debris <i>Stephen H. Knowles, Naval Space Command</i>	121
Search, Detection and Tracking of Micrometeoroids, Orbital Debris, Near Earth Objects and Other Satellites <i>James A. Hand, L.J. Freier, D.G. Sargent - Charles Stark Draper Laboratory</i> <i>James L. Monroe, Los Alamos National Laboratory</i>	129
Stare-and-Chase at TRADEX <i>Dale L. Izatt - MIT Lincoln Laboratory</i>	145
ALCOR Sensitivity and Detection Enhancements <i>Kevin J. Witt and Randy K. Avent - MIT Lincoln Laboratory</i>	155
95 GHz Sensitivity Improvements at the Kwajalein Missile Range <i>Jeffrey C. McHarg and Robert F. Lucey, Jr. - MIT Lincoln Laboratory</i>	159
Remote Sensing of LAGEOS I/II Rotational Motion. Scientific Exploitation of Space Surveillance Techniques <i>Douglas G. Currie, Kenneth E. Kissell, P. Avizonis, D. Wellnitz - University of Maryland</i>	169
The Small Expendable Deployer System (SEDS) <i>George Gorski-Popiel - MIT Lincoln Laboratory</i> <i>Jeffrey J. DeLong - Raytheon RSE</i>	179
Spectral Signatures Predicted from Detailed Satellite Models <i>Amy E. Prochko - W.J. Schafer Associates, Inc.</i> <i>M. Culpepper, Susan Durham, J. O'Hair - Phillips Laboratory</i>	185
Initial Results from the New Sensor System on the UK SOI Facility at Herstmonceux <i>James Dick, A. Sinclair - Royal Greenwich Observatory</i> <i>A. Greenaway and Peter Liddell - Defence Research Agency</i>	195

IOTA: Operational Status and Measurements	201
<i>William Traub, N.P. Carleton, M.G. Lacasse, P. Nisenson, M.R. Pearlman, R.D. Reasenberg, X. Xu, C.M. Coldwell, A. Panasyuk - Smithsonian Astrophysical Observatory</i>	
<i>H.M. Dyck - University of Wyoming</i>	
<i>J.A. Benson, C. Papaliolios - Harvard University</i>	
<i>R. Predmore, F.P. Schloerb - University of Massachusetts at Amherst</i>	
The Accuracy of General Perturbations and Semianalytic Satellite Ephemeris Theories	209
<i>Richard N. Wallner, S.J. Casali, and W.N. Barker - Kaman Sciences Corp.</i>	
Air Force Space Command Space Surveillance Requirements Task	219
<i>Maj. Betsy Pimentel - AFSPC/XPX</i>	
<i>Lt. Col. Simon Willis - AFSPC/DOY</i>	
<i>Mrs. Linda Crawford - GTE Government Systems</i>	
Ranking Satellite Propagators: A Statistical Approach	227
<i>Thomas D. Platt and L.E. Herder - Kaman Sciences Corp.</i>	

## **Joint Operations Planning For Space Surveillance Missions On The Msx Satellite**

Grant Stokes, Lincoln Laboratory, Massachusetts Institute of Technology  
Andrew Good, Johns Hopkins University/Applied Physics Laboratory

**Abstract** - The Midcourse Space Experiment (MSX) satellite, sponsored by BMDO, is intended to gather broad-band phenomenology data on missiles, plumes, naturally occurring earthlimb backgrounds and deep space backgrounds. In addition the MSX will be used to conduct functional demonstrations of space-based space surveillance. The JHU/Applied Physics Laboratory (APL), located in Laurel, MD is the integrator and operator of the MSX satellite. APL will conduct all operations related to the MSX and is charged with the detailed operations planning required to implement all of the experiments run on the MSX except the space surveillance experiments. The non-surveillance operations are generally amenable to being defined months ahead of time and being scheduled on a monthly basis. Lincoln Laboratory, Massachusetts Institute of Technology (LL), located in Lexington, MA, is the provider of one of the principle MSX instruments, the Space-Based Visible (SBV) sensor, and the agency charged with implementing the space surveillance demonstrations on the MSX. The planning timelines for the space surveillance demonstrations are fundamentally different from those for the other experiments. They are generally amenable to being scheduled on a monthly basis, but the specific experiment sequence and pointing must be refined shortly before execution. This allocation of responsibilities to different organizations implies the need for a joint mission planning system for conducting space surveillance demonstrations. This paper details the iterative, joint planning system, based on passing responsibility for generating MSX commands for surveillance operations from APL to LL for specific scheduled operations. The joint planning system, including the generation of a budget for spacecraft resources to be used for surveillance events, has been successfully demonstrated during ground testing of the MSX and is being validated for MSX launch within the year. The planning system developed for the MSX forms a model possibly applicable to developing distributed mission planning systems for other multi-use satellites.

## **INTRODUCTION**

The Midcourse Space Experiment (MSX) is a satellite-based experiment sponsored by the Ballistic Missile Defense Organization (BMDO) to be flown in a low-earth orbit beginning in late 1994. MSX was initially conceived as the first extended duration, long wave infrared (LWIR) phenomenology measurement program sponsored by BMDO; however, these early objectives have evolved into a more comprehensive experiment. MSX is now a multi-year experiment designed to collect broad-band phenomenology data on missiles, plumes, naturally occurring earthlimb backgrounds and deep space backgrounds. In addition, MSX will be used to collect spacecraft contamination data, to integrate, validate, and transfer advanced technologies to current and future BMDO systems, and to conduct functional demonstrations of space-based space surveillance.

The Johns Hopkins University Applied Physics Laboratory (APL) is the integrator and operator of the MSX satellite. MSX will be launched from Vandenberg Air Force Base into a near-polar, low-earth, near sun-synchronous orbit. The MSX, shown in Figure 1, consists of the satellite superstructure, three primary optical sensors, contamination instrumentation and the spacecraft support subsystems. The optical axes of the three primary sensors (Space Infrared Imaging Telescope (SPIRIT III), Space-Based Visible (SBV) sensor, and Ultraviolet/Visible Imagers and Spectrographic Imagers (UVISI)) are parallel to one another and point in the +X direction. The support subsystems consist of the power subsystem, the thermal control subsystem, the command and data handling subsystem and the attitude determination and control

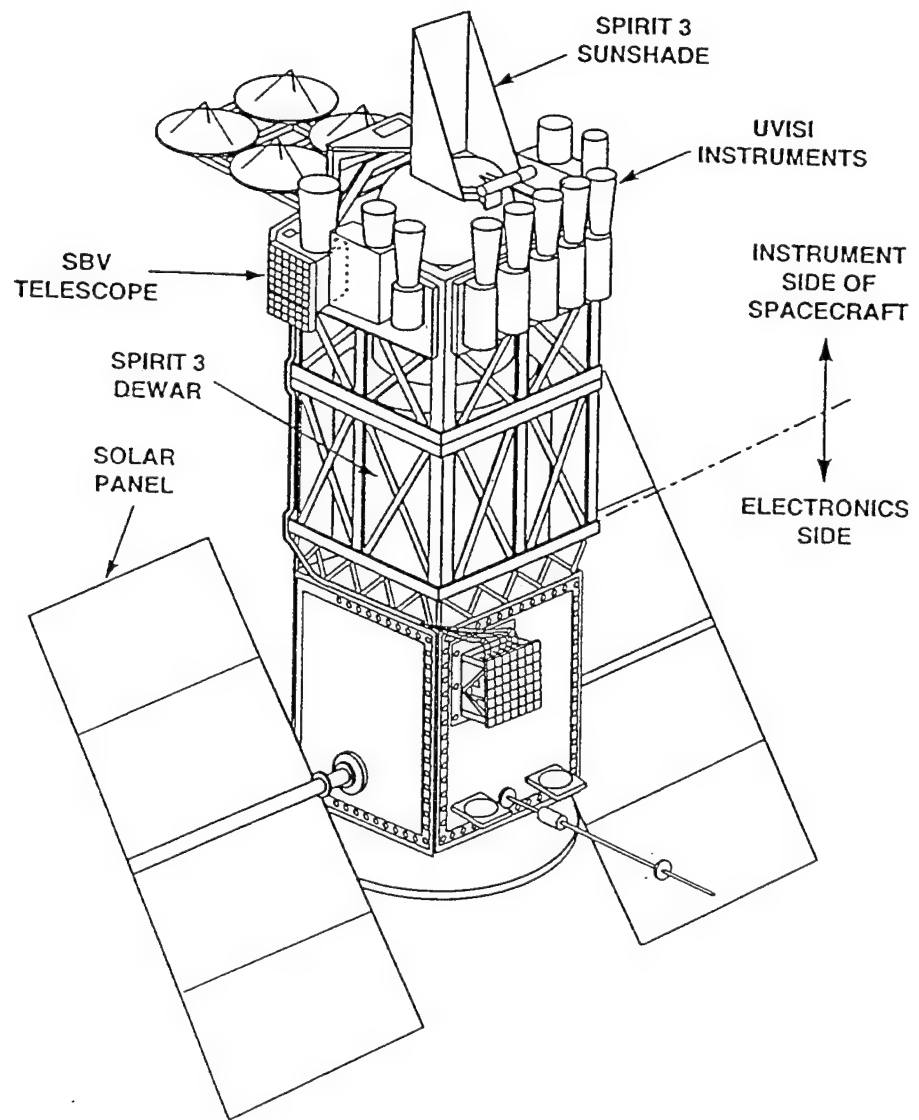


Figure 1. MSX satellite

subsystem, the command and data handling subsystem and the attitude determination and control subsystem. In addition, MSX houses a Beacon Receiver and On-board Signal and Data Processor (OSDP).

The SPIRIT III sensor has been developed by the Utah State University Space Dynamics Laboratory (USU/SDL). It is a passive mid to very long wavelength infrared (M/VLWIR) sensor and is the primary instrument aboard MSX for collecting target and background phenomenological data. SPIRIT III consists of a telescope with a 35.5 cm diameter aperture, a six-channel interferometer, a six-band radiometer and a cryogenic dewar/heat exchanger. The lifetime for SPIRIT III operations, which will be limited by the cryogen supply, is currently projected to be 18-24 months.

The UVISI sensor has been developed by APL with a primary mission to collect data on celestial and atmospheric backgrounds. Other UVISI missions include target characterization in the UV regime and observation of contamination particulates in conjunction with the contamination instruments. The UVISI sensor consists of four imagers and five spectrographic imagers (SPIMs) covering a spectral range from far UV to near infrared. The imagers include wide and narrow field-of-view sensors in both the visible and UV ranges and also include filter wheels to select various passbands. UVISI also includes an image processing system which will be used for closed-loop tracking of targets and aurora.

The SBV sensor, developed by the Lincoln Laboratory, Massachusetts Institute of Technology (LL), is the primary visible wavelength sensor aboard MSX. It will be used to collect data on target signatures and background phenomenologies, but the primary mission of SBV will be to conduct functional demonstrations of space-based space surveillance. SBV incorporates a 15 cm, off-axis, all-reflective, reimaging telescope with a thermoelectrically-cooled CCD focal plane array. SBV also includes an image processing system, experiment control system, telemetry formatter, and a data buffer for temporary data storage.

The collective suite of MSX instruments and supporting subsystems provide a broad range of data collection potential; however, a significant number of operational constraints have been imposed by spacecraft and instrument designers in order to achieve safe operations and to maintain the desired mission life (five years overall including two years for SPIRIT III). These constraints include limitations on boresight pointing relative to the sun, moon, and earth, restrictions on warming of the SPIRIT III dewar and baffle, bounds on battery depth-of-discharge and temperature, and thermal and duty cycle limits for the on-board tape recorders. The combination of these operational constraints with the BMDO goal of 14 data collection events per day represent a significant challenge to the MSX flight operations system.

The MSX flight operations system consists of facilities at APL (Operations Planning Center (OPC), Mission Control Center (MCC), Mission Processing Center (MPC), Performance Assessment Center (PAC), and Attitude Processing Center (APC)), at LL (SBV Processing, Operations and Control Center (SPOCC), and at the USAF Test Support Complex (TSC) at Onizuka Air Force Base. This collection of facilities is referred to as the "extended" MSX Mission Operations Center (MOC). A BMDO-led Mission Planning Team (MPT) instructs the MOC on a monthly basis on the type, number, and priority of experiments to be conducted. The OPC/SPOCC then develop operations planning products (e.g., schedules, contact support plans, command loads) which are provided to the MCC and TSC for execution. Spacecraft science and housekeeping data are collected by the MCC and TSC and then processed by the MPC, APC, and PAC as well as disseminated to the MSX data community.

## SPACE SURVEILLANCE

Currently the United States maintains a world wide network of ground based sensors tasked with the acquisition of tracking data on all manmade objects in orbit around the earth. These sensors include a network of passive optical systems which are limited to a short duty cycle by poor weather and by daylight. Since foreign based sites are progressively more expensive and inconvenient to support, it is natural to ask whether ground based sensors could be supplemented or replaced by satellite based sensing systems. Satellite based sensors are not limited by daylight operation or poor weather and a single satellite borne sensor can sample the entire geosynchronous belt satellite population several times per day.

One of the missions of the MSX satellite is to demonstrate the feasibility of space-based space surveillance operations. One of the three principle MSX sensors, the SBV sensor has been specifically designed to provide visible-band satellite tracking data. The SBV consists of a six inch optical telescope with high off-axis rejection optics designed to acquire good quality satellite track data quite near the bright earth limb. In addition to the visible data from the SBV, track and optical signature data from the other MSX sensors is of interest to the space surveillance community. This is especially true for data from the SPIRIT III long-wave infrared sensor which promises the ability to detect satellites in the shadow of the earth.

The mission planning required to execute space surveillance activities is fundamentally different from that required to execute the other MSX missions. Normally space surveillance sensors are tasked on a day at a time basis by Space Command. In addition, Space Command provides special updates to the sensor tasking for special events, such as new launches, which require reactions on short time lines (minutes to hours). This operational tempo is significantly shorter than the normal MSX mission planning process which requires the operation to be well defined at the monthly planning level, which occurs as much as 10 weeks before the execution of the event on the spacecraft. If the routine MSX planning timeline were followed and space surveillance experiments were pre-planned, the ephemeris of many low altitude satellites targeted for observation will have changed enough to put them out of the sensor field of view by the experiment execution time. In addition, the normal MSX planning procedure contains no provision for generating observations in response to quick reaction experiments such as the launch of a new satellite.

The mission planning for the Space Surveillance experiments on the MSX satellite requires the ability to leave considerable flexibility in the experiment timing and attitude profile to be followed by the MSX in the experiment execution until late in the experiment planning process. Under "normal" circumstances the details of the operation, consisting of the list of satellites to be observed, the attitude profile for the MSX and the data acquisition times can be defined one to two days before the execution on the MSX. Special "quick reaction events", such as acquiring track data on a newly launched satellite in its transfer orbit to the geosynchronous belt, require reaction times on the order of hours.

## JOINT PLANNING PROCESS

The mission planning required to operate a satellite as complex as the MSX is a large task under any condition; however, it is complicated further by the breadth of the experimental missions to be conducted by the satellite. Most of the MSX experiments are amenable to a long-term planning process either because their targets are slowly changing (eg., naturally occurring earthlimb and deep space backgrounds) or because they are under the control of the experimenter (eg., dedicated missile shots). This long-term planning process allows time for the mission planners to communicate with the Principle Investigators to clarify the details of a specific experiment in the planning process. On the other hand the space surveillance experiments designed at Lincoln Laboratory, Massachusetts Institute of Technology require fundamental modifications late

in the planning process on timelines that admit little manual intervention. Thus, the MSX program was faced with a fundamental decision to either implement a highly automated and expensive general purpose planning system which would accommodate the complete set of diverse MSX experiments or to build a long-term planning system for the majority of the experiments and allow a link into the planning process from a more automated system dedicated to planning the space surveillance experiments. For reasons of economy and to minimize the complexity of the entire implementation, the second option was chosen. Since the expertise needed to fulfill the space surveillance mission planning function resides at Lincoln Laboratory, the center for surveillance experiment planning was located there in the SBV Processing, Operations and Control Center (SPOCC).

In order to simplify the planning procedures and to allow the parallel planning of experiments at APL and LL centers, the following three principles were adopted by the organizations involved:

- I. The planning team at LL is responsible for complete operation of the MSX spacecraft and all its sensors during the time period scheduled for a surveillance experiment. Thus, the LL team will receive the MSX in a given standard configuration, known as parked mode, will generate all the command information for both the satellite and sensor sub-systems required to implement the data collection and will return the spacecraft to the standard parked mode upon completion of the event. The LL planning team is responsible for abiding by all spacecraft constraints and operating rules during the conduct of surveillance events
- II. The long-term planning for the space surveillance events will consist of allocating time intervals and resource budgets to the space surveillance events. Thus, it has been agreed that the specific modes of satellite operation for surveillance experiments will be left to be filled in the day prior to conduct of the event. However, during the long-term planning process, the experiment will be scheduled during a specified time interval and the integrated effect on the MSX resources, such as battery depth-of-discharge (DOD) and changes to the spacecraft thermal state will be agreed on a "not to exceed" basis.
- III. The final responsibility for safe spacecraft operations will belong to APL which will check all command information generated by LL. The check will be automated and will be conducted shortly before upload of the commands to the MSX.

These three principles enable the parallel planning of operations at the two centers by clearly separating the responsibilities of each planning center during each of the planning intervals necessary to operate the MSX. However, they also require an overlap of capability between the two planning sites because both must be able to generate command information for the entire satellite. This duplication was accepted as a cost of having a distributed planning system.

The planning system for the MSX goes through four phases of activity as shown in Figures 2 and 3 in order to generate a data collection event for the satellite. The phases and the interaction between the planning centers for surveillance events are described below:

Opportunity Analysis - The planning centers are given experiment priorities on a monthly basis by the BMDO run Mission Planning Team. The priorities are provided six weeks before the start of the month being planned. Once the priorities are received each planning center, the OPC at APL and the SPOCC at LL, analyzes the experiments for which they are responsible to determine feasible times for which data may be collected. For surveillance experiments, items such as target visibility, sun angle and proximity to the earth limb or earth shadow are considered and a list of feasible times is compiled. The opportunity list includes the start and duration of each feasible event start time, the event duration, the relative desirability of that particular feasible time compared with others on the list, an indication of the accuracy of the estimated event start time (eg., if the

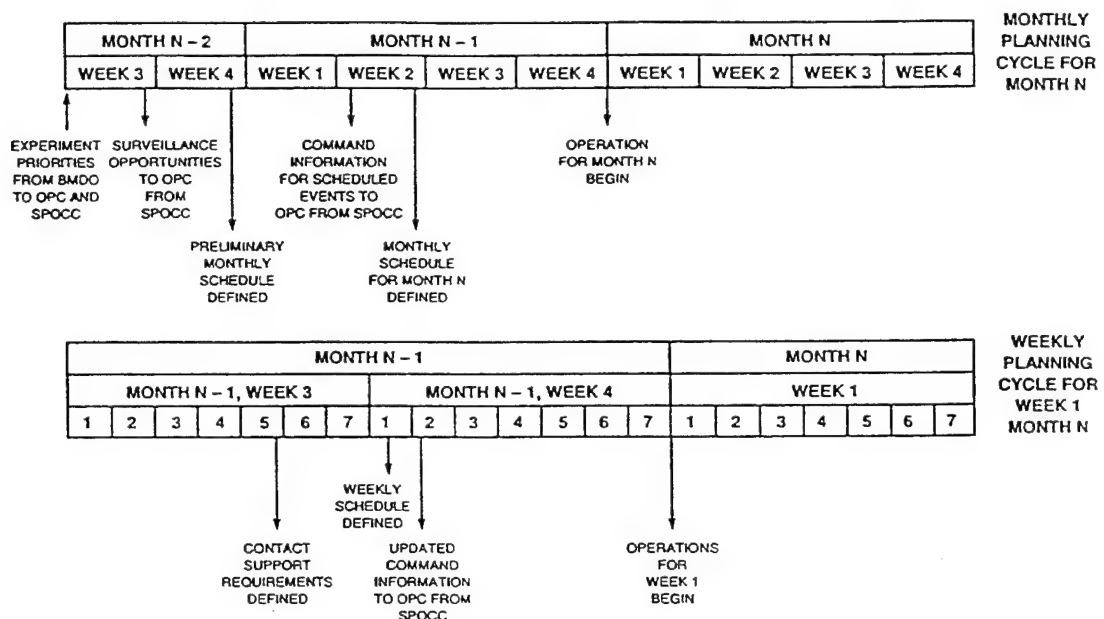


Figure 2. Monthly and weekly planning cycles for MSX experiment

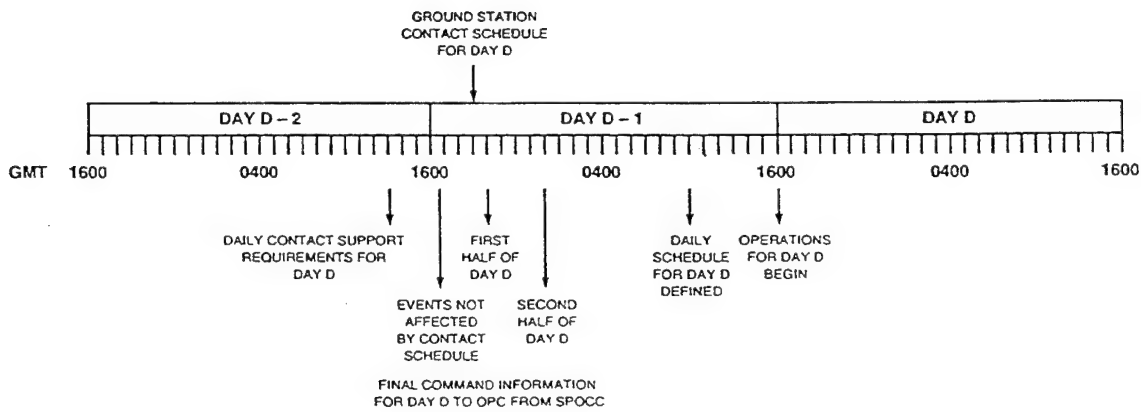


Figure 3. Daily planning cycle for MSX experiments

243594-1

satellite to be observed has a low altitude, the time it becomes visible will not be precisely known (10 weeks in advance) and a pointer to an example set of command information for that type of event. The space surveillance opportunity list and the example command information sets are provided to the OPC for integration with the other experiments in the Monthly Planning Process.

Monthly Planning - The OPC combines the opportunity lists for each of the different types of experiments and constructs a schedule of data collection events to be conducted during the month. Since the MSX spacecraft is not designed for 100% duty cycle, the scheduling process must pay close attention to the use of spacecraft resources. In addition, the cryogenic SPIRIT III sensor is very sensitive to the thermal state and history of the MSX. In order to estimate the resources which will be used by the space surveillance events, the OPC analyzes the sample command information provided by the SPOCC for each event type and estimates the change in battery DOD and the thermal deltas for critical elements. These estimated resource expenditures now become a "not to exceed" budget for the conduct of the surveillance data collection event. The actual pointing and targets may be considerably different, but the integrated effect on the spacecraft resources may not be any larger than that defined during the monthly scheduling process. The OPC generates a monthly schedule for the MSX operations during the month and, after suitable iteration with BMDO and the SPOCC, the schedule is published and the SPOCC provides the OPC with preliminary command information for all of the space surveillance events as scheduled. The Weekly Planning process is then started for the first week of the planning month as shown in Figure 2.

Weekly Planning - Weekly planning is largely used by the OPC to update non-space surveillance experiments to reduce the amount of work needed at the daily planning level. In addition, the uplink and downlink requirements for the earth stations in the SGLS network are compiled and input into the scheduling process at the TSC. For surveillance experiments, the automated SPOCC planning system is re-run taking into account the updated ephemerides for the intended targets (if known at the time) and the MSX, and an update of the event start times is provided to the OPC along with revised command information for each event to be executed during the planning week.

Daily Planning - The final mission planning occurs at the daily planning level, which occurs the day before the events are to be executed on the MSX, as shown in Figure 3. At that time the final uplink/downlink schedules are known, the orbital geometry of the MSX and the targets are available with sufficient accuracy and tasking lists are available from Space Command for tasked experiments. At that time the SPOCC generates final sets of command information for each event during the day and provides them to the OPC for analysis and inclusion in one of the three command upload creation cycles run during each day for the MSX. The SPOCC is responsible for generating command information that is compliant with all MSX constraints, operation rules and resource budgets determined during the scheduling process. The OPC conducts a final, automated analysis of the events as provided by the SPOCC and, if they are compliant with the agreed rules, incorporates them into the command load.

Quick Reaction Events - A number of space surveillance events require shorter timelines than provided by the daily planning process described above. These include events such as the launch of a new satellite, which is scheduled well in advance, but the specific launch time is not known with sufficient accuracy until after the launch. A series of special procedures have been developed to plan events requiring a very quick response from the planning system. The procedures require that an interrupt window be defined at the monthly planning level. The window defines a range of times during which normal MSX operations can be disrupted in order to collect data on a specific event if it happens. The ability to capture the event depends on the availability of suitable pre-scheduled ground station uplinks which may be used to uplink new commands to the MSX. Once a quick reaction event has been declared, the SPOCC will generate commands to observe the satellite based on tipoff information from Space Command (such as the time of launch in the case of a new launch) and will forward the new commands to APL for inclusion in an uplink which will

cancel the existing commands and replace them with those required to execute the quick reaction event observations. Preliminary timing tests run on the planning process indicate that the SPOCC can have the required command information ready for transmission to APL within 30 minutes of the launch and that APL can process the results in time to track a satellite in a transfer orbit to geosynchronous altitude. Final timing tests and procedure verification will take place after a period of operational experience with the MSX under the normal planning process.

## CONCLUSIONS

In order to accommodate the mission planning for a broad range of diverse experiments to be run on the MSX satellite, a distributed mission planning system has been defined and implemented. Under this model, the MSX mission planning is accomplished for all non-surveillance experiments using a long-term planning process at the APL OPC. Space surveillance experiments are planned by LL and carried in the APL planning schedule as event durations and resource utilization budgets without the details of the operation which are provided to the OPC during the final Daily Planning process in command ready form.

This system of distributed mission planning has been developed for a complex, multi-function/multi-mission spacecraft where the expertise needed to conduct mission planning for various mission types is distributed between two locations. The advantage of the process as defined is that the two planning centers can conduct the mission planning functions in parallel, each adding the details of the operation as they are available or according to the capabilities of each planning system. The event is held in the master schedule by budget allocations and schedule place holders until the final details are available. Having each planning center responsible for generating command information for the entire spacecraft for the events for which they are responsible simplifies the interaction between planning centers considerably since each can consider the other's events as "black boxes" until the final details are provided in a complete package. The disadvantage of this approach is that each planning center needs to understand and be capable of commanding every satellite function that will be needed to satisfy their events.

Given that many of the satellites launched currently are large multi-function payloads containing a broad range of instruments, collecting data for a diverse user set, the MSX planning system experience may yield broadly applicable lessons learned. The main requirement to implementing such a cooperative planning system has been a mutual understanding of each participant's mission requirements and a willingness on the part of all parties to consider all the alternatives and to negotiate a sensible approach to solving the mission planning puzzle.

## The MSX Operations Planning Center's Role in the Scheduling and Analysis of Space-Based Surveillance Experiments

R.B. Dickey, J.H. Polaha (The Johns Hopkins University Applied Physics Laboratory)

**Abstract** - The Midcourse Space Experiment (MSX) is a broad-band, multi-sensor satellite sponsored by BMDO. Scheduling, analysis and execution of MSX space-based surveillance experiments is a joint operation between the MSX Operations Planning Team at The Johns Hopkins University/Applied Physics Laboratory (APL) and the Space-Based Visible (SBV) Processing, Operations and Control Team at the MIT/Lincoln Laboratory (LL). This paper will report on the role of the APL MSX Operations Planning Center in the scheduling and analysis of MSX surveillance experiments. MSX operations planning is accomplished in four phases: Long Range, Monthly, Weekly, and Daily Planning. APL is tasked with the direction of all operations planning activities for MSX on-orbit operations. Six to ten weeks in advance of the experiment's execution, the LL provides APL with a list of opportunities when specific surveillance experiments may be scheduled and representative spacecraft configurations for each experiment. APL then interleaves opportunities for both surveillance and non-surveillance experiments in order to develop a monthly (28 day) schedule of MSX activities. Via an iterative scheduling process, which accounts for scheduling priority, difficulty, and resource usage, APL ultimately develops a final monthly schedule which establishes experiment execution times and a resource "cost budget" (e.g., power, thermal, and tape allocations) that must be maintained for each scheduled experiment. On a week-by-week basis, APL refines the monthly schedule and coordinates ground site contact support for all experiments. A day in advance of an experiment's conduct, LL provides APL with the specific command sequence and schedule adjustments for surveillance experiments to be executed. APL analyzes the final version of all experiments, confirms and plans all ground site contact support, produces final daily schedules, and generates spacecraft commands which are transmitted to ground control teams for uplink to the spacecraft. Throughout the monthly/weekly/daily scheduling process, surveillance experiment specifications are analyzed by APL to ensure the operational constraints and spacecraft usage rules are not violated, and the established spacecraft resource budgets are maintained.

### **1.0    Introduction**

The Midcourse Space Experiment (MSX) is a broad-band, multi-sensor, multi-user spacecraft sponsored by the Department of Defense Ballistic Missile Defense Organization (BMDO). MSX will be flown in a circular, near sun-synchronous, low-earth orbit inclined 99° at an altitude of approximately 900 km. The MSX spacecraft launch is expected to occur in the Spring of 1995 from Vandenberg Air Force Base. MSX is capable of simultaneous observations with multiple sensors covering a wide range of wavelengths, from the far-infrared to the far-ultraviolet. Figure 1 shows the configuration of the MSX spacecraft. The primary optical sensors, which all have their optical axes co-aligned with the spacecraft +X axis, are the cryogenically cooled Space Infrared Imaging Telescope (SPIRIT III) Radiometer and Interferometer, the Ultraviolet and Visible Imagers and Spectrographic Imagers (UVISI), and the Space-Based Visible sensor (SBV). SBV is the primary surveillance sensor. Also, MSX has a suite of contamination instruments to characterize the local environment and

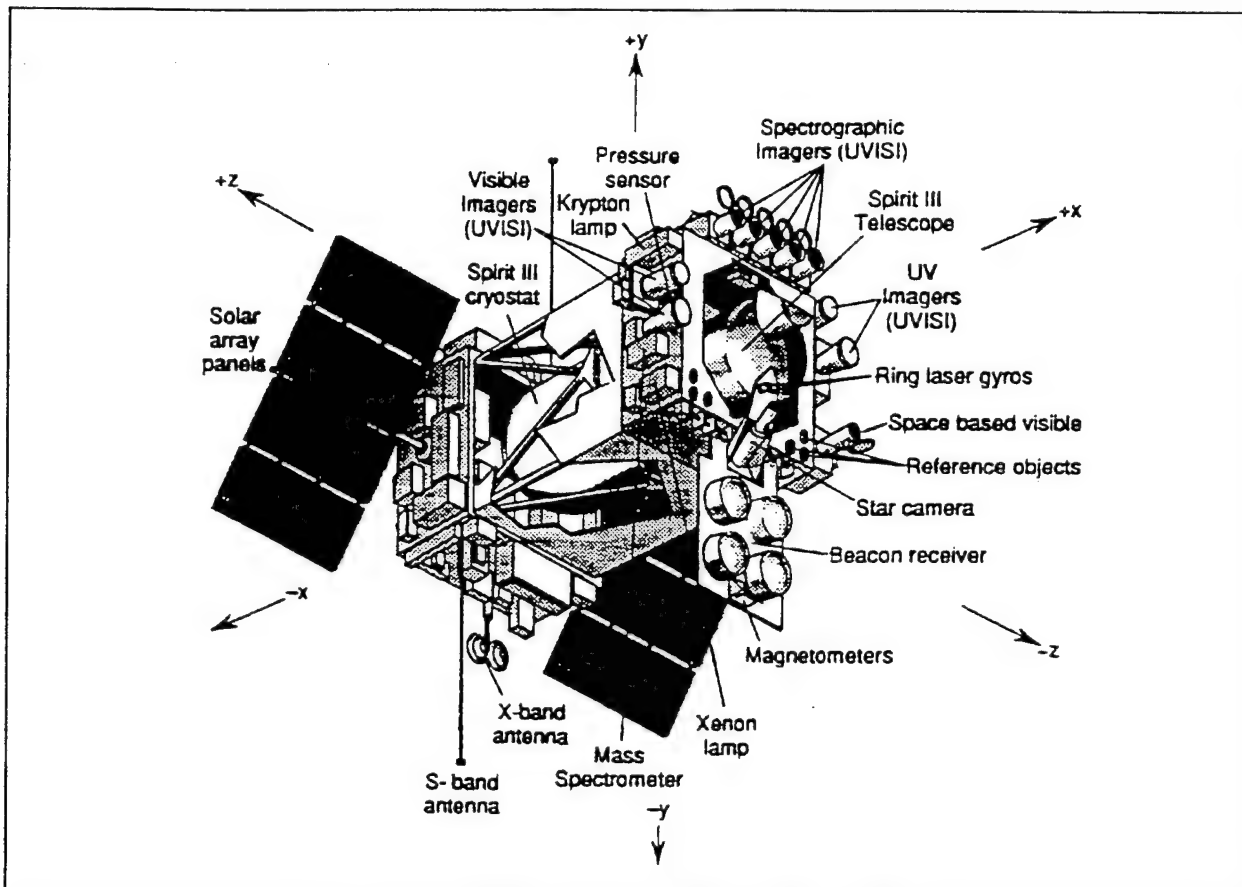


**Figure 1 MSX Spacecraft Configuration**

evaluate its effect on the spacecraft and the primary optical sensors. MSX was designed for a mission life of five years, the first two years of which are for the SPIRIT III cryogenic cooling system.

The MSX spacecraft is designed to detect, track, and discriminate targets against terrestrial, earth limb, and celestial backgrounds. MSX will demonstrate the ability to build, integrate and operate extended duration space-based mid to long wavelength infrared, ultraviolet, and visible surveillance sensors. The functional demonstrations will include target acquisition, cluster track through resolved closely spaced objects, space surveillance, bulk filtering, target tracking data hand-off and data fusion, target discrimination, and the utility of a visible surveillance sensor. Also, MSX with its advanced capabilities has been recognized by the Environmental Task Force, commissioned by Vice President Al Gore, as a dual-use environmental data collection asset that will provide data on global climate change and ozone depletion. Principal Investigators for the MSX program are assigned according to the eight major experiment areas: Early Midcourse Targets, Late Midcourse Targets, Shortwave Terrestrial Backgrounds, Contamination, Data Certification and Technology Transfer, Celestial Backgrounds, Earthlimb/Auroral Backgrounds, and Space-Based Surveillance.

The Johns Hopkins University Applied Physics Laboratory (APL) is the prime contractor, integrator and operator of the MSX spacecraft. Flight operations will be conducted from APL in Laurel, Maryland. A detailed description of the MSX program and the spacecraft is available in the BMDO MSX Mission Planning Document [1]. The MSX Flight Operations Concept of Operations (CONOPS) document [2] describes in detail how the MSX Flight Operations Team will conduct spacecraft operations on orbit. Scheduling, analysis and execution of MSX space-based surveillance experiments is a joint operation between JHU/APL, and the MIT Lincoln Laboratory (MIT/LL). JHU/APL is tasked with the overall direction of all operations planning activities for MSX on-orbit operations. The MIT/LL is involved in operations planning only for surveillance experiments.

MSX Surveillance Experiments are planned at the Space-Based Visible Processing, Operations and Control Center (SPOCC) located at the MIT/LL. The SPOCC uses an automated planning process which includes both detailed and simplified models of MSX spacecraft performance. The SPOCC is responsible for commanding the MSX spacecraft and all its sensors during surveillance experiments. The SPOCC provides the Operations Planning Center (OPC) at APL with representative spacecraft configurations (command sequences) for each surveillance experiment. The OPC, with final responsibility for the spacecraft, performs the final analysis/verification for all SPOCC generated representative spacecraft configurations, otherwise known as Data Collection Events, using APL developed detailed models of MSX spacecraft performance and resource usage. The OPC performs this analysis throughout the planning process and prior to command generation and upload to ensure spacecraft resources are properly used and operational constraints are not violated.

Operations planning for surveillance experiments is unique, compared to non-surveillance experiments, and requires an integrated, coordinated timeline of planning activities and data products between the SPOCC and the OPC. The exchange of data products is intended to allow each planning center to operate as much as possible in their own environment. Each of the planning centers has its own approach, terminology, and tools for operations planning. The SPOCC and OPC work together by exchanging and transforming data files into structures compatible with their own planning tools.

The role of the SPOCC has been reported in various papers by MIT/LL staff members [3, 4]. This paper will report on the OPC role in the scheduling and analysis of MSX space-based Surveillance Experiments.

## **2.0 Scheduling and Analysis of MSX Space-Based Surveillance Experiments**

Operations Planning is accomplished in four stages: Long Range Planning, Monthly Planning, Weekly Planning, and Daily Planning. Each of these phases is discussed below. During the planning process, all phases are occurring simultaneously and continuously. The analysis operations, conducted in the OPC for space-based surveillance experiments, are fundamentally the same during each phase; however, the timelines and emphasis vary. Figure 2 illustrates the overall flow of operations planning for an experiment. Figure 3

illustrates the concurrent three phase Monthly, Weekly, Daily scheduling process.

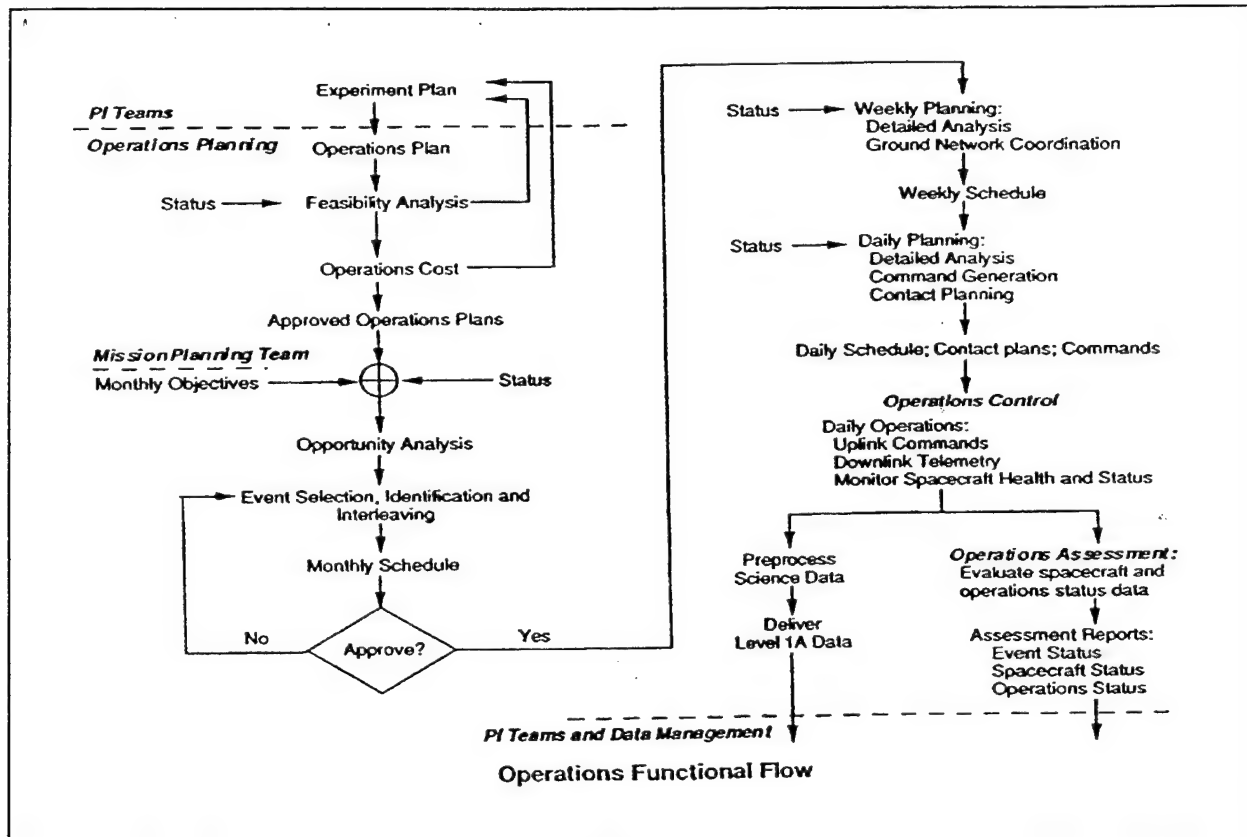


**Figure 2 Operations Planning Functional Flow**

A Data Collection Event, sometimes loosely referred to as an Event (e.g., a Surveillance Event), is a segment of activity on the spacecraft which starts when the spacecraft leaves the Parked Mode configuration, acquires science data, and ends when the spacecraft returns to the Parked Mode configuration. Park Mode is the quiescent mode of the spacecraft, with the +X axis pointing towards zenith and the -Y axis pointing towards the sun, solar panels sun tracking, no data being recorded, and power and thermal equilibrium maintained.

## 2.1 Long Range Planning

Long range planning is the phase where the feasibility of each experiment is determined. Feasibility analysis, as defined in the CONOPS [2], is the evaluation of a proposed experiment using a representative event specification (set of spacecraft commands) to determine whether or not the experiment can be supported by the MSX system, taking into account the spacecraft and ground support network capabilities and constraints. The long range planning period is generally the period of time prior to the MSX spacecraft launch.

		Date shown is Monday of the Week																																
		3-Apr	10-Apr	17-Apr	24-Apr	1-May	8-May	15-May	22-May	29-May	5-Jun	12-Jun	19-Jun	26-Jun	3-Jul	10-Jul	17-Jul	24-Jul	31-Jul															
MPT Monthly Objectives Gen		Month 3				Month 4				Month 5				Month 6																				
		Month 3 Planning Operations						Month 4 Planning Operations						Month 5 Planning Operations						Month 6 Planning Operations														
Monthly Planning Process																																		
Weekly Planning Process								Month 3						Month 4						Month 5														
								Wk 1		Wk 3		Wk 1		Wk 3		Wk 1																		
Daily Planning Process								Month 3		Month 3		Month 4		Month 4		Month 4		Month 5																
								Wk 2		Wk 4		Wk 2		Wk 4		Wk 4		Wk 2																
Month of Mission								Month 3 Wk 1		Month 3 Wk 2		Month 3 Wk 3		Month 3 Wk 4		Month 4 Wk 1		Month 4 Wk 2		Month 4 Wk 3		Month 4 Wk 4												
		Month 1						Month 2						Month 3						Month 4														
																				Month 5														

Figure 3 MSX Advanced and Daily Planning Timeline

Proposed MSX experiments are submitted to the Mission Planning Team by the Principal Investigators. The Mission Planning Team reviews and publishes the proposed experiment plans. The experiments must be declared feasible by APL before the Mission Planning Team will allocate time on the spacecraft for the specified experiment.

The feasibility analysis process for Surveillance Experiments is unique compared to non-surveillance experiments, in that MIT/LL has the primary responsibility for defining the event. APL provides MIT/LL with information on the realities of spacecraft and operational capabilities, and sanity-checks the event. APL is fully responsible for defining and analyzing all non-surveillance experiments. MIT/LL conducts the initial feasibility analysis and transmits detailed information to APL in an Event Definition File (EDF). Each EDF contains all the information required by the OPC to perform event analysis. The OPC processes the EDF, converting it into an Event Specification so it can be analyzed using standard OPC analysis software tools. An Event Specification is a data structure that represents a timed sequence of spacecraft command information that completely defines a single spacecraft event. Event Specifications are used to drive the OPC analysis, command building, and scheduling software.

The OPC performs feasibility analysis for Surveillance Events by conducting a detailed event analysis. The purpose of this analysis is to verify maneuvers and evaluate compliance

with spacecraft operational constraints, verify that the spacecraft power subsystem can support the proposed operation, and estimate the SPIRIT III cryogen usage and thermal recovery time. The results of the analysis are iteratively fed back to the Surveillance Principal Investigator and the SPOCC until all predicted spacecraft performance parameters are within acceptable limits and the experiment is declared feasible.

Where most non-surveillance MSX experiments can be planned in detail months in advance of their execution, only requiring minor timing and/or pointing modifications at the last minute; space-based Surveillance Experiments generally require fundamental modifications the day preceding their execution. Uncertainties in the orbital data for the MSX spacecraft and Resident Space Object targets prevents detailed long range planning and requires last minute fundamental changes on tight timelines for Surveillance experiments. Thus long-term planning of Surveillance Experiments is necessarily limited to allocation of time intervals and resource "cost budgets" based on representative EDF based Event Specifications.

## **2.2 Monthly Planning**

The Mission Planning Team evaluates experiments that have been declared feasible and generates a set of Monthly Objectives, which are transmitted to the OPC no later than six weeks before the first day of the month to be planned.

At the beginning of the monthly planning process, a monthly planning meeting is convened in the OPC to discuss the strategy for planning the month in question. Four weeks of planning are required to plan a month of spacecraft activity. The result of the meeting is a schedule order table which is used to determine the order in which the experiments are to be placed on the monthly schedule. This schedule order table takes into account the Mission Planning Team Priority obtained from the Monthly Objectives and the scheduling difficulty of the event.

An Event Opportunity is a potential time window in which an event could be scheduled. The OPC is responsible for generating event opportunities that satisfy some or all of the objectives for an experiment, except the Surveillance Events. The SPOCC is responsible for the Surveillance Event opportunities, which will not be checked or validated by the OPC. The SPOCC sends the OPC a file containing all the Surveillance Event Opportunities for the planning month. The OPC incorporates these Surveillance Event Opportunities with the non-surveillance events and uses all of these opportunities when scheduling the events for the month being planned.

The SPOCC also sends an EDF, which contains all the information necessary to perform event analysis for surveillance experiments. The EDF is converted into an Event Specification, analyzed as previously described, and used to establish the "cost budget" used in support of the event scheduling process.

Once scheduling opportunities have been defined, the Scheduler begins to place events on the monthly schedule. While placing both surveillance and non-surveillance events on the schedule, the Scheduler must continuously monitor five key cost parameters: (1) tape recorder usage, (2) tape recorder head temperature, (3) battery depth-of-discharge, (4) battery temperature, and (5) SPIRIT III baffle temperature. These cost parameters must be maintained within predetermined tolerance levels, and if any one of the five parameters stray outside the limits, the offending event must be deleted and/or rescheduled.

Several different types of analysis are performed in the OPC to support monthly planning. These analysis processes are grouped into three general areas: orbit analysis, opportunity analysis, and event analysis.

**Orbit analysis** predicts the MSX spacecraft's position, velocity, park mode attitude, orbit milestones, and the visibility of the spacecraft from specified ground stations. Orbit analysis is performed using a spacecraft state vector received from the USAF Test Support Complex. The state vector is validated and then propagated for the month being planned and the results are stored in files which are used to support subsequent event analysis. The orbit analysis files are also transmitted to the SPOCC to support generation and analysis of Surveillance event opportunities and event definitions by the SPOCC.

**Opportunity analysis** is the identification of opportunities to execute a data collection event associated with a feasible experiment in the time frame currently being scheduled. As previously stated, the SPOCC performs the opportunity analysis for Surveillance Events and sends a file of opportunities, along with a set of representative EDF, that establish a preliminary "cost budget" for each opportunity. Before the opportunities are processed and scheduled, all of the representative EDF must be converted into event specifications and verified feasible using the OPC event analysis software.

**Event analysis** includes the functions of kinematic and engagement analysis, power/thermal analysis, and cost analysis. Event analysis also includes an automated verification of proper spacecraft command usage based on a set of rules, and a summary of hard and soft spacecraft operational constraint violations. The event analysis software provides formatted output that feeds other analysis software, can be plotted, or used to create spacecraft configuration, relative geometry, and cost summary reports. The results of this analysis are transmitted back to the SPOCC as verification of successful EDF processing in the OPC.

**Schedule Cost analysis**, a subset of Event analysis, provides the five key cost parameters monitored by the Scheduler. Schedule Cost Analysis is unique in that it is an automated batch process that concatenates all scheduled events and evaluates the ensemble effect for the time period being analyzed, whereas routine Event analysis can only be conducted on one event at a time.

Once the surveillance opportunities are selected by the Scheduler, the schedule times are transmitted to the SPOCC. Mid-way through the monthly planning process, the SPOCC generates and sends to the OPC a separate representative EDF for each scheduled opportunity. After the EDF are converted to Event Specifications, Event analysis is repeated to determine the actual (predicted) effect of each event on the spacecraft. This establishes the final "cost budget" which is not to be exceeded for each Surveillance data collection event.

The monthly planning process ends with the generation and distribution of the Final Monthly Schedule two weeks before the start of the month being planned.

### **2.3 Weekly Planning**

Weekly planning begins two weeks before the start of the week being planned. Orbit analysis is performed for the week being planned. As in Monthly Planning, the orbit analysis files are used to support OPC analysis of all scheduled data collection events. The files are also transmitted to the SPOCC to support generation and analysis of Surveillance Events by the SPOCC.

At the weekly level, the SPOCC analyzes and updates the EDF as necessary for each scheduled Surveillance data collection event and sends them to the OPC. The OPC repeats the event analysis process to verify that all events remain within their allocated "cost budget" and that changes in the event execution time (T-zero) are within acceptable limits. A Daily To-Do List is prepared that describes any special last minute processing and/or analysis requirements and a list of Mission Planning Team authorized constraints violations.

A Weekly Support Plan is generated that contains the ground contact support requirements for (both real-time and non-real-time) downlinking of SBV 1-Mbps science data and MSX housekeeping data. The weekly planning process ends with the generation and distribution of the Weekly Schedule, which is a refinement of part of the Final Monthly Schedule. The weekly planning process requires two weeks to plan one week.

### **2.4 Daily Planning**

Orbit analysis is performed at the start of each planning day to provide both the OPC and SPOCC with the latest orbit geometry data available to support the final analysis of all scheduled data collection events and planning for the day's ground station contacts and science data downlink events.

The ground station contact schedules (both APL and non-APL sites) are confirmed for each day, approximately twenty four hours in advance, and sent to the SPOCC. Final event specifications are completed between thirty six hours and two hours before the uplink of the event command set. The SPOCC uses the latest MSX and target Resident Space Objects orbit geometry data, contact schedules, and tasking lists for tasking experiments, to plan the final version of each Surveillance data collection event. The EDF for these updated

surveillance events are received in the OPC midway through the daily planning process. The OPC converts the EDF into event specifications and performs the final analysis on each one to verify compliance with the "cost budget" established during monthly planning. Data collection events violating any constraint, operational rule, or cost parameter without prior approval will be canceled. Time constraints and staffing limitations do not allow opportunities for last minute correction of events that are determined to be unfeasible by the OPC.

In addition to final analysis of all data collection events, the OPC also plans, schedules and analyzes all of the spacecraft maintenance, ground contact, and science data downlink events for the day being planned. This includes the detailed planning for the SBV 1Mbps science data downlink contacts requested by the SPOCC for each Surveillance Event. At the conclusion of this planning activity, the OPC generates and verifies the spacecraft commands for each Event.

During daily planning, the OPC generates and distributes Daily Schedules, Daily Schedule Updates, Daily Support Plans, Daily Contact Schedules, Contact Plan Reports (Planned), and daily versions of the on-board Tape Recorder Logs.

### **3.0 Conclusion**

The MSX mission planning system design allows for the parallel planning of complex spacecraft operations by two separate planning centers. One remote center contains the expertise and tools to plan specific operations or experiments, while the other center maintains overall responsibility for coordinating all planning operations and for the safe operation of the spacecraft. This system allows the center with overall planning responsibility to conduct independent advanced planning, at the monthly and weekly level, using "cost budgets" established by the remote center early in the planning process. The success of this planning system requires a coordinated interface and exchange of data products on a rigid timeline. The approach used to simplify this interface is to have each center specify all spacecraft commands required for the events for which they are responsible. The disadvantage of this approach is the necessity for each planning center to maintain the redundant capability to command all spacecraft functions needed for their events. The success of this system will establish a legacy for the surveillance community, which has the expertise to plan and conduct space surveillance missions, to support placing surveillance sensors on non-surveillance mission spacecraft. Using the MSX model, future space-based surveillance operations could be conducted without the spacecraft operations center having to acquire an intimate knowledge of the space surveillance mission.

#### **4.0 References**

- [1] "Midcourse Space Experiment Mission Planning Document," Ballistic Missile Defense Organization, PD-0402000-0001-F01.00-930420, 20 April 1993
- [2] "Midcourse Space Experiment (MSX) Flight Operations Concept of Operations," The Johns Hopkins University Applied Physics Laboratory, Space Department SDO-9873, October 1992
- [3] G. Stokes, MIT/Lincoln Laboratory, A. Good, The Johns Hopkins University Applied Physics Laboratory, "Joint Operations Planning for Space Surveillance Missions on the MSX Satellite." Proceedings of the Third International Symposium on Space Mission Operations and Ground Data Systems (Space Ops 94), Greenbelt, Maryland, 15-18 November 1994, 319-326
- [4] R. Sridharan, T. Fishman, E. Robinson, H. Viggh and A. Wiseman, MIT/Lincoln Laboratory, "Mission Planning for Space-Based Satellite Surveillance Experiments with the MSX." Proceedings of the Third International Symposium on Space Mission Operations and Ground Data Systems (Space Ops 94), Greenbelt, Maryland, 15-18 November 1994, 295-303

## The Space-based Space Surveillance Experiment Simulator for the MSX Spacecraft

A. J. Wiseman (Lincoln Laboratory)

### **1.0 Introduction**

The Mid-Course Space Experiment (MSX) spacecraft has been designed and built under the sponsorship of the Ballistic Missile Defense Organization. The spacecraft carries three primary instruments: the SPIRIT III built by Utah State University, the UVISI built by Johns Hopkins University's Applied Physics Laboratory (APL), and the Space-Based Visible sensor (SBV) built by the Massachusetts Institute of Technology's Lincoln Laboratory. APL also built the spacecraft bus and integrated the instruments. The spacecraft will be launched into a near polar, near sun synchronous, low altitude orbit.

The MSX will collect phenomenology data on missiles, plumes, backgrounds, and Resident Space Objects (RSOs). In addition, it will demonstrate the ability to conduct space-based space surveillance. The SBV will be the primary instrument for space surveillance and will be operated by the SBV Processing, Operations, and Control Center (SPOCC) at Lincoln Laboratory. The SPOCC will also gather data using the other instruments.

The mission planning section of the SPOCC will plan, analyze, and command space surveillance experiments. The heart of the mission planning software is the MSX simulator. This paper will discuss the simulator in detail, including its architecture, capabilities, output products, and role in mission planning.

### **1.1 MSX Spacecraft**

The spacecraft's three primary sensors are the SPIRIT III, a cryogenically cooled, multi-band infrared sensor; the UVISI which consists of two visible, two ultraviolet, and five spectrographic imagers and an image processor; and the SBV, a broad-band visible instrument. The SPIRIT III and SBV have on board signal processors. These instruments are co-aligned and rigidly mounted to the spacecraft.

The bus contains the power, thermal, attitude control, and communications systems. The attitude control system has a sophisticated tracking processor which can track a target using sensor data, various tracking algorithms, or commanded attitudes.

The MSX operates under many constraints. These include pointing constraints associated with the sensors

(e. g. thermal loading of the cryogenically cooled SPIRIT III) as well as spacecraft power and thermal limitations.

### 1.3 The SPOCC Mission Planning Pipeline

The SPOCC Mission Planing software performs the following functions:

1. Feasibility Analysis: determine if an experiment can be performed within the operational constraints of the spacecraft.
2. Opportunity Analysis: when can the experiment be performed?
3. Performance optimization: how can the experiment be modified to minimize spacecraft resources usage and improve data collection?
4. Commanding: produce the spacecraft commands needed to conduct the experiment.

The software consists of the mission planning pipeline, its associated data bases, and various analysis tools. The mission planning pipeline (Fig. 1) consists of the simulator, the automatic command generator (ACG), and the command vettor and translator (CVT). The simulator accepts as its primary input a SLED (SBV Language for Experiment Design) file. The SLED file contains all the information needed by the simulator to process an experiment. The simulator in turn drives the rest of the system producing performance data and an Instantiated Mission Timeline (IMT) file. The ACG/CVT parses the IMT and produces an EDF (Event Definition File). This file contains all the data needed by APL to command (and evaluate) the experiment.

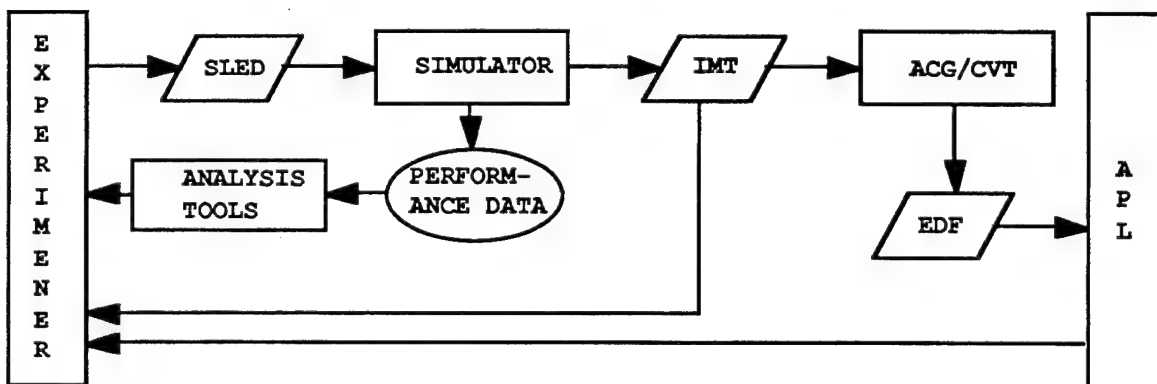


Figure 1. The SPOCC Mission Planning Pipeline

Feasibility analysis, performance analysis, and performance optimization are conducted using the performance data and a set of tools developed by the SPOCC. Note that mission planning is an iterative process. The experimenter processes a SLED file and then gets feedback by analyzing the performance data, examining the IMT, and receiving information from APL after they have concluded their processing. The SLED file can then be modified if necessary and reprocessed.

## 2.0 Simulator Inputs

Figure 2 shows the simulators inputs, outputs and analysis tools. The simulator accepts inputs from both an ORACLE relational data base and flat files.

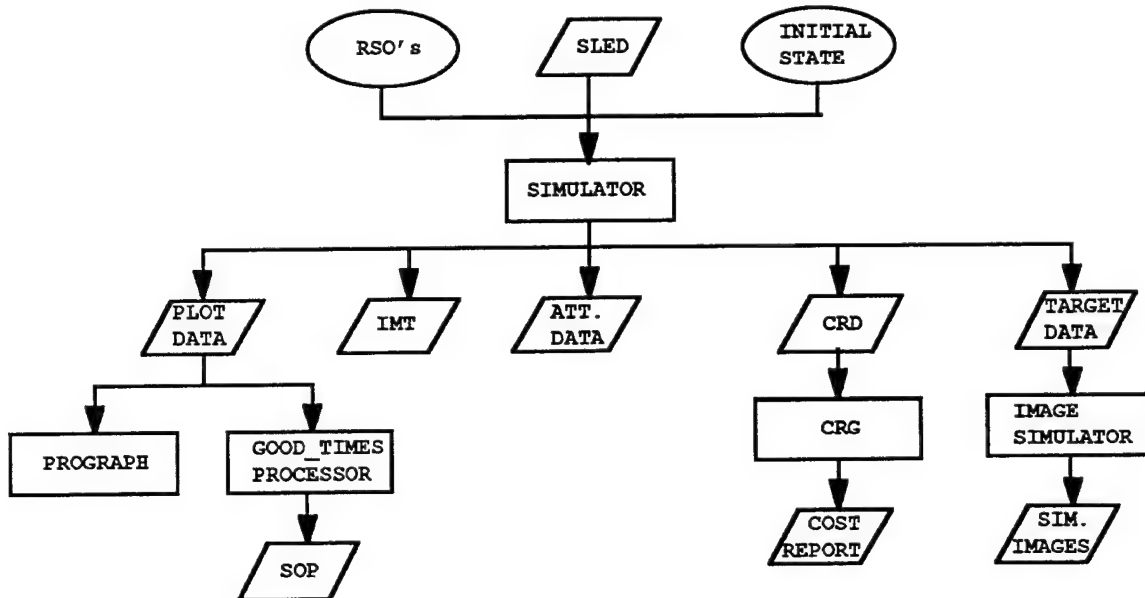
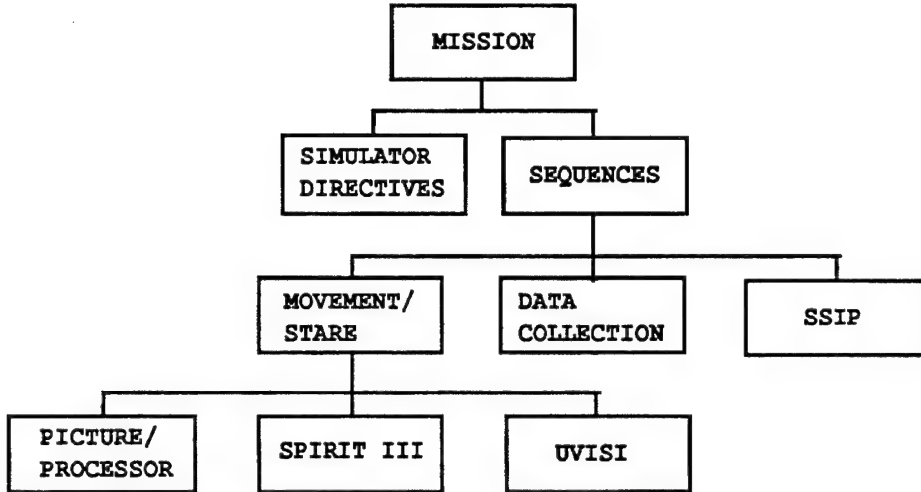


Figure 2. Simulator I/O

### 2.1 SLED

SLED is a compact, high-level language which is used to specify all aspects of an experiment and its simulation. It is structured in such a way as to free the user from the details of experiment timing and commanding. This allows the development of a set of SLED templates, each defining a particular data collection strategy. Once an experiment is scheduled, the user need only set the start time and duration in the template and the experiment is ready for processing.

SLED is hierarchical and has two major branches (Fig. 3). The first branch is composed of the simulator directives which specify the parameters that effect the simulation itself. These include the start time, processing options, and specification of input and output products.



*Figure 3. SLED Structure*

The second branch contains the sequence definitions. A sequence definition can either specify the use of SSIP (the simulator's internal scheduler, see below) or a time ordered, high-level specification of the desired spacecraft operations. The specifications include:

1. Spacecraft tracking mode - MOVEMENT definitions
2. Spacecraft configuration - DATA COLLECTION definitions.
3. Sensor configuration - STARE definitions.

Figure 4 is an example of SLED for a metric calibration track of object 19751. It will take thirty minutes of data and store it on the MSX's tape recorder. At the beginning of the SLED are the simulator directives (SIMDIRs). In this example they are used to set the experiment start time and to specify the output products desired.

## **2.2 Initial State Data**

These data are used to set the initial conditions of the simulator's models. Currently the data base contains:

1. The battery state of charge.
2. The battery temperature.
3. The SPIRIT III baffle temperature.

```

DEF:MISSION(METRIC_CAL)
    SIMDIR(START-TIME = 94:209:11:57:0.0
        ,PROGRAPH-DATA = YES
        ,COST-REPORT-DATA = YES))
    SEQUENCE(RAW_CAL)
ENDDEF()

DEF:SEQ(RAW_CAL)
    DATA-COLLECTION(RAW_DATA_MODE)
    TRACK(ORIGIN(CCD = 3, Y = 210, X = 210)
        ,ROLL(LAW = -Y-TO-EARTH, ANGLE = 0)
        ,OBJ-ID(19751)
        ,STARE(RAW_STARE)
        ,EXPOSURES(1))
ENDDEF:SEQ()

DEF:DATA-COLLECTION(RAW_DATA_MODE)
    TELEMETRY(5-ALT-2)
    SBV-MODE(RAW-DIRECT)
ENDDEF:DATA-COLLECTION()

DEF:STARE(RAW_STARE)
    ALL(1,, PICTURE = RAW_PIC)
ENDDEF:STARE()

DEF:PIC(RAW_PIC)
    CCD(3)
    GAIN(LOW)
    FRAME-COUNT(TIME = 30:0)
ENDDEF:PIC()

```

*Figure 4. Example of SLED*

### **2.3 MSX Orbit Data**

MSX orbit data is used to determine the position of the spacecraft. The user can specify a mean Keplerian element set either in the SLED itself, as an input file, or as a data base entry. Alternatively, an orbital geometry file can be used. This contains a time-tagged listing of the MSX's position, velocity, and park mode attitude and the position of the sun and moon. The data is in Earth Centered Inertial (ECI) coordinates referenced to J2000.

### **2.4 Resident Space Objects**

The simulator can read in a list of Keplerian element sets and their associated object numbers. These can be stored in either a file or in the SPOCC data bases. These element sets allow the user to specify pointing using an object number rather than having to list the element set itself. They are also used in target file processing.

### **3.0 Simulator Outputs**

The simulator produces a variety of outputs. With the exception of the plot and cost report data files, these are human readable. Three tools, Prograph, the Good\_times processor, and the Cost Report Generator (CRG) have been built to analyze simulator output. In addition, there is software to generate the spacecraft commands.

#### **3.1 Instantiated Mission Timeline**

The Instantiated Mission Timeline (IMT) is written to an ASCII text file. It contains a time ordered, time-tagged list of the events that occurred during the simulation. Each event corresponds to a command or set of commands for the MSX (see sec. 4.0). It is passed on to the ACG/CVT where it is translated into the EDF. The IMT file can also be examined by the user (Fig. 5 shows a typical startup sequence).

```
TIME EVENT# EVENT-TYPE EXPOSURES TRACKPTR STAREPTR OBJPTR
0.000      4      TRACK          1          1          1          1

TIME EVENT#           EVENT-TYPE INDEX
0.000      18 DATA-COLLECTION      1
EVENT# 18 COMPLETED AT TIME = 162.000

TIME EVENT# EVENT-TYPE RATE
0.000      8    TAPE_ON 5_2
EVENT# 8 COMPLETED AT TIME = 12.000

TIME EVENT# EVENT-TYPE RESET
1.000      3    SBV_ON  YES
EVENT# 10 COMPLETED AT TIME = 70.000

TIME EVENT# EVENT-TYPE TELEMETRY
13.000     12    TP_ON       5
EVENT# 18 COMPLETED AT TIME = 162.000
```

*Figure 5. IMT Startup Sequence*

#### **3.2 Plot Data**

The plot data file contains the details of resource usage and spacecraft performance. The data includes constraint angles, power and thermal data, target data, and ground station visibility information. This in turn can be used by Prograph and the Good\_times processor. Prograph is a graphical interface tool which allows operations personnel to analyze, manipulate, and format the simulated data (Fig. 6). The Good\_times processor uses the plot data to automatically determine and list all the feasible times that an experiment can be scheduled.

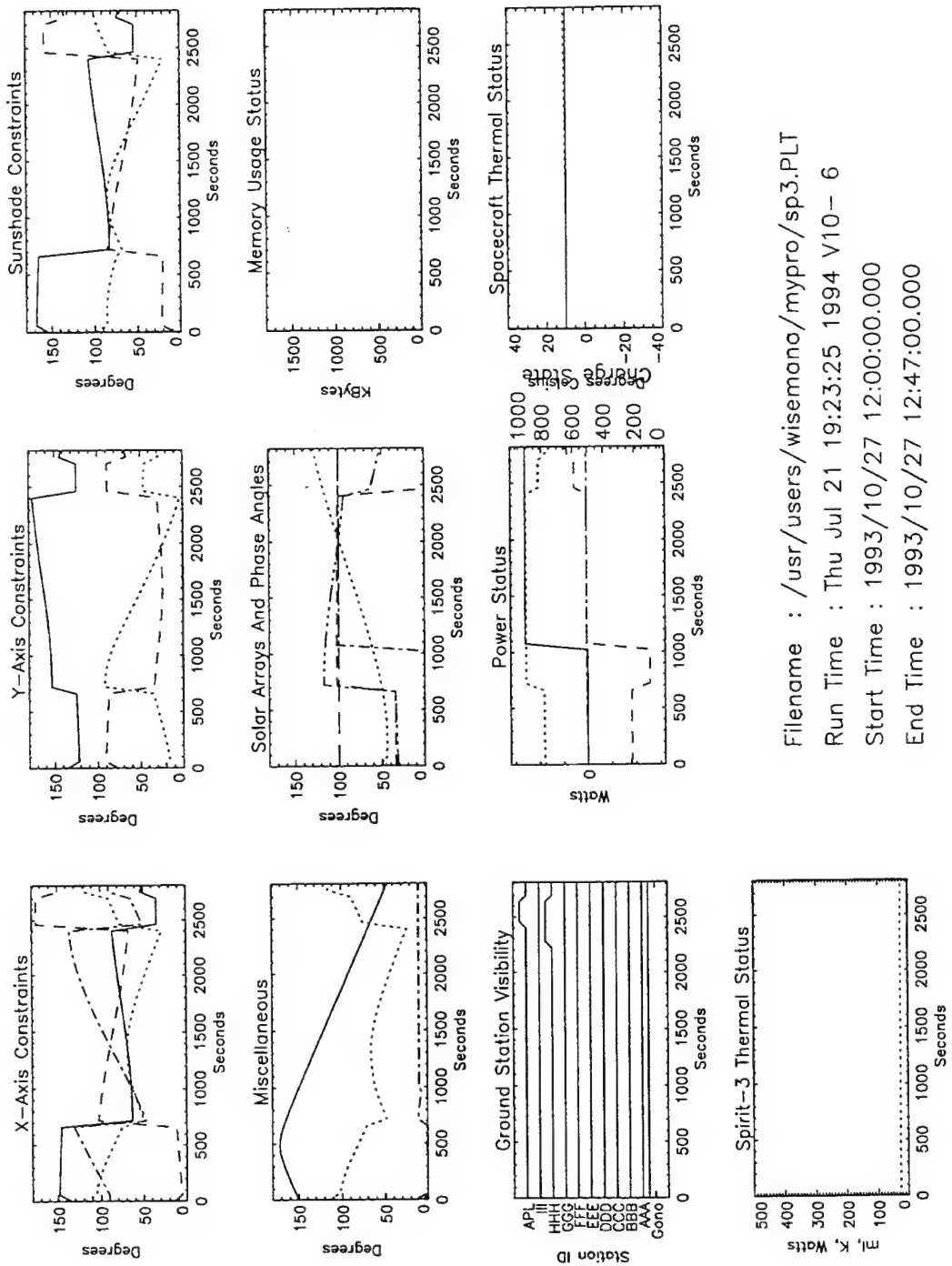


Figure 6. *Program output*

### **3.3 Attitude Data**

The attitude data file is an ASCII text listing of the position, velocity, and attitude of the MSX spacecraft; the position and velocity of the target (where the MSX is pointing); and the position of the sun and moon. The data is in ECI coordinates referenced to J2000.

### **3.4 Target Data**

The target file is a listing of the results of each SBV observation and is used to predict the data quality of an experiment. It can be examined by an operator or it can be used to create simulated SBV data with the SBV Image Simulator.

The simulator can be configured to read in a list of element sets of candidate RSO's and produce a listing of the ones that were visible to the SBV. For each SBV observation the simulator lists the time, position, velocity, and attitude of the spacecraft and the state of the SBV camera. Next it determines which candidate RSO'S are visible to the SBV. For each visible RSO the simulator lists its position and velocity, approximate focal plane position, illumination status, and relevant phase angles. At the end of the file is a summary of all of the data.

### **3.5 Cost Reports**

The cost report data (CRD) file contains power/thermal values, constraint avoidance angles, and timing information. This in turn can be passed on to the Cost Report Generator (CRG) which produces a compact listing of resource usage (Fig. 7).

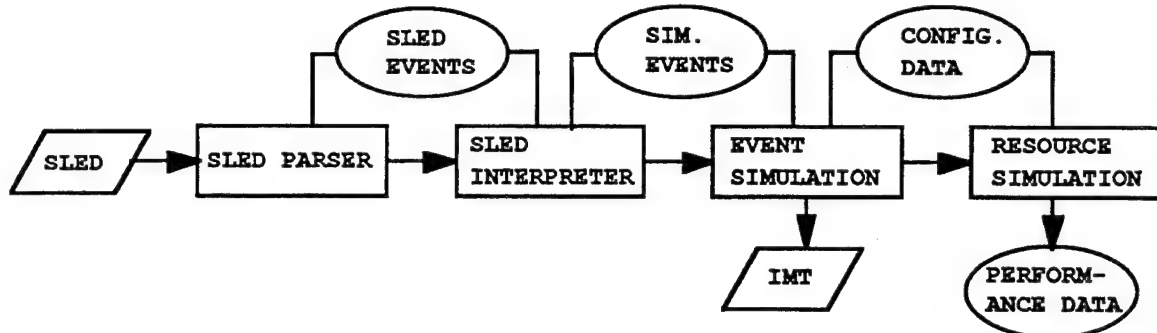
## **4.0 Architecture**

Figure 8 shows an overview of the simulator's architecture. A SLED file is parsed and checked for syntactical and logical errors. The parser then produces a time ordered, parameterized queue of events to be simulated along with a set of associated data tables.

The SLED interpreter takes each SLED generated event and decomposes it into a series of simulation events. Each simulation event corresponds to a configuration change in the spacecraft, a new set of tracking processor commands, or a new set of sensor commands. These events are in turn used to drive a standard discrete event simulation. The time-tagged listing of the relevant events is output as the IMT file. The event simulation also loads data structures with the spacecraft configuration as a function of time including the parameterized tracking processor commands. These

EVENT SPECIFICATION SUMMARY		YYYY:DDD HH:MM:SS.SSS		YYYY:DDD HH:MM:SS.SSS	
FIRST COMMAND	1995:001:12:05:00.000	PREVIOUS ECLIPSE EXIT	1995:001:10:50:27.000	PRESENT ECLIPSE ENTRY	0:00:00:00:00:000
FIRST MANEUVER	1995:001:12:07:25.000	PRESENT ECLIPSE EXIT	0:00:00:00:00:000	NEXT ECLIPSE ENTRY	0:00:00:00:00:000
EVENT T-0	1995:001:12:05:00.000				
LAST MANEUVER	1995:001:13:47:55.000				
LAST COMMAND	1900:001:13:48:30.000				
Status at event start, nominal?		YES	NO	If NO, attach details	
Status at event end, within constraints?		YES	NO	0	
Tape Recorder Starts (# of starts)				00:00	
Tape Recorder storage at 25 Mb rate (MM:SS)				542	
Command memory storage (# of commands)				52.073966	
Aperture Heat Load (Watt*hr)				86.820408	
Final baffle temperature (K)				12.891654	
Cryogen Depletion during event (grams of solid H2)				0.000050	
Cryogen depleted while returning to steady state (grams of solid H2)				0.000000	
Total cryogen depleted (grams of solid H2)				12.891654	
Depletion is 0.230000 times amount depleted if left in park mode.					
Time to return to steady state (HH:MM:SS)				0:38:24	
Coordinated Range Events?	YES	NO	NO	If YES, attach details	
Collateral Sensor Events?	YES	NO	NO		
POWER/THERMAL SUMMARY					
Total Energy consumed (kwatt*hr)	1.633	MAX	MN	Ave	START END
Total Power (watt)	908.000	881.000	907.11	881.000	896.900
Array Power (watt)	1300.000	0.000	954.050	1300.000	1300.000
Battery Power (watt)	419.000	-908.000	46.879	419.000	403.100
Battery Voltage (v)	34.100	26.400	32.531	34.100	34.100
Battery DOD (percent)	25.222	0.000	13.019	0.000	2.778
Tape Recorder 1 Temperature (deg C)	10.000	10.000	10.000	10.000	10.000
Tape Recorder 2 Temperature (deg C)	10.000	10.000	10.000	10.000	10.000
Spirit III Sunshade Temperature (deg C)	0.000	0.000	0.000	0.000	0.000
Battery Temperature (deg C)	10.000	10.000	10.000	10.000	10.000
SIMPLE POWER/ THERMAL MODELS					
Total Energy consumed (kwatt*hr)	1.633	MAX	MN	Ave	START END
Total Power (watt)	908.000	881.000	907.11	881.000	896.900
Array Power (watt)	1300.000	0.000	954.050	1300.000	1300.000
Battery Power (watt)	419.000	-908.000	46.879	419.000	403.100
Battery Voltage (v)	34.100	26.400	32.531	34.100	34.100
Battery DOD (percent)	25.222	0.000	13.019	0.000	2.778
Tape Recorder 1 Temperature (deg C)	10.000	10.000	10.000	10.000	10.000
Tape Recorder 2 Temperature (deg C)	10.000	10.000	10.000	10.000	10.000
Spirit III Sunshade Temperature (deg C)	0.000	0.000	0.000	0.000	0.000
Battery Temperature (deg C)	10.000	10.000	10.000	10.000	10.000
POINTING/TARGET SUMMARY					
Time X axis to RAM < 20 deg (MM:SS)	00:00	Range to target		Min (km)	42112.764
Min X axis to Sun (deg)	38.465	Max (km)		Max (km)	4299.271
Moon (deg)	31.962	Start (km)		Start (km)	42317.775
RAM (deg)	90.000	End (km)		End (km)	42611.220
Max angular accel (deg/sec**2)	.019	Min LOS tangent (km)		Min LOS tangent (km)	891.737
Max angular velocity (deg/sec)	1.022	Max wheel power (watts)		Max wheel power (watts)	300.000
Max wheel torque (Nm)	1.547	ROLL LAW		SCAN PATTERN	
TRACKING PROCESSOR MODE		3 - body -Y axis towards earth		5 - time reference scan	
7 - local vertical with azimuth, elevation					

Figure 7. Cost report



*Figure 8. Simulator Architecture*

configuration data are used to drive a simulation of the attitude control, power, and thermal systems. The resulting performance data is processed and/or formatted and output to the various data files.

#### **4.1 Models**

##### **4.1.1 Orbital Mechanics**

ORBLIB is a library of orbital mechanics routines developed at Lincoln Laboratory. It consists of two analytical propagators developed at Lincoln (ANODE and ANODER), SGP4, and a numerical propagator along with a set of utility routines. ORBLIB is used to determine the position of the MSX, RSO's, and the moon and sun, and for routine calculations such as coordinate conversions.

##### **4.1.2 Attitude Control System**

The attitude control system is modeled using software developed at APL (Magellan). Magellan is very similar to the system on the spacecraft but with the mechanical inputs and outputs modeled in software. It takes as input a set of files corresponding to spacecraft commands and uploadable parameters and produces an attitude history. Optionally, the operator can select a very simple model which ignores spacecraft dynamics (the simulation assumes pointing error is always 0). This can be used for quick look and opportunity analysis.

##### **4.1.3 Power/Thermal Systems**

There is a detailed model of the power system which was also developed at APL. It includes modelling of the solar panels, batteries, and power electronics. Again, there is a simple model available for quicklook analysis.

General Research Corporation (GRC) has developed a model of the thermal behavior of the SPIRIT 3 sensor. It takes as inputs the relative position of the sun and earth, the operating mode of the instrument, and the temperatures of the

baffle, shell, and sunshade. It tracks aperture heat load, baffle temperature, and cryogen usage.

Finally there are simple, linear models of the battery and tape recorder temperatures. APL has also developed a detailed nodal analysis of the spacecraft's critical temperatures. At present this is not implemented.

## 4.2 Automation

Due to the complexity of the MSX system and available staffing levels, every effort has been made to automate mission planning tasks. In the simulator, the Space Surveillance Interface Processor (SSIP) has been developed to automatically generate search and tasking scenarios. The simulator also handles contact scheduling and processing.

### 4.2.1 SSIP

The SPOCC has developed the SSIP to schedule tasking and searching experiments while minimizing MSX resource usage. The SSIP accepts a tasking file as input (Fig. 9). The tasking file is used to specify the scheduling algorithm and

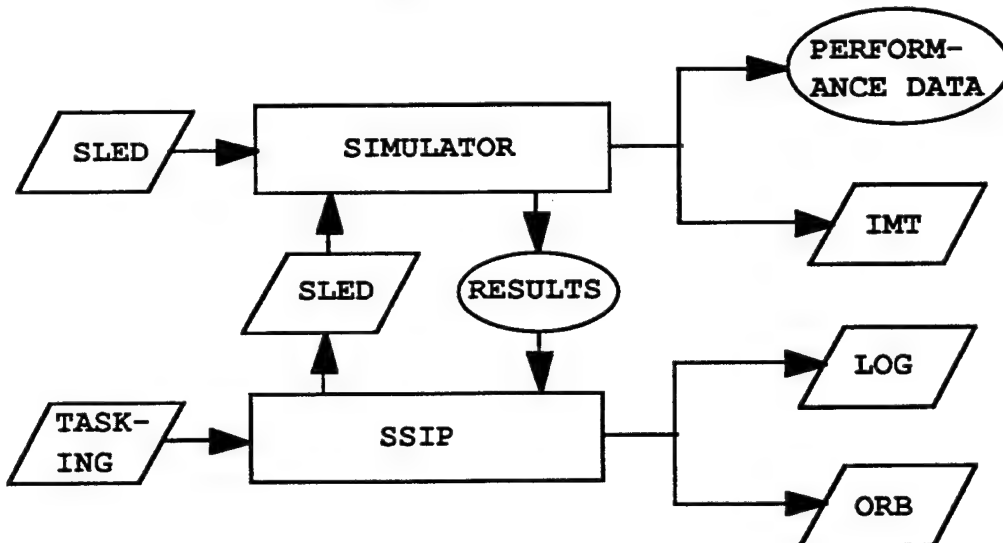


Figure 9. SSIP Processing

its parameters, tasking information, and processing options. It allows the user to specify a complicated set of observations in a very compact format. At present SSIP has two schedulers, one for geosynchronous searches and one for tasking. The structure of the software allows for the addition of more algorithms.

SSIP processing begins with the SLED file specifying the use of SSIP. The simulator calls SSIP which schedules a set of observations and outputs a SLED file. The simulator processes

the SLED and returns the results of the intermediate simulation which SSIP uses to update its schedulers. This continues until the schedule is complete. Finally the simulator finishes its normal processing and produces its standard outputs.

Two types of output are produced: log and ORB files. The log file contains a detailed listing of the SSIP's processing. Optionally, SSIP can also produce an ORB input file. ORB is a Lincoln developed, three dimensional, animated graphics display which shows the results of a simulation including the MSX, sun, moon, targets, other RSO's, and tracking information.

There are two concepts of interest in SSIP, pseudo-objects and the figure of merit (FOM). Pseudo-objects are used to produce search spaces. For instance, to search along the geosynchronous belt a set of pseudo-objects would be generated. Each object would have a mean anomaly less than one field of view apart. As SSIP tasks an observation of each object, the search space is covered.

The FOM is computed to determine which object should be tracked next. It is calculated by multiplying a series of weighting factors. These factors include the geometry and dynamics of the orbits of the RSOs, their reflectivity-area product, and the characteristics of the background against which they are observed.

#### **4.2.2 Contact Scheduling**

The MSX spacecraft relies on a set of ground stations to upload commands and download data. The simulator is capable of automatically requesting and responding to contacts with these ground stations. Once a data collection event (DCE) is scheduled, a simulation of the event is conducted. It determines the number of contacts needed to download the data in the SBV's RAM. These contact requests can then be sent to APL. After contacts are scheduled, the simulator automatically responds to them by generating the commands necessary to achieve the appropriate spacecraft configuration and attitude.

### **5.0 Summary**

The simulator, its data bases, and the ACG/CVT along with the various analysis tools comprise the SPOCC mission planning system. The simulator and its output products drive the rest of the system.

The MSX is extremely complex. The MSX simulator was designed and built to minimize the complexity that the user sees. This has been accomplished through a combination of a sophisticated user interface, analysis tools, and automation.

The user interface, SLED, has been designed to free the user from the details of spacecraft timing and commanding. SLED also allows the user to build up a library of experiment templates. The three analysis tools Program, Good\_times and the CRG allow the user to quickly and easily analyze the data produced by the simulator.

Finally, the simulator's ability to automatically schedule contacts and to do search and tasking schedules internally frees the operator from a lot of tedious analysis.

## **6.0 References**

1. The SPOCC Team, private communication, 1992.
2. SPOCC Mission Planning Team, private communication, 1994.
3. R. Sridharan, et al.: "Mission Planning for Space-based Satellite Surveillance Experiments with the MSX", Third International Symposium on Space Mission Operations and Ground Data Systems, NASA Conference Publication 3281, Nov. 1994.

## Geosynchronous Surveillance With A Space Based Sensor

W.F Burnham, R. Sridharan (Lincoln Laboratory, Massachusetts Institute of Technology)

### **1. Introduction**

The geosynchronous equatorial belt contains a variety of vital strategic, communications and weather satellites. In addition, there are also inactive satellites, rocket bodies and other debris in the belt. A major task of space surveillance is to maintain a catalog of orbital elements on resident space objects (RSOs).

USAF operates the Space Surveillance Network, part of whose mission is to collect adequate data to support cataloging and monitoring of these geosynchronous RSOs. The sensors contributing to the task are all ground-based. Such a sensor has restricted visibility of RSOs in the geosynchronous belt due to synchronism with the earth's rotation. Hence, at least three ground-based sensors are required for complete coverage of the belt.

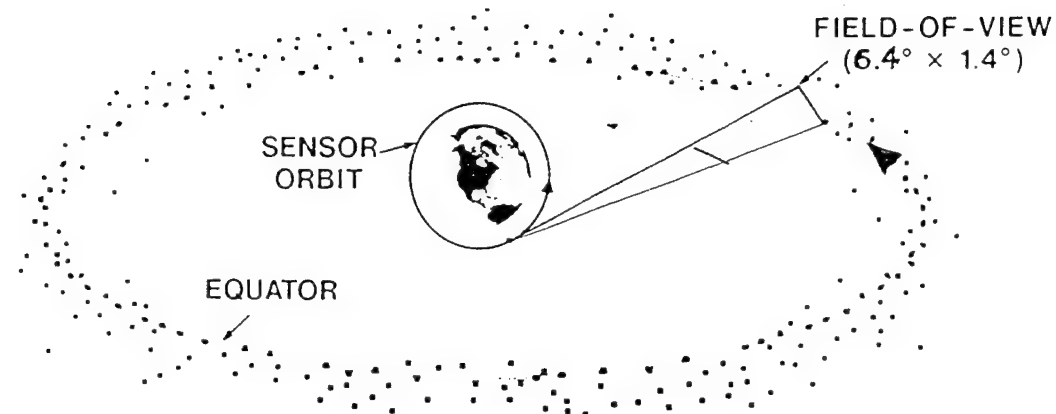
The USAF sensors are comprised of active microwave radars, passive visible wavelength optical sensors and RF telemetry instruments. Radars are all-weather sensors but they are slow in surveillance of targets at geosynchronous distances. Telemetry sensors can of course track active satellites only, which constitute less than 10% of the catalog of objects. Visible wavelength optical sensors generally have larger field-of-view (FOV) than the radars, and can also detect the RSOs in geosynchronous orbit more rapidly, but they are dependent on clear night-time conditions for operation, particularly in long-range surveillance. Hence, the operational efficiency of the ground based optical sensors is poor.

A space based optical sensor would have the advantage that cloud cover would no longer be a problem nor would they be precluded from operating in "daylight". Thus, near continuous operation can be achieved.

A space-based sensor in low altitude orbit also has unrestricted access to the entire geosynchronous belt due to its orbital motion. Hence, a single sensor has the unique capability of surveying all geosynchronous RSOs (see Figure 1).

Demonstration of space-based space surveillance is one of the tasks of the MSX satellite which will be launched in 1995. The MSX has been built by the Applied Physics Laboratory of Johns Hopkins University. The primary sensor for space surveillance experiments is the Space-Based Visible (SBV) sensor. This sensor was designed and built by MIT Lincoln Laboratory. The SBV uses a 6" aperture off-axis reimaging telescope, a sensitive CCD camera and an on-board signal processor to detect RSOs against the stellar background.

This paper describes the development of a scheduling strategy for geosynchronous surveillance with a space-based optical sensor. The problem is described and the design of the Scheduler is elaborated with particular stress on aspects that are conditioned by the spacecraft. The population characteristics of the RSOs in the geosynchronous belt are exploited in the design to enhance the efficiency of the search. Simulation results are presented. The concepts will be tested with the MSX satellite in the near future.



MSX Geosynchronous Coverage  
Figure 1

## 2. The Problem

The problem addressed in this paper is the design of a Scheduler to search the geosynchronous belt with a space-based sensor (the SBV) and collect metric data on all detectable resident space objects in the belt. The Scheduler generates an “optimal” search and data collection strategy given the constraints of MSX location, visibility of the geosynchronous belt and, most importantly, the constraints of the sensor (SBV) and the spacecraft.

Geosynchronous satellites occupy orbits with a range of inclinations to the equator. A fundamental requirement on the Scheduler is to conduct a leak-proof search of the geosynchronous belt for all detectable cataloged and uncataloged RSOs below a user specified orbital inclination.

The Scheduler must also contend with the method of allocation of spacecraft time for experiments. A long continuous block of time is unlikely to be available. Hence, the Scheduler has to be able to split a single search experiment over several non-contiguous blocks of time.

## 3. Description of the MSX and the SBV

The MSX satellite is due to be launched in 1995 and will be placed into a slightly retrograde, nearly sun synchronous circular orbit ~900 kilometers above the earth. Several sensors are available on the satellite, including the Space Based Visible (SBV) sensor. Relevant parameters of the SBV are given in Table I.

It is anticipated that the SBV will be able to detect satellites which are dimmer than 14th magnitude. The SBV telescope uses four CCD's as detectors, arranged in a row as shown in Figure 2. The total field of view of the 4 CCDs is 6.6 deg. x 1.4 deg. because of the considerable distortion of the off-axis telescope design. The design of the SBV enables data from only one CCD to be processed at a time. The SBV has a signal processor that enables detection of stars and target streaks by processing a set of frames of raw data from a CCD. Data can be read out of the camera at a rate of one frame per 0.4 s. or 1.6 s. Typically, either 4,8, or 16 frames of data (a frame set) are collected and sent to the signal processor. The signal processor takes ~50 seconds to process the data, thus slowing the rate of operation of the sensor.

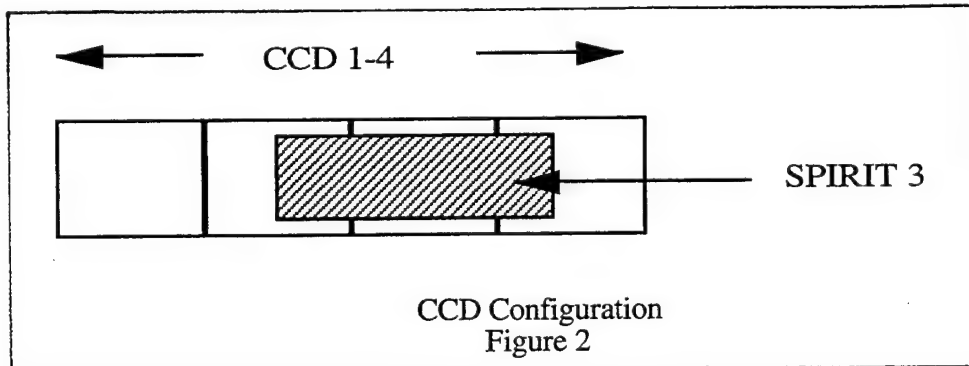
TABLE I

PARAMETER	VALUE
Instantaneous Field-of-View	1.4 deg. x 1.4 deg. per CCD
Number of CCDs	4
Number of pixels per CCD	420 x 420
IFOV per pixel	12"
Detection Sensitivity	pφA of 0.5 m <sup>2</sup> at 36000 Km.
Processed Metric Accuracy	4"

The SBV is rigidly fixed to the main platform and is not gimballed. All sensors on the MSX are coaligned and point along the spacecraft X-axis. The angular acceleration and angular velocity of the platform are subject to restrictions of 0.0250/s<sup>2</sup> and 1.60/s. The solar panels are articulated about the Z-axis, but can rotate only at 0.10/s to track the sun.

The SPIRIT 3 infrared (IR) sensor aboard the MSX has a dewar containing solid hydrogen to cool the focal plane. Control of the depletion of the cryogen due to thermal inputs from the sun or the earth is a very important factor in prolonging the life of the sensor. Hence, there are constraints on the attitude of the spacecraft.

The MSX is in a near-sun-synchronous orbit, with shadow periods that could be as long as a fourth of the orbital period. The solar panels generate approximately 1.2 KW when in full sun. A set of NI-H batteries provide power during shadow, or when demand exceeds power generated by the panels. Overall system requirements restrict the battery depth of discharge to 40%.

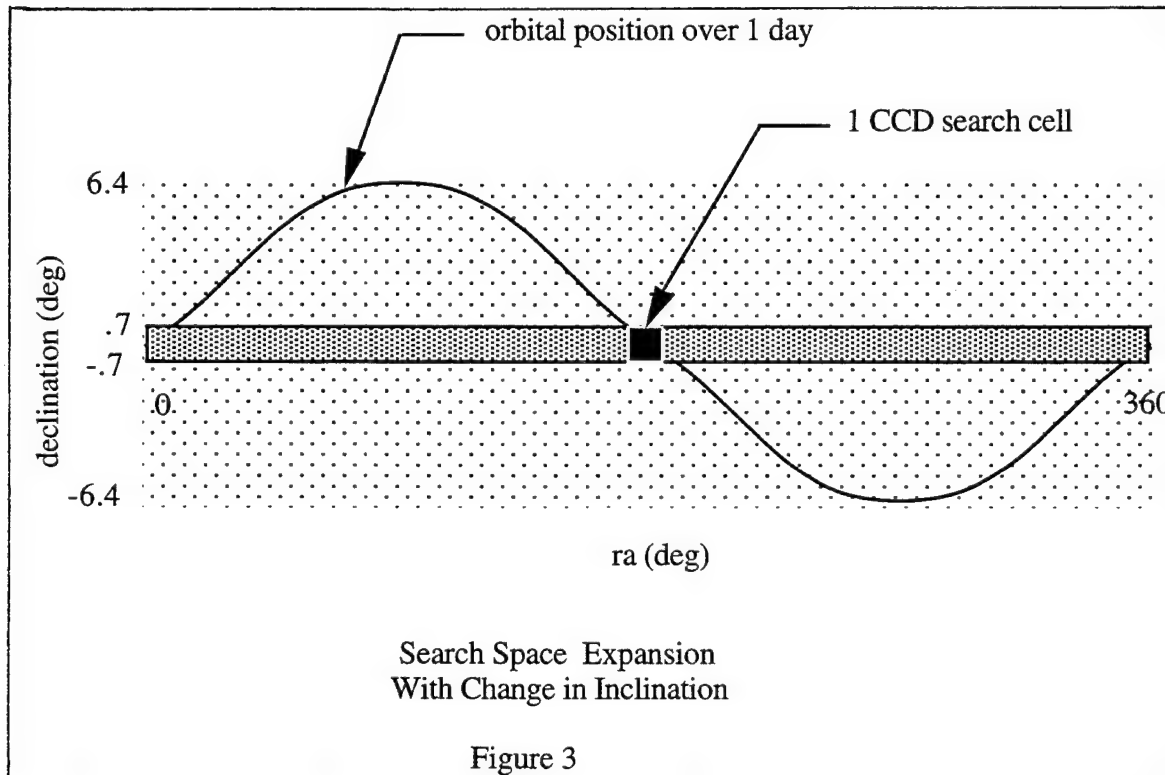


#### 4. Scheduling Concepts

The Scheduler chosen is designed to be locally optimized in time. It chooses the "best" search location based on the current time. This method has been used in schedulers designed for the Millstone Hill radar as well as other sensors of the space surveillance network.

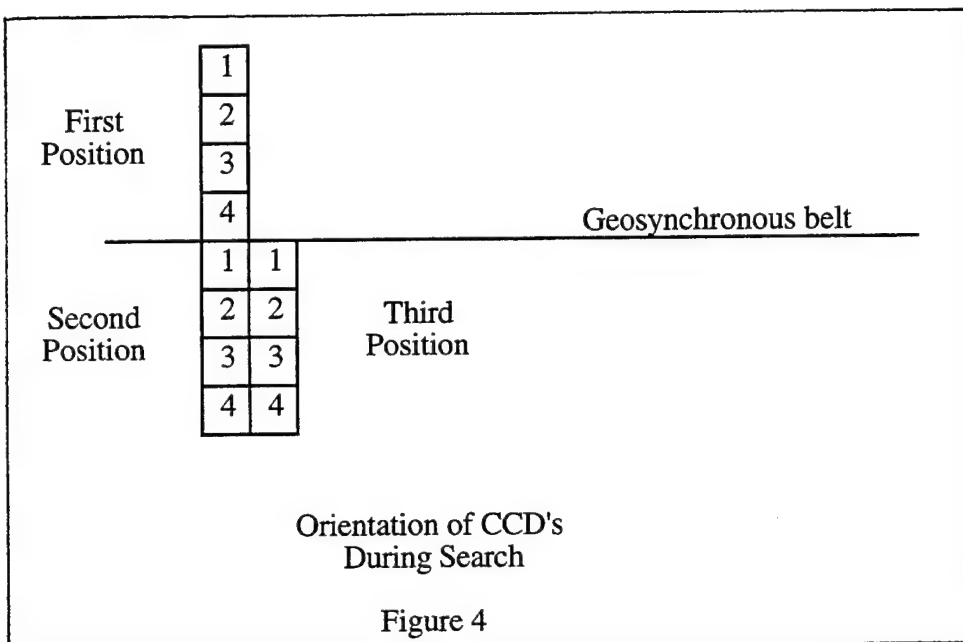
#### 4.1. Search Algorithm

The inclinations of the orbits of geosynchronous satellites usually are small, but can range to greater than 15 degrees. This implies that a 2-dimensional search is required - both along the equatorial belt and across the belt - for efficient, rapid search. Figure 3 shows that the search area increases significantly as the inclination uncertainty increases.



The search algorithm chosen is designed to find all objects with an orbital inclination less than 6.4 degrees. This range of inclinations covers 63% of the known catalog of geosynchronous RSOs. Since an object with a non-zero inclination can be located either above or below the equator at any instant, it is necessary to search both  $\pm$  6.4 degrees from the equator at each position. The SBV contains four CCD's, with a total field-of-view of 6.4 degrees. Therefore, if the SBV focal plane is oriented normal to the plane of the equator, and uses all four CCD's, it is possible to cover the across orbit uncertainty with only 2 movements of the spacecraft (see Figure 4). A total of 8 frame sets are needed to cover the inclination search space for this single position along the belt. This search method is used for each position along the geosynchronous belt chosen by the scheduler.

It is evident that other orientations of the focal plane can also achieve the same objective. Also, some geosynchronous RSOs in orbits with inclinations higher than 6.4 deg. will be detected in this fence. Further, a fraction of the entire high altitude satellite population will also be detected in this search. These ideas will be quantified later in this paper.



## 4.2. Concept of Pseudo-Objects

The search algorithm is seeded by "pseudo-objects". A pseudo-object is an element set for a RSO that shares the characteristics of the population of RSOs being sought.

An element set is created for an object located at any chosen longitude along the geosynchronous belt. Additional pseudo objects that vary in mean anomaly (and therefore longitude) from this "seed" element set are then created so as to cover the entire belt (or any subset) by varying the mean anomaly only. The Scheduler then examines each of the pseudo objects as though it were a discrete object, and determines which of the objects is the best to attempt at the current time.

A leak proof fence is assured by choosing the granularity of the pseudo objects (i.e. the longitudinal separation from its neighbor) such that at least two pseudo objects are visible within the FOV of a CCD. If the completeness test fails, additional pseudo-objects are created to meet the condition.

## 4.3. Scheduler Operation

The Scheduler generates a sequence of search positions in the geosynchronous belt for the SBV. Given a group of (pseudo)objects to schedule, the scheduler creates a figure of merit (FOM) for each object using a set of criteria. The objects are ordered by the value of the FOM and the object with the highest FOM is scheduled. If for any reason the selected object cannot be scheduled, the object with the next highest FOM will be attempted until the list is exhausted. Thus, the determination of the figure of merit is the crux of the scheduling process.

## 4.4. Algorithm for the Figure of Merit

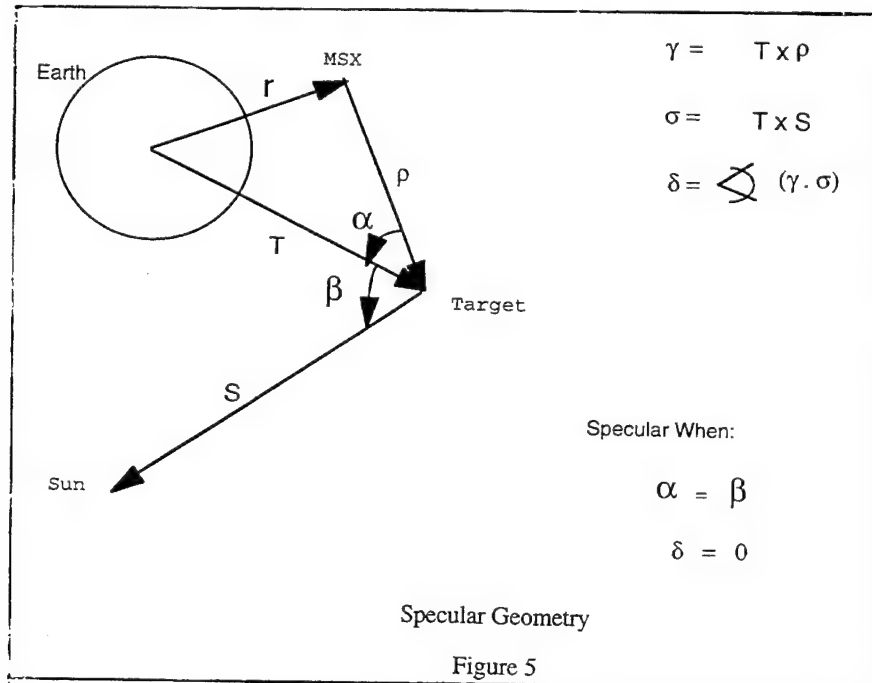
The FOM is the product of a series of factors.

$$FOM = f_1 * f_2 * \dots$$

Any factor set to zero will cause the FOM to be zero and the object cannot be scheduled.

The geosynchronous scheduler uses 9 factors in computing the figure of merit. A command is available within the program that lets the user select any or all of the 9 factors for consideration. Those not selected will be set to the neutral value of 1.

- $f_1$  - a conditioning factor  
always set to 300 for the Geosynchronous Scheduler
- $f_2$  - specular reflection factor  
increases the FOM if the object is near the specular reflection geometry condition as shown in figure 5.
- $f_3$  - soft constraint factor:  
decreases the FOM if the object violates certain soft constraints. Soft constraints are those that temporarily degrade the MSX operation but do not cause damage. Hard constraints are those that potentially can cause damage or permanent degradation of the spacecraft or the sensors and therefore will never be violated.
- $f_4$  - right ascension factor:  
(see the following section on the right ascension factor)
- $f_5$  - current pointing factor:  
increases the FOM if the object is near the current pointing of the X-axis of the spacecraft
- $f_6$  - time to set factor:  
sets factor to zero if the object is visible for less than 15 minutes from current time.
- $f_7$  - observation factor:  
reduces weighting after some observations have been taken on the object
- $f_8$  - observations on adjacent object factor:  
attempts to create "strings" of search space by increasing the FOM of objects whose neighbor has already been tracked
- $f_9$  - phase angle factor:  
raises the value of the FOM if the phase angle (sun-target-sensor) is small.



#### 4.5. Right Ascension Factor for the FOM

The algorithm in the Scheduler is designed such that all geosynchronous objects with orbital inclinations less than 6.4 deg. will be within the search coverage area. However, as shown in Table II, there are a significant number of objects near the geosynchronous belt that have inclinations greater than 6.4 deg. The Scheduler solves this problem by taking advantage of the population characteristics of cataloged RSOs in the geosynchronous belt. It is assumed that the uncataloged population follows the same distribution.

TABLE II  
Catalog Breakdown by Drifters

Inclination	Synchronous	Drifters	Total
< 6.4 deg	194	53	247 (62.81)
>6.4 deg	76	70	146 (37.21)
Total	270	123	393

Figure 6 is a plot of the orbital inclination vs right ascension of the ascending node of all the objects near the geosynchronous belt. A very interesting observation can be made from this plot. Nearly all of the objects with high inclinations are within a relatively small right ascension band. Also, it is evident from Figure 7 that objects at a given longitude seem to be in phase. That is, in general, they are all near their respective maximum declination points together. Therefore, if a search for these objects is attempted when they are at either of their nodal crossings, a significant portion of the objects will be within the 6.4 deg. window.

The scheduler looks at the current right ascension position of each of the pseudo objects and increases the FOM if the position is from either 350 deg. to 90 deg. or from 170 deg. to 270 deg. Many of the high inclination objects associated with the same longitude as these pseudo objects will be near their nodal crossing during these times, allowing them to be observed within the search space.

#### 4.6. MSX Orbital Constraints

The MSX satellite is in a nearly sun synchronous orbit. The solar panels supply enough power when fully sunlit to operate the spacecraft and the sensor for the geosynchronous surveillance experiment. The battery will be drawn upon when the spacecraft is in shadow. The Scheduling algorithm must monitor the power condition to ensure that the battery is not depleted below 60% of its full charge.

There are restrictions on the attitude of the spacecraft. These are levied to prevent damage to sensors and/or due to thermal considerations. The geosynchronous Scheduler must model these constraints in its search algorithm.

GEOSYNCHRONOUS SATELLITES  
INCLINATION vs RIGHT ASCENSION OF ASC NODE

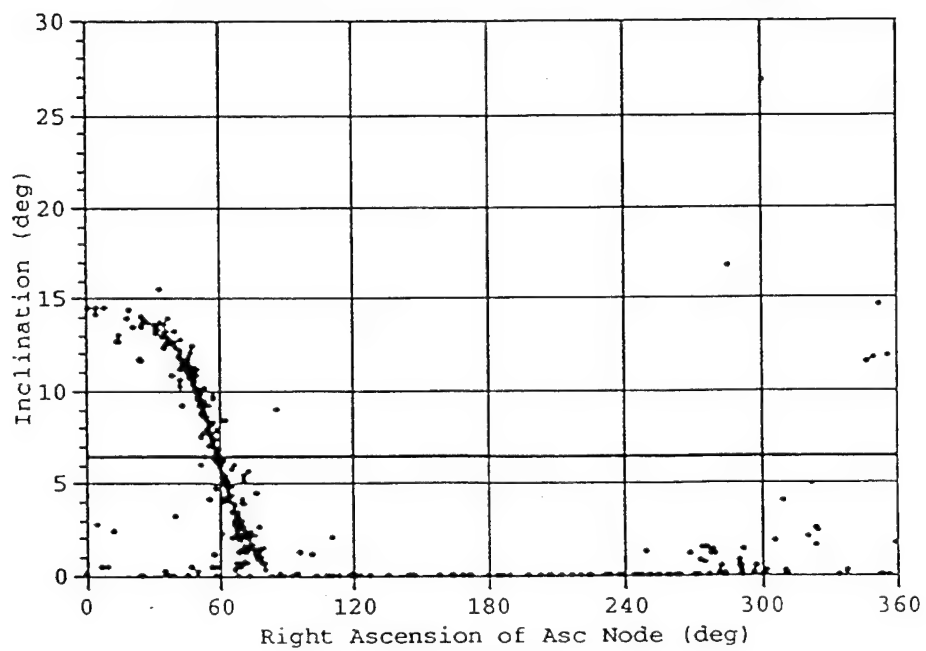


Figure 6

DISTRIBUTION OF GEOSYNCHRONOUS SATELLITES  
IN LATITUDE AND LONGITUDE

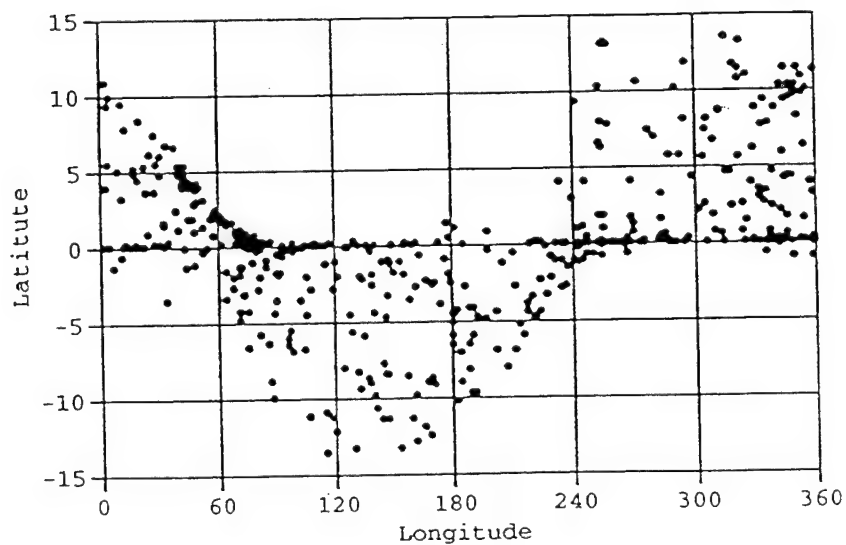


Figure 7

#### 4.7. Experiment Time Allocation

The scheduling of experiment time on the MSX is a complex task and is being performed by the Applied Physics Laboratory at Johns Hopkins University. Eight Principal Investigator (PI) teams have experiments that use the satellite. Therefore, experiment time blocks allotted will be much shorter than the 51 hours required to complete the entire geosynchronous search. Hence the scheduler was built to be able to save the state of the system at the conclusion of an instantiation of the experiment, and resume the search using those previous conditions. This technique ensures the experimental demonstration of geosynchronous surveillance without the need for uninterrupted spacecraft resources.

#### 5. Simulation Results

Preliminary testing shows that the SBV should be able to search a longitude extent of 7.0 degrees of the geosynchronous equatorial belt per hour. During a 12 hour simulation test 84 degrees (non-contiguous) of the belt was searched. The search time includes data collection, signal processing, and spacecraft maneuvering. The entire geosynchronous belt can be searched in 51 hours. In addition to the geosynchronous satellites that will be detectable using this scheme, it is expected that data will also be collected on other classes of deep space satellites such as Molniya, or GPS.

Tests were conducted to determine how many objects could be expected to be seen per hour using the geosynchronous scheduler. Preliminary tests, as shown in Table III, indicate that the scheduler would find 5 geosynchronous (or near geosynchronous) objects and 2 other deep space RSO's from the known catalog per hour. The estimates here assume that all the targets visible within the FOV were bright enough to be detected.

TABLE III  
Expected Object Encounter Frequency  
Using Geosynchronous Scheduler

Type	Time(hr)	Objects Available	Objects Seen	Objects Per Hour	% Seen Per Hour
Near Geosynch	12	393	65	5.44	1.37
Other Deep Space	12	760	26	2.17	0.29

Although the quantity of observations from the SBV on serendipitous non-geosynchronous RSO targets using the Geosynchronous Scheduler will not be sufficient to determine an initial orbit, it will be sufficient to correlate the target against the RSO catalog.

A test was performed to evaluate how this scheduler would perform verses a strategy of either using a single ccd centered on the belt, or an array of four ccds, where the array would straddle the belt with two cells covering above the belt and two covering below the belt.

In the case of a single ccd, coverage of the complete belt took 18 hours. As can be seen in Figure 8, this method finds significantly more objects within the initial 6 hour search period, however, the rate at which objects are found drops off more quickly and less objects will be found within a 54 hour period. In addition, a single ccd is capable of assuring only a .8 degree inclination leak proof fence.

The 4-ccd case also outperforms the 8-ccd case during the initial time periods, and covers the entire belt in 36 hours. The total number of objects found after 54 hours is still less than that produced with the 8-ccd case. The 4-ccd case assures an inclination coverage of 3.2 degrees.

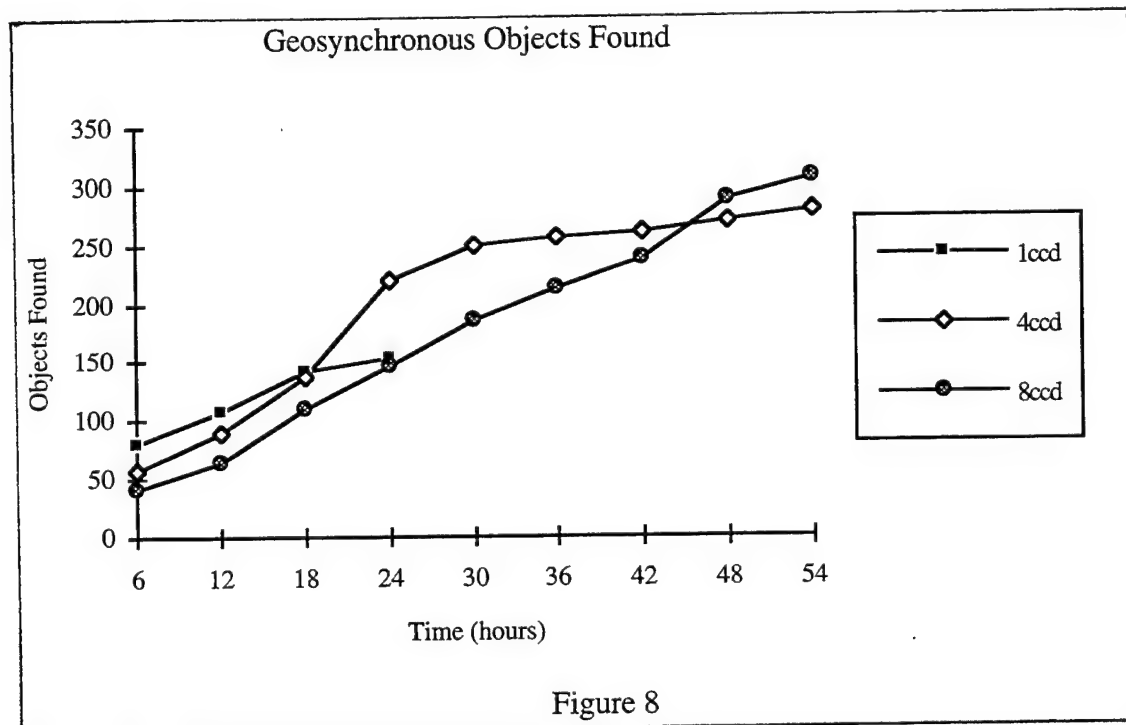


Figure 8

Testing indicates that in each of the cases examined, given a complete 360 degree belt scan, the search algorithm will find all objects within the inclination coverage applicable to the search.

The results of the simulation testing for the full 8-ccd geosynchronous scheduler, as well as the 1-ccd and 4-ccd cases are shown in Tables IV.

**TABLE IV**  
**Tracking Statistics for 360 Degree Coverage**  
 $(\#-\text{found}/\#-\text{available})$   
**8-CCD (54 hours)**

Inclination	Synchronous	Drifters	Total
< 6.4 deg	194/194	46/53	240/247
> 6.4 deg	33/76	34/70	67/146
Total	227/270	80/123	307/393

4-CCD (36 hours)

Inclination	Synchronous	Drifters	Total
< 3.2 deg	163/163	30/32	193/195
> 3.2 deg	34/107	29/91	63/198
Total	197/270	59/123	256/393

1-CCD (18 hours)

Inclination	Synchronous	Drifters	Total
< 0.8 deg	110/110	9/9	119/119
> 0.8 deg	17/160	6/114	23/275
Total	127/270	15/123	142/393

## 6. Summary

A Geosynchronous Scheduler has been designed and implemented to provide an efficient means of searching for all detectable geosynchronous objects with an inclination less than 6.4 deg. In addition, population characteristics of catalogued RSOs have been used to enable collecting data on a significant portion of the geosynchronous objects with inclinations greater than 6.4 deg. Serendipitous data will also be collected on some non-geosynchronous deep space objects.

The method employs the concept of pseudo-objects to cover the search space, and uses a well tested scheduling technique of assigning a figure of merit to each object to produce a locally optimized schedule.

Constraints of the SBV sensor and the MSX are included in the software of the Scheduler. A method of saving the state of the search enables the use of non-contiguous experiment intervals to demonstrate the objectives of the experiment.

The Geosynchronous Scheduler awaits the launch of the MSX for operational testing.

## MSX Spacecraft Sensor Demonstration of BMD Target Tracking Against Stressing Infrared Backgrounds Using Resident Space Objects

B. Klem, G. C. Light, J. M. Lyons, C. J. Rice, N. W. Schulenburg (The Aerospace Corporation), and E. A. Zack (USAF/SMC), 28 March 1995

**Abstract:** An experiment using the Midcourse Space Experiment (MSX) infrared radiometer to demonstrate the acquisition and tracking of resident space objects (RSOs) serving as surrogate BMD targets in the presence of stressing backgrounds is described. The plan calls for performing remote passive optical observations of RSOs at large slant ranges such that they appear as point sources to the Spatial Infrared Imaging Telescope (SPIRIT) III sensor. Up to 48 data collection events against a complete set of stressing backgrounds is scheduled over an 18-month period using 35 to 40 RSOs as surrogates for expended boosters, post-boost vehicles, and reentry vehicles. This presentation introduces the objectives and context of the Experiment Plan. RSO targets are described along with their signature producing components. The set of stressing backgrounds against which those RSOs are to be tracked is identified. An overview is provided of the operations planning concepts and the organizational relationships involved. The data processing and analysis scheme is described along with the results of a simulated encounter to extract an RSO target signal from a stressing hard earth background in the midwave infrared (MWIR).

**Experiment Overview:** MSX is a BMDO program to provide a long duration observatory style sensing platform in low earth orbit with the primary objectives of demonstrating ballistic missile defense midcourse surveillance functions, collecting target and background data, and demonstrating space-based passive optical sensor technology. The spacecraft carries sensitive radiometers, imagers, and spectrometers covering most of the optical range from 110 nm to 28  $\mu\text{m}$ . A primary instrument is the SPIRIT III scanning radiometer containing six spectral bands from 4  $\mu\text{m}$  to 26  $\mu\text{m}$ , with sensitivities (NEFD) on the order of  $(1 - 10) \times 10^{-18} \text{ W/cm}^2$ . The MSX Program designations for the bands are A, B1, B2, C, D and E corresponding to the spectral regions 6.0 - 10.9, 4.22 - 4.36, 4.24 - 4.45, 11.1 - 13.2, 13.5 - 16.0, and 18.1 - 26.0  $\mu\text{m}$ , respectively. There are eight MSX Principal Investigator teams responsible for development of experiment plans and for data analysis for all spacecraft observations. The Early Midcourse Target Experiments Team (EMTET) is responsible for performing functional demonstrations and target signature data collections in support of a space based surveillance sensor viewing targets during the deployment and early midcourse phase of ballistic missile flight.

The EMTET is responsible for several experiment plans, including that for the Resident Space Objects Experiment whose principle objective is to perform functional demonstrations of target acquisition and tracking against stressing backgrounds using RSOs as surrogate BMD targets. The use of such targets can be rationalized by recognizing that it is impractical, from both cost and scheduling considerations, to arrange with dedicated targets and a single sensor platform like the MSX satellite the viewing of ballistic missiles and their deployed objects against a complete variety of stressing backgrounds. RSO surrogate targets represent a partial solution based on such factors as (1) the limited number of dedicated target missions currently being funded, (2) constrained observation geometry, target test range location, and scheduling limitations, (3) the unpredictability and low frequency of occurrence of specific backgrounds, and (4) the multiplicity of compatible RSO types with predictable optical signatures and orbits. The RSOs are selected to represent (1) burned out boosters and PBVs observed in the MWIR against hard earth and earthlimb backgrounds, and (2) PBVs and deployed RVs observed in the LWIR against space and earthlimb backgrounds. In addition to demonstrating sensor acquisition and tracking, the experiments will contribute to quantifying sensor performance for these important BMD functions against the stressing backgrounds. At this time the background types have been prioritized, the RSOs have been selected for MSX observation against specific backgrounds types, and communication with operations planners and ephemeris providers has been established.

Targets: RSOs consist of active and inactive satellites, rocket bodies, and space debris. Of these, active or operational spacecraft are the preferred RSOs to serve as surrogate BMD targets. They are selected based on their key signature producing components which result in predictable optical signatures for mission planning. A specific set of RSOs has been selected for observation based on their orbital characteristics for conjunction with MSX and their optical signatures for observation over a full range of signal-to-noise ratio (SNR). Over eleven classes of active payloads have been characterized in detail in recent years in support of a number of surveillance and defense programs. Optical signature extremes for conditions ranging from full solar illumination and maximum viewing projected area to earth shadow cooled objects with minimum viewing aspects present signature values from a high of  $625 \text{ W/sr } \mu\text{m}$  to a low of  $0.5 \text{ W/sr } \mu\text{m}$ . Representative expended boosters, PBVs and RVs also fall within this signature range. Mission planning has evolved around the RSOs identified in Figure 1(a). Although most of the RSOs under consideration have stable and predictable orbits, the constantly maneuvering shuttle requires special consideration for orbit predictions. Low fidelity signature characterization of these RSOs has been found to be sufficient for operations planning to observe the target/background scene over a wide range of SNR. These targets are also amenable to increased

fidelity modeling which permits experiments with prescribed SNR levels . The large variable projected area, sunlight irradiated/earth shadow cooled solar panels are the predominant self emission signature producing components for most of the RSOs. Shuttle and Mir convex body signatures are the result of self emission from the variable projected area surfaces characterized by complex temperature gradients. Observations are being planned to track RSOs with solar panels when sunlight produces nominally high panel temperatures of 330 K. Shuttle is planned to be tracked when the sun soaks the lower black tiled underside which reaches temperatures of up to 390 K.

Backgrounds: The stressing backgrounds specified for the RSO experiment cover the gamut of real backgrounds against which a space-based surveillance sensor may be required to operate. Backgrounds to be addressed are identified in Figure 1(b). The data to be collected on these backgrounds are not being gathered for high fidelity background characterization purposes. That work is being done with other experiment plans under the direction of the Earthlimb Backgrounds Team in MSX. The experiments have been designed such that the SPIRIT III sensor will be observing the background scene incidentally to acquiring and tracking targets. As such, the emphasis of the experiment is to determine the effect of specific backgrounds on the acquisition and tracking function of the sensor and algorithms which are intended to mitigate the background effects. Engagement conditions have been designed to permit RSOs to be observed against the specific conditions in Figure 1(b). For the hard earth, clear and cloudy, land and sea scenes will be observed at various viewing aspect angles. The earthlimb will be observed for both non-auroral and auroral zones during periods of moderate and, if possible, high levels of geomagnetic activity. Various illumination conditions of the atmosphere being viewed at the limb will be considered in the collections. Engagements will be selected to track RSOs both parallel to and perpendicular to the ecliptic plane. RSO engagements against celestial backgrounds will also occur with tracking parallel and perpendicular to the galactic plane at specified longitudes and latitudes.

Operations Planning: The RSO Experiment has been allocated up to 48 data collection events (DCEs) over an 18-month period with each collection taking place for a minimum duration of one minute and a normal duration of five minutes. The plan calls for filling a matrix of stressing background observations using specific classes of RSOs for tracking. Prior to the collections the elements of the matrix will be identified with one or more RSOs from either the same or from multiple classes, and conjunctions will be simulated using mission planning software developed especially for the MSX program. The concept for Operations Planning is illustrated in Figure 2. The flow depicts input consisting of RSO and MSX ephemeris sets, along

with auroral activity (as applicable) and RSO attitude/configuration status data for use in preselecting targets to satisfy mission requirements. The encounter simulation calculates when an MSX conjunction occurs and outputs specifics of the conjunctions so the optimum one can be selected. The conjunctions are prioritized and sent to the Operations Planning Center (OPC) for satellite constraint verification, determining the effect of satellite system lifetime and post-conjunction recovery (i.e., a cost report), and assessing possible conflicts with other experiments. The OPC schedules the data collection based upon the target identification, observation times, state vectors, and specific backgrounds. After feedback to the EMTET the OPC issues commands to MSX.

An example of the results from one of the mission planning software tools is presented in Figure 3(a) which illustrates the relationship between solar panel size, temperature, and observation range to track specific RSOs against the hard earth in the MWIR while achieving a SNR of 10. For comparison purposes, three classes of RSOs configured with extended solar panels are indicated along with the convex surface shaped Space Shuttle. When the range constraint is integrated with the available target projected area and achievable temperature values, the analyst is able to assess the variability of conditions that permit RSO inherent signature levels sufficient for tracking. Figure 3(b) represents the primary set of RSOs selected for observation as described by their space object catalog number, class of spacecraft to which they belong, and their assignment by order of their effectiveness for demonstrating tracking against specific background scenes.

Typical results of mission planning simulation and analysis are summarized in Figures 4(a) and 4(b). The former estimates the SNR variation with time for observing the Space Shuttle in the MWIR against the hard earth scene for constant surface viewing aspects, at a time when the shuttle underside receives peak thermal loading from the sun. Target detectability is seen to be a strong function of observation time and surface viewing aspect. The latter estimates the SNR variation with time for observing the GPS spacecraft in the 6 - 11  $\mu\text{m}$  spectral band against the celestial background. Results are presented for constant viewing aspect of GPS with the solar panels viewed near broadside and near edge on under extreme conditions of solar thermal loading. It is apparent that RSO signature indirect control is available through both viewing aspect and surface temperature.

Data Processing and Analysis: RSO Experiment processing and analysis is performed using the EMTET Baseline Algorithm Chain developed to support both above-the-horizon (ATH) as well as below-the-horizon (BTH) functions. The primary difference in the operation of the algorithm

chain between ATH and BTH is the number of SPIRIT III sensor bands used. ATH processing takes advantage of the simultaneous measurements of all five infrared bands, whereas BTH processing uses only one or the other of the two MWIR bands because the other infrared bands are saturated when viewing the hard earth.

The processing algorithms are illustrated in Figure 5 and are summarized as follows. The SPIRIT III scan data first passes through a time-dependent processing (TDP) algorithm, which essentially identifies detection events (exceedances) in the scan data and extracts those "packets" of background-subtracted data to a file. The primary purpose is to reduce the amount of data that needs to be processed by downstream algorithms. The measures of performance of TDP are the fraction of scans that the RSO target is extracted (ideally 1.0) and the number of false alarm packets per scan identified as potential targets (ideally 0.0). The data then is transformed into sensor boresight coordinates from the field-of-view coordinates in which TDP operates. The main function of the coordinate transformation is to align the multiple focal planes to the sensor boresight. At this point the packets are sent through the parameter estimation algorithm which estimates the amplitude and position of any targets in the FOV. The measure of performance of the parameter estimation is the accuracy of the position estimates compared to the "truth" position. For the simulation, the "truth" is known exactly. For the flight data, the position "truth" is computed using ground based radar measurements or ephemeris data from NORAD sources tracking RSOs. The estimated positions are transformed from sensor boresight to earth-centered-inertial (ECI) unit vectors which are input to the tracker algorithm, which forms a three-dimensional track on the targets. The derived track is also compared against the "truth" track. The bulk filter is skipped in BTH processing because it is designed to utilize multiband measurements. In the future the algorithm may be modified to do a goodness-of-fit filter for single band processing. Only a single target is viewed during the RSO experiments, so the discrimination algorithms downstream of the tracker are not necessary.

An overview of processing/analysis data products is provided in Figure 6. The flow shows how the data received from the RSO DCE is used for both demonstration of the acquisition/tracking functions, and for phenomenology to improve the RSO signature models for planning future collections.

Simulated Encounter: An encounter between MSX and a fully solar illuminated Class II RSO was simulated for MSX viewing against the hard earth background in the MSX MWIR band. The background chosen was the so-called cirrus monsoon which was generated using the Strategic Scene Generation Model (SSGM). This scene is characterized by 88% cirrus cloud

cover with 11.3 km mean cloud altitude. In order to provide a more stressing background for the simulated encounter, the structure in the SSGM scene was artificially enhanced by a factor of 50 without changing the overall mean radiance in the scene. For the B2 band the mean in-band scene radiance is  $3.8 \times 10^{-6}$  W/cm<sup>2</sup> sr with a resulting (after 50 X multiplication) standard deviation of  $1.0 \times 10^{-8}$  W/cm<sup>2</sup> sr. The RSO optical signature resulting primarily from solar panel self emission is on the order of 50 W/sr in-band.

The results of extracting the target signal from the background are illustrated in Figure 7(a) for which the parameter estimation algorithm amplitude measurements are compared to the truth intensities that were input to the simulation. On average, the differences between the measurement estimates and truth is 0.4 W/sr with a standard deviation of 2.8 W/sr. This results in errors on the order of 6 to 10%. The tracker position estimates have been compared to the truth trajectory (in radial-intrack-crosstrack coordinates) input to the simulator. Figure 7(b) shows the combined tracker error of Line-of-Sight (LOS) and cross-LOS, which is dominated by the LOS error, to be on the order of 100 m.

Status: The RSO Experiment is ready to begin collecting data. The baseline targets have been selected and their signature models have been implemented in the mission planning software. Stressing backgrounds have been prioritized and specific RSOs have been assigned for observations against those backgrounds. Communication has been established for ephemeris, configuration, and attitude data. Procedures for performing mission planning are complete and processing/analysis software are in place. Simulated encounters are still being generated and analyzed to improve efficiency in the mission planning process.

### RSOs for MSX Conjunctions Against Stressing Backgrounds

- DMSP
- GPS
- Hubble Telescope
- Mir Space Station
- Space Shuttle
- Others now being evaluated

Figure 1(a)

### Stressing Backgrounds for RSO - MSX Conjunctions

- Hard earth
  - Clouds
  - Desert
  - Sea/land Interfaces
  - Near-nadir and near-limb viewing
- Earthlimb
  - Day, night and terminator
  - Aurora zone
- Zodiacal
  - In-plane of ecliptic
  - Cross-plane of ecliptic
- Celestial (galactic plane)
  - Scan through galactic center and anti-center
  - Scan across galactic plane

Figure 1(b)

## Concept for Operations Planning

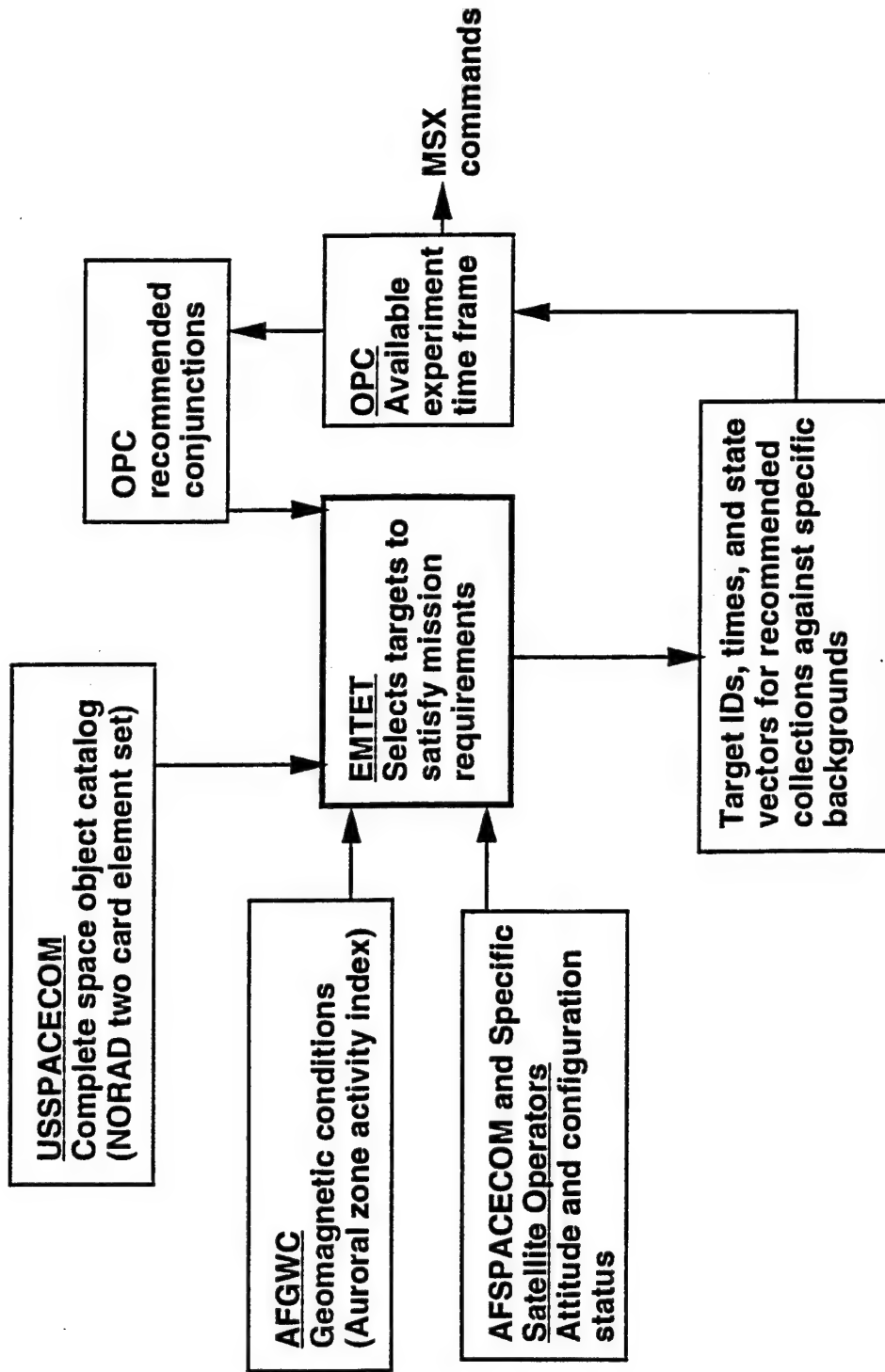
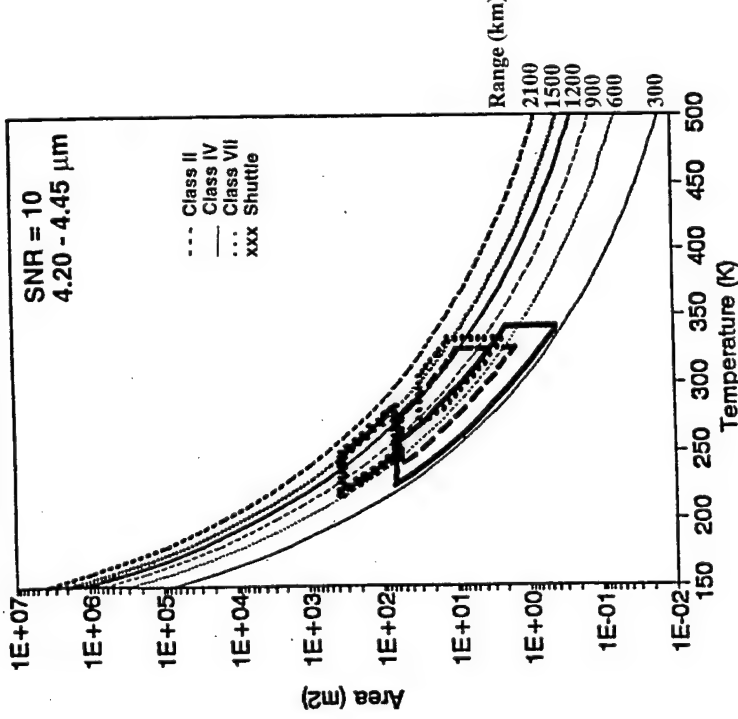


Figure 2

### Signature Sizing



53

Figure 3(a)

### CANDIDATE RESIDENT SPACE OBJECTS FOR THE RSO EXPERIMENT as of 1 November 1994

SOC#	CLASS	BACKGROUND	SOC #	CLASS	BACKGROUND
16609	V	E, L, C	21930	III	C, L
18123	-	L, C	22014	III	C, L
18822	-	L, C	22108	III	C, L
19802	III	C, L	22231	III	C, L
20061	III	C, L	22275	III	C, L
20185	III	C, L	22246	III	C, L
20302	III	C, L	22581	III	C, L
20361	III	C, L	22643	II	E, L, C
20452	III	C, L	22657	III	C, L
20533	III	C, L	22700	III	C, L
20580	IV	L, C, E	22709	II	E, L, C
20724	III	C, L	22779	III	C, L
20830	III	C, L	22808	II	E, L, C
20959	III	C, L	22877	III	C, L
20978	-	L, C	23027	II	C, L
21552	III	C, L	23233	-	L, C
21798	-	L, C	(TBD)	VI	E, L, C
21890	III	C, L			

SOC# - Space Object Catalog Number  
CLASS - Space Object Class  
E - Hard Earth, L - Limb, C - Celestial

Figure 3(b)

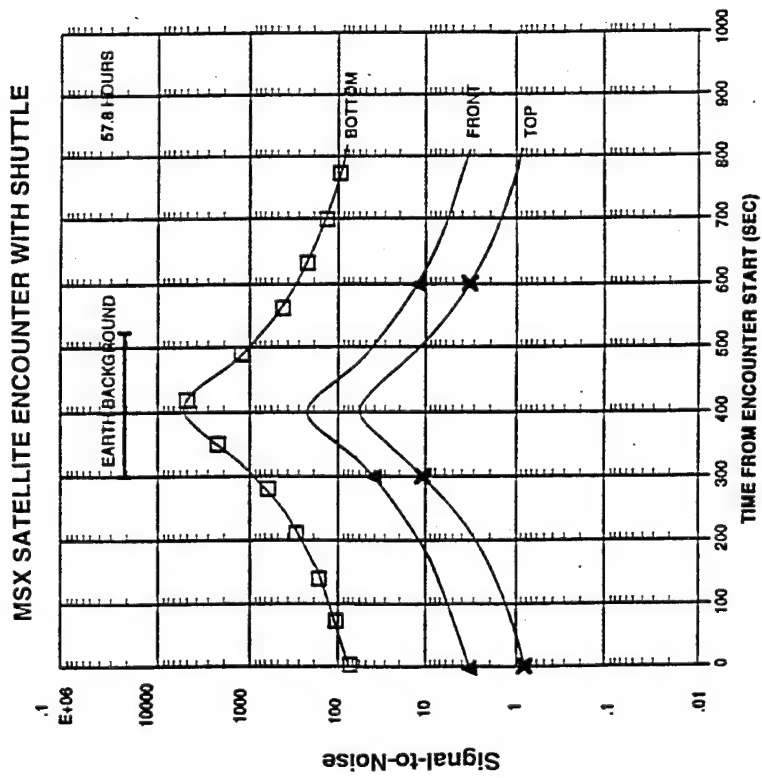


Figure 4(a). SPIRIT III Band B SNR Variation with Time for Shuttle Bottom, Top and Front Viewing Aspects at 57.8 Hours

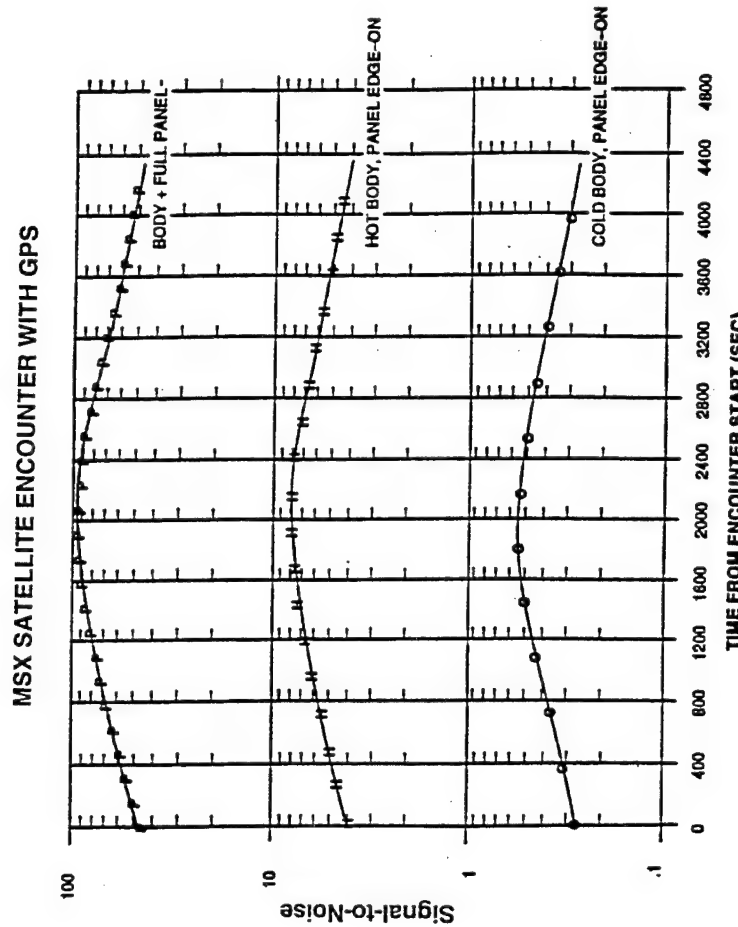
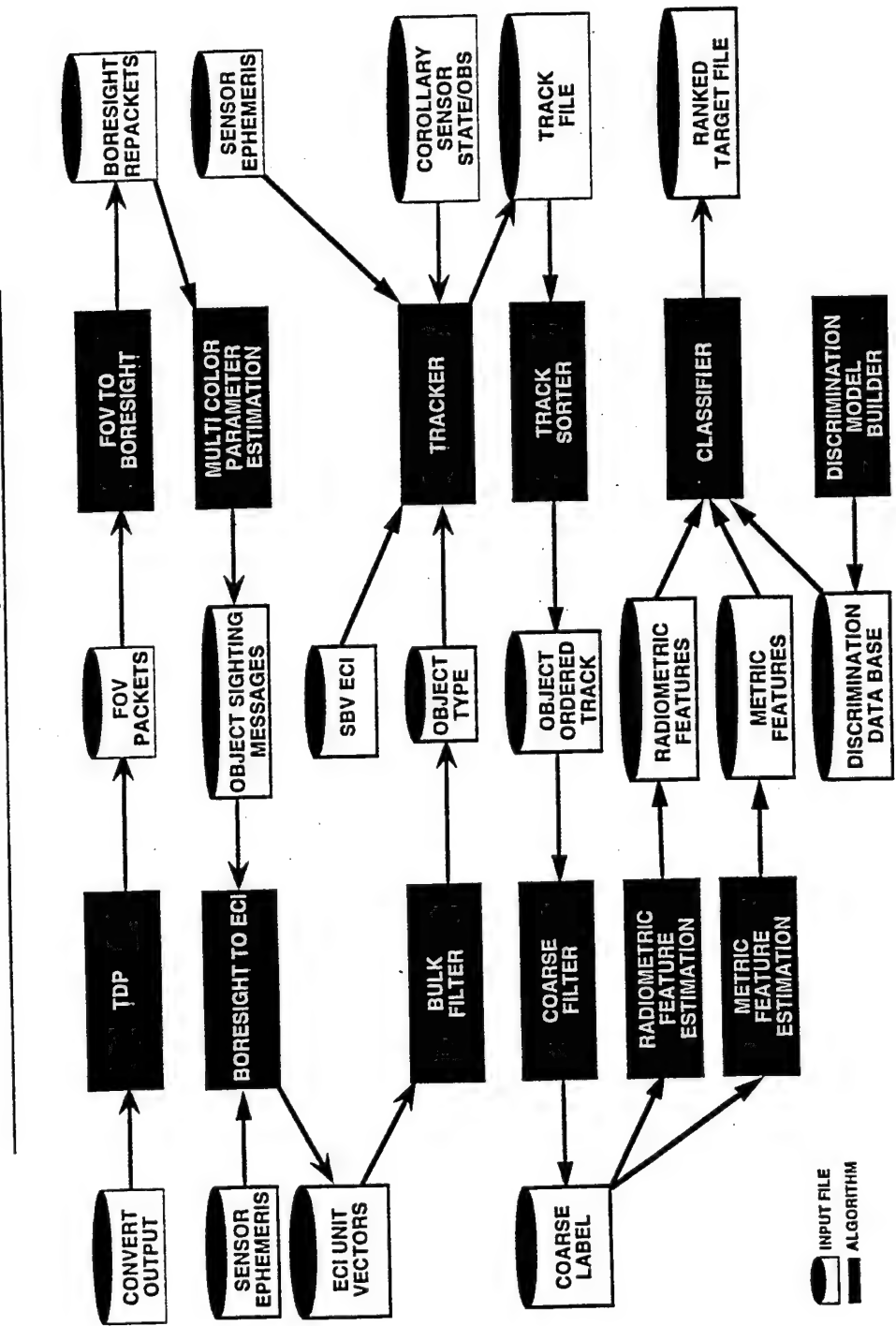


Figure 4(b). SPIRIT III Band A SNR Variation with Time for Three Encounter Conditions Between MSX and GPS

**EMDAC BASELINE ALGORITHM/DATA  
FLOWCHART (U)**



**Figure 5**

## Top Level Data Products

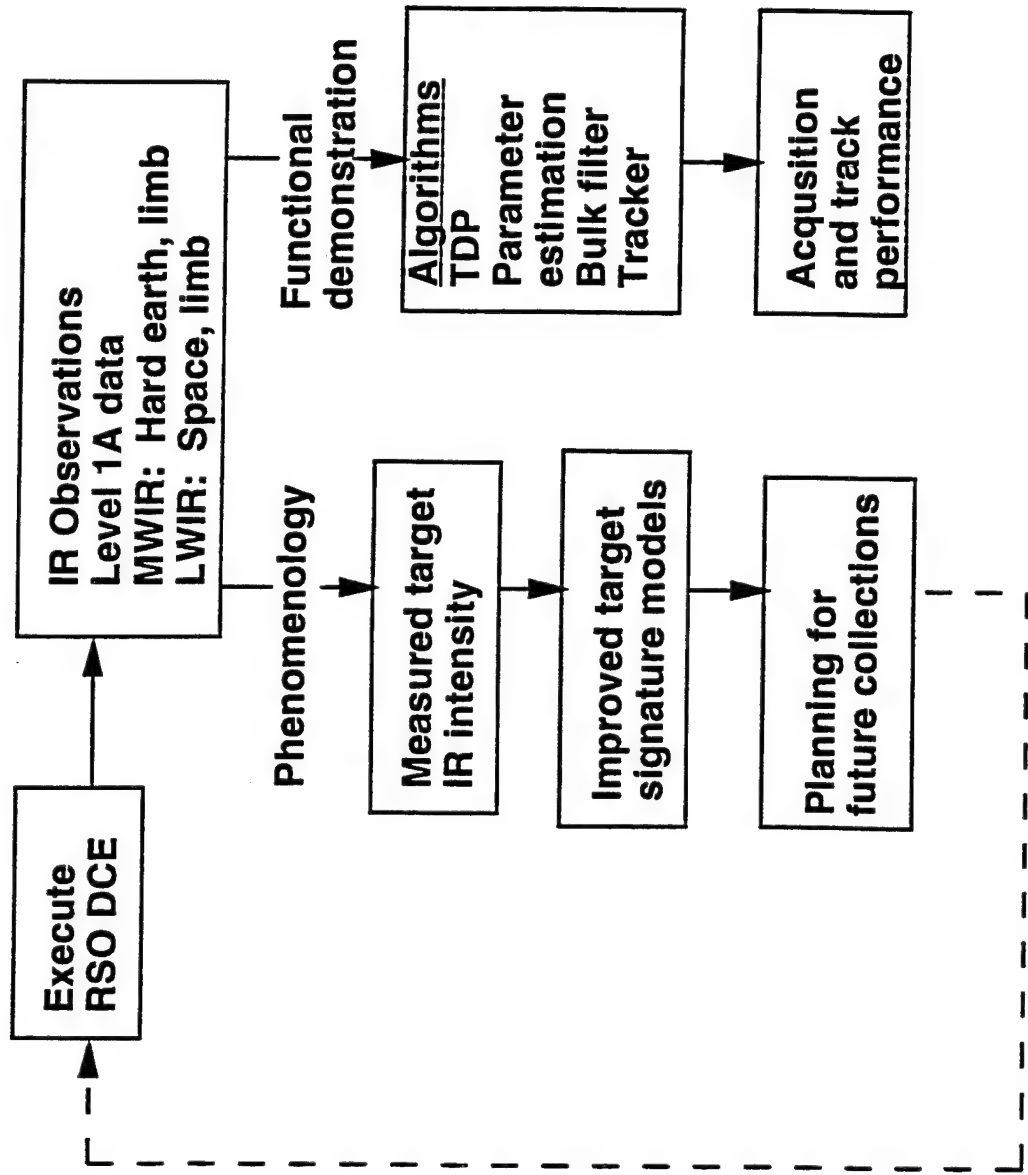
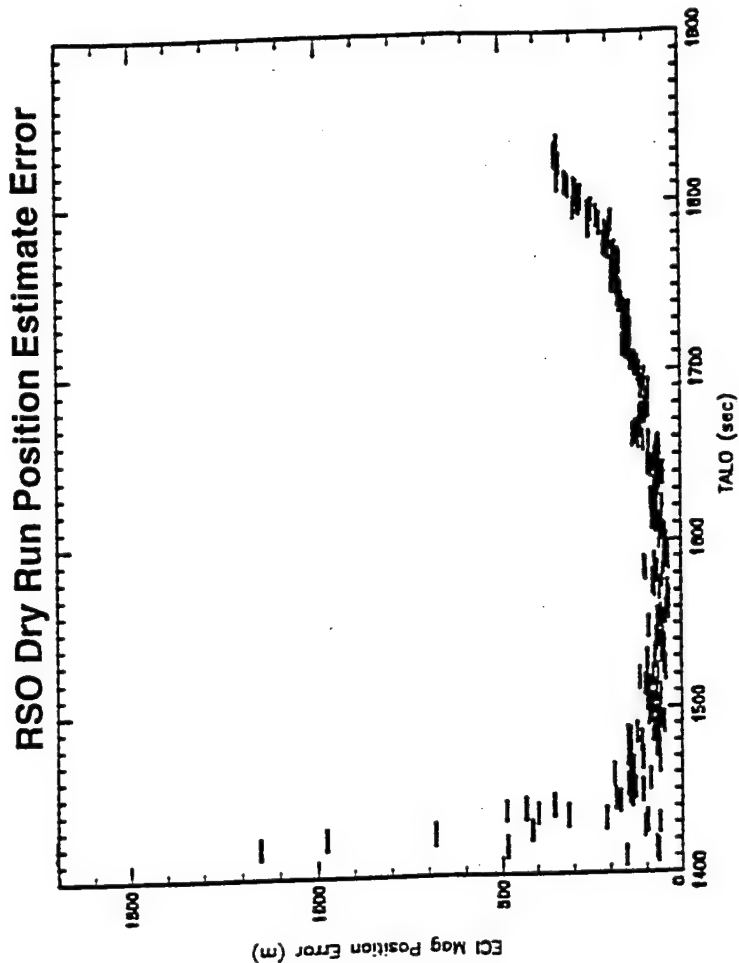
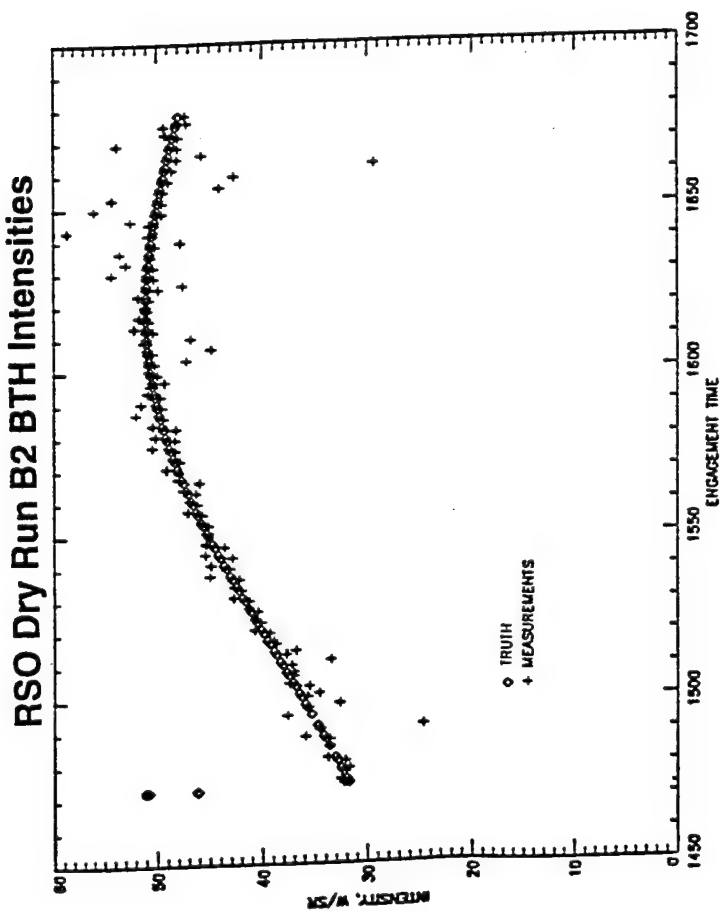


Figure 6



**Figure 7(b)**



**Figure 7(a)**

# A Metric Analysis of IRAS Resident Space Object Detections

Mark T. Lane\*, Joe Baldassini\*, and E. Mike Gaposchkin<sup>+</sup>

## ABSTRACT

The InfraRed Astronomy Satellite (IRAS) was launched and operated during a 10 month period in 1983. The orbit was close to the MSX orbit design, but the science data were collected in a mode where the focal plane was pointing directly away from the Earth. The Space Research Institute at Groningen, Netherlands collected approximately 139,000 tracks of data which had focal plane motion different than astronomical sources, and the IRAS Processing and Analysis Center (IPAC) determined the boresite pointing of IRAS to within 20 arcseconds. This talk will focus on the non-astronomical detections from IRAS, of which many are Resident Space Objects (RSO). In particular, the focus of the study is on how many are correlated to the known RSO catalog for 1983 and the calibration and characterization of the metric accuracy for the correlated data. This study was undertaken to prepare for analysis of RSO detections from the MSX satellite, and in particular, so that automatic analysis tools designed for analysis of surveillance experiment data could be tested. The supporting analysis tools, required corollary data, and metric calibration procedure will be described, and the results of the accuracy of the IRAS ephemeris and metric RSO detections will be presented.

## 1 INTRODUCTION

The InfraRed Astronomy Satellite (IRAS) was launched in early 1983 and operated for a 10 month period to collect repeated observations on the star background in each of four infrared wavelengths, 12, 25, 60, and 100 microns. The orbit was selected to be near-circular with a 103 minute period close to a Sun-synchronous inclination of 99 degrees. IRAS always pointed its focal plane away from the Earth and used a scan rate of 3.85 arc-minutes per second, which is slightly faster than the orbital motion. This way a stellar point source will go through several detectors during a typical scan.

Processing of the IRAS raw data (aimed at extracting all inertially-fixed point source detections) was carried out at the IRAS Processing and Analysis Center (IPAC) at the Jet Propulsion Laboratory (JPL) and involved three aspects of a metric screening process: a "Seconds Confirmation" test, an "Hours Confirmation" test, and a "Weeks Confirmation" test. The Seconds Confirmation test verified that a point source traveled across the IRAS focal plane during a scan at the predicted rate (3.85 arc-minutes per second) and in the predicted (in-scan or 'image') direction. The success of this test indicated that the point source was a large distance away from the IRAS platform and was probably astronomical in nature. The Hours Confirmation test verified that the point source was observed again after a full orbit of IRAS was completed and the focal plane was looking in the same part of the sky as before. This test indicated that the point source is moving very slowly with respect to the IRAS focal plane and is probably a very large distance away. The Weeks Confirmation test was used when (after several weeks) IRAS was again directed to look in the same part of the sky as the first detections. IRAS was designed to repeat coverage of the sky three times during the 10 month mission. About 96 percent of the sky was visited at least twice and about 76 percent of the sky was visited a third time. If the Seconds, Hours, and Weeks Confirmation tests were all passed, then the point source is considered to be inertially fixed upon the sky. Those which fail the Weeks

\* Staff Members, MIT Lincoln Laboratory, Lexington, MA 02173 (617)-981-0973

+ Senior Staff Member, MIT Lincoln Laboratory, Lexington, MA 02173 (617)-981-3403

This work was sponsored with the support of the Department of the Air Force under Contract F19628-95-C-0002. Review of this material does not imply Department of Defense endorsement or opinion.

Confirmation test can be asteroids or some other astronomical point source at a large distance from the IRAS focal plane, and those which fail the Hours test can be faster-moving asteroids, pieces from comets, or other space debris particles. Those which fail the Seconds Confirmation test (that is they have a focal plane rate different than 3.85 arc-minutes per second and in possibly a different direction than the in-scan direction) are possibly artificial Earth satellites, known as Resident Space Objects (RSOs), and can be close to the IRAS focal plane. An on-board procedure attempted to preclude data on particles or infrared sources very close to the IRAS focal plane, and therefore, if an RSO was observed by IRAS, it would typically be seen at a range of 1000 km or greater.

It is the potential RSO observations from this last category of point sources which become the focus of this study, and several questions are to be addressed. The first is: How many of these potential RSOs were observed by IRAS and how many are correlated to the known RSO catalog from 1983? The second is: What is the metric accuracy of the correlated RSO detections and metric error budget for the reduced data and how can the metric data be calibrated? The third is: How reliable are the uncorrelated detections to provide an observed sample of the 1983 debris population?

This study was undertaken to prepare for analysis of surveillance experiment data from the Midcourse Space Experiment (MSX) satellite program. The MSX is scheduled for launch sometime in 1995 and is a space flight program designed, in part, to demonstrate surveillance of space and the RSO background from space. The technical challenges include cryogenic technology for cooling an infrared sensor, low noise high performance focal planes, high off-axis stray-light rejection optics, on-orbit signal processing and data compression, and contamination control. The orbit is specified to be 903 km altitude circular at nearly a Sun-synchronous inclination of 99.23 degrees. The lifetime of the infrared sensor is expected to be 20 months, and the visible and ultra-violet sensors are expected to have a planned operation period of 60 months. The infrared sensor involves a five-band scanning radiometer (from 4.3 microns to 26 microns) with a 14 inch telescope. The pixel size is 90 micro-radians, and there will be an on-board signal and data processor for compression and data processing. The IRAS non-astronomical data become a real space-based data source for testing the automatic analysis tools designed for MSX RSO detections, and all facets of the analysis are involved. The suite of test data from IRAS includes potential RSO detections from the IRAS sensor, a precise ephemeris for the IRAS platform, and supporting corollary data such as a catalog of RSO element sets updated for each observation day of 1983 and independent metric observations on each RSO that IRAS observed. Each of these aspects of the analysis will be described, and the calibration of the IRAS detections and results from an automatic analysis of the data will be presented.

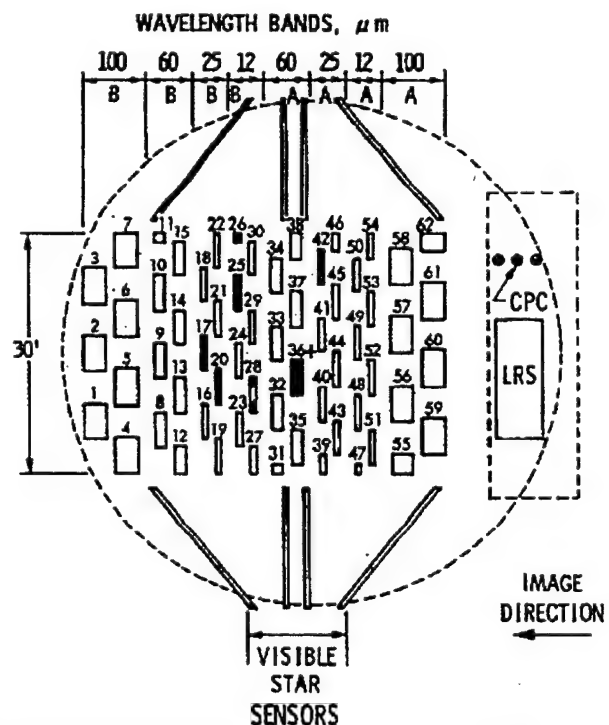
## 2 CALIBRATED IRAS METRIC OBSERVATIONS

### 2.1 Reduction of Focal Plane Detections to Inertial Coordinates

It was described in the introduction that detected point sources which could be potential observations of RSOs are those which have different (and often faster) focal plane motion from the scan rate of 3.85 arc-minutes per second. Often these sources will also have a focal plane direction different from the in-scan direction, although this is not a necessary condition. It is said in [1] that the Seconds, Hours, and Weeks Confirmation tests were designed to glean from the "hundreds of thousands of detections per day" the inertially-fixed sources, and in this way a nice series of metric tests can be used. In the case of the present study, however, where we are interested in those sources which are not inertially fixed upon the sky, there is no metric test which can indicate whether the detections are noise, radiation hits or infrared sources near (or from) the spacecraft (such as material emitted by IRAS itself), or actual RSOs. The Space Research Institute at Groningen, Netherlands, [2] collected approximately 139,000 tracks of IRAS data (involving nearly than 520,000 individual detections) which satisfied the following properties: a) the focal plane motion was different than the 3.85 arc-minutes per second scan rate, b) there were three or more detectors in the focal plane that were involved in the track, and c) each detector had an observed flux value of .2 Janskys or more. This database, referred to herein as the "debris database", was designed to capture all possible RSO

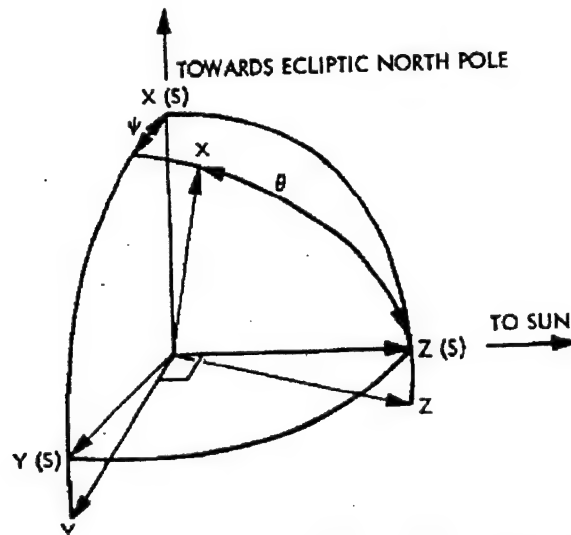
detections (and in particular debris measurements), and using the IPAC database of raw IRAS observations, the database included the absolute time a track passed a line through the boresite perpendicular to the image direction, the flux value and detector identification for each detector involved, and the in-scan velocity across the focal plane. No 100 micron detector values were included in the debris database.

Figure 1 (extracted from [1]) displays the focal plane detector suite. The line for which the absolute time is calculated for each track is the imaginary vertical line going through the boresite (denoted by the + symbol). It is important to note that each detector can be up to 4.75 arc-minutes long and up to 1.51 arc-minutes wide. For the focus of the present study, absolute time and position in the focal plane for each observation from a detector is required, and therefore the following calibration of the data from the debris database was performed: The center of each detector belonging to a track was selected for a set of initial points and a line was fit in a least squares fashion to these positions. If the line went through a lit detector, then the calibrated focal plane position was taken to be the point on the line half-way through the detector on the line. If the line was off of the detector, then the nearest corner of the detector was chosen as the focal plane position. With the in-scan velocity provided in the database, the relative time of the observed point on a detector was determined by calculating the distance of the point to the absolute reference time line along the track and dividing by the in-scan velocity. This provides the number of seconds from the absolute reference time and the absolute time of each detection in the track can thereby be determined. The image direction is perpendicular to the ecliptic plane, and therefore the declination direction is skewed from the image direction by the inclination of the ecliptic. Figure 1 shows that the image direction is horizontal from right to left. The right ascension direction is skewed from the cross-scan direction by the same amount, and since the detectors are longest in the right ascension direction and no information is contained in the database concerning the resolution of an observation on a detector, the right ascension measurements can be more noisy than the declination due to the uncertainty of the position on the detector in the cross-scan direction.



**Figure 1:** The IRAS focal plane and suite of detectors (from [1])

Once the absolute focal plane position for each IRAS detection is determined, calibrated boresite pointing data are used to transform the data to inertial right ascension and declination measurements. Figure 2 (extracted from [1]) shows the IRAS control axes with respect to the Sun. The Y axis is the boresite axis with the angle  $\psi$  determining the scan-rate. The angle  $\theta$  completes the orientation of the focal plane in this reference system. During a viewing scenario,  $\theta$  remained roughly constant and  $\psi$  changed in nearly a linear fashion. If  $\psi$  and  $\theta$  are known, then the inertial position of any point on the focal plane can be determined by first rotating the point on the focal plane to the solar reference frame and transforming this frame to the inertial frame using the known apparent ephemeris of the Sun about the Earth. These values were supplied for the entire mission by IPAC, as a result of an intensive analysis of the IRAS on-board attitude sensors and stars observed by IRAS. An estimated one-sigma accuracy of these values is 10 - 20 arc-seconds (or 3 - 7 milli-degrees) [3].



**Figure 2:** The IRAS spacecraft control axes (X, Y, and Z) as referred to the Sun and North Ecliptic Pole (labeled X(S), Y(S), and Z(S)), (from [1])

Mathematically, if  $(x,y)$  denotes a focal plane position, and  $w$  denotes a unit vector in the IRAS focal plane coordinate frame  $w = (-x,y,z)$  (with  $z^2 = 1 - x^2 - y^2$ ), then one can de-rotate the vector  $w$  using the boresite reference angles  $\psi$  and  $\theta$  for the specified time

$$v = R_3(-\theta) R_2(-\psi) w,$$

and calculate angles  $\psi'$  and  $\theta'$  in the Sun-reference coordinate frame depicted in Figure 2 for the point  $(x,y)$ . These angles are calculated as  $\theta' = \tan^{-1}(v(2)/v(1))$  and  $\psi' = \cos^{-1}(v(3))$  and can be transformed to the inertial coordinate frame using the position of the Sun with respect to the inertial frame.

## 2.2 Problems with Reduction and Screening of the Data

A significant problem with the way the debris database has been collected is that if even one detector in a track is lit falsely (as is possible from the radiation sources mentioned above or because a detector is behaving in a noisy fashion), then the fit of the line to all the detections in the track can be thrown off, and therefore the calibrated positions of each of the other detectors can be in error. In fact, this is entirely possible. It is stated in [1] that most of the detectors in the focal plane have a measured response for the mean rms noise floor of .15 - .2 Janskys and some of the detectors exhibited a measured mean rms noise value of > .3 Janskys. Since the debris database had used a noise floor of .2 Janskys (in the hope of gathering all the orbital debris data), it is opened up to the possibility of a large amount of spurious data with no means of screening the tracks metrically.

Combinatorial statistics from the IRAS debris database are shown in Table 1. There one can see that more than 47% of the observations involve flux values of less than 0.6 Janskys, and more than 77% have flux values of less than 1 Jansky. Moreover, there are more than 26% of the tracks which have an in-scan velocity of less than 4 arc-minutes per second, and these tracks may be on astronomical objects rather than RSOs. (The typical geosynchronous RSO will have an in-scan velocity between 4.5 and 4.6 arc-minutes per second).

**Table 1: Combinatorial Statistics from the IRAS Debris Database (In-scan Velocity Limits are Given in arc-minutes per second and Flux Limits are Given in Janskys)**

Total Number of Observations	519988	
Total Number of Tracks	138902	
Number of Days	277	<u>Percentages</u>
Number of Tracks with In-Scan Velocity < 4	36321	26.15%
Number of Tracks with In-Scan Velocity $\geq 4$ and $< 6$	41222	29.68%
Number of Tracks with In-Scan Velocity $\geq 6$	61359	44.17%
Number of Observations with Flux Value $< 0.6$	244454	47.01%
Number of Observations with Flux Value $\geq 0.6$ and $< 1.0$	156960	30.19%
Number of Observations with Flux Value $\geq 1.0$ and $< 1.5$	65085	12.52%
Number of Observations with Flux Value $\geq 1.5$	53489	10.29%

The noisy response functions from the detectors also make it difficult to screen out bad data using the radiometric flux measurements. A three sigma value for confidence in the flux measurements implies that most measurements have an uncertainty of .6 - 1 Jansky. These figures question the reliability of tracks of small-sized objects (such as debris), where flux values less than 1 Jansky are typical. Moreover, the sensitivity of the detectors preclude screening tracks by temperature (as determined by ratios of flux measurements from the different wavelength passbands), since uncertainties of this level can produce temperature deviations as much as 50% for faint targets.

It appears then that only a metric confirmation (of a track with an orbit of a known RSO) can be made on tracks containing flux values less than .6 Janskys, and observed RSOs with flux values greater than 1 Jansky are generally bigger than small (centimeter-sized) debris. We will demonstrate that IRAS did see a large number of known RSOs from ranges of 1000 km to the geosynchronous orbit range of 35000 km, but we cannot say with any measure of confidence what type of debris that was seen (or how many debris measurements are available).

### 2.3 The Metric Error Budget for the Reduced Data

From [1], the timing estimate for each detection is made by estimating the response function near 1-second boundaries and taking the absolute time to fall at the peak of the response function. The error from this procedure should be no worse than 10 milli-seconds, which translates into an ephemeris error of at most 70 meters. This affects the accuracy of the data in a worst-case scenario as follows: at 1000 km range, a 70 meter ephemeris error will produce an observed angle error of 4 milli-degrees.

For tracks with no erroneous measurements, a bias in the reduced right ascension and declination measurements will be induced by the error in boresite pointing (3 - 7 milli-degrees). For worst case scenarios, the standard deviation of the individual error can be up to 0.7 arc-minutes (12 milli-degrees) in the in-scan direction and up to 2.5 arc-minutes (42 milli-degrees) in the cross-scan direction. If the track contains data from four or more separate detectors, then the bias error will

remain the same, but the standard deviation of the error can be smaller by a factor of 2. If there is one or more false detections in a track, then the error from a good measurement can increase to 5 arc-minutes (or 83 milli-degrees) in the cross-scan direction, but most likely these tracks will show up with large standard deviations because the track is skewed to include the erroneous data.

A summary of the metric error budget for IRAS observations is provided in Table 2. This table shows the error source, a worst-case estimate for the error, when the worst case can be realized, a normal-case estimate, and assumptions assumed for the normal-case error. In each category, the root of the sum of the squares (rss) of the errors is provided. Table 2 shows that a worst case metric error for an individual IRAS observation is 80.7 milli-degrees with a normal case 10.8 milli-degrees.

**Table 2: The Metric Error Budget for IRAS RSO Observations**

Error Source	Worst Case	Worst Case Description	Normal Case	Normal Case Description
Time Error	4 mdeg	10 milli-sec error at 1000 km range	0.4 mdeg	10 milli-sec error at > 10000 km range
IRAS Ephemeris	5.7 mdeg	100 meter error at 1000 km range	0.3 mdeg	40 meter error at > 10000 km range
Pointing Error	8 mdeg	Upper Pointing Error Limit	4 mdeg	Lower Pointing Error Limit
Focal Plane Position	80 mdeg	4.75 arc-minute position error due to erroneous parts of the track	10 mdeg	1/2 arc-minute position error
Total Error	80.7 mdeg		10.8 mdeg	

### 3 THE PRECISE IRAS PLATFORM EPHEMERIS

In order to perform a precise metric analysis of IRAS observations, it is necessary to have a precise ephemeris of the IRAS platform for any time of interest. This was not a prime requirement for IPAC and for performing analysis of inertially-fixed point sources and other slowly changing astronomical data from IRAS, but a precise platform ephemeris is critical in analyzing the metric accuracy of RSO detections. In order to obtain a precision ephemeris for IRAS, it was necessary to collect metric measurements of IRAS throughout the 10 month operational life. The archives of NAVSPASUR and the SSC were utilized to obtain all of the available tracking data on IRAS throughout 1983. Precision orbits were fit to the data using 8 day arcs with 1 day overlap. A special-perturbations orbit determination routine was used for this job with an accurate model of the gravitational and non-gravitational forces acting on IRAS.

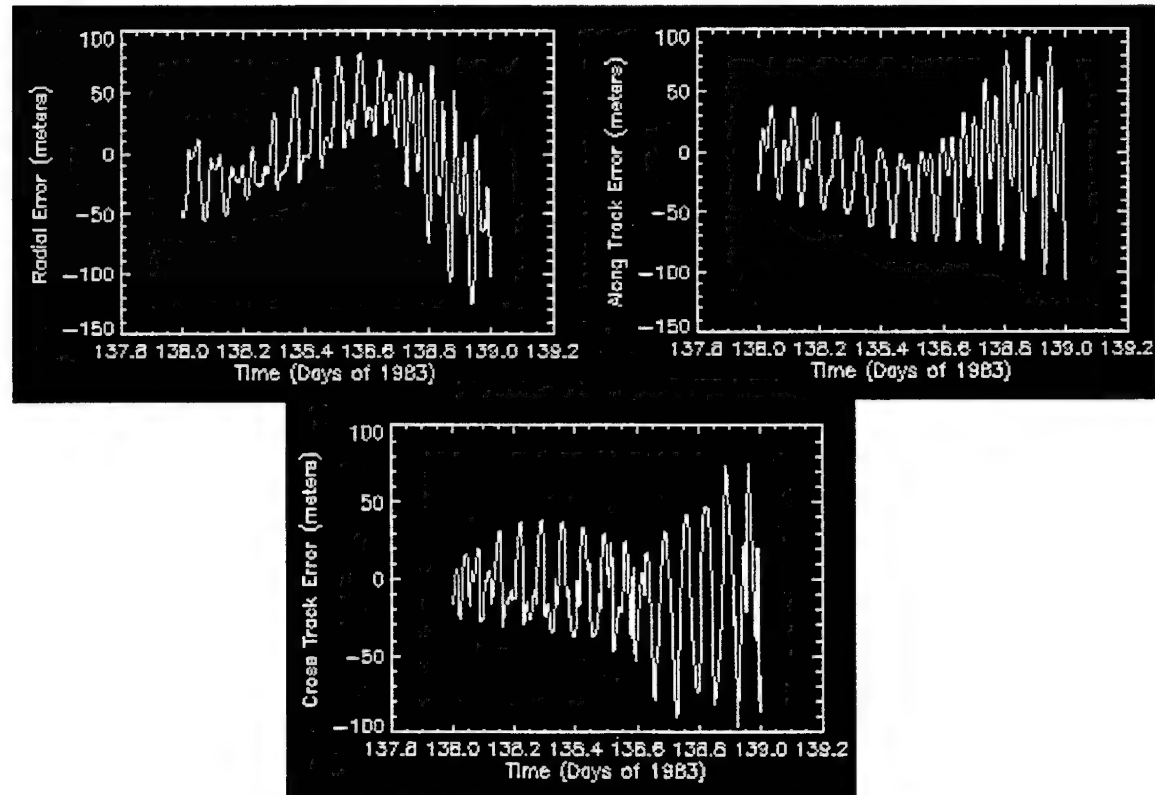
The IRAS focal plane was cooled to 3 - 4 degrees Kelvin using a solid Helium cryostat which sublimated as the operation period proceeded. This produced a small thrust on the platform of IRAS which had to be modeled in the orbit fitting procedure. This was modeled as a thrust in the along track direction whose value was a free parameter estimated daily during each weekly fit. The non-gravitational force model for IRAS also included atmospheric drag, solar radiation pressure, and Earth shine pressure. The gravitation model included the geopotential to degree and order 30, the Sun and Moon, and solid Earth and ocean tides.

Table 3 presents the results of comparing adjacent weekly fit one-day overlaps over the entire time period of interest, from day 26 to 334, 1983. The average and maximum magnitude errors for the differenced position vectors are displayed for each day that an overlap test was performed. Most of the 1-day overlaps show an average magnitude error of about 60 meters with a maximum of 100 meters, but there are occasional instances where the average shoots up to 500 - 700 meters with a maximum error of close to 1 km. The reason for these anomalies is not well-understood. The data tabulated actually represent a worst case, since the comparisons are made at the ends of each fit.

interval, which has the largest error. In order to show a typical weekly fit comparison result, the errors for 1-minute spacing in the radial, along-track, and cross-track components for the day 138 overlap are plotted in Figure 3. Although the plot shows an expected periodic behavior with an amplitude reaching 100 meters, the estimated error for the accuracy of the position of IRAS for an arbitrary time during the mission is closer to 40 meters. As discussed in Section 2, a 100 meter ephemeris error during a worst-case observation scenario of 1000 km range will produce an angle error on the order of 5.7 milli-degrees.

**Table 3: Average and Maximum Magnitude Errors for Weekly IRAS Ephemeris Overlaps**

Day	Ave (m)	Max (m)	Day	Ave (m)	Max (m)	Day	Ave (m)	Max (m)
033	316.8603	768.3221	138	57.5055	161.0116	243	42.1016	116.6946
040	195.5644	382.1880	145	65.1359	141.1725	250	755.8905	1221.6632
047	59.5224	99.1698	152	184.3700	607.9505	257	14.9914	24.7978
054	62.8377	160.0769	159	734.3669	968.6793	264	63.9642	195.0128
061	45.5191	103.8426	166	29.7051	89.6015	271	49.8849	105.6900
068	81.4597	192.2516	173	32.6626	87.3699	278	49.7028	126.2174
075	63.1766	98.0586	180	106.6018	204.6294	285	50.1838	137.7953
082	18.9503	48.9553	187	276.1734	426.6822	292	62.5013	168.5320
089	58.9166	122.5194	194	103.6623	344.4290	299	35.1568	83.8734
096	50.9448	127.8486	201	34.5102	66.4774	306	60.4901	123.1479
103	28.1980	55.6057	208	17.6178	44.1519	313	93.9371	264.6979
110	42.7681	82.6781	215	212.5613	852.0574	320	99.4806	239.0126
117	65.1880	167.5741	222	323.6604	483.7886	327	42.5203	94.4586
124	578.9186	785.9730	229	42.8074	93.2743	334	17.3608	41.5920
131	32.2592	57.2873	236	61.7742	134.8810			



**Figure 3: Orbit error for IRAS during a 1-day overlap of two adjacent weekly fits**

#### 4 THE AUTOMATIC ANALYSIS DATA FLOW

The IRAS metric data were analyzed with automatic software in the MSX Surveillance Data Analysis Center (SDAC) called the Metric Pipeline. Its job is to characterize the accuracy of metric data supplied to the pipeline. It utilizes UnCorrelated Target (UCT) processing to tag the data, independent metric observations from the U.S. Air Force Space Surveillance Network (SSN), and analytic orbit determination to provide an initial orbit as a front end for follow-on precision orbit determination. Residuals of the test data from the precision orbit determination are then isolated and sent to a database for the analyst to consider pass statistics.

Figure 4 illustrates the data flow. First a UCT Processor is invoked to attempt to correlate every metric observation to the known RSO catalogue, and any observation which does not correlate will be removed from additional processing. What remains are sets of observations which have tags associating them with known RSOs. As shown in Figure 4, each set of IRAS metric observations on a particular object will follow a multi-step procedure to characterize the metric accuracy of the data: All other SSN metric data on the particular RSO within, say, +/- 20 revolutions of the object's orbit will be retrieved. The most recent element set on the object from the RSO catalogue data base will be retrieved. The element set will be fit to the SSN metric data using a least squares algorithm tied to an analytic propagation model. This will produce a good starting estimate for a precision orbit fit tied to a special perturbations model utilizing the same tool which was used to produce the IRAS ephemeris. Pass statistics from the precision orbit of the target compared to the IRAS metric data form the basis for assessing the quality of the data.

Much of the challenge in automating this procedure is to stop, check, and re-start the orbit fitting algorithms in case of failure or non-convergence. To do this effectively, ten sub-intervals of the basic arc of data are utilized to avoid maneuver windows or tracks of bad data. If the orbit is still unable to converge with the provided data in one of the ten intervals, then the orbit is left for an analyst to work with interactively.

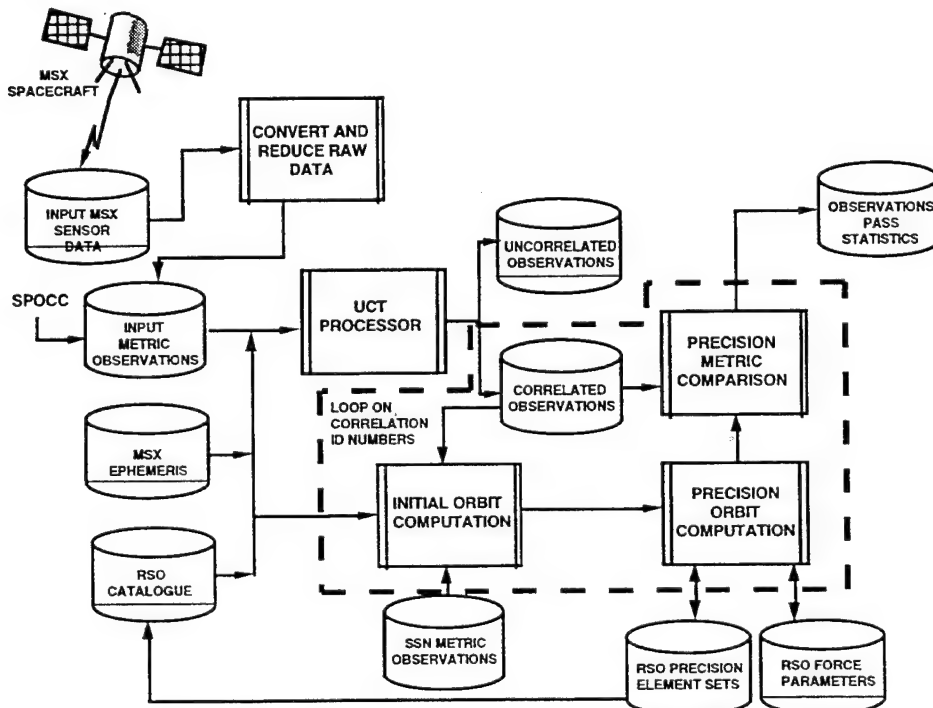


**Figure 4: Automatic Processing of Metric Observations in the SDAC**

## 5 COROLLARY DATA TO SUPPORT THE ANALYSIS

In this section, the corollary data required to support the automatic metric pipeline will be outlined and the source of the data in our processing will be revealed. The SDAC automatic metric pipeline requires the IRAS observations in terms of right ascension and declination, a catalog of RSO element sets for each day of the IRAS mission, and independent SSN metric observations on every object observed by IRAS.

A first pass of the UCT processor on the IRAS RSO detections was performed in late 1992 using catalogs of element sets for 1983 from the Millstone Hill Radar archives. However, these catalogs contain only deep-space satellites, and many of the satellites above the IRAS altitude and with a period less than 225 minutes were not included. Moreover, Millstone does not routinely receive SSN metric data on these low-to-mid altitude satellites. NAVSPASUR was requested complete both the required element set data and the SSN metric data, and complete catalogs of RSO element sets for each day of 1983 (totaling over 4500 element sets per day) and archived metric data on all tracked objects for the year (totaling more than 570 MBytes) were provided.

The metric data from the NAVSPASUR archives from 1983 were not of the same quality that is available for the 1995 SSN. This fact clearly demonstrates the quality calibration work done over the past 12 years to enhance the SSN metric data and (as a by-product) the element set catalog. The optical sensors in use during 1983 included GEODSS and the Baker-Nunn cameras. The latter produced poor quality angle data on the order of 10 - 30 milli-degrees, while GEODSS produced angle data with 5 - 10 milli-degree accuracy, 1 sigma. Radar sites in use included the Millstone Hill radar, the ALTAIR radar, and Pirinlik, Turkey (the FPS-79). Pirinlik data were of poor quality with range errors on the order of 60 - 100 meters, Millstone data had a range quality of 5 - 10 meters with angle accuracy of 5 - 20 milli-degrees, and ALTAIR data were somewhat worse.

The density of the archived metric data provided by NAVSPASUR was smaller than when each object was tracked, to save on resources. In order to trim the amount of archived data, NAVSPASUR consolidated measurements from the tracks and made Earth-centered state vectors out of some of the tracks of observations. This has the effect of causing the precision orbit program to produce orbits of a poorer quality. Many of the orbits computed for characterizing the metric accuracy of an IRAS track are of a similar quality to the IRAS ephemeris itself, about 40 - 100 meters. Thus the reference orbits also contribute to the metric error budget as a bias in the residuals.

## 6 RESULTS

A summary of the results from processing all of the IRAS data from the debris database is shown in Table 4. There it is tabulated the total number of RSO tracks based on a precision metric correlation, the number of days, the number of distinct satellites, the average and standard deviation of the tracks per day, and pass statistics for the tracks. In this part, the following results are displayed: the average and standard deviation of the bias errors in both right ascension and declination for the tracks and the average and standard deviation of the standard deviations in both right ascension and declination for the tracks. All values for the statistics are given in milli-degrees. One can see the following from Table 4: The average right ascension and declination bias errors are small, but there are large standard deviations for these values. Thus the tracks sometimes exhibited very large biases (> 30 - 50 milli-degrees) and other times had smaller values. The average standard deviation in right ascension was about 10.9 milli-degrees while the value for declination was considerably better (7.0). There is also a large value (close to 13 milli-degrees) in the standard deviation of these results in both right ascension and declination.

IRAS saw a wide variety of objects, including non-circular low altitude orbits with apogees higher than the IRAS orbit. The metric error budget for IRAS data, which includes time and IRAS ephemeris errors, can be smaller for certain classes of objects. The time and errors from the IRAS

ephemeris can be negligible for objects in geosynchronous orbit because the observation range exceeds 35000 km. Unfortunately, precision reference orbits for these objects are difficult to produce because of the lack of good quality angle tracking data from the independent SSN sensors. Accurate range data is of little value if the angle tracking data have a metric accuracy of 10 milli-degrees or more. Nevertheless, it is interesting to consider all of the IRAS tracking data on geosynchronous RSOs. These are tabulated in Table 5, showing that IRAS saw a large number of geosynchronous objects with much better declination accuracy and slightly better right ascension accuracy. The nature of the bias errors do not change for this category of objects, which suggests that pointing and reference orbit errors may be the chief contributors.

**Table 4: Results from all of the IRAS Tracks on Known RSOs**

Total Number of Tracks	1168
Number of Days Processed	277
Number of Distinct Satellites Observed	399
Average Number of Tracks Per Day	4.2
Standard Deviation of Number of Tracks Per Day	2.3
Average Right Ascension Bias (Over # of Tracks)	-5.9
Average Declination Bias (Over # of Tracks)	-0.6
Standard Deviation of Right Ascension Biases (Over # of Tracks)	33.0
Standard Deviation of Declination Biases (Over # of Tracks)	27.6
Average Right Ascension Standard Deviation (Over # of Tracks)	10.9
Average Declination Standard Deviation (Over # of Tracks)	7.0
Standard Deviation of Right Ascension Standard Deviations (Over # of Tracks)	13.1
Standard Deviation of Declination Standard Deviations (Over # of Tracks)	12.2

**Table 5: Results from all of the IRAS Tracks on Known Geosynchronous RSOs**

Total Number of Geosynchronous Tracks	137
Average Right Ascension Bias (Over # of Tracks)	-4.7
Average Declination Bias (Over # of Tracks)	-1.2
Standard Deviation of Right Ascension Biases (Over # of Tracks)	42.8
Standard Deviation of Declination Biases (Over # of Tracks)	26.4
Average Right Ascension Standard Deviation (Over # of Tracks)	9.5
Average Declination Standard Deviation (Over # of Tracks)	3.6
Standard Deviation of Right Ascension Standard Deviations (Over # of Tracks)	11.4
Standard Deviation of Declination Standard Deviations (Over # of Tracks)	7.0

The results in Table 5 are not as good as one might expect, due in part to a number of tracks plagued by some of the issues outlined in Section 2.2. Table 6 shows two example IRAS tracks on the geosynchronous orbit SSC #13900. The IRAS track numbers are respectively 547347 and 547348. Table 6 shows for each track the absolute time, the residuals in right ascension and declination, the detector number (for mapping on Figure 1), the wavelength of the detector (in microns), the range from IRAS, and the flux (in Janskys). Recall that it was mentioned in Section 2.2 that noise values for most of the detectors were on the order of .2 Janskys and can be as much as .3 Janskys. All of the flux values for track 547347 are greater than 3 times the noise floor, and the standard deviation of the data in right ascension is roughly 4 milli-degrees and about 2 milli-degrees in declination. Now consider track 547348 and notice the small 60 micron detector values (.32, .14, and .29 Janskys).

These may corrupt the metric accuracy considerably by skewing the direction and the in-scan velocity, and consequently the calibrated metric positions. However, when noticing the absolute time, we see that the time at detector 50 in track 547347 and the time at detector 50 in track 547348 are only .071 seconds apart. At a rate of 4.58 arc-minutes per second, the object would travel a distance of .32 arc-minutes, which leads one to believe that these two detections are part of the same detection and track. The same is true for detectors 54 and 42. If we reject detectors 37, 14, and 9 from track 547348 and merge data from detectors 54, 50, and 42 into track 547347, then this leaves detector 29 from track 547348 which does not fit. Its flux value is much lower than the other 12 micron values for this object, and we conclude that it is not part of the track of this RSO. Unfortunately, examples such as this are not rare in the IRAS data, and since most of the analysis was done automatically, there was no attempt to screen out all the bad tracks from the overall statistics. These will contribute to larger biases and standard deviations.

**Table 6: Example of 2 IRAS Tracks Correlated to the Same Object Closely Spaced in Time**

Correlated Object Number : 13900

IRAS Track ID Number 547347 (In-Scan Velocity = 4.58 arc-min/s)							
#	Day (1983)	$\Delta\alpha$ (mdeg)	$\Delta\delta$ (mdeg)	Det#	Bnd( $\mu$ )	Range(km)	Flux(Jy)
1	91.3953633231	9.4	-8.3	54	12	34878.5	4.50
2	91.3953667841	4.4	-7.7	50	12	34877.8	1.49
3	91.3953782325	3.7	-7.8	42	25	34875.7	4.33
4	91.3953864390	3.2	-8.0	38	60	34874.2	1.72
5	91.3954006481	2.4	-8.3	30	12	34871.6	4.41
6	91.3954121979	1.7	-8.4	22	25	34869.5	4.15
7	91.3954246848	1.0	-8.7	15	60	34867.2	1.46
8	91.3954330330	9.0	-10.2	11	60	34865.7	0.84

IRAS Track ID Number 547348 (In-Scan Velocity = 4.62 arc-min/s)							
#	Day (1983)	$\Delta\alpha$ (mdeg)	$\Delta\delta$ (mdeg)	Det#	Bnd( $\mu$ )	Range(km)	Flux(Jy)
1	91.3953605921	12.8	-0.1	54	12	34879.0	4.77
2	91.3953659632	-4.6	-1.5	50	12	34878.0	1.58
3	91.3953783547	-44.7	-4.7	42	25	34875.7	4.42
4	91.3953874091	-74.0	-7.0	37	60	34874.0	0.32
5	91.3954025895	-123.1	-10.9	29	12	34871.2	1.29
6	91.3954274591	-203.6	-17.4	14	60	34866.7	0.14
7	91.3954355422	-229.7	-19.4	9	60	34865.2	0.29

## 7 SUMMARY

An automatic procedure has been used to process all potential RSO observations from IRAS. Required corollary and auxiliary data include a catalog of RSO element sets updated for each day during IRAS operation, independent metric observations from sensors in the SSN for each object that IRAS observed, and a precision IRAS ephemeris. The latter was calculated in-house using SSN metric data on IRAS throughout 1983. A procedure of metric calibration was outlined and a metric error budget was formulated. The results illustrate the following points:

- 1) While IRAS was pointing away from the Earth in a configuration conducive to astronomical observation, RSOs were seen on the average of 4 tracks per day. IRAS observed nearly 400 distinct RSOs with representatives from most satellite orbit classes, except those with apogee height less than the height of IRAS.
- 2) Even though the database of potential detections contains nearly 139,000 tracks, an absolute metric correlation with known RSOs was made for nearly 1200 tracks (or less than 1 percent). It is speculated that there may be as much as an additional 1 percent of the database that is comprised of uncorrelated satellites (debris and uncatalogued objects), but more than 97 percent of the database is uncertain and many of the detections may be spurious.

3) Metric calibration of the tracks of observations is difficult because of the potential for erroneous detections corrupting the in-scan velocity and direction and, consequently, the absolute position. It is estimated that (for tracks without erroneous observations) the accuracy of the right ascension is 10 milli-degrees and of the declination is 3 milli-degrees. These are comparable to GEODSS metric accuracy values for 1983.

## 6 REFERENCES

- [1] **Infrared Astronomical Satellite (IRAS) Catalogs and Atlases. Vol I: Explanatory Supplement**, Edited by C. Beichman, G. Neugebauer, H. Habing, P. Clegg, and T. Chester, Joint IRAS Science Working Group, 1984.
- [2] de Jonge, A.R.W., van Hess, R.M., Viersen, B., and Wesselius, P., *Detecting Space Debris using IRAS*, Final Report and Workpackages, Groningen Space Institute, Netherlands Document ROG-DEB-91-11, May, 1991.
- [3] McCallon, H. (at IPAC), Private Communication, 1994.

## **Orbital Debris Radar Calibration Spheres**

T. J. Settecerri (Lockheed Engineering & Sciences Company),  
E. G. Stansbery (NASA/JSC/SN3)

### **INTRODUCTION:**

The Space Shuttle Discover (STS-60) deployed six Orbital Debris Radar Calibration Spheres (ODERACS) on February 9, 1994. Since, that time the United States Space Command Space Surveillance Network has continuously maintained orbital elements sets on the spheres. The German FGAN radar located near Bonn has also maintained similar orbital element sets. The primary purpose of this flight experiment was to calibrate the principal polarization channel of the Haystack X-band Radar located in Tynsboro, Ma and to validate the Orbital Debris Analysis Software located at NASA/JSC. Secondly, to provide highly characterized spheres for radar and optical sites worldwide to calibrate/validate their systems/associated software. This paper presents the orbital elements for the 4- and 6-inch spheres; but, only the mean altitude for the 2-inch spheres. Data is based on the United States Space Command two line element sets. The perturbations that change the orbital elements are described to show the effect of secular perturbation, gravitational potential ( $J_2, J_3$ ), atmospheric drag, solar wind, and Solar/Lunar radiation pressure. Lastly, the drag coefficients will be contrasted with B-star. Table 1 shows the order of deployment, catalog number, size, mass, material, retrograde deployment velocity and deployment time. The state vector for the shuttle just prior to deployment is shown below:

94040.6210887	X	-1038.329981	Y	-3763.378695	Z	5472.952243
	X-dot	7.543079798	Y-dot	.163826862	Z-dot	1.541115470

### **ODERACS FLIGHT PARAMETERS**

Seq	Catalog Number	Size (in)	Mass (kg)	Material	Vel (m/s)	Time (GMT)
1	22990	4	1.48157	Chrome Plated Aluminum	3.34	14:54:23.764
2	22991	4	1.48157	Sand-blasted Aluminum	2.64	14:54:26.476
3	22992	2	0.53198	Polished Stainless Steel	1.82	14:54:28.779
4	22993	2	0.53198	Sand-blasted Stainless St	1.86	14:54:31.448
5	22994	6	5.00029	Chrome Plated Aluminum	1.55	14:54:35.886
6	22995	6	5.00029	Sand-blasted Aluminum	1.53	14:54:38.422

**Table 1**

The following discussion and charts show the actual orbital element's history and describes the phenomena that perturbs each one. It is known that only where reduced accuracy is required a mean element set provides adequate position of an orbiting body around the earth. For other applications the following perturbations should be included.

1. The attraction of the Sun, Moon and Planets (secular perturbations).
2. The nonsphericity of the Earth (gravitational potential).
3. Atmospheric drag, solar wind, and Solar/Lunar radiation pressure.

**Note:** To stay within the length limit for this paper, only figures for spheres 22990 and 22994 are included. All figures will be shown during the presentation.

### INCLINATION:

The inclination of a satellite's orbit is the angle between the orbital plane and earth's equator. For ODERACS, STS-60 was in at nearly 57-degrees. Figure 1 shows the complete inclination history for satellite 22990 and Figures 2 shows the inclination for satellite 22994 from deployment through January 6, 1995. The slight drift in inclination is due to several different perturbations and possibly radiation pressure. Secular perturbations can be modelled by the following inclination rate formula (reference 4).

Inclination rate:

$$\frac{di}{dt} = -15 / 8 \pi \mu_1 / \mu_0 (a / r_1)^3 (e^2 / \sqrt{1 - e^2}) \sin 2i \sin 2\omega \quad (\text{eqn 1})$$

where:

i = inclination

e = eccentricity

$\omega$  = argument of perigee

$\mu_0$  = gravitation potential of the earth

$\mu_1$  = gravitation potential of the perturbing body

a = semi-major axis

$r_1$  = distance from the center of the perturbing body to the satellite

The ODERACS inclination drift is seen to be a function of the semi-major axis, inclination, and argument of perigee. Assuming these are constant for one orbit the inclination rate is then a function of two ratios: gravitational potentials and semi-major axis to distance. Using the above equation it can be shown that the effect of secular perturbations is negligible (see table 2).

The observed inclination drift was determined using the Microsoft Excel Linear Regression Tool. For the ODERACS satellites, which all have very similar orbits the inclination rates were seen to be approximately -7.5e-5 degrees/day for the 4-inch spheres and -2.8e-5 for the 6-inch spheres.

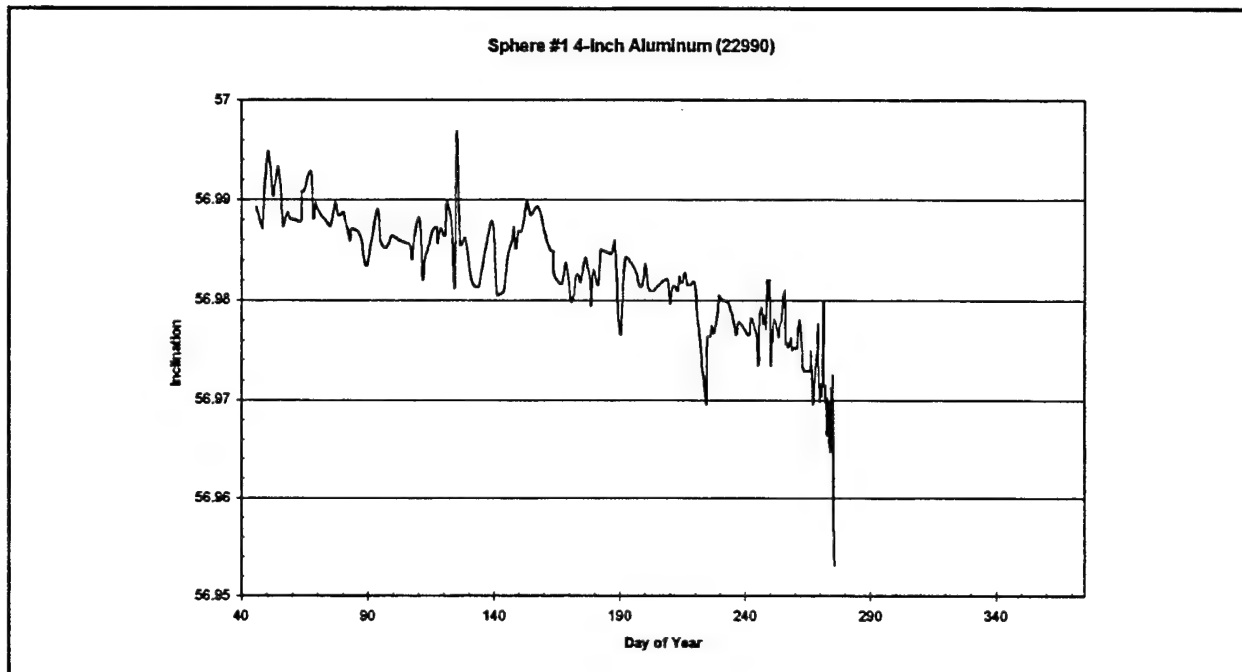


**Figure 1**

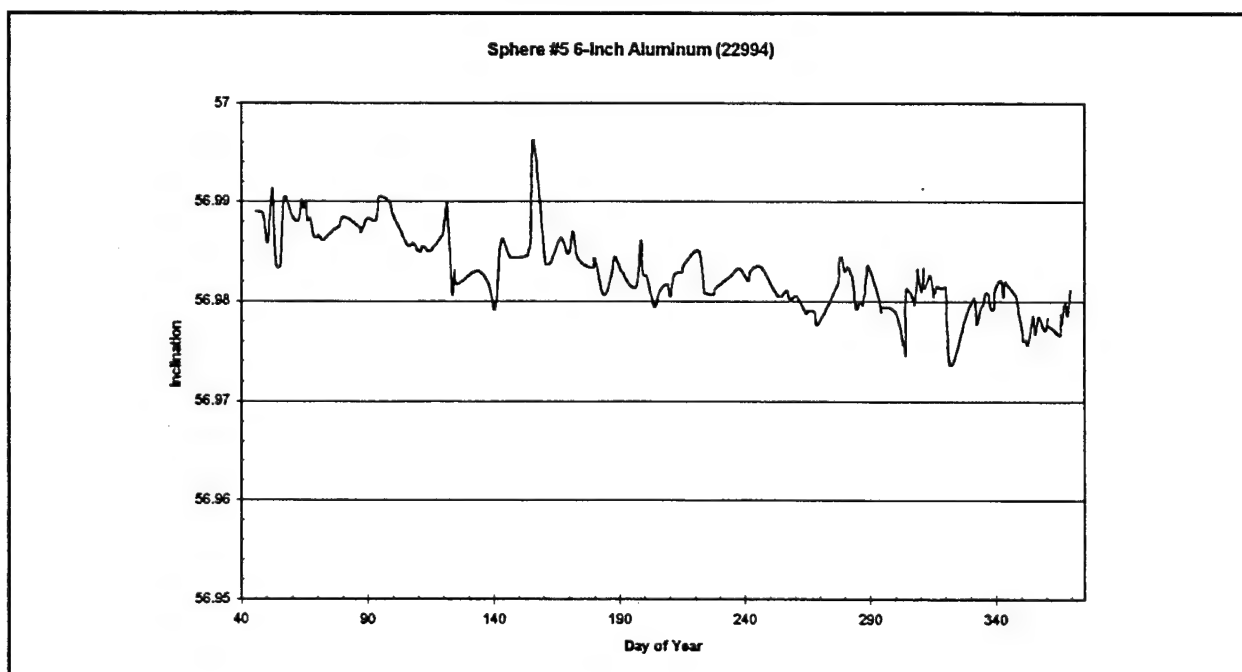


**Figure 2**

**INCLINATION RATE**  
**Degrees/Day**

Satellite	22990	22991	22994	22995
Theoretical	$\approx 10^{-15}$	$\approx 10^{-15}$	$\approx 10^{-15}$	$\approx 10^{-15}$
Observed	-8.0598e-5	-7.1953e-5	-3.0269e-5	-2.7007e-5

**Table 2**

Comparing the ratio of inclination rates for the 4-inch and 6-inch spheres leads to an out-of-plane force related to area and mass. Radiation pressure is one force that is a function of area and mass. Another is co-rotational atmospheric winds (transverse drag). I suspect that the latter is the primary cause of this drift because the drift is in one direction. However, calculations have not been made to support this conclusion.

**RIGHT ASCENSION OF THE ASCENDING NODE (RAAN)**

The RAAN ( $\Omega$ ) is defined as the longitude of the orbital plane on the earth's equator. Figure 3 shows the complete RAAN history for satellite 22990 and Figure 4 shows the RAAN for satellite 22994 from deployment through January 6, 1995. The RAAN drift is due to several forces: equation 2 (reference 4) shows the RAAN rate due to perturbing bodies and equations 3 and 4 (Reference 2) show the rate due to the earth's gravitational potential.

RAAN Rate:

$$\partial\Omega = -3/2 \pi \mu_1/\mu_0 (a/r_1)^3 (\cos i / \sqrt{1-e^2}) (1 - e^2 + 5 e^2 \sin^2 \omega) \quad (\text{eqn 2})$$

$$\partial\Omega = -3 \pi (r_e/r_0)^2 \cos i * J_2 / (1 - e^2)^2 \quad \text{radian per period} \quad (\text{eqn 3})$$

$$\partial\Omega \approx -9.97 ((r_e/r_0)^{1.5} \cos i * / (1 - e^2)^2) \quad \text{degrees per day} \quad (\text{eqn 4})$$

where:

$r_e$  = radius of the earth

$r_0$  = distance from the center of the earth to the satellite

$J_2 = 1.082.645e-6$

Since the forces due to lunar and solar perturbations are several orders of magnitude below the earth's gravitational potential the theoretical values shown in table 3 only considered the latter.

By using the Microsoft Excel Linear Regression Tool the following right ascension rates (degrees/day) were calculated (see Table 3).

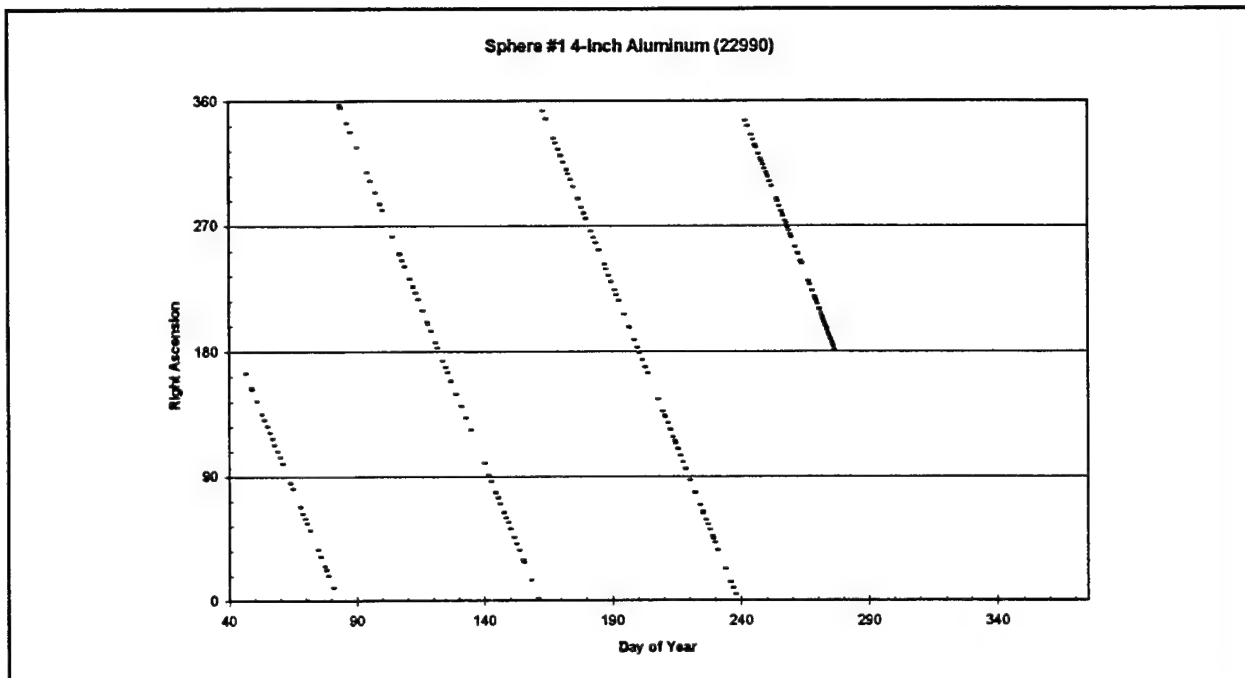


**Figure 3**

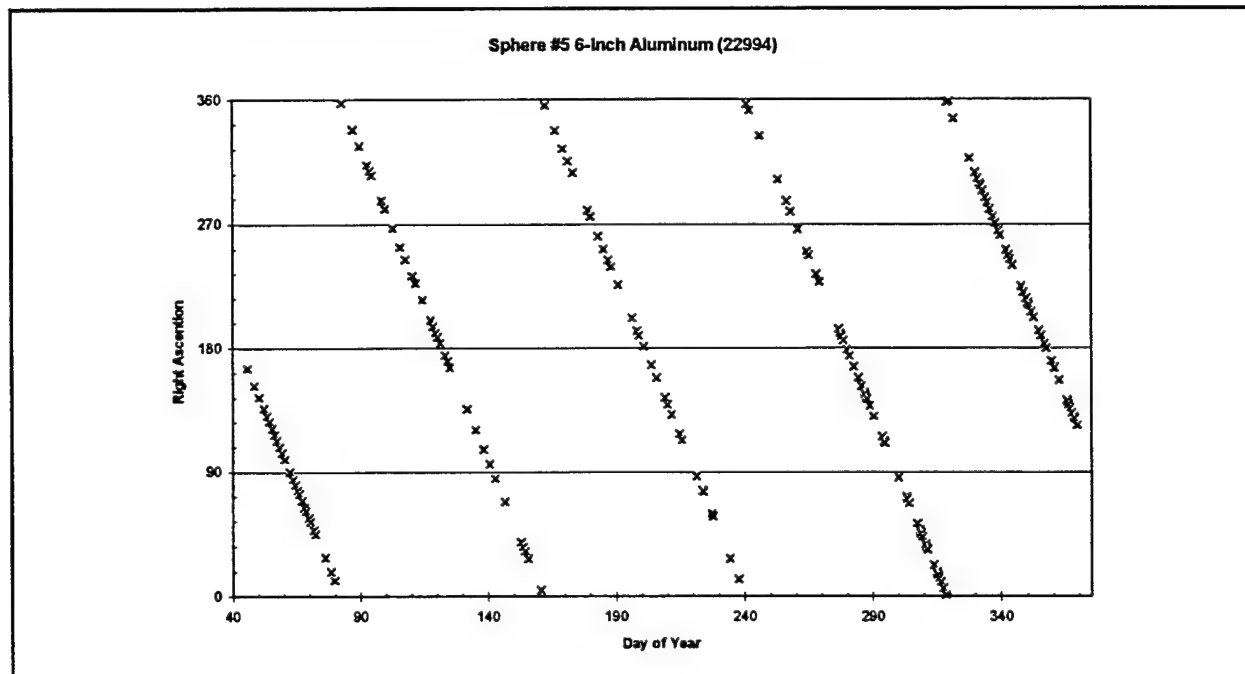


**Figure 4**

**RIGHT ASCENSION RATES**  
**Degrees/Day**

Satellite	22990	22991	22994	22995
Theoretical ( $J_2$ )	-5.09	-5.09	-5.05	-5.05
Observed	-4.6126	-4.609	-4.574	-4.576

**Table 3**

The theoretical inclination rate, (with  $J_2$ , alone) differs from observed inclination rate by nearly 10-percent. Hence, the Right Ascension rate for the ODERACS satellites is weakly effected by Solar/Lunar perturbations and possibly transverse drag.

**ARGUMENT OF PERIGEE:**

The argument of perigee (ArgP) is the angle between perigee point and the ascending node. Figures 5 shows the ArgP history for satellite 22990 and Figures 6 shows the ArgP for satellite 22994 from deployment through January 6, 1995. The ArgP drift is also due to several forces, equation 5 shows the rate due to perturbing bodies and equations 6 and 7 show the rate due to the earth's gravitation potential.

**Argument of Perigee Rate:**

$$\begin{aligned} \partial\omega = & 3/2 \pi \mu_1 / \mu_0 (a/r_1)^3 (e^2 * \sqrt{1-e^2}) * \\ & [5 \cos^2 i \sin^2 \omega + (1-e^2)(2-5 \sin^2 \omega)] \end{aligned} \quad (\text{eqn 5})$$

$$\partial\omega = 6 \pi (r_e/r_0)^2 (1 - 5/4 \sin^2 i) J_2 (1 - e^2)^{-2} \quad \text{radian/period} \quad (\text{eqn 6})$$

$$\partial\omega \approx 4.98 (r_e/r_0)^{1.5} (5 \cos^2 i - 1) (1 - e^2)^{-2} \quad \text{degrees/day} \quad (\text{eqn 7})$$

Table 4 shows the observed ArgP drift and the calculated drift due to  $J_2$ . The observed and theoretical ArgP rates are very close. The primary difference is that the theoretical does not included solar/lunar perturbations or radiation pressure. Calculating the secular perturbation shows a negligible contribution. Noting the different observed drift rates points to an area to mass contribution. This again suggests radiation pressure or atmospheric drag.

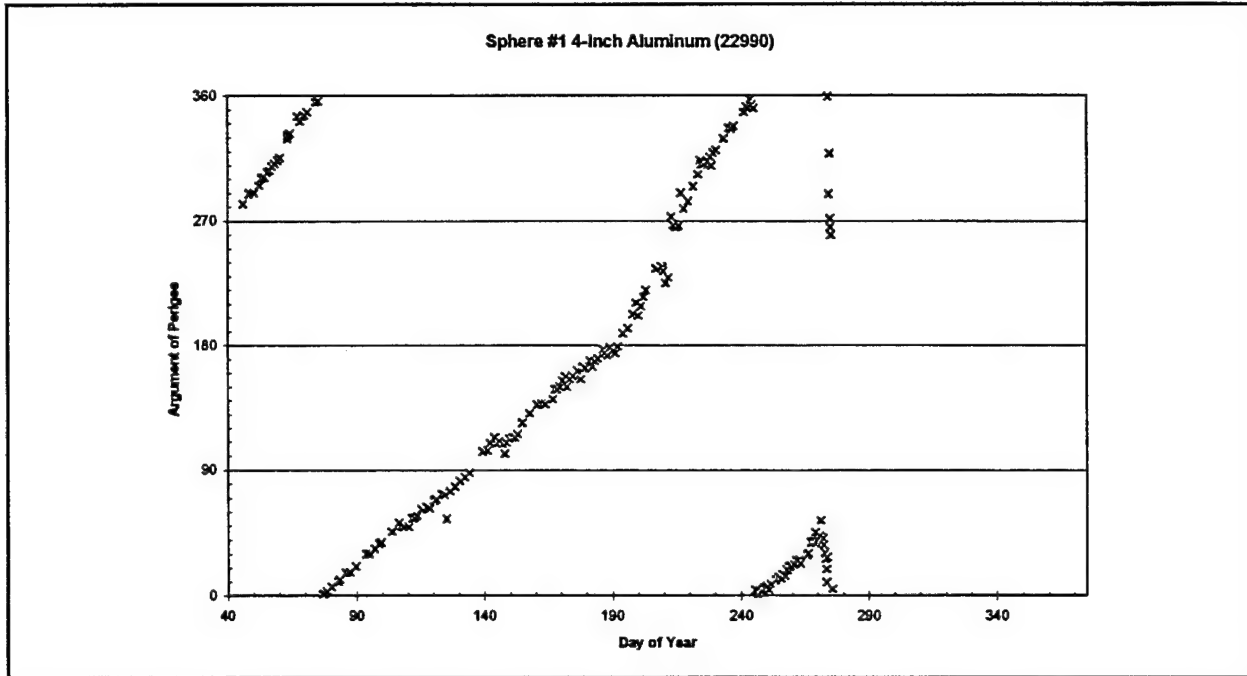


**Figure 5**

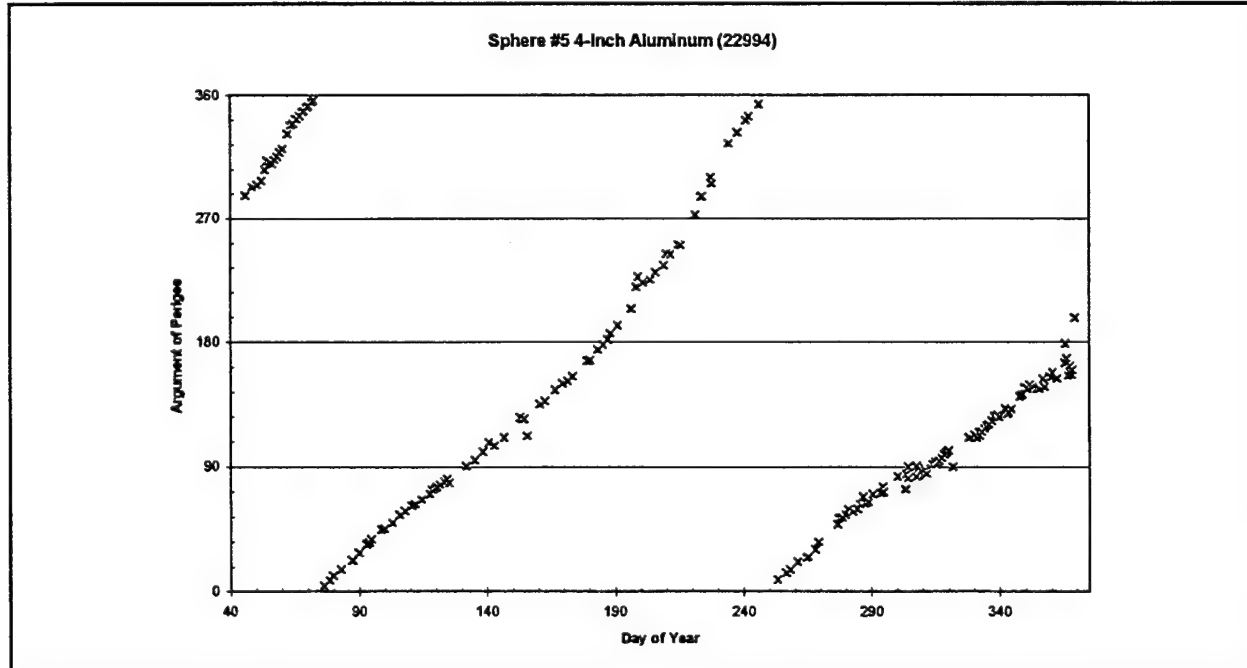


**Figure 6**

## ARGUMENT OF PERIGEE RATE

Satellite	22990	22991	22994	22995
Theoretical	2.31	2.31	2.29	2.29
Observed	2.174	2.169	1.906	1.910

**Table 4**

### **ECCENTRICITY:**

The eccentricity describes the shape of the satellite's orbit plane. Figure 7 shows the complete eccentricity history for satellite 22990 and Figure 8 shows the eccentricity for satellite 22994 from deployment through January 6, 1995. From these figure is can be seen that the eccentricity has a slightly decaying-sinusoidal behavior. The decay is a natural phenomena--over time a satellite's orbit tends towards circular due to atmospheric drag. The long-term sinusoidal period can be calculated using the peak values, the results is shown in Table 4. The eccentricity rate due to secular perturbations (equation 8) shows that the sinusoid period is a function of twice the argument of perigee (Reference 4). However, this contribution is negligible. Drag and solar pressure also have a slight effect; but, would not display the long term period shown in figures 7 and 8. Reference 1 discusses that gravitation potential  $J_3$  has a periodic effect on the shape of the orbit.

Eccentricity rate:

$$\partial e = -15/4 \pi \mu_1 / \mu_0 (a/r_1)^3 (e^2 * \sqrt{1-e^2}) \sin^2 i \sin 2\omega \quad (\text{eqn 8})$$

### **LONG TERM ECCENTRICITY PERIOD (Days)**

Satellite	22990	22991	22994	22995
Observed	127	125	179	175

**Table 4**

### **MEAN ALTITUDE:**

The mean altitude is derived from the mean motion (revolution/day) and eccentricity. The time history for satellites 22990, 22992, and 22994 are shown in figures 9 - 11 respectively.

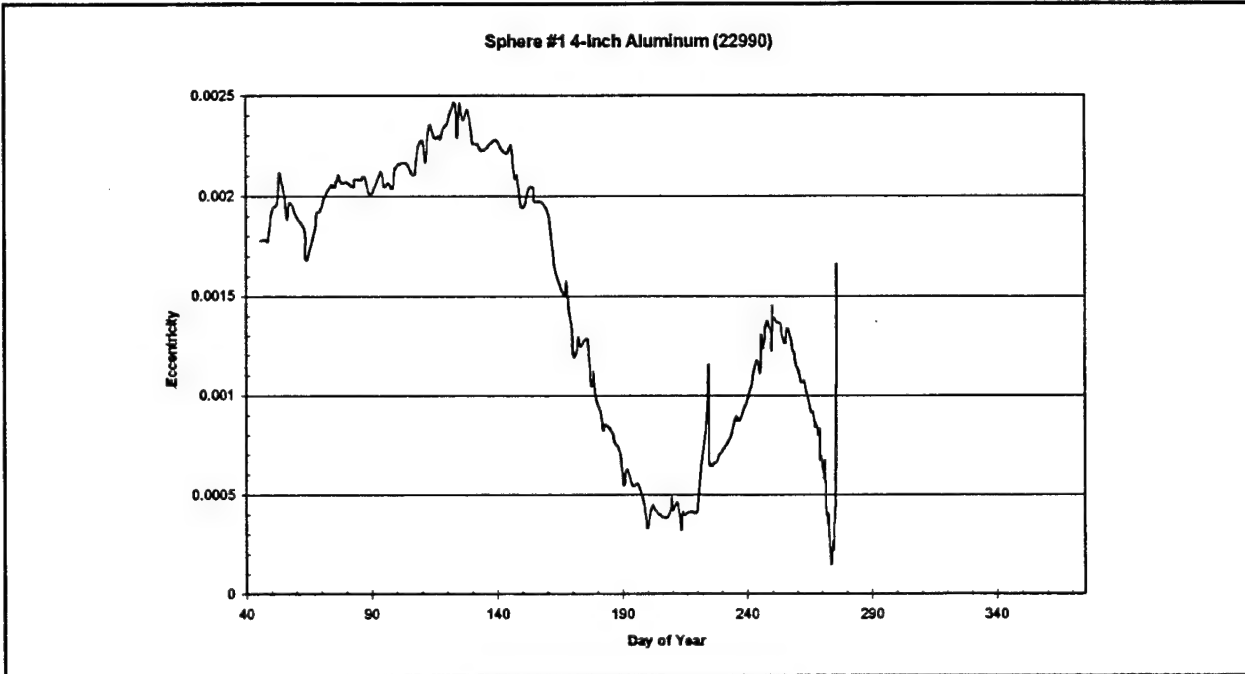


**Figure 7**

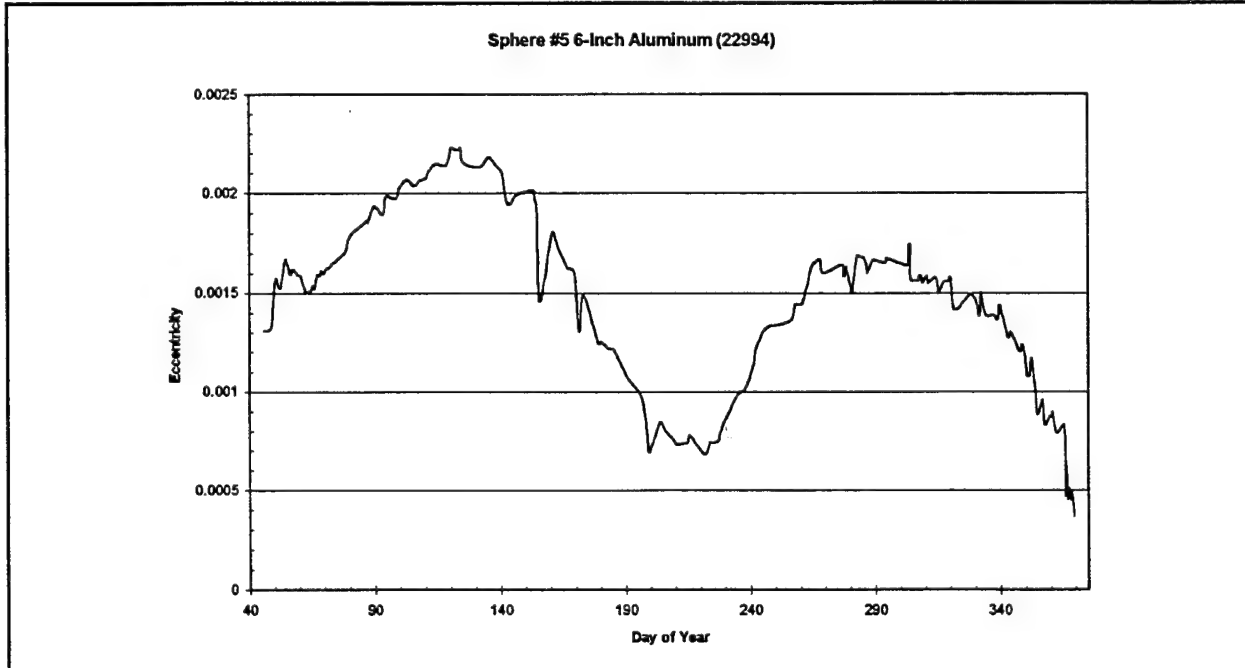


**Figure 8**

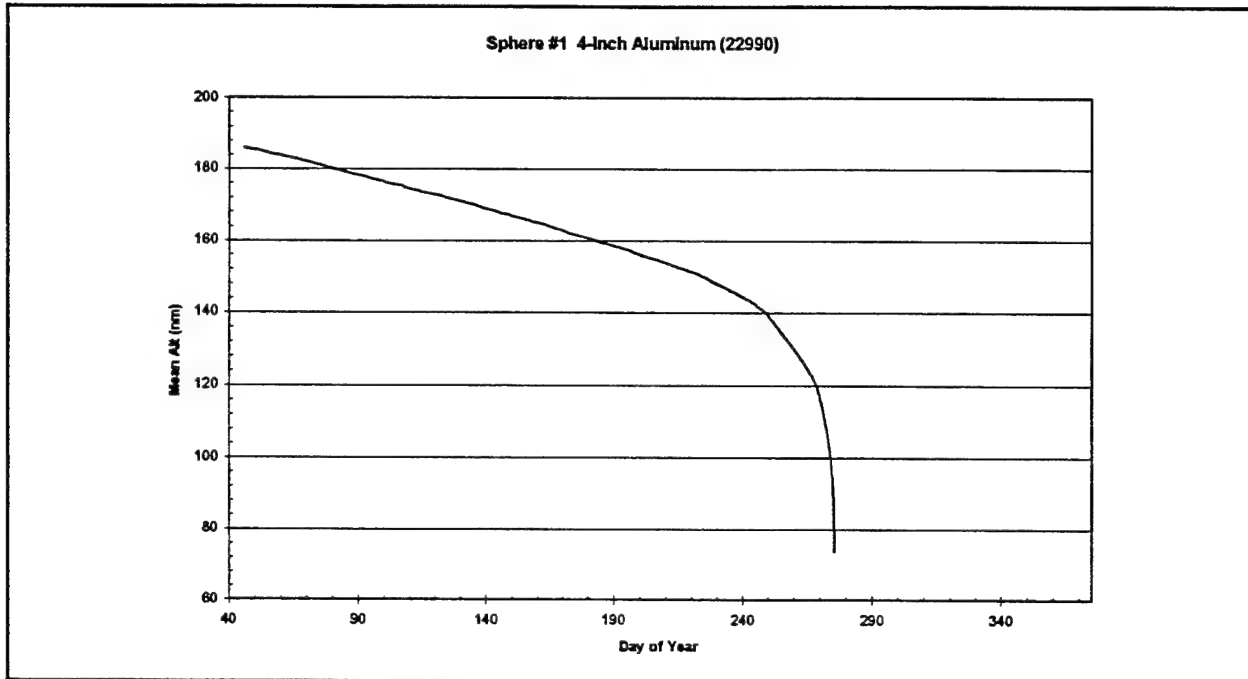


**Figure 9**

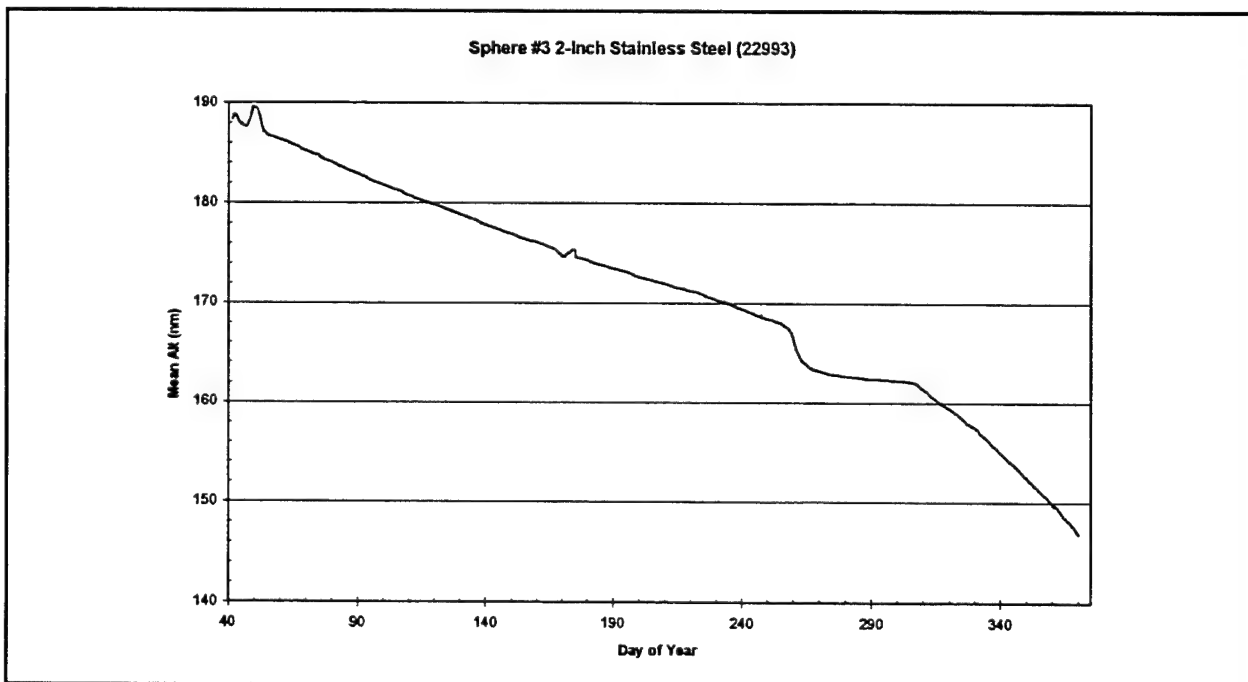


**Figure 10**

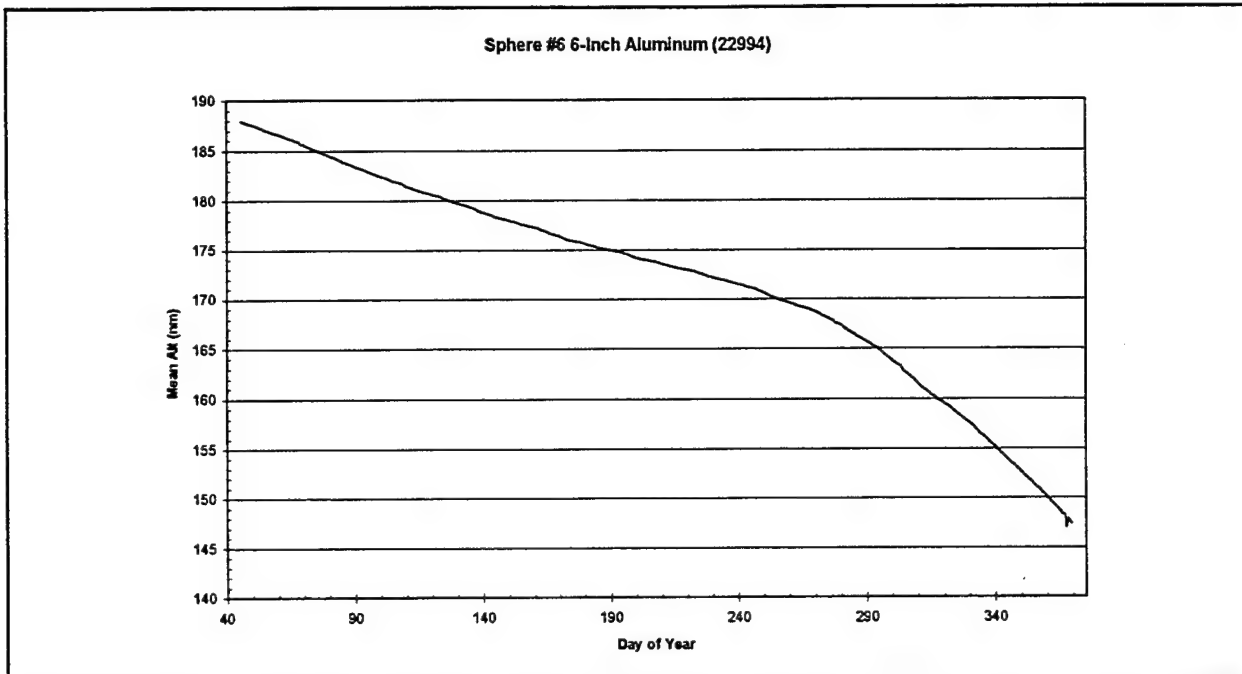


**Figure 11**

#### **ODERACS ORBITAL DECAY:**

Figures 12 and 13 show the F-10, B-star and the N-dot values for satellite 22990 and 22994. It can be readily seen that the solar flux changes the rate of decay. However, none of the decay models used were able to accurately predict the ODERACS lifetimes. Scientific groups worldwide all underpredicted the lifetimes of the spheres; as was seen by the ODERACS contest. Several months after deployment, we ran the codes again and over-predicted the lifetimes of the 2-inch and 6-inch spheres. After some trial and error, it appears that the programs needed to be broken down into two altitude segments. Each altitude-region calculation was then run separately and the results combined. Using two of JSC/SN3 most popular codes produced very good results on satellite 22990, when we divided the altitude into regions below and above 140 nm (259 km). From Figure 9, it can be seen that at this altitude the derivative of the decay takes a big jump.

#### **Conclusion:**

The ODERACS elements sets provide a wealth of information to study: secular perturbations, the earth's gravitational potential, mass dependent perturbations, and radar/optical signatures. The spheres were characterized at numerous radar frequencies and optically. Also, their mass and size are precisely known. This data can be investigated much further.

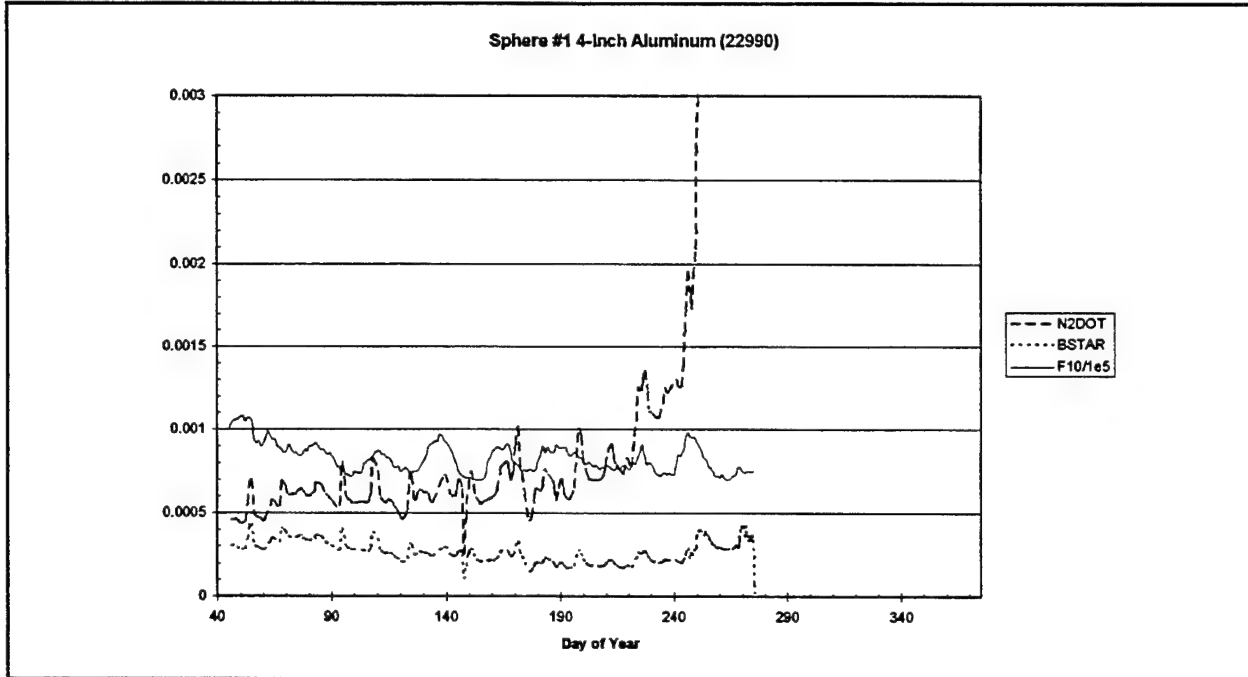


**Figure 12**

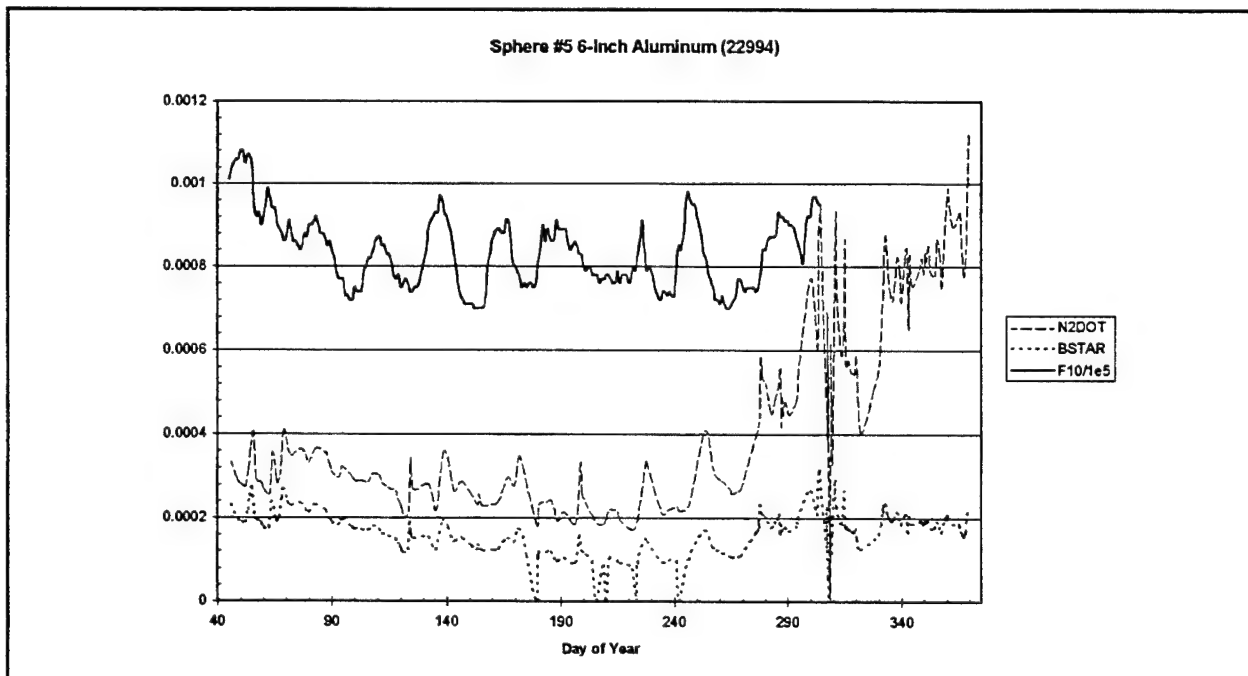


**Figure 13**

## LIST OF REFERENCES

1. Bate, Roger R., Mueller, Donald D., White, Jerry E., Fundamentals of Astrodynamics, New York, NY, Dover Publications 1971.
2. Lang, Kenneth R. Astrophysical Formulae, New York, NY, Springer-Verlag, 1980.
3. Siedelmann, P. Kenneth, Explanatory Supplement to the Astronomical Almanac, Mill Valley, CA, University Science Book, US Naval Observatory, Washington, DC, 1992.
4. El'Yasberg, P. E. Introduction to the Theory of Flight of Artificial Earth Satellites, Translated from Russian by the Israel Program for Scientific Translations, Jerusalem, 1967.

## THE NASA/JSC IONIZATION RADAR

Walter Marker (NASA Johnson Space Center), Herbert R.A. Schaeper (University of Houston/CI), Greg E. McCaskill, Sassan Yerushalmi (Lockheed Engineering and Sciences Company)

### **Abstract**

The NASA Johnson Space Center has upgraded an existing Ionization Radar to enhance its capabilities for conducting studies of re-entering space debris. The radar operates on 49.92 MHz at 85kW peak power, with maximum power of 400kW under the current expansion program. The antenna consists of 8 Yagi arrays, having a total gain of about 21 dBi. The radar is a monopulse system with electronic beam steering. The entire Yagi array is mechanically steerable 360° in azimuth and 90° in elevation, allowing complete hemispherical coverage. The radar system has been designed for easy transportability and use at remote sites.

The primary purpose of this multifunction radar is the observation and measurement of the ionization trails of submillimeter particles, both man-made and cosmic, entering the atmosphere. Observation of the trajectory and velocity of the particles should allow reliable discrimination between man-made debris and meteors.

Another purpose of the radar is to observe the breakup and footprint of debris from re-entering rocket components. Measurements of the Ariane 5 external tank re-entry and breakup to take place in November 1995 are currently planned for 1995.

Preliminary observations of the 1994 Perseid shower, the MIR space station and also lightning ionization trails are reported.

### **1.0 Introduction**

NASA Johnson Space Center is the lead NASA center for Orbital Debris studies. Orbital debris is a constant hazard for orbiting space craft. For example, the Space Shuttle routinely makes orbital adjustments to avoid debris whose orbit is tracked by the Air Force. However, there is a population of debris that is too small to be tracked by the Air Force's radar system which nevertheless is large enough to do considerable damage to orbiting spacecraft. The population density of this debris is predicted by a series of NASA computer models. A critical term in these models is the "settling" term or rate at which debris particles re-enter the atmosphere. NASA/JSC begin investigating VHF radars several years ago as a method of measuring the re-entry rate of this small debris so as to aid in the validation of the NASA debris models.

VHF radars have long been used to observe the ionization trails of natural meteors as they enter the atmosphere. The literature is filled with many reference, but one of the best classical overviews is McKinley, 1961. While considerable advances in electronics and data processing have been made since this publication, the basic physics discussed in this reference remains unchanged. The challenge for our design team was to develop a VHF radar that can distinguish between the meteors entering our atmosphere from re-entering man made debris. In the size range of interest, it is known that the natural meteors are far more frequent. Thus even a small misidentification of meteors as debris will cause great errors in the estimation of the re-entry rate of debris.

## **2.0 The NASA/JSC Ionization Radar**

The NASA transportable ionization radar has been used on numerous field campaigns such as the Delta II PMG plasma ionization experiment in Hawaii, 1993; the STS-31 External Tank re-entry and breakup measurement, Hawaii, 1990; the STS-30 related debris re-entry experiment, Puerto Rico, 1989; the Delta 181 re-entry trajectory measurements, Diego Garcia, 1988; and the Delta re-entry ionization tests, Hawaii, 1986. The experiences gained on these field campaigns form the basis of the present radar improvement program.

### **2.1 Transmitter**

The ionization radar under the current upgrade program will use four separate VHF transmitters, each generating 100 kW peak power, driving the four quadrants of a monopulse antenna array. The transmitter power amplifiers use 3CPX5000 triodes driven by 3CPX800 tubes. At the present initial development and testing phase two transmitters are in operation driving a multiple Yagi antenna array in a dual-parallel mode. The timing pulses of the T/R switches in the transmitter output circuits are controlled by the PRF and the transmitter pulsewidth. In addition, the timing pulses also have a 10  $\mu$ s front and rear porch safety feature. The T/R pulses are generated in a dedicated PC radar controller.

### **2.2 Power Supply**

Two high voltage power supplies are used for the four transmitters. Each provides 6kV and 3kV for two power amplifiers and driver stages respectively. All the transmitter bias voltages are also generated in each unit. The supplies operate off the 220V mains.

### **2.3 Receiver**

The receiver system is a 5 channel quadrature unit operating in the homodyne mode. It also provides the control and reference signals for the radar system. A 49.92 MHz xtal master oscillator generates the transmitter carrier as well as the LO signal for the homodyne mixers. TTL level pulses are also generated for synchronizing the transmit/receive modules. The receiver is subdivided into the RF modules and the Baseband modules.

#### **2.3.1 RF Modules**

There are five RF modules. Each accepts RF from either the radar transmitter antennas through the T/R switches or a separate receive-only antenna in an interferometer mode. The output of each channel consists of the I/Q video signal that is further amplified in the Baseband modules.

### **2.3.2 Baseband Modules**

Five Baseband modules amplify and filter the outputs from the RF modules, using low-pass Chebychev filters. The modules are initially configured to produce four selectable bandwidths, namely 1 MHz, 200kHz, 50 kHz, and 20 kHz.

All receive channels from the homodyne mixers to the magnetic data recorder are DC coupled for down to zero frequency Doppler response.

## **3.0 Antenna System**

Several different antenna configurations are available, depending upon the specific research objectives to be supported. The original system began with a simple crossed dipole with a reflecting ground plane. This evolved to a pair of Yagi 5 element antennas. This in turn evolved to form a Yagi array of 8 antennas in the form of an H. Each corner of the H is outfitted with a pair of Yagi antennas at  $\frac{1}{2}$  wavelength separation. The Yagi pairs are separated by 1 wavelength in both the horizontal and the vertical. The antennas are mounted on SS pipe that forms the H. The entire antenna array is mounted on a 10m tower. The H frame is steerable in both azimuth and elevation under computer control. Figure 1. shows the VHF antenna array. The patterns of the antenna array have been modeled using the ELNEC plotting software. A sample pattern is shown in figure 2 for the antenna spacing specified above an imperfect ground.

## **4.0 Data Recorder**

The data storage system consists of a Honeywell 14 track magnetic recorder/reproducer, model 101e. The recorder has a coaxial reel system that transfers the tape between the reel planes without distorting the tape path. There are no pinch rollers or mechanical adjustments in the tape path. The recorder can operate either in a direct 2MHz mode, or a FM mode with a 900 kHz carrier. For radar data collection the unit is operated exclusively in the FM mode. Beside the radar echo record, additional tracks are used for the system sync pulses and the GOES satellite time code signals.

## **5.0 Data Processing**

The data are processed in two ways. The data is recorded on magnetic tape for post analysis. In addition a limited amount of calculations are performed in realtime. The intention is to perform more and more calculations in realtime, so as to allow realtime optimization of the radar parameters. The realtime data reduction is done with a DATEL PC-430 A/D card mounted in a dedicated computer. This same card is used in postmission data reduction by playing back the recorded data.

## **5.1 Analog to Digital Data Conversion**

The analog to digital conversion is performed by the DATEL PC-430 very high speed ISA A/D-DSP coprocessor board. This processor can acquire up to sixteen analog input channels, digitize them and store them in local memory while DSP math processing and data transfer are performed concurrently. The processor is also used for continuous FFT processing and simultaneous graphics display of spectral data.

## **5.2 Data Thinning Algorithm**

Because of the large computational load placed on the processing system it is not convenient to achieve complete data reduction off the data tapes in one single pass. Therefore to optimize the data reduction process a method is in development that consists of series of passes to reduce the radar data successively.

### **5.2.1 Radar Echo Identification Pass**

The data system reviews the entire data tape and records the exact time at which every event over a predetermined receiver threshold occurs. This is the Echo Event Data Base. Entries consist of an event number and time of threshold crossing using GOES satellite Time Code.

### **5.2.2 Event Selection Pass**

The raw data is again passed through the system. Having prior knowledge of when to expect data, the computer will process each event by comparison with a "rule set" to determine if the event meets the criteria to be included in the next level of processing. The computer can predetermine if the latency time involved in this process will cause the next sequential event to be ignored. If so, the system will so note in the internal data log, and on the next pass it will skip those events which have been investigated on prior passes. This process will continue until all events have been investigated. This is the Ionization Trail Object Data Base. Entries consist of Event Number, Temporal Width (half power points), the Peak Amplitude, and Range at which the peak amplitude occurred for each sample within the temporal range.

### **5.2.3 Velocity Pass**

The computer will digitize and store a high time resolution (but short duration) image of the I and Q channels from the recorded data within the main memory. Data sets consisting of sequential samples at each range within the event will be subjected to Fourier transformation into the frequency domain. Velocity profiles thus obtained will be input into the next data base. This pass generates the Velocity Data Base. Entries consist of Event Number and Velocities for each range in which the event was recorded.

#### **5.2.4 Correlation Pass**

When data have been collected from multiple debris observation sites, the individual data sets will be merged. For each event, the data from all sites will be searched. When a correlation in time is noted, the range and velocity from multiple locations will be used to determine (within the accuracy of the measurements) the trajectory of the object and its velocity along the flight path. This pass creates the 3-Space Data Base. Entries will include Event Number(s) and the derived vector for each event.

#### **5.2.5 Meteoroid Discrimination Pass**

During this pass a statistical classification algorithm will be used to classify detected events as natural or man-made based on differences in speed and angle at which the objects enter the atmosphere.

#### **5.2.6 Data Presentation**

Data from any level of the reduction process may be viewed in either tabular or graphic format.

### **6.0 Preliminary Data Acquisition**

In order to test the various system upgrades such as the new antenna and RF feed system in conjunction with the keyboard control of the Az and El tracking rotators various radar targets of convenience have been used.

#### **6.1 Perseid Meteoroid Shower**

A simplified configuration of the radar was used to observe the 1994 Perseids meteor shower. The radar used a 5 element twin Yagi array with a  $\lambda/2$  spacing between the two booms. The gain of this antenna was about 15 dBi. Only one 50kW transmitter was utilized. Approximately 20 hours of data were recorded over two days. The data analysis of this shower is still continuing. The maximum count rate observed was about 150/hour. A typical strong echo from the Perseids shower is shown in figure 3.

#### **6.2 MIR Space Station**

The Russian MIR Space station is routinely observed when it passes over the site of Johnson Space Center. As of February 1995, fourteen observations of MIR were made. These observations were taken with the radar in its intermediate configuration. The radar utilized all eight Yagi antennas. In the MIR mode two separate transmitters were used, each driving four Yagis with a total power output of 65kW. The MIR is primarily observed to test the pointing accuracy

of the radar system and to gain experience in the use of multiple transmitters. The MIR is observed with the radar in staring mode. The orbital position of the MIR is calculated and the antenna is pointed at the predicted location in space. The echo signal is recorded on magnetic tape and is post mission digitally analyzed.

The observed RCS of MIR varied significantly from pass to pass. The variation is primarily a function of the orientation of the solar panels relative to the radar site. The maximum cross section observed was 23.8 dBm<sup>2</sup>.

Upgrades to the tracking system of the radar are currently in progress. When completed these upgrades will allow the radar operator to drive the antenna along the predicted path of selected targets. This should allow the variation of RCS to be studied as a function of observation angle.

### **6.3 Lightning Ionization Trails**

During a recent severe thunderstorm a series of measurements of lightning ionization trails were made with the VHF radar. Data reduction and analysis is currently in progress.

## **7.0 Summary**

The NASA Johnson Space Center is presently upgrading a field transportable VHF radar in order to provide greater system sensitivity for ionization trail observation of re-entering space debris. The basic radar system has been used on various field campaigns in conjunction with Space Shuttle External Tank re-entry measurements. In its final configuration the radar will operate with 400kW and a monopulse antenna system with about 21 dBi gain. The present status and preliminary results have been discussed in this paper.

## **8.0 Acknowledgements**

It is with pleasure to acknowledge the many thoughtful suggestions received from: Dr. E.T. Dickerson, Dr. Eldon Husband, University of Houston; Eugene Stansbery, NASA/JSC; Thomas Settecerri, Lockheed Engineering and Sciences Company.

## **9.0 References**

1. David Barton, "Modern Radar System Analysis", Artech House, Inc., 1990
2. Nadav Lebanon, "Radar Principles", John Wiley and Sons, Inc., 1988
3. Eli Brookner, "Radar Technology", Artech House, Inc., 1977
4. Toru Sato et al, "Shape of Space Debris as Estimated from Radar Cross Section Variations", Journal of Spacecraft and Rockets, Vol 00, 1994
5. Eugene Stansbery, Herbert R.A. Schaeper, "Space Debris Measurements in the Staring Mode with the ALCOR Radar", 1990 Space Surveillance Workshop, MIT Lincoln Laboratory, Lexington, MA, 1990
6. W.A. Stutzman, G.A. Thiele, "Antenna Theory and Design", John Wiley and Sons, Inc., 1981
7. D.W.R. McKinley, "Meteor Science and Engineering", McGraw-Hill, 1961

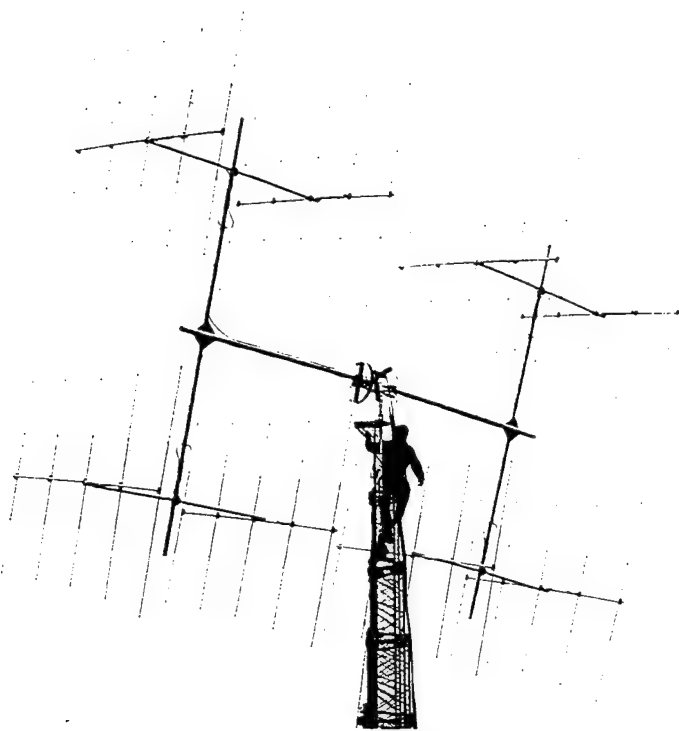


Figure 1. The VHF Ionization Radar Antenna System

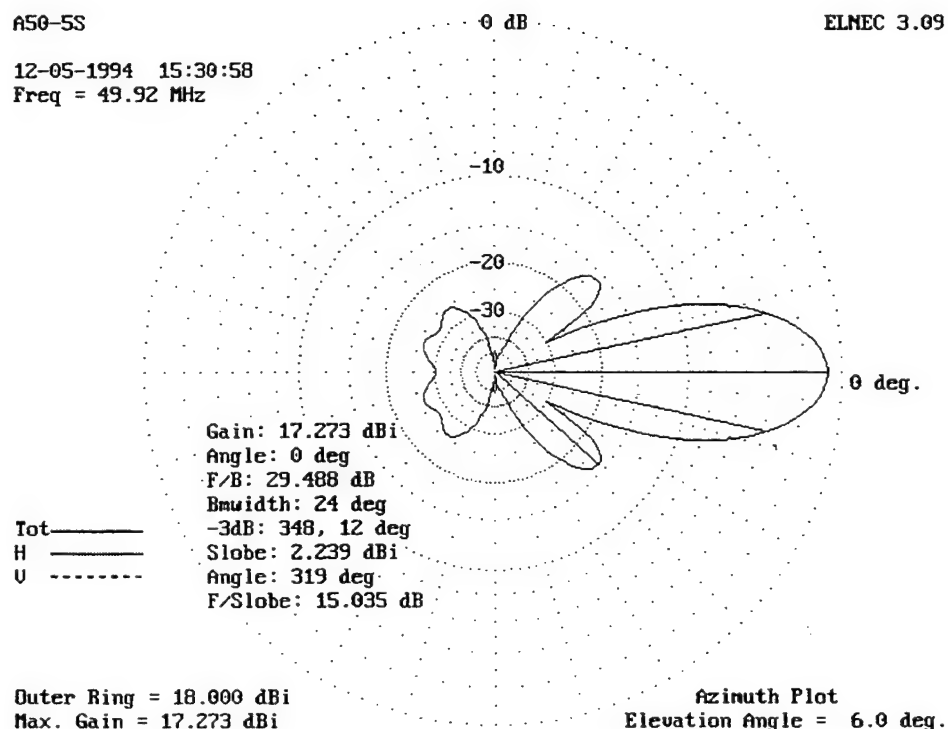


Figure 2. VHF Antenna Pattern of four Yagis in the Horizontal Plane

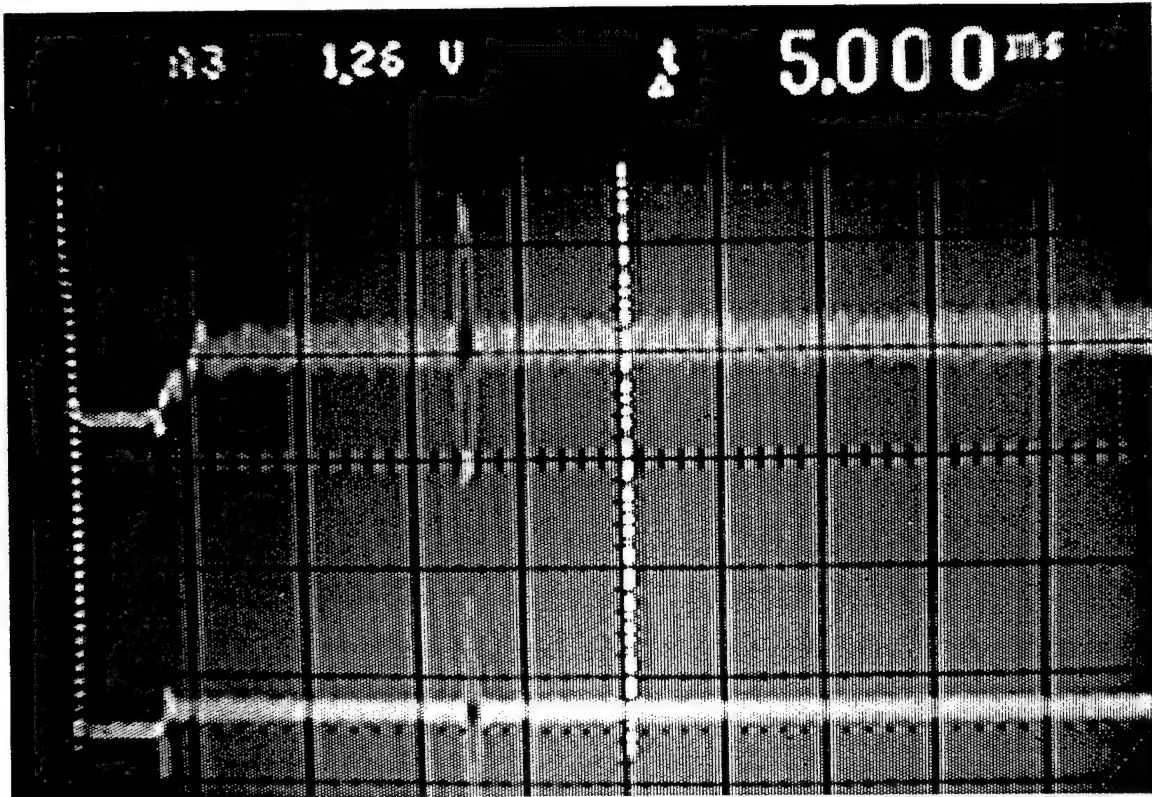


Figure 3. Perseid Ionization Trail Radar Echo

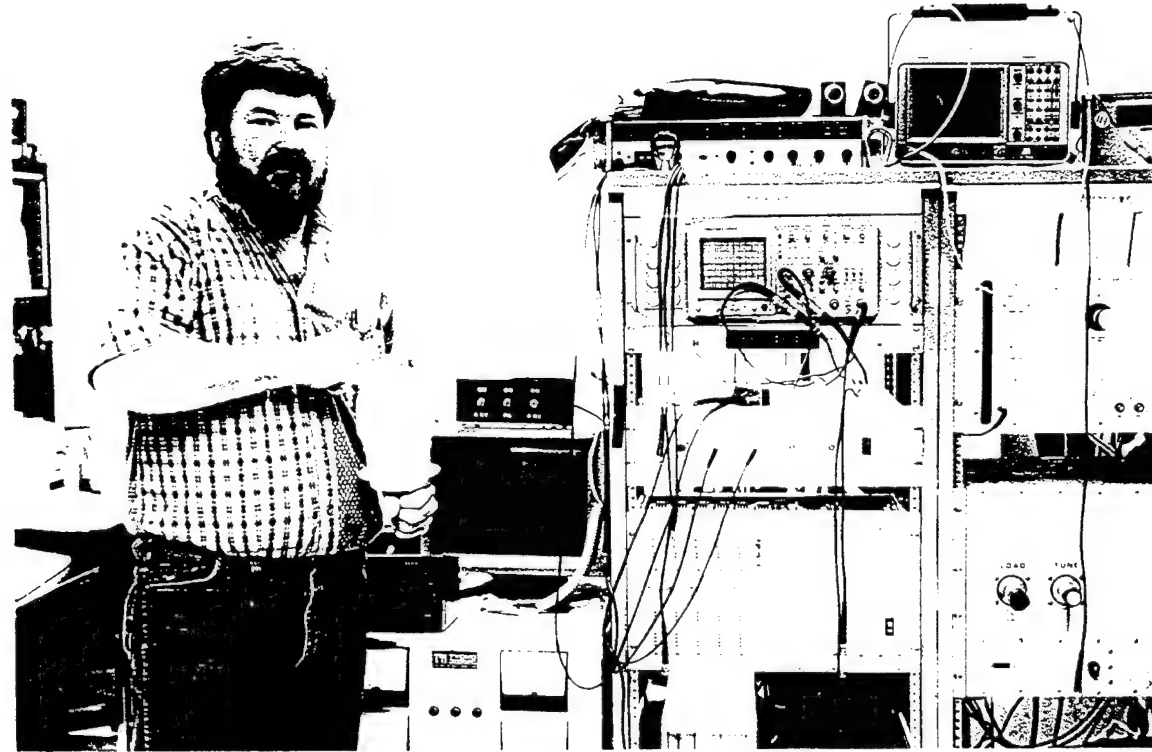


Figure 4. Radar Set Up with Engineer holding one of the TX Output Tubes

# The Los Alamos Photon Counting Detector Space Object Detection Project:

## An Update

Cheng Ho, Bill Friedhorsky, Miles Baron, Don Casperson  
(Los Alamos National Laboratory, MS D436, Los Alamos, NM 87545)

### ABSTRACT

At Los Alamos, we have been pursuing a project for space object detection using a photon counting detector with high spatial and time resolution. By exploiting the three dimensionality of the high quality data, we expect to be able to detect an orbiting object of size below 2 cm, using a moderate size telescope and state-of-the-art photon counting detector. A working tube has been used to collect skyward looking data during dusk. In this paper, we discuss the progress in the development of detector and data acquisition system. We also report on analysis and results of these data sets.

### 1. DETECTION CONCEPT

During dawn and dusk, a telescope located on the night side of the earth can detect sunlight reflected by an object in low-earth orbit. The orbiting object moving at a high velocity relative to a fixed background of stars and diffuse light provides a unique signature for detection. It is, however, difficult to detect small objects with an imaging detector collecting 2-dimensional data: the faint track left by a small object with length corresponding to the image integration time will be overwhelmed by the background. With the advance of fast imaging photon counting detector, the data can be collected, instead, in a 3-dimensional format, i.e.  $(x, y, t)$  of individual photons. This additional dimensionality greatly enhances the statistical significance of linear features in the data. The purpose of this project is to demonstrate this detection concept. For more details of the scheme, see Ref. 1.

### 2. PROJECT OVERVIEW AND EXPERIMENTAL SETUP

Since 1993, Los Alamos National Laboratory, with support from the US Air Force Phillips Laboratory, has been pursuing an end-to-end brassboard demonstration of this detection concept, utilizing the microchannel plate/crossed delay line (MCP/CDL) detector under development for DOE programs (Ref. 2). Expected performance of the detector is: active area of 40 mm diameter, about 20 microns FWHM spatial resolution, average quantum efficiency of about 10% depending on the photocathode, much better than 1 millisecond time resolution, and a maximum count rate of  $5 \times 10^5$  cts/sec. We are currently developing the next generation of electronics which will allow us to push the maximum count rate to well above  $10^6$  cts/sec. A baseline space object detection system will incorporate a moderate size telescope with the detector, coupled to a fast data acquisition system with large storage capacity.

At the moment, we have one working sealed tube. An end-to-end system from telescope to detector the data acquisition and analysis system has been constructed. The system has been taken to a dark site near Los Alamos on moonless nights for observation in three separate field trips. During each field trip, we pointed the telescope skyward to acquire

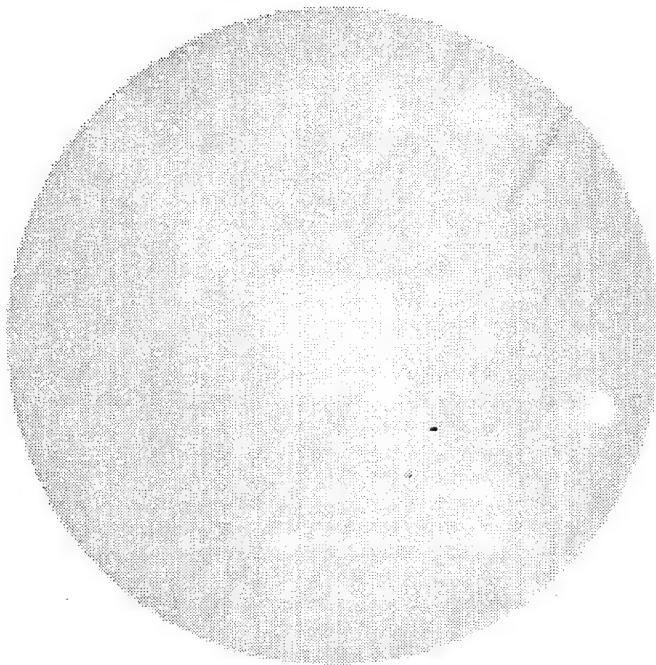


Fig. 1 – Raw *negative* image of the data set collected at 21:45 on July 5, 1994.

data suitable for small object detection. In the rest of this paper, we describe the detailed experiment set up and results for one particular exposure. During most of the field trips, the MCP/CDL detector was mounted on a primary telescope which is attached to a portable mount. The telescope consists of a 15 cm aperture Melles Griot lens with 1 m focal length. The site is located at longitude 106.23° West and latitude 35.77° North.

On July 5, 1994, at around 21:45 local Mountain Daylight Saving Time, the telescope was pointed at an elevation of about 57.8° and azimuth of 107.1°. This pointing was selected since the ALEXIS satellite (Ref. 3) was scheduled to pass over at this maximum elevation with favorable viewing angle. The telescope mount is steerable. During this observation, it was set at a fixed pointing relative to the earth. The data were acquired in a mode which continues until 128 MBytes of RAM (random access memory) in the data acquisition system is filled. Taking into account data recording headers, the entire data set contains about 8 million recorded events, with each raw photon events requiring 8 bytes. The entire exposure lasted 413 seconds. The digital data acquisition electronics provides time resolution of 100 microsecond. As a result of instrument adjustment immediately prior to the exposure, the detector was left at a position focussed at a distance of several hundred meters instead of infinity. As we will see, this blurred the stellar images and reduced the detection sensitivity. A green filter with transmission (> 50%) between 480 and 616 nm was placed in the light path.

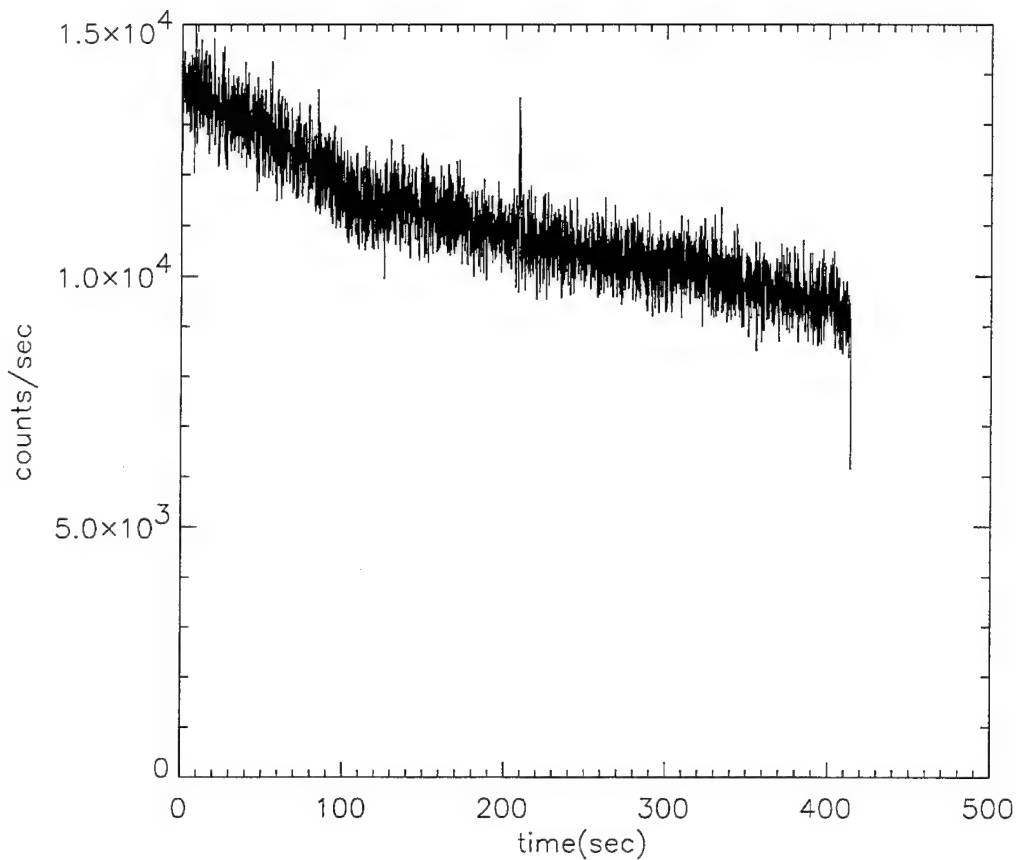


Fig. 2 – Time history of the data set collected at 21:45 on July 5, 1994.

### 3. ANALYSIS AND RESULTS

The raw *negative* image of this data set following standard reduction and analysis procedures is shown in Figure 1. (In this paper, images are shown as negatives, i.e. visually darker pixels have higher intensity.) In this image, several defects in the detector are easily visible. 1) The diagonal band from upper left to lower right results from gain suppression in MCP due to over-exposing of the tube to UV light. 2) The dark spots throughout the entire image are believed to be dead spots on the photocathode. 3) The two bright spots in the lower right quadrant are believed to be hot spots in the MCP. Furthermore, the window of the detector induces scattered light near the edge of the detector's active area. To eliminate these contaminating artifacts, photon events near the edge were removed in software, reducing the active area to about 35 mm diameter, with a corresponding field of view of about 2 degrees. The total count in the reduced data set is about  $4.5 \times 10^6$  counts.

The streaks going from the lower left to the upper right are stars in the FOV. The direction of the apparent motion of the stars, due to the earth's rotation, is from the lower

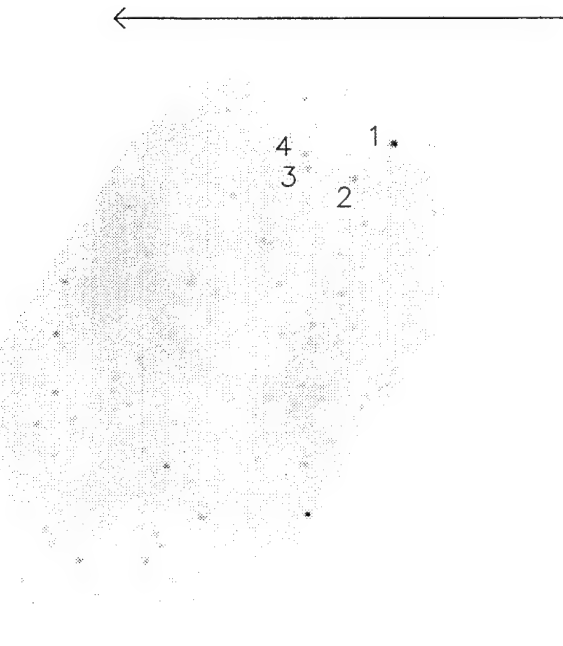


Fig. 3 – Sky image after correction for the earth's motion. See Table 1 for a partial list of identified stars.

Table 1. Identified Stars in FOV

Star Number	Designation	R.A.	Dec.	V Magnitude
1	HR6638	$17^h 48.4^m$	$20^\circ 34'$	5.69
2	SAO85445	$17^h 49.6^m$	$20^\circ 38'$	7.6
3	SAO85452	$17^h 50^m$	$20^\circ 52'$	7.9
4	SAO85448	$17^h 49.7^m$	$20^\circ 55'$	8.0

left (east) to the upper right (west). The time history of the entire reduced data set is shown in Figure 2, with the sky darkening easily visible.

Given the fine time resolution, we can apply a correction for the earth's motion. After re-registering each photon's position as a function of time, we get the image shown in Figure 3. It is straightforward to identify individual stars. Table 1 gives a partial listing of identified stars. Analysis of the image shows that the 5.7 mag star HR6638 yields a count

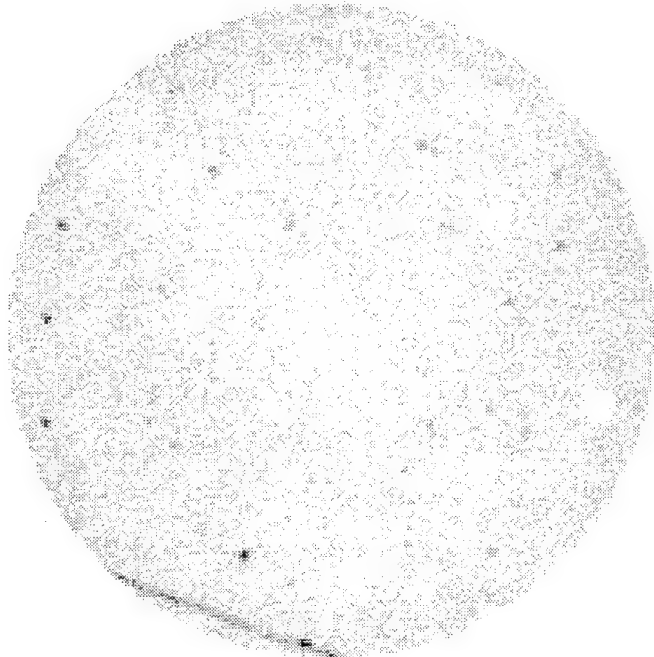


Fig. 4 – Raw image between 206 and 210 seconds of the data set.

rate of about 300 counts/sec. The full width half maximum (FWHM) of the reconstructed stellar image is about 370 microns or 1.25 arcmin. This is consistent with the detector located at an image plane whose conjugate is at about 400 m. (Skyward looking data sets taken later in the same night indicate a point source FWHM of about 70 microns, consistent with laboratory measurement made under the operating configuration.) From Figure 2, the average count rate during the exposure is about  $10^4$  counts/sec. Ignoring the difference in color and scaling to HR6638, we estimate the sky brightness to be about 21 mag/square arcsec.

After reviewing the ephemeris of the ALEXIS satellite, it was realized that the exposure started about 30 seconds after the satellite has passed the maximum elevation. The ALEXIS satellite's trajectory would cross the sky shown as the horizontal arrow in Figure 3.

An examination of the time history of the observing run (Fig. 2) reveals a very significant increase in count rate at around 209 seconds after the start of the exposure. Figure 4 shows the raw 2D image of the data set between 206 and 210 second. A linear track is clearly visible. Figure 5 shows the 3 dimensional view of the same data set. The 3D view confirms that the 2D linear feature in Figure 4 is indeed a linear track in the 3D space, indicating that this is a fast moving foreground object in a low-earth orbit. It is easy to envision rotating this data set until the projected plane is normal to this linear track. Figure

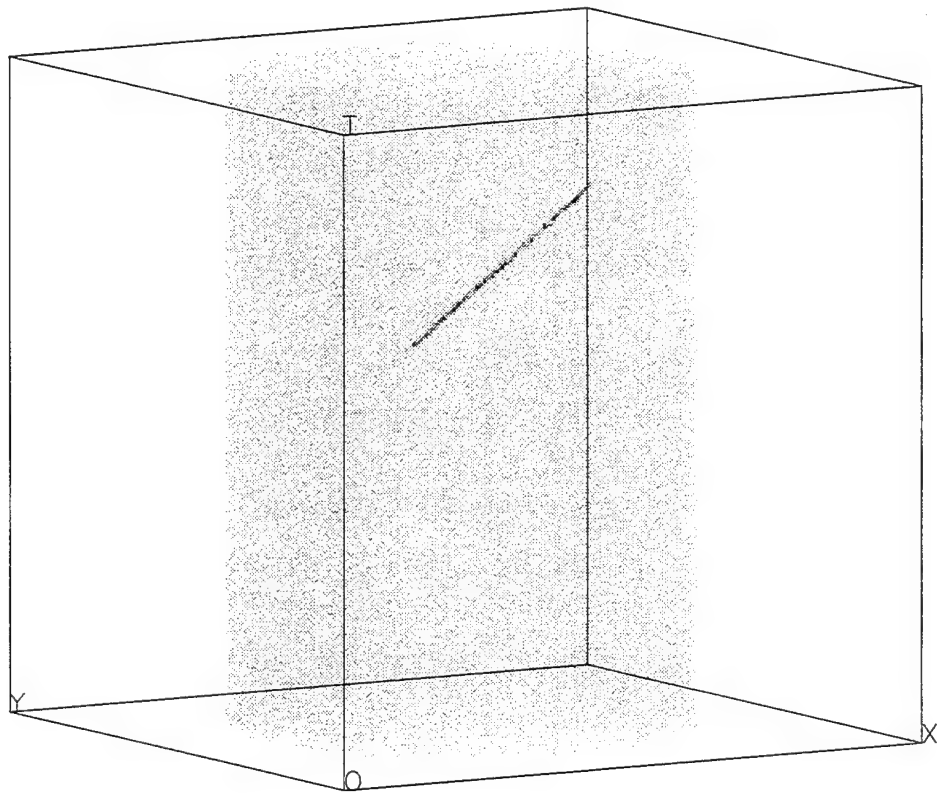


Fig. 5 – Three dimensional view of the data set of Figure 4.

6 shows the surface plot of a portion of the projected plane near the orbiting object. The zoomed region is 5 arcmin on the side. The total counts for this object during the 1 second transit time is about 1500 counts. In contrast, a neighboring region with the same area in the projected plane contains about 30 counts. The point source in the projected plane has a FWHM of about 1.2 arcmin, consistent with the measured FWHM from field stars. The significance of this object, based on an estimate image size of 1.5 by 1.5 arcmin, is much more than  $500\sigma$ .

The orbiting object has an estimated count rate of about 1500 counts/sec. Scaling to HR6638 in Figure 3 yields a brightness of about 4th magnitude. It is moving at an estimated angular velocity of 46 arcminutes/sec. Assuming that the object is moving at a linear speed of 8 km/sec, the range is estimated to be 600 km. Assuming circular orbit, it is at an altitude of about 500 km. The direction of the motion indicates that this object has a very high inclination angle. This object was visible by naked eyes from a lighted site at Los Alamos National Laboratory (Jeff Bloch, private communication).

#### 4. DISCUSSIONS

Comparison between figures 1 and 3 definitely demonstrates that additional dimensionality in the data set will help enhance the significance of linear features: We can clearly

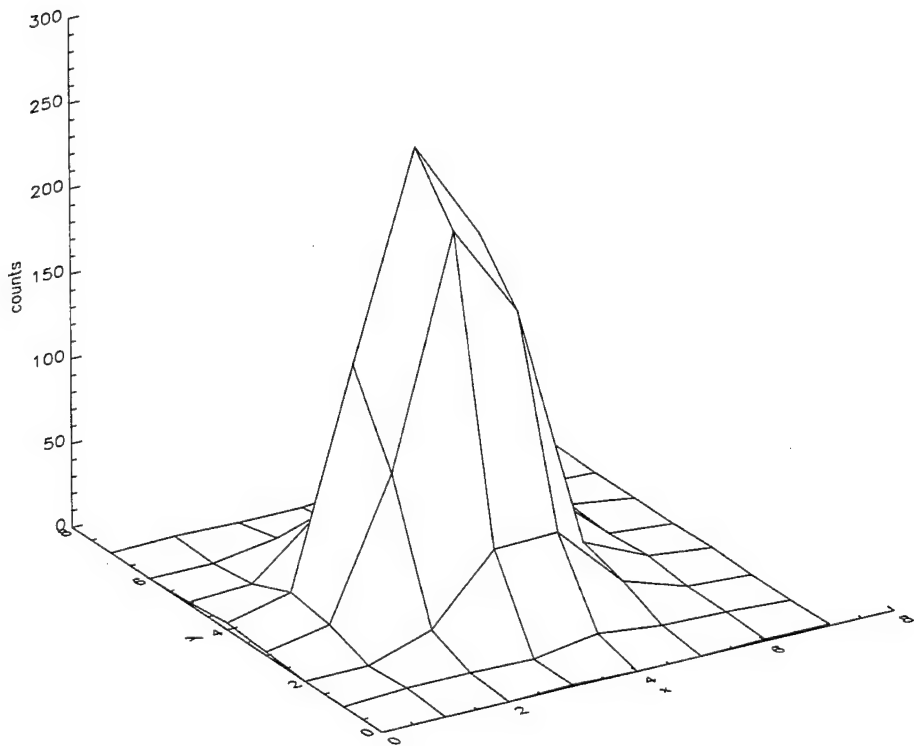


Fig. 6 – Surface plot of the area in the projected plane around the object.

see many more star-points in figure 3 than star-streaks in figure 1, keeping in mind that both figure are generated from exactly the same data set.

To further examine the sensitivity limit, let's examine figure 4. Some stars in Figure 4 have been identified. Specifically, the detected orbiting object passed through the star SAO 85583 of 7.7 magnitude near the bottom of the image. Other identified stars in this FOV are between 7th and 8th magnitude. This clearly indicates that we should be able to detect an orbiting object between 8th and 9th magnitude with this out-of-focus configuration.

We expect the sensitivity limit to improve from the following contributions.

1) The sensitivity limit scales linearly with the point source's FWHM. We foresee no difficulty in improving the FWHM by at least a factor of ten with a good tube and exposing in focus.

2) Figure 2 shows that we are not operating at the maximum count rate sustainable by the delay line readout and electronics (current system can support  $5 \times 10^5$  counts/sec). The key reason is that the quantum efficiency has degraded significantly since the tube was built. (Skyward looking data collected during earlier field trips achieved a count rate in excess of  $10^5$  counts/sec.) A good tube with consistent QE will enhance the sensitivity limit, scaling roughly like the square root of the QE.

3) In the current analysis, the stellar photons are left in. Removing these photons will reduce the total number of background counts.

4) As mentioned earlier, the sky background is estimated to be 21 mag/square arcsec. With the July 5th observing site nestled between Los Alamos, Santa Fe and Albuquerque, city lights increase the sky background. The current detector system is mobile. And we plan to take the detector system to darker site for better observation condition in the future. We are also pursuing collaboration with existing space monitoring site to mount our detector on existing telescopes.

Combining all of these factors, we do not anticipate difficulty in reaching the theoretical sensitivity limit projected between 15th to 16th magnitude.

In the field trips to date, we have acquired useful data to demonstrate the basic concept. More importantly, we have gained valuable experience which will help us perfect our observation procedure and develop an operational system. As with all developmental programs, experimental protocols continue to evolve. Mistakes such as not having the perfect focus and starting the exposure too late will no doubt be corrected as the project progresses.

As described in a previous paper (Ref. 1), data processing is a major challenge for this detection scheme. We have developed a prototype algorithm to handle the data analysis task and applied the algorithm to simulated data. However, the quality of data we have acquired to date is sub-optimal and we have chosen not to perform a full scale adaptation and optimization of the algorithm to these data sets. We expect to successfully fabricate another sealed MCP/CDL tube in the very near future. Field trips will soon follow and we fully anticipate the acquisition of high quality data. At that point we shall resume the algorithm development and adaptation to exploit the sensitivity of this space object detection scheme.

#### ACKNOWLEDGEMENTS

We thank all team members of the MCP/CDL development and applications programs for their diligence in putting together a complex system. The Los Alamos space object detection project is supported by the US Air Force Phillips Laboratory's Space Debris Research Program. This work was performed under the auspices of US Department of Energy.

#### REFERENCES

1. Cheng Ho, William C. Priedhorsky, and Miles Baron, 1993, SPIE Proc. vol. 1951, p. 67.
2. Miles H. Baron and William C. Priedhorsky, 1994, SPIE Proc. vol. 2006, p. 188.
3. William C. Priedhorsky, et al. 1994, SPIE Proc. vol. 2006, p. 114.

## **1994 Space Debris Campaign - Preliminary Results**

Taft DeVere (SenCom Corp)

Tim Payne (SWC/AE)

Capt. Gary Wilson (HQ AFSPC/DOYY)

### **INTRODUCTION**

To help satisfy the need for orbital debris measurements, Air Force Space Command (AFSPC) sponsored a Space Surveillance Network (SSN) Space Debris Campaign in 1994. The primary purpose of the 1994 Space Debris Campaign was to employ SSN and other cooperating sensors to detect, track and identify uncataloged space debris. The operating parameters of some SSN sensors were altered to improve the likelihood of detecting debris objects. The sensor data was then transmitted to the Space Control Center where correlation, element set formation and analysis occurred. Other facilities assisted with these functions as well. This paper does not attempt to assess the importance of tracking debris, but is intended to provide an understanding of one effort to measure the debris population in orbit. Only objects penetrating the near-earth regime (perigee altitudes less than 5555 kilometers) were considered during this campaign. This boundary is an operational concern because most of the sensors employed for the campaign cannot provide wide area detection capabilities beyond this range.

The primary objective of the campaign was to exploit the currently available sensor and command and control assets to further understand the debris population. In this regard, it is important to note that this effort was conducted with available operational resources. It was not a closely monitored scientific experiment with laboratory tolerances on the equipment in use. As a result, some of the data may exhibit unexpected variations or may be incomplete. This is to be expected when dealing with data collected by a widely disbursed network of ground based sensors, and is not assessed to have had a substantial impact on the overall campaign results.

## CAMPAIGN OVERVIEW

The specific details of the campaign operations are contained in the "1994 Space Debris Campaign Plan" dated 30 September 1994, and this section summarizes the campaign as an overview. There were two classes of sensors used for this campaign. The first set were determined to be "primary debris sensors" and they were assessed to be of key importance to the success of the campaign. These primary sensors were the main source of observational data during the campaign and were relied on to support the campaign with special configurations or operational modes. The other group of sensors (secondary sensors) were the sensors that were expected to respond to tasking and to assist with campaign support as required. It should be noted that GEODSS sensors are located at Socorro, NM; Maui, HI; and Diego Garcia, and that the Kwajalein Missile Range (KMR) sensors include both ALTAIR and TRADEX radars. Table 1 shows the primary and secondary sensors.

SENSOR (TYPE)	DEBRIS CAMPAIGN SUPPORT TYPE
Eglin (UHF Radar)	Primary
Cavalier (UHF Radar)	Primary
Millstone (L-Band Radar)	Primary
GEODSS (Optical)	Primary
ETS (Optical)	Primary
AMOS/MOTIF (Optical)	Primary
KMR Sensors (Radar and Optical)	Primary
PAVE PAWS (UHF Radar)	Secondary
BMEWS (UHF Radar)	Secondary
Ascension (C-Band Radar)	Secondary
Antigua (C-Band Radar)	Secondary
SENSOR (TYPE)	DEBRIS CAMPAIGN SUPPORT TYPE
Pirinclik (UHF Radar)	Secondary
NAVSPASUR (VHF Radar)	Secondary
Haystack (X-Band Radar)	Secondary
HAX (K-Band Radar)	Secondary
Anderson Peak (Optical)	Secondary

Table 1  
Debris Campaign Sensors

The general concept of operations for the campaign employed two consecutive two week periods, referred to as Phase 1 and Phase 2. Phase 1 involved the use of ALTAIR, Eglin, and Cavalier in special modes to contribute data on unknown objects or Uncorrelated Targets (UCTs) to the Space Control Center (SCC). (It should be noted that the term "SCC" will be used to denote the processing facility at Cheyenne Mountain Air Station (CMAS). However, most of the actual debris processing took place in the Space Analysis Center (SAC) at CMAS.) The data was used to establish a set of new debris object element sets. Maintenance of these element sets was attempted by tasking appropriate sensors. Some objects were identified for handovers and more detailed data collection as a precursor to Phase 2. These were satellites with good quality, maintainable element sets in interesting orbits. Their element sets were selected by the Debris Campaign Team and provided to the optical sensors (and other sensors as appropriate) for additional tracking. Phase 2 involved the use of all primary debris campaign sensors to accomplish the goals established in the previous section. This included the handover of element sets to sensors of different types for multi-spectral data collection. This handover process was frequently attempted using element sets that were generated by the detecting sensor and transmitted to the SCC and other sensors.

Phase 1 began on 12 October 1994 at 0000Z. (This equated to 1800 local Colorado Springs time on 11 October.) Phase 2 began on 26 October 1994 at 0000Z. Phase 2 of the campaign ended on 8 November 1994 at 2359Z.

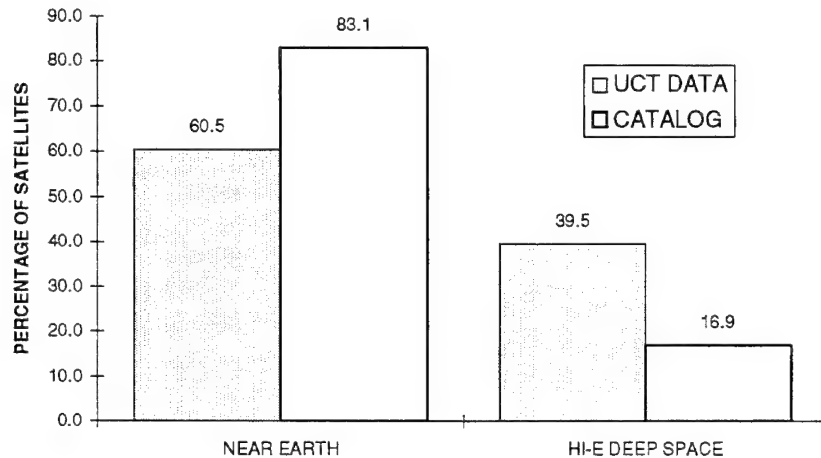
## CAMPAIGN DATA ANALYSIS

The data presented in this section represents a preliminary analysis of the data collected during the 1994 Debris Campaign. There are some portions of the analysis that are not complete, or were performed using only a limited amount of data. In general, it is believed that this information is representative of the general trends that exist in the debris population observed during the campaign. Also, all of the data presented in this section represents the subset of 841 debris objects remaining after correlation activities. The debris objects that correlated with other satellites were not included to prevent skewing the data in an inappropriate fashion.

### Debris Population Trends

To understand areas of interest with respect to the debris population, histograms were created comparing the 1994 Debris Campaign element set data with a sample of the known object catalog collected on 27 October 1994, representing the approximate mid-point of the campaign. The legend on most of the histograms refers to "UCT data", meaning the data collected on debris, and "Catalog" representing information from the known object catalog. To provide a more accurate representation of the actual population as compared with the debris population, all objects in geosynchronous type orbits were removed from the satellite catalog sample. Also removed from the catalog were those objects in GPS-type (circular, semi-synchronous) orbits. The reason for the removal of these two classes of objects is as follows. The debris campaign did not attempt to detect or collect data on objects in these orbital regimes, and in fact no information was collected on any objects in these type of orbits. Therefore, the population information in these two orbital regimes was eliminated to facilitate a more accurate comparison of the debris data with the known population. Of special interest was data collected on object 81214. Initially detected by the ETS, this object has a bright optical signature but appears very small to radar sensors, and may indicate the presence of many more objects of this type.

*Near Earth/Deep Space Trends.* As noted above, the geosynchronous and GPS-type populations were not included in this effort. The remaining class of deep space orbit therefore includes essentially only objects in highly elliptical (or high eccentricity) orbits. For this effort, objects with eccentricities greater than 0.1 are considered to be in highly elliptical orbits. Figure 1 contains the population distribution information.

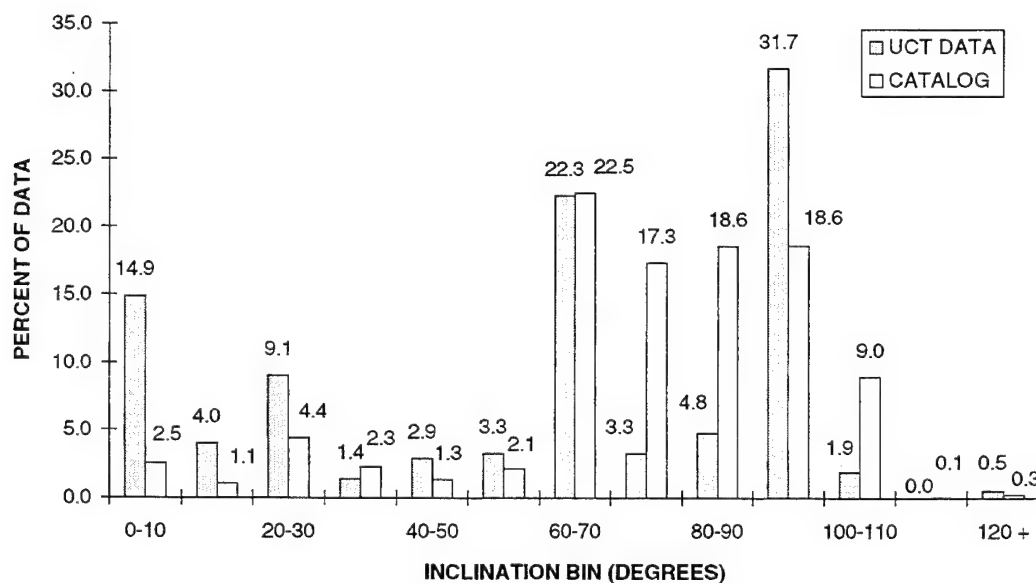


**Population Distribution**

**Figure 1**

The information contained in this figure shows that a considerable amount of debris exists in the highly elliptical deep space regimes, and that the amount is disproportionate when compared to the known catalog populations. It can be inferred from this data that the highly elliptical deep space debris population is not well tracked by SSN sensors.

*Inclination Trends.* The previous section contained data suggesting that the distribution of debris (or UCT) data with respect to orbit type does not follow the trends noted in the satellite catalog. To examine the data further, the inclination values of the debris objects from the campaign were separated into 10 degree inclination bins, and compared to a catalog sample. Figure 2 provides this data in a graphic form.

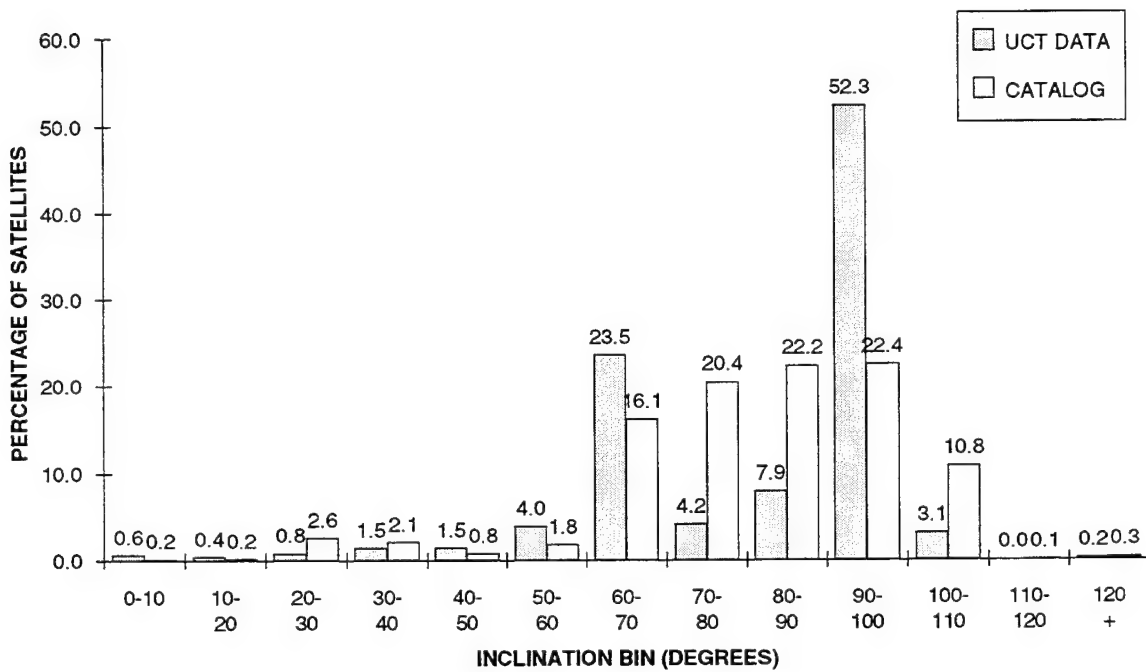


**Inclination Distribution**

**Figure 2**

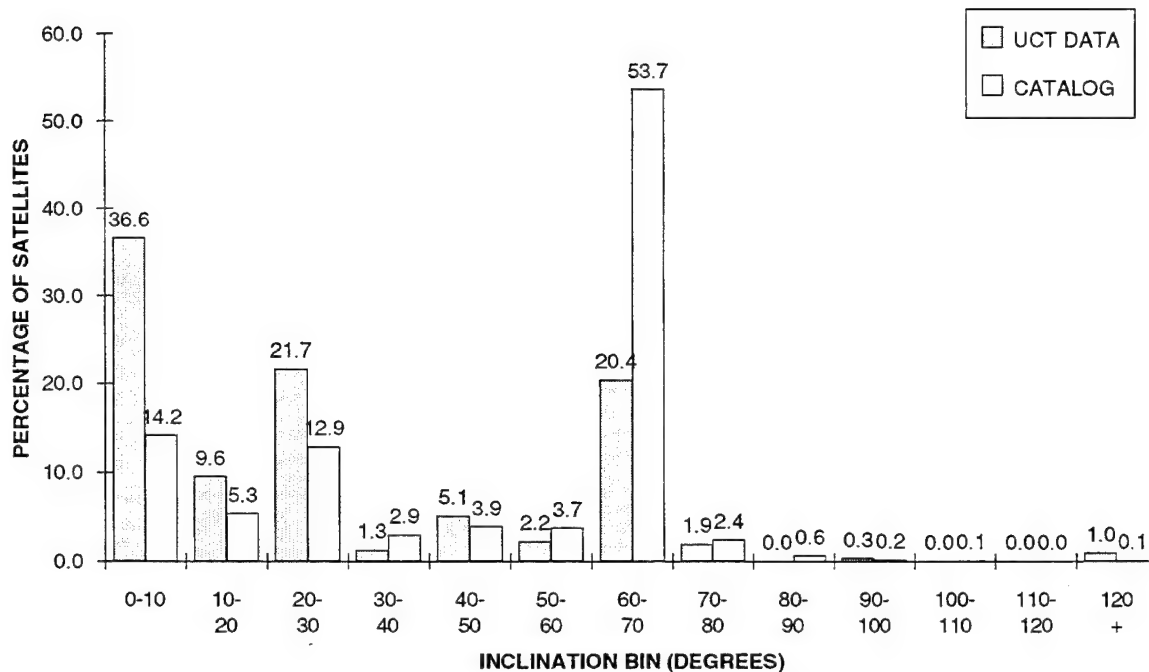
The debris data from the 1994 campaign shows a disparity from the catalog data in the 90 to 100 degree bin. The reason for this difference can be directly attributed to the breakup of Cosmos 1484, and the apparent "shedding" of pieces from the COBE (Cosmic Background Explorer). Both of these satellites are in sun synchronous orbits, with inclinations near 98 degrees, although the orbital altitude of COBE is somewhat higher than Cosmos 1484. In some respects, these high inclination debris pieces hindered the processing of other debris campaign data, because almost one third of all 1994 campaign data was collected on objects in these orbit regimes. The shedding of pieces from COBE presented a particular challenge, because of the apparently continual appearance of new pieces from this payload. Previous reports from the COBE operators suggested that no degradation to the operational performance of COBE had occurred, making the appearance of these pieces even more interesting.

To examine the data further, Figure 3 presents the near earth inclination data, while Figure 4 presents the deep space inclination information.



Near Earth Inclination Distribution  
Figure 3

The information in this figure clearly shows a difference in the 90 to 100 degree inclination bin. The catalog has 22.4 percent of all near earth objects in this inclination regime. However, well over half of all near earth debris was detected in this region. This dramatically shows the impact that breakups and satellite anomalies can have on the unknown satellite population. It is also of note that there were very few objects detected in other inclinations bins. Specifically, the low inclinations regions (less than 30 degrees inclination) had few debris. This was expected, given low percentages of cataloged satellites in these regions. To present information on the other debris objects, Figure 4 contains similar data for deep space satellites.



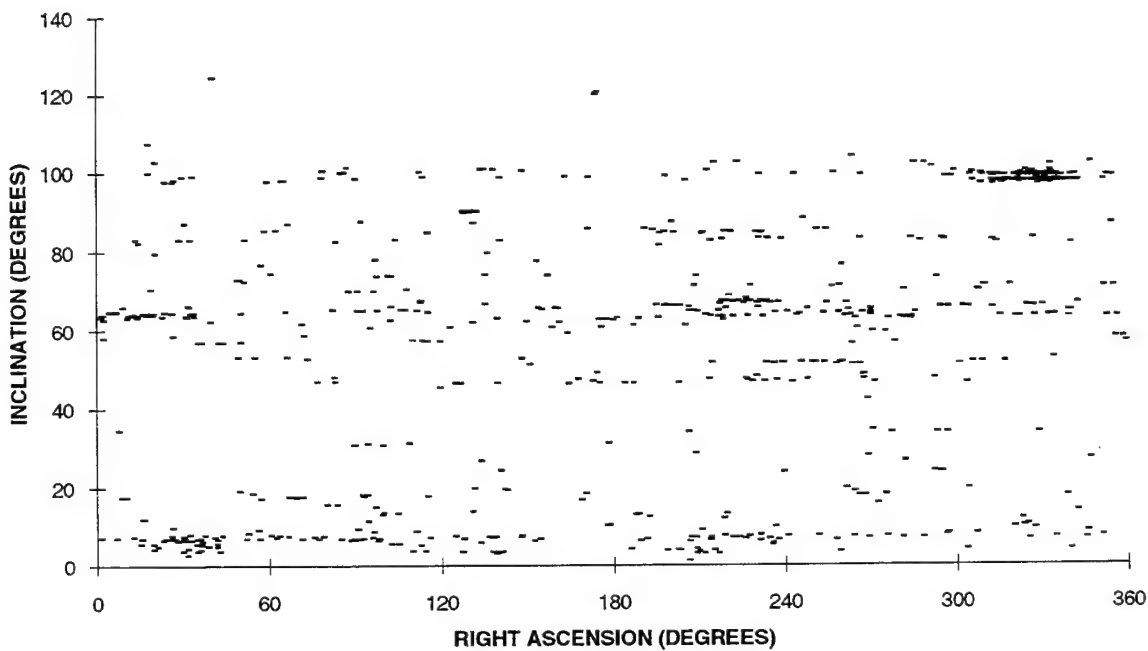
**Deep Space Inclination Distribution**  
**Figure 4**

Examination of the element sets generated on deep space debris objects in the 0 to 10 degree regime shows a disparity from the catalog, and that most have inclinations near seven degrees, and this is the inclination used for transfer to geosynchronous orbits from Kourou, French Guiana, using Ariane boosters. No other launch facility is known to use this type of orbit, nor would it be practical because of the large energy expenditure that would be needed to transfer satellites into this orbit from known launch facilities. Preliminary assessment of the data suggests that there may have been several breakups of Ariane transfer orbit rocket bodies in this region. Unfortunately, the limited low inclination coverage of SSN sensors precludes routine detection of this orbit type except during efforts such as the debris campaign, so it is difficult to assess the actual population in this region. It should also be noted that higher than expected debris populations were noted in the 20 to 30 degree regime, typically used by the United States as a geosynchronous transfer orbit. Again, the limitations of SSN coverage hinder routine tracking of this orbit class.

Another trend that was noted involved the tracking of small objects in orbits with inclinations near 120 degrees and eccentricities near 0.7. In the 1994 campaign, three objects were detected and tracked by Cavalier in this orbit regime. Subsequent tracking data was obtained by Cavalier on at least two of these objects, and radar cross section data indicates that these objects are between 0.01 and 0.001 square meters in radar cross section. It is of note that these were not among the smallest debris objects observed during the campaign. The origin of satellites in this region is uncertain. Review of launches into high inclination regions shows that some satellites have been launched into orbits with similar inclinations, but that no satellites have apparently been launched into these specific orbits. It is possible that these objects were launched in the early days of the space program when limited sensor assets were available, and these objects might not have been cataloged. It is also possible that these objects are pieces from an errant launch. In any event, it is probable that these objects originated from a launch from Vandenberg AFB, due to the difficulty in attaining orbits of this type from other launch facilities. Reports from experienced SSN personnel indicate that these objects have been observed on previous occasions, but have not been entered into the formal satellite catalog. This class of debris object may warrant further evaluation.

*Other Orbital Parameter Trends.* Preliminary evaluations were performed on several other orbital parameters. It is recognized that there are a large number of combinations of the orbital parameters that can be evaluated, and further efforts are needed in this area. However, the analysis to date has revealed some interesting aspects of the

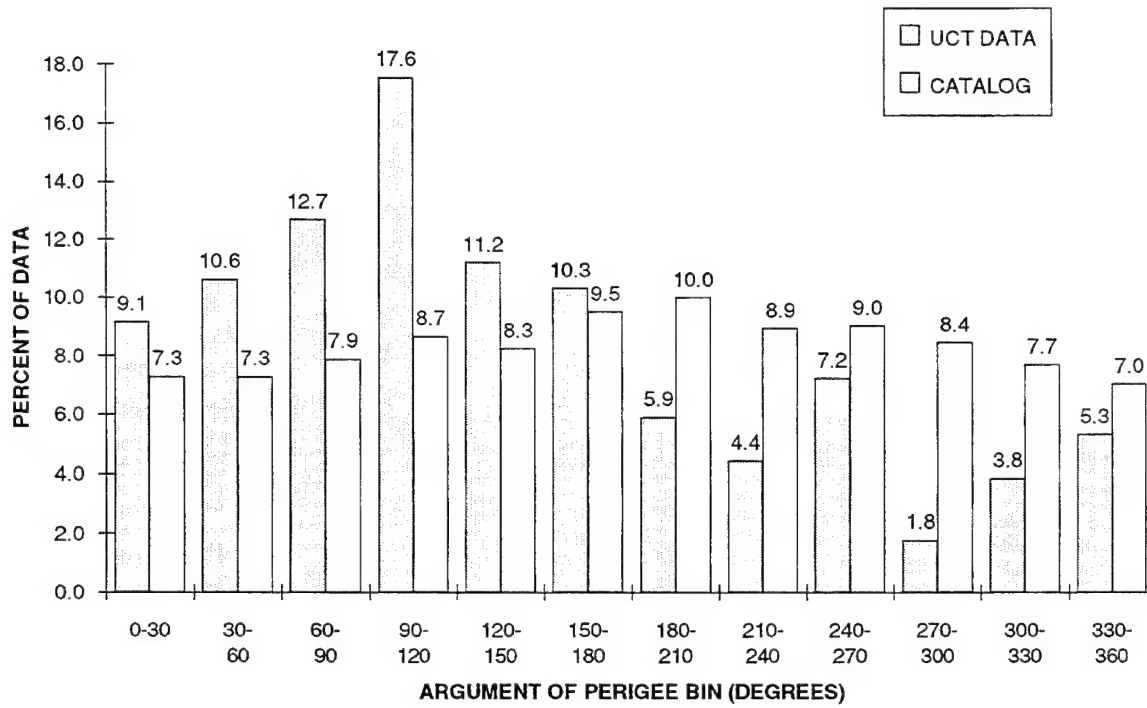
debris data. In particular, the correlation between right ascension and inclination were examined. Also, some interesting facets of the argument of perigee data were observed. Figure 5 shows the inclination values for all debris objects along with their corresponding right ascension values.



**Inclination versus Right Ascension Distribution**  
**Figure 5**

The data presented in this figure shows the right ascension of the ascending node value for each debris object along the X axis. The corresponding inclination of the debris objects is shown on the Y axis. There are trends that can be noted in this data that are of interest. There are some clusters of data that can be observed in this figure. In particular, the grouping of data in the upper right corner is of note. Examination of this data showed these to be the debris assessed to originate from the COBE and Cosmos 1484 satellites discussed earlier. Also, the specific inclination regimes can be observed. For example, the large number of objects near seven degrees inclination can be seen, as can the dispersion in the right ascension values for these objects. Further evaluation of this data is planned.

In the past, it has been suggested that the location of SSN assets results in detection of debris that have perigee locations in the northern hemisphere. This is because most SSN sensors are located in the northern hemisphere, and the detection of debris objects is easier when the objects are near perigee, thereby shortening the range to the targets. To evaluate the perigee locations of the debris objects, a histogram was created for the argument of perigee values. Figure 6 presents this information.



**Argument of Perigee Distribution**

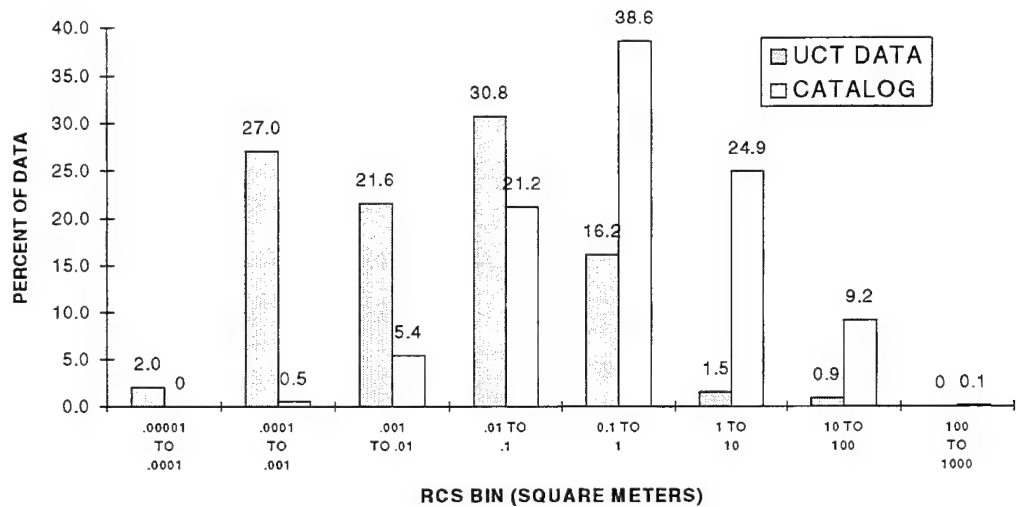
**Figure 6**

The catalog distribution is fairly constant between the various argument of perigee bins, however the Debris Campaign argument of perigee data shows that the majority of debris satellites (over 71 percent) had perigee locations in the northern hemisphere (values between 0 and 180 degrees). This is to be expected, given that the locations of most SSN sensors are in the northern hemisphere. For objects in orbits with even moderate eccentricities, the location of perigee can affect the detection by a sensor due to the range to the target. This information does suggest that there may be undetected objects with perigee locations in the southern hemisphere.

#### Radar Cross Section Data

The information in this section only presents the average RCS data from sensors, and does not attempt to make estimates regarding the actual physical size of the debris objects. UHF RCS data on 588 satellites was available. In some cases, several RCS values were available from different sensors on the same object. For this preliminary assessment, the first (earliest) RCS value was selected. A histogram was prepared for the data, and the following figures show the information. All data shown was collected by UHF sensors.

The figure indicates that more small debris was tracked in the 1994 campaign than is present in the catalog. It is noteworthy that the percentage of objects in the 0.001 to 0.0001 square meter bin was significantly different. Also, a few objects were observed with RCS values smaller than 0.0001 square meters during the campaign, whereas none are in the catalog.



**RCS Distribution**

**Figure 7**

### Summary

One of the significant findings of the 1994 Debris Campaign was the large population of debris objects in low inclination, high eccentricity orbits. Many objects were observed with inclinations near seven degrees, and these are probably associated with Ariane geosynchronous transfer stages. It is possible that several breakups have occurred in this orbit class, but have not been detected due to the sparse sensor coverage of low inclination orbits.

Several objects were observed in high eccentricity, 120 degree inclination orbits. The source of these objects is not known. The amount of debris in this area is not substantial, but the existence of unexpected orbit types is of note and warrants further evaluation. It is probable that these objects are satellites that were launched from Vandenberg AFB in the early days of the space program. This is based on the existence of other objects in circular 120 degree inclination orbits launched from this site.

A considerable amount of data was collected on an interesting object. Satellite 81214 appears moderately bright to optical sensors, suggesting a large physical size. However, radar tracking on this object indicates that it is quite small. Millstone data at L-Band indicates a radar cross section of approximately 0.00003 square meters, suggesting an object with a small physical size. Several highly sensitive UHF radars have been unable to track this object, despite the existence of a good quality element set. Optical sensors have had little trouble tracking this object, however. Even the telescope sensor at Anderson Peak, CA, that is normally not involved with satellite tracking had no difficulty tracking this satellite. The existence of this object and the data that has been obtained lend credence to the theory that there is a population of optically bright objects that appear quite small to a radar. In fact, it is possible that many of the unknown objects detected by optical sensors could fall into this area. Further analysis of the data on this object may reveal more information.

A considerable amount of debris from two satellites, Cosmos 1481 and COBE, was observed during the campaign. These two satellites, in similar sun-synchronous orbits, were assessed to be responsible for more than 50 percent of all near earth debris observed during the campaign. This demonstrates the effect that debris from two larger satellites can have on the unknown satellite population.

Overall, the campaign was considered a success. A significant amount of data was collected on debris objects that were not part of the formal space surveillance catalog. In addition, some interesting objects were observed during the campaign. Finally, the campaign demonstrated the capabilities of a large network of sensors to collect and provide meaningful data on space debris.

## **Kwajalein Missile Range Contribution to the 1994 Debris Campaign**

A. Gerber, G. Duff, and D. Izatt  
MIT Lincoln Laboratory, Kwajalein Missile Range

### **Introduction**

Kwajalein Missile Range (KMR) played a major role in the 1994 Space Debris Campaign conducted by Air Force Space Command. The goals of the 1994 Space Debris Campaign were: 1) to improve estimates of the number and orbital distributions of small debris objects not currently part of the Space Surveillance Network (SSN) catalog, 2) to determine the difficulty of maintaining stable orbital element sets on such objects, and 3) to collect multi-frequency signature data to better estimate the physical size and characteristics of these objects. KMR's contribution to each of these goals is described in the following sections.

KMR is a component of the DOD Major Range and Technical Facility Base operated by the United States Army at Kwajalein Atoll in the Marshall Islands. A number of unique assets make KMR well-suited for the study of debris objects in space. KMR's technical facilities include a set of highly sensitive, coherent sensors designed for the collection of precise metric and signature data. KMR sensors participating in the 1994 Debris Campaign included ALTAIR (VHF, UHF), TRADEX (L- and S-band), ALCOR (C-band) and MMW (Ka-band), and SuperRADOT visible-band optics. Simultaneous signature data at such a diversity of frequencies allows detailed analyses on the physical characteristics of space debris objects. In addition, ALTAIR radar is a regular contributing sensor to the Space Surveillance Network, routinely providing observations on near-Earth and deep-space objects. Finally, KMR's near-equatorial location (at 9° N latitude) makes it an ideal location for the observation of space debris in low-inclination, highly-eccentric orbits.

KMR participation was divided into three areas: TRADEX stare-and-chase activities, ALTAIR response to Debris Campaign tasking, and multi-spectral tracking of debris objects. Results from each of these areas are detailed below.

### **TRADEX Stare-and-Chase Activities**

TRADEX radar recently completed development of an L-band stare-and-chase capability to detect and track small, uncataloged debris objects between 300 to 1200 km altitude. The system has the sensitivity to detect a -40 dBsm (approx. 2.8 cm diameter) target at 500 km range. This capability was used during several dedicated sessions to contribute new debris objects to the Debris Campaign database. Details of the system design and performance are described in another paper in these proceedings (Ref. 1).

The TRADEX stare-and-chase mode was used for a total of 39.5 hours during the Debris Campaign. During this time period, a total of 39 uncataloged objects and 38 known objects passed through the TRADEX beam, were detected, and put into track.

---

This work is sponsored by the Kwajalein Missile Range, US Army Kwajalein Atoll, Department of the Army under Air Force contract F19628-95-C-002.

Of the 39 uncorrelated targets (UCTs) tracked, 23 UCT element sets were flashed to the Space Control Center (SCC) for use by the Debris Campaign. Pulse-by-pulse and 10 Hz signature recordings were made on each track.

The L-band UCT cross sections are shown versus detection range in Figure 1. The majority of detections occurred between 750-1200 km in range, with a second band clustered around 500 km. About half of the UCTs detected showed large variations in cross section (greater than  $\pm 2$  dBsm), while the other half exhibited relatively stable RCS. The most curious feature of Figure 1 is complete absence of UCT detections with RCS less than -32 dBsm (4 cm diameter) at ranges less than 900 km. The absence of such objects was also noted during a 25-hour study performed for NASA in August, 1994 (Ref. 1). As shown by the solid curve in Figure 1, the system should have ample sensitivity to detect objects of this size at ranges less than 900 km. Models predict an exponential increase in the cumulative flux of debris objects with decreasing size (Ref. 2); however, no small objects were observed to date during the TRADEX stare-and-chase activities. The absence of such detections may have important implications regarding the population of small debris objects (< 4 cm) in low altitude orbits. More stare-and-chase time is required to obtain a statistically significant sampling of this debris population.

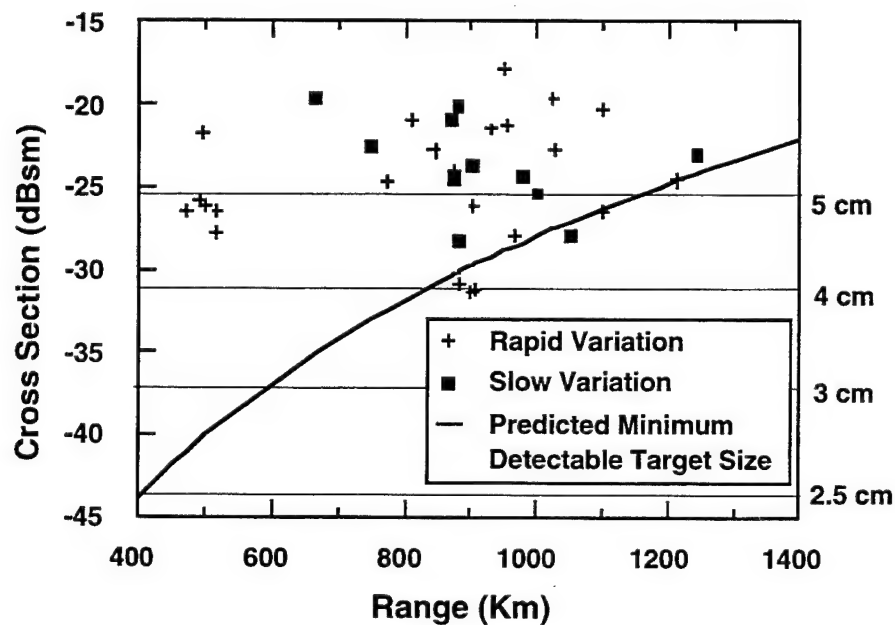


Figure 1. Results from TRADEX Stare-and-Chase Activities.

### ALTAIR Tracks of Campaign Debris Objects

During the Debris Campaign, ALTAIR radar supplanted part of its normal SSN tasking to perform daily tracking on a large number of campaign debris objects. These metric observations aided in the maintenance of debris element sets over the course of the campaign.

ALTAIR performed 233 tracks on 100 different debris objects of the 80xxx-81xxx series tasked by the SCC during the course of the campaign. A total of 4927 observations

were sent in to the SCC. Of these 100 objects tracked, 51 objects were maintained in the final campaign database. The other 49 objects were eventually deleted from the campaign database, presumably because they were correlated either with objects in the existing catalog or with other objects in the study. A total of 120 tracks were performed on these 51 new Debris Campaign objects, with 2205 observations sent in to the SCC.

All objects were tracked at UHF using a 1000  $\mu$ sec waveform with no coherent integration. This UHF waveform gives a single pulse signal-to-noise ratio of about 9 dB on a -40 dBsm target at 1000 km. VHF tracks were established on objects of sufficient size or at sufficiently close ranges to provide adequate signal-to-noise. 10 Hz signature recordings of both the principle (PP) and orthogonally polarized (OP) channels were made on each of the tracks. Summary edits were performed on the 10 Hz data to extract mean, 5th and 95th percentile RCS values for each track.

Figure 2 shows the repeat track history for the 51 new Debris Campaign objects tracked by ALTAIR during the course of the campaign. About half of the objects were tracked two or more times, with some objects being tracked as many as 11 times. In general, the objects were more difficult to maintain in track than standard catalogued objects. On the average, approximately one unsuccessful track attempt was made for each track successfully obtained. In several instances, an object would be successfully tracked one day, not be found the following day (at approximately the same range), and then reappear on its elset the day after that. The success rate improved continuously throughout the course of the study, as objects were tracked repeatedly and element sets were refined.

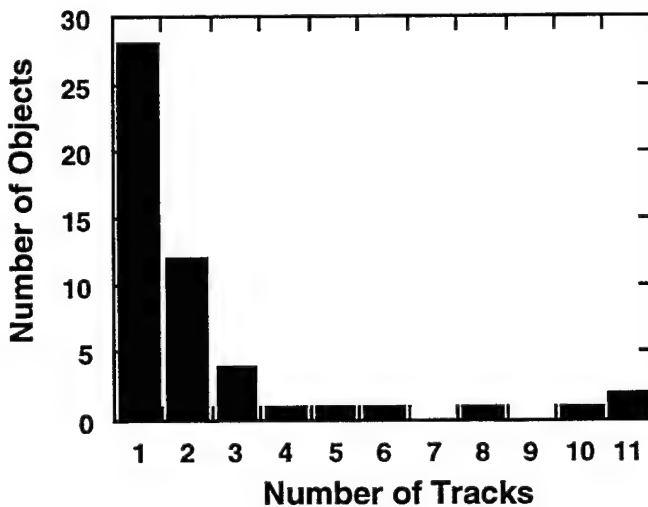


Figure 2. ALTAIR Repeat Track History for New Campaign Debris Objects.

The distributions of orbital inclinations and eccentricities for the campaign objects tracked by ALTAIR are shown in Figure 3. Several interesting trends are noticeable. The large band of objects around 98° inclination in near-Earth (low eccentricity) orbits resulted from two "breakups" which occurred over the past year: the breakup of Cosmos 1484, and the "shedding" of pieces from the COBE (Cosmic Background Explorer) payload (Ref. 3). A second group of objects, totaling 5 in number, was tracked in low inclination (5°-10°) deep-space orbits with eccentricities > 0.6. These objects are fragments from Ariane boosters launched from Kourou, French Guiana, and

left in geosynchronous transfer orbit. Figure 4 shows the inclination distribution by percent of campaign objects tracked by ALTAIR, along with the percentages for objects in the regular SSN catalog. The percent of uncataloged objects tracked by ALTAIR in low-inclination ( $< 10^\circ$ ) orbits exceeds the percent of cataloged objects in these orbits. This trend is corroborated by the inclination distribution for campaign debris objects as a whole. Of the approximately 841 uncataloged objects tracked during the course of the campaign, 14.9% were found in orbits of less than  $10^\circ$  inclination, as opposed to 2.5% for the objects in the SNN catalog (Ref. 3). In addition, 28% of the campaign debris objects were found in orbits of less than  $30^\circ$  inclination, as opposed to 8% for the catalog. The reason for this large population of uncataloged debris in low-inclination orbits is the lack of Space Surveillance Network assets which can track objects in these orbits. KMR, because of its near-equatorial location ( $9^\circ$  N latitude) is one of the few sites that can easily track objects in this orbit class.

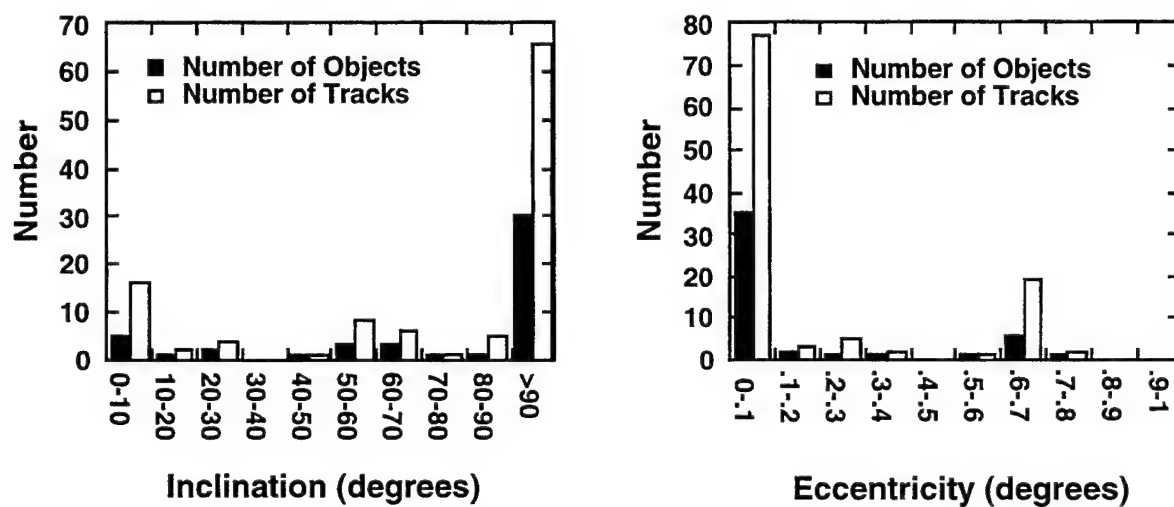


Figure 3. a) Inclination and b) Eccentricity Distributions of Campaign Debris Objects Tracked by ALTAIR.

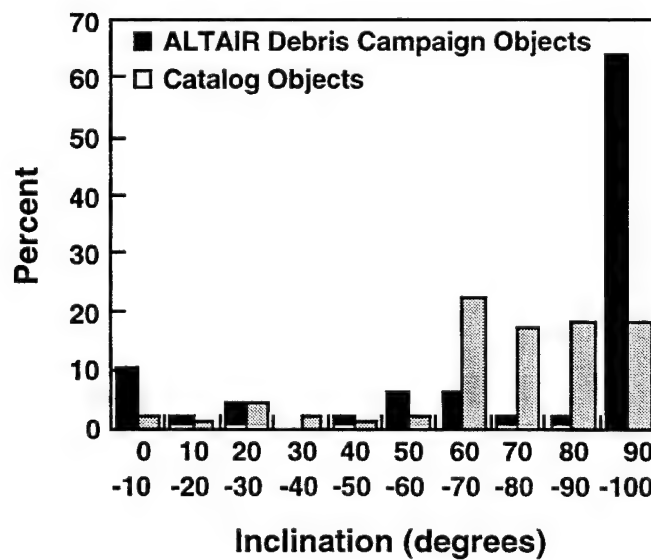


Figure 4. Inclination Distribution, by Percent, of Debris Campaign Objects Tracked by ALTAIR and Cataloged Objects.

The uncataloged objects in low-inclination orbits are important not only because of their number, but also because of their size. Figures 5-6 show the average UHF cross sections taken from tracks on Debris Campaign objects, sorted by inclination and eccentricity. It is clear that the uncataloged debris in low inclination, highly eccentric orbits have, on the average, much higher cross-sections than debris objects in other orbit classes. Again, the reason why these objects are not part of the SSN catalog is the lack of sensors available to detect and track them. However, such large uncataloged objects could possibly pose a threat to high-value space assets. Efforts should be made to accurately characterize the debris population in these orbits, and to bring the larger objects under control in the catalog.

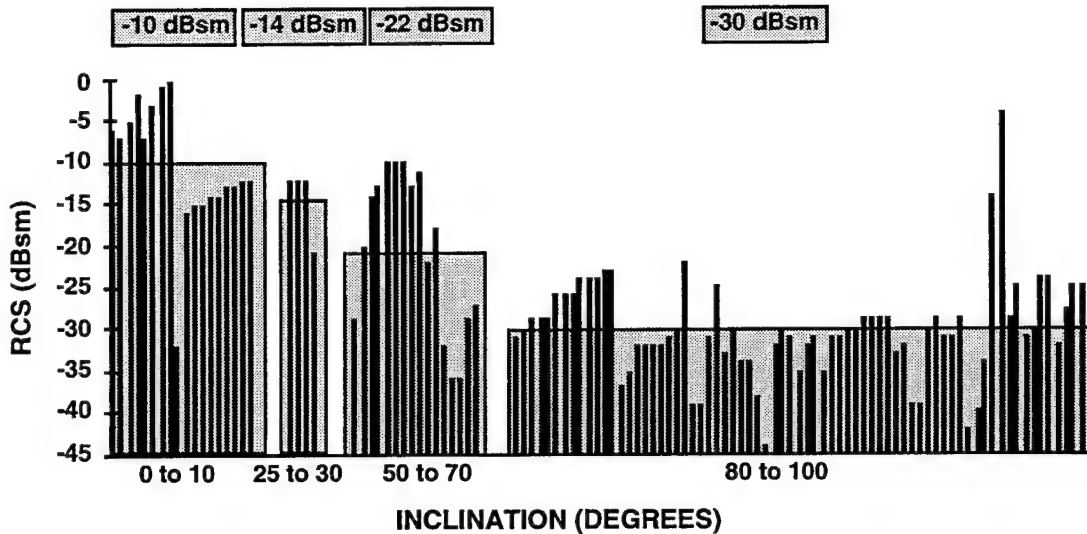


Figure 5. RCS vs. Inclination for ALTAIR Campaign Debris Tracks.

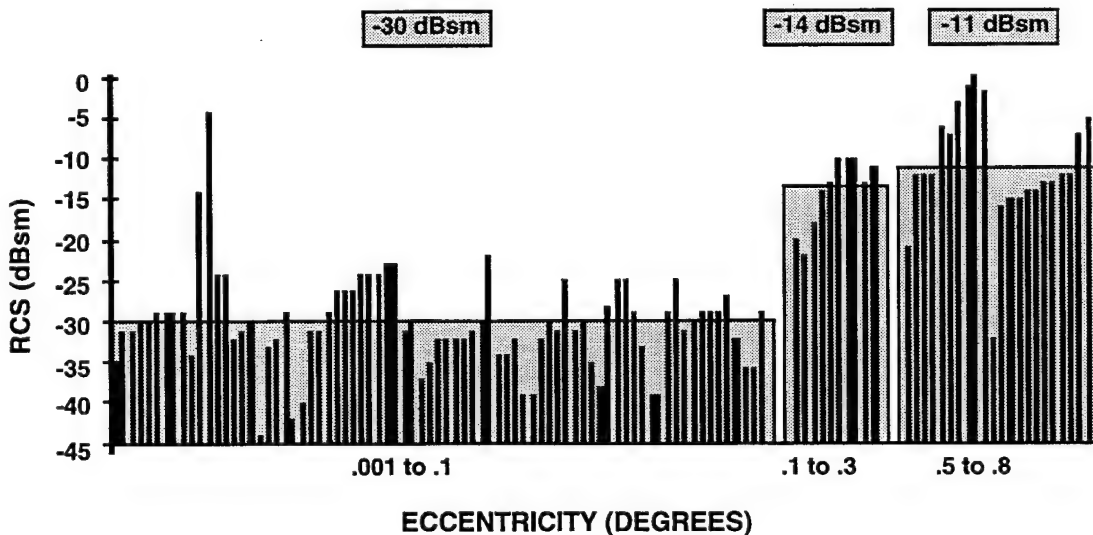


Figure 6. RCS vs. Eccentricity for ALTAIR Campaign Debris Tracks.

The overall distribution of UHF cross sections for the Campaign debris objects tracked by ALTAIR is shown in Figure 7. The distribution is peaked around -31 dBsm, corresponding to a sphere size of approximately 8.5 cm diameter. The four objects with cross-sections between -10 and 0 dBsm were all detected in orbits between 5° and 7° inclination.

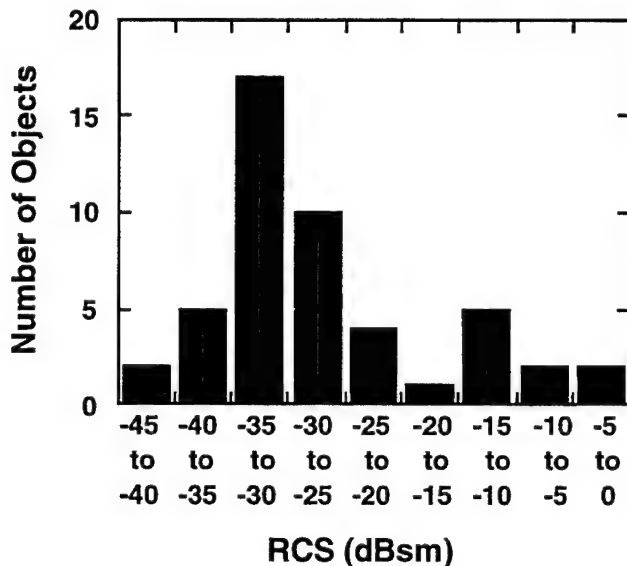


Figure 7. UHF RCS Distribution of Campaign Debris Objects Tracked by ALTAIR.

### Multi-Sensor Tracking of Debris Objects

During six dedicated evening sessions, the ALTAIR, TRADEX, ALCOR and MMW radars and two SuperRADOT visible-band optical sensors (SR1 and SR5) jointly tracked Campaign debris objects, for a total of 21.5 hours of tracking time. High-quality metric and signature data was recorded to create a database for analyses on the physical and orbital characteristics of debris in space. 55 debris objects were tracked with two or more sensors, and 5 debris objects were jointly tracked by radar and optics. One object (object 81214) was tracked by optics alone. Calibration spheres were tracked by each sensor to validate system performance. The following table summarizes the number of tracks taken at each frequency:

Sensor	Debris Tracks
ALTAIR (VHF)	20
ALTAIR (UHF)	54
TRADEX (L-Band)	55
TRADEX (S-Band)	52
ALCOR (C-Band)	11
MMW (Ka-Band)	30
SR1 (Optical)	4
SR5 (Optical)	4

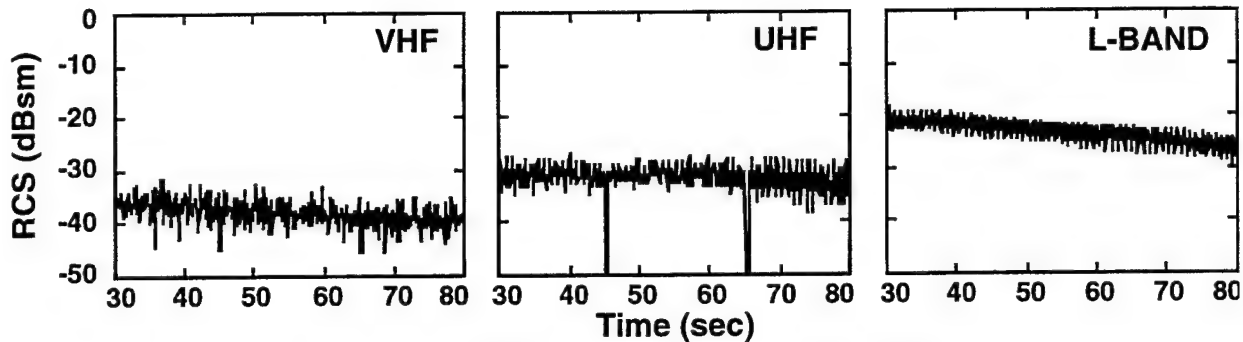


Figure 8a. RCS for Object 80220, DOY 306.

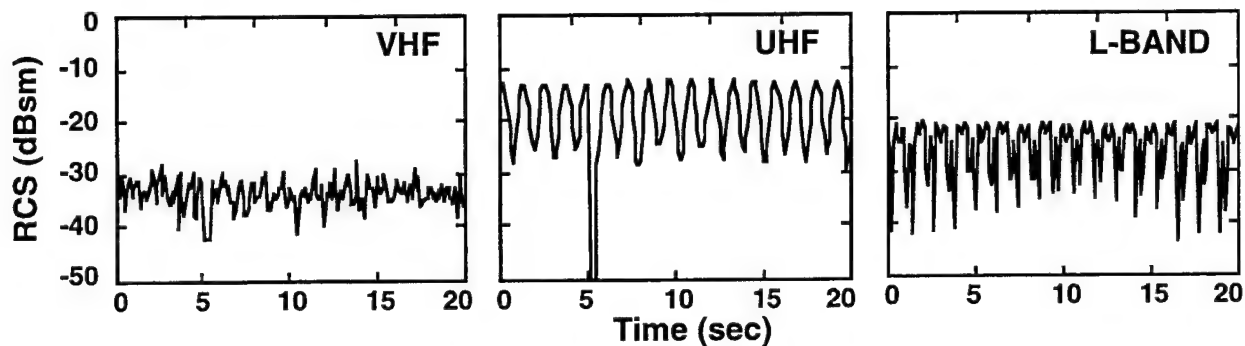


Figure 8b. RCS for Object 80432, DOY 306.

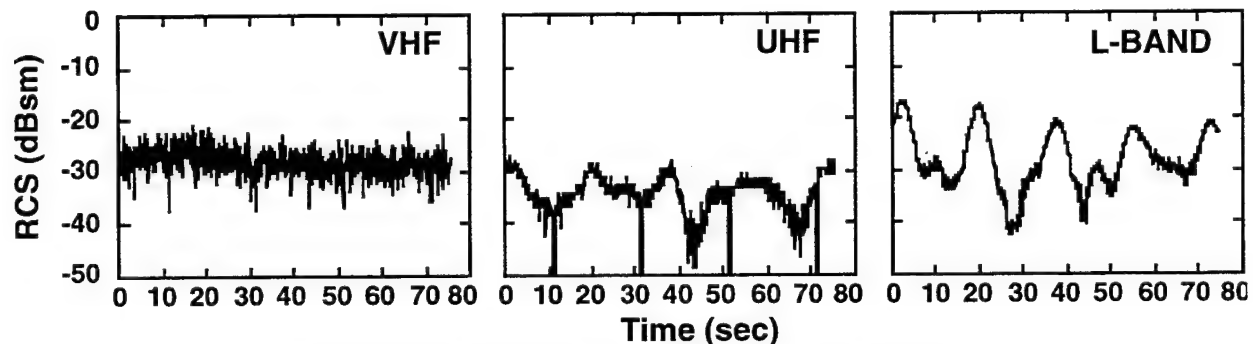


Figure 8c. RCS for Object 80379, DOY 309.

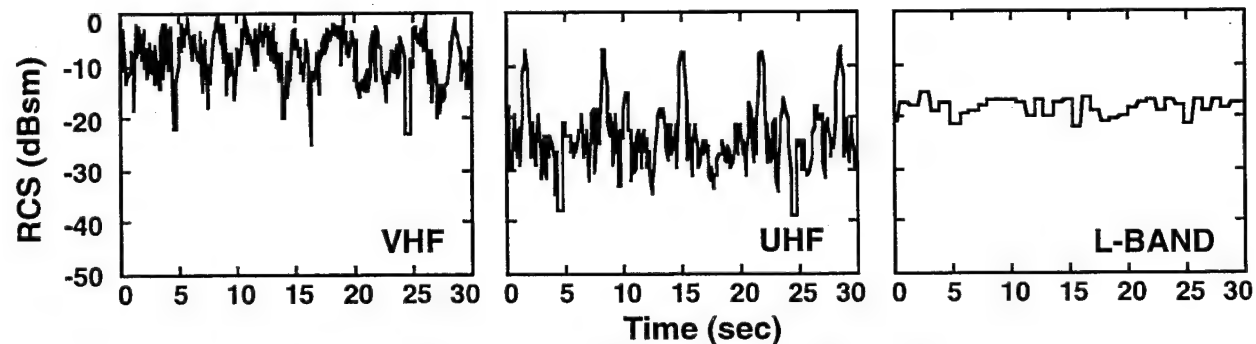


Figure 8d. RCS for Object 81016, DOY 294.

10 Hz signature data was recorded in the PP and OP channels from each of the radars on each track, and pulse-by-pulse data was recorded on a selected set of interesting objects. Post-mission processing was performed on the 10 Hz data to extract mean, 5th and 95th percentile RCS values and other pertinent track information. VHS video recordings were made on each of the optics tracks.

Figures 8a-d provide examples of the different types of signatures observed on debris objects at the different frequencies. Figure 8a, taken on object 80220 shows a rather structureless signature, with the RCS increasing with increasing frequency, as expected for an object in the Rayleigh scattering region. Figure 8b, taken on object 80432, shows distinct structure in UHF and L-band with a period of slightly under 1 second. Interestingly, the average RCS is larger at UHF than that at L-band. Figure 8c, from object 80379, shows very strong structure in UHF and L-band, with about an 18 second period. Figure 8d, from object 81016, also shows strong periodic structure in UHF. The cross-section at L-band is larger than that at UHF, but the VHF cross-section is the largest of the three. This effect of an unexpectedly large VHF signature was seen on a number of debris objects. The step-like profile of the L-band cross-section is the result of coherent integration. The "dips", or apparent dropouts, in the VHF and UHF cross-sections in each of the figures are markings of the noise floor, which are made every 20 sec.

Figure 9 compares the average RCS values at VHF, L-band and C-band to the RCS at UHF for the same object. For the smallest objects (in the Rayleigh scattering region), one expects the RCS to be larger at the higher frequency. This behavior is more or less observed in the L-band/UHF and C-band/UHF comparisons, although in the VHF/UHF comparison it is less apparent. In general, the scaling of RCS with frequency suggests that the debris objects, as one might expect, do not behave as simple spherical-shaped objects.

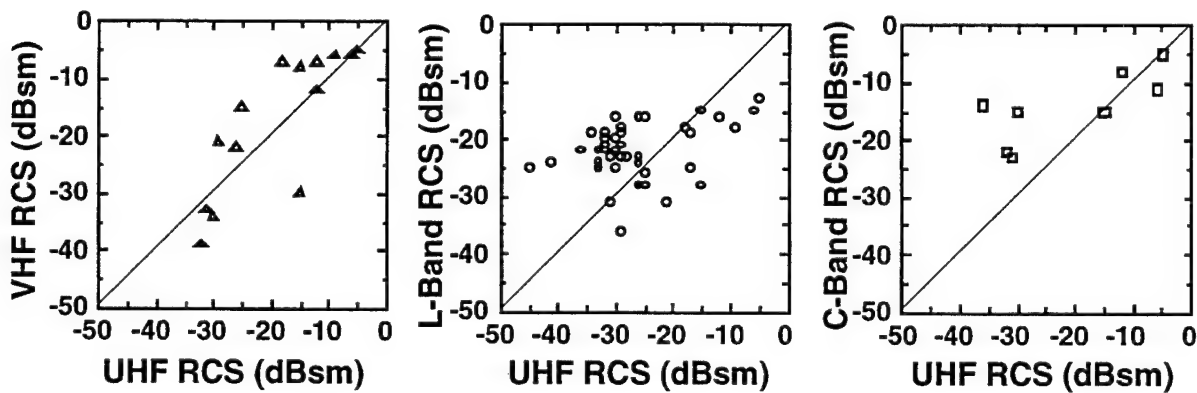


Figure 9. VHF, L-Band and C-Band RCS vs. UHF RCS for Joint Debris Tracks.

Many of the joint tracks were chosen to give optimal lighting conditions for optics. Five tracks were taken in which one or more optical sensors and multiple radars collected simultaneous signature data. The most interesting optical track was on object 81214, which was extremely bright to the SuperRADOTs, but was so small in radar cross-section as to be untrackable by the radars at the 1756 km point of closest approach.

## **Summary**

The 1994 Space Debris Campaign, and, in particular, KMR's contribution, yielded several interesting results which warrant further investigation and additional data-collection sessions. First, the unexpected number of uncataloged objects with large radar cross-sections found in low-inclination, highly-eccentric orbits suggests that these objects are not well accounted for either in existing debris models or in the SSN catalog. A follow-up campaign would be of great value to better characterize the debris population in these orbits. KMR could contribute to such an effort using TRADEX radar in stare-and-chase mode to detect such objects and ALTAIR to perform follow-up tracking and element set maintenance. Also, an ALTAIR UHF scan (comparable to the VHF scan currently used for new foreign launch detection) could be employed to search for low-inclination debris over very large volumes of space.

A second puzzling result which warrants further investigation was the lack of detection of small debris objects (< 4 cm) in low altitude orbits (< 800 km) during TRADEX stare-and-chase sessions. Debris models predict a large number of such objects; TRADEX has the sensitivity to see them; and yet no such objects were detected. Knowledge of the actual density of small, low altitude debris is extremely important for determining the actual risk that orbital debris poses to high-value space assets. More stare-and-chase observation time is needed to further validate system performance, and to obtain a statistically significant sampling of this debris population.

Finally, the multi-frequency signature data collected during the Campaign should provide an interesting testing ground for theories on the size estimation of space debris from radar cross-section and optical intensity measurements. Anomalies, such as the unexpectedly large VHF signature of certain classes of debris objects, and the large visual magnitude (but small radar cross-section) of object 81214, require additional analysis.

Kwajalein Missile Range played a significant role in the 1994 Space Debris Campaign, demonstrating some of its unique capabilities for contributions in this area. The 1994 Campaign brought to the forefront several important issues on orbital debris which still remain to be answered. KMR is prepared to play a leading role in future work to resolve these unanswered questions.

## **References**

1. Izatt, D., Stare-And-Chase at TRADEX, *Proceedings of the 1995 Space Surveillance Workshop*, 1995.
2. McKnight, D., Flury, W. et al, IAA Position Paper on Orbital Debris, *Acta Astronautica*, Vol. 31, pp. 169-192, 1993.
3. *1994 Space Debris Campaign Preliminary Report*, 6 December 1994.

# Use of a NAVSPASUR-type Radar to Track and Catalog Orbital Debris

Stephen H. Knowles  
Naval Space Command  
Dahlgren, VA, U.S.A.

## ABSTRACT

There is an important need to statistically characterize and, if possible, track all near-earth space debris. The present international network of optical and radar tracking sites is inadequate to accomplish this to the 1 cm. diameter size requirement. An engineering study has shown that an adaptation of the U.S. Navy's NAVSPASUR radar fence concept is an optimal way to accomplish this task. This adaptation would be at X-band, but would make use of the interferometric radar fan beam that is the core of the NAVSPASUR concept. A monostatic system would characterize all debris and catalog at least some, while a multistatic configuration could accomplish a complete cataloging. The cost for a monostatic configuration, while significant, is not unreasonable because no technology development is required. Detailed analysis will be presented of significant design considerations, including hardware realization, different types of radar tracking concepts, cataloging considerations, and location factors.

## INTRODUCTION

There is a growing awareness of the need to keep track of objects in the near-earth environment. This has been done routinely for many years for large payloads. However, pieces of debris as small as 1 cm. in size can cause severe damage, and the present networks are incapable of tracking this type of object. Considerable effort has been expended to statistically characterize the threat population. It is known that the debris density and, and the physical factors controlling its evolution, vary in different altitude regimes. The largest single interest is in protecting man in space which is essentially a near-earth issue. In the near-earth regime, the task of actually maintaining a discrete catalog is much more difficult than mere statistical analysis, but this must be done if actual protection against collisions is to be afforded. This paper will discuss an optimum type of cataloging sensor, the NAVSPASUR-type asymmetrical fan beam, in light of the kinematics of the near-earth object population.

## PHYSICS OF CATALOGING

During the formation of a large space object catalog, it will initially appear that almost every object is unidentified, and appears as an 'uncorrelated target', or UCT. The important question is: is it necessary to correctly identify every object on its first pass

through the debris sensor system, or can the catalog be constructed gradually? The author suggests that the catalog creation can indeed be done gradually, as long as a certain fundamental criterion is obeyed. This criterion is: The accuracy of orbit identification at the first attempt must be sufficient so that the probability of correct identification at the next sighting is quite high. Underlying this seemingly simple statement are the following factors:

The distribution and accuracy of sensors

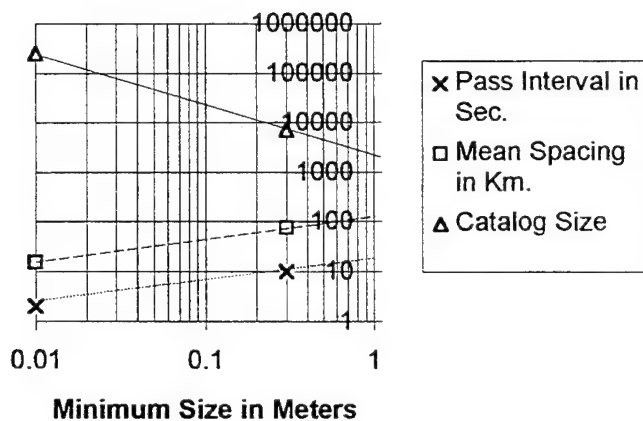
Spatial density of catalog

Drag degradation of orbital accuracy

From this criterion follows a simple working rule, to wit: the typical error in predicted arrival time of objects must be significantly less than the average arrival time interval. If this criterion is satisfied, most objects will be reidentified correctly, and the catalog will be

'kept'. If this criterion is not satisfied, the catalog will fail due to a large number of misidentifications, and no cataloging will be possible. The spatial density and thus arrival time interval may be computed approximately for LEO objects by, for example, taking the actual or predicted catalog size and dividing by the approximate volume of the LEO orbit range of about 300 to 800 km. In terms of population, the commonly accepted total LEO population is about 250000 for a catalog complete to 1 cm., and of course the baseline is a catalog of

### Debris Catalog Parameters



7000 for objects 20 cm. in size or larger. The corresponding numbers are a spatial density spacing of about 1.5 km. for a 1 cm. catalog, and a mean interval of about 2 seconds between objects passing through a radar fence (the mean interval between passes through the present NAVSPASUR fence is about 10 seconds). This means that each object's pass time must be predictable to about 1 km., or 0.3 seconds, to enable correct identification (the discrepancy between these two numbers represents the uncertainty in the estimation methods used). If this criterion is satisfied, most objects will be correctly identified and the catalog will succeed. Otherwise, it will fail.

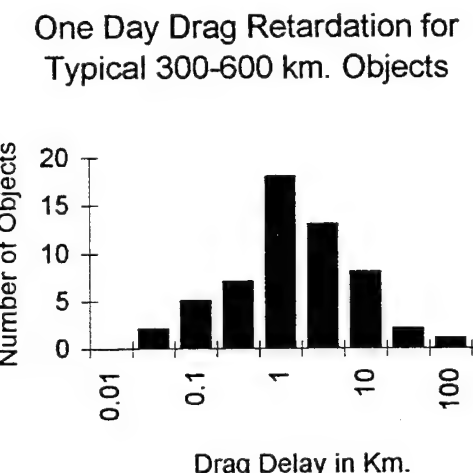
Now that the question of the accuracy necessary to keep a catalog has been addressed, it is time to consider the related question of what requirements must be met to achieve this accuracy. In general, there are three factors limiting the accuracy of an orbit obtained from surveillance observations. These include sensor observation accuracy, propagator accuracy, and drag-related accuracy degradation. Under normal conditions, the limitation in knowledge of atmospheric drag is the limitation that sets requirements on

observation frequency for LEO orbits. It is actually not the drag itself but the unavoidable error in the drag that sets limitations, normally dwarfing errors in the propagator and observation errors. Typical drag values for medium to large objects in the 300 to 600 km. altitude range are several kilometers per day (under quiet sun conditions) but can be much

more. The most optimistic estimate of the accuracy with which the drag can be determined is +/- 15%; this means that an uncalibrateable prediction error of several kilometers per day is accumulated. This, combined with the catalog success requirement, means that observations at least once daily of every debris piece are essential. The mean drag delay for small debris pieces can be expected to be at least 3 time higher than the

numbers discussed above for catalog objects. The surface area to mass ration, which controls ballistic coefficient, varies inversely as satellite diameter. This factor is somewhat compensated fro by the fact that density can be expected to be higher for a debris piece because of the lack of void spaces present in a typical payload.

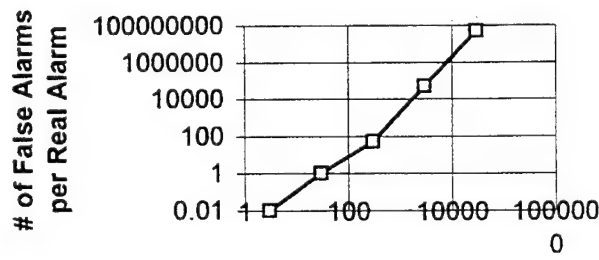
The accuracy needed for effective collision prediction/avoidance is desirably very significantly better than customarily obtained for surveillance quality orbits. This is because any actual conjunction prediction to be used effectively



postulates actually thrusting the target. This event is of moderate significance for any system, and for a target as complex as a space station is not to be taken lightly. Unfortunately the current prediction accuracies inevitably require a high ratio of unneeded maneuvers for each needed maneuver, because the prediction error ellipse is much larger than the physical size of either object. If the number of false alarms is too great, collision/conjunction predictions will inevitably be ignored.

The figure at right is an indication of the number of false collision predictions for each real prediction for a space station 30 meters in size, and assuming a 5:1:1 error ellipsoid. It will be seen that when the along-track error is greater than about 500 meters, the number of false alarms for each real danger situation is such as to discourage use of this protection

#### False Alarm Rate for Collision Predictions



Prediction Error in Meters

tool. Thus, the debris catalog mandates the difficult requirement of achieving 500 meter along-track accuracy or better for prediction spans of up to 1 day in advance.

### **Computational requirements**

The computational power required is obviously a function of the catalog size. present computers are 'barely able to handle the catalog'; but this is primarily because they have been sized to handle the problem. There are now machines available of much higher capacity, and the appropriate question is an economic one; how much computing does it take to handle the job, and how much will the appropriate machine cost? As a baseline, computing differential corrections for 7000 objects now take Naval Space Command about 3 hours on a 5 megaflop Control Data Cyber 760 (1 megaflop = 1 million floating point operations per second). This amounts to 2.5 million floating point operations per differential correction (flop-seconds). Thus, a differential correction for a 250,000 object catalog would take about 65 gigaflop seconds, which means that it could be accomplished by a 2 gigaflop machine in about 1 minute. Such a machine is well within the supercomputer range

### **Sensor Requirements and Design**

Most interest is focused on debris that is either in the LEO range below 1000 km. altitude range or on GEO orbits - this interest is limited for the obvious reason that that corresponds to the altitudes of satellite systems. The parameters of a sensor system for debris tracking are fundamentally different for the two altitude ranges. The large ranges and thus large path losses make design of a GEO 1 cm. debris radar extremely if not prohibitively expensive. Thus, heavy use must be made of optical techniques for GEO tracking. On the other hand, the free-space path loss involved is not prohibitively great for even small debris for near-earth tracking. For GEO tracking, one must have a network of at least three sensors to maintain track of all objects. Normal LEO orbits precess westward about 20.5 degrees per orbit. As a result, a single sensor has a viewing opportunity of almost all objects twice per day. Multiple sensors are needed in principle only if one sensor cannot observe all debris, or if accuracy or confusion avoidance requirements are such that more frequent observation than twice per day is needed.

Thus, the fundamental criteria needed for a sensor network for cataloging of space debris are that it must be sensitive enough to see debris of the desired size, but also that it must guarantee observation often enough, and with an accurate enough element set, that each piece can be unambiguously identified on reacquisition. In general, it is easy to show that the existing space surveillance networks of both the United States and Russia are inadequate for the task. They were both designed to detect payloads of 1 square meter or larger in size. While debris with a radar cross section of -14 dBsm (20 cm. in diameter) can in fact be detected reliably by the American network, this still would leave a performance improvement of 26 dB to be attained in modification of any existing radar. Unfortunately, it does not seem as if there is any realistic prospect of attaining this. The

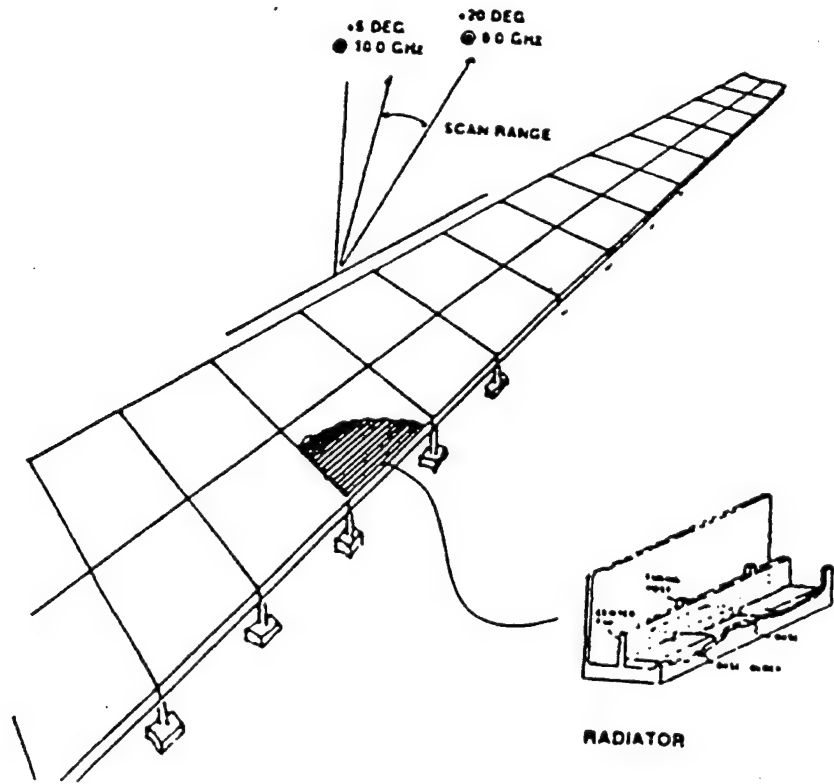
situation is made worse by the Raleigh effect loss, which is quite severe because the operating wavelength of all space surveillance radars is much greater than the 1 cm. debris target size. Thus, it is necessary to design a new radar for this purpose or use one of the new radars being planned for other purposes - the existence of new defense radars has recently become much less likely with the decline of defense budgets.

If construction of a new radar is required, a leading contender is one patterned after the U.S. Navy's specialized Naval Space Surveillance Radar (NAVSPASUR). This unique radar generates a fan beam that is very narrow in the north-south direction but extends from horizon to horizon in the east-west direction. The kinematics of unpowered satellite motion dictate that all non-synchronous near-earth orbits with an inclination greater than the latitude of the beam will pass through this radar fence twice per day. The Navy has maintained such a fence since the first days of space flight for purposes of satellite cataloging (Ref.). This fence consists of six receiver stations and three transmitters located on a great circle across southern CONUS, with data fusion at Dahlgren, VA. An asymmetric fan beam is generated by means of interferometer techniques at a frequency of 217 MHz; the system design is a distant derivative of the original Minitrack arrays that were used to track the first Sputniks. For cataloging purposes, this concept has the special virtue that no pre tasking is necessary; the system detects whatever crosses its beam. This principle has also historically proven invaluable for breakup events, when the unambiguous order in which the pieces crossed the beam has assisted in sorting out orbits.

The NAVSPASUR system can serve as an excellent design model, but it cannot in itself be modified to serve as the proposed Debris InterFerometer (DIFR). The first reason is the choice of operating frequency. The NAVSPASUR system operates at a wavelength of 4 feet, and can detect LEO objects about 30 cm. in diameter. The Rayleigh effect makes detecting 1 cm. diameter objects with a probe of this wavelength essentially impossible. Thus, a redesign to a much shorter wavelength is unavoidable. This new operating wavelength should clearly be much shorter than the current NAVSPASUR wavelength. A general technical consensus exists for a wavelength in the vicinity of 3 cm. (X band). This frequency minimizes the Raleigh effect loss and provides improved antenna gain, while avoiding the technology problems and rain loss attendant upon higher frequency bands. Although the basic operating principle carries over to an X-band system, the detailed design does not because of the physical scaling and different construction techniques at X-band. Technical possibilities for X-band construction include stripline arrays and leaky-waveguide construction. Transmitter power would be generated by several traveling-wave tubes.

Several design characteristics of the NAVSPASUR system, while important for its existing purpose, would probably not be included in a minimum-cost debris system. The NAVSPASUR system uses separate transmitting and receiving sites. It is easy enough, and very cost-saving, to transmit and receive from a single site by using standard radar

T/R techniques. The NAVSPASUR system uses 12 subarrays at each receiver site to obtain resolution for an east-west angle measurement. This is another refinement that is not absolutely necessary for detection. Raytheon has developed an interesting concept that allows for some east-west resolution. It should be noted that the present NAVSPASUR system makes use of dilute aperture techniques to achieve high angular resolution. Some use of these techniques may be desirable in the X-band DIFR. Also, the present system has a total of three transmitters and six receivers that provide the high degree of redundancy necessary in a defense system. With high current electronics reliability, a single station is sufficient initially for a debris system.



A single site with full east-west coverage will cover a range in orbital longitude of about 17 degrees for LEO orbits. This is almost but not quite equal to the near-earth precession rate of about 20.5 degrees west per orbit. Thus, a system with two properly spaced stations will provide guaranteed detection and obtain two observations on almost all objects, while a single-site system will get a single observation on almost all objects. Two observations will provide a good velocity vector on an object by subtraction, thus enabling orbit determination. With a single position measurement, however, a follow-up tracking measurement must be used. The sites used should obviously be as close to the equator as possible. However, it is not necessary they be extremely close, as it is easily possible to design the beam so that it is skewed north or south from the zenith. Another method of determining a velocity vector is to obtain more than one measurement during a pass to establish a track. The fan beam can be slewed from north to south by various

methods; the largest beam throw achievable will result in the best velocity measurement. Two separate arrays can be constructed, or electronically adjustable phase shifters can be used on each element for beam throw. Raytheon's ingenious design uses frequency scan on a leaky waveguide system to achieve a beam throw of 20 degrees. By this means, a 'flash elset' element quality is achieved, that will enable handoff to another radar after several orbits.

An important parameter is the size of radar system required, both in terms of transmitter power and antenna area (or gain, which is an equivalent parameter). A NAVSPASUR system is of course subject to application of the usual radar equation, with the substitution of an asymmetrical beam. The NAVSPASUR main transmitter array is in fact so large (2 miles) that near-earth objects can be in the near field, but this should not be the case for the DIFR. A more serious problem is that the narrow north-south beam size causes a dwell time of only a few tens of milliseconds at X-band, limiting the use of coherent integration signal enhancement techniques. Nevertheless, calculations by several independent sources have showed that detection of near-earth debris of 1 cm. size (and reasonably high radar reflectivity) can be accomplished by a radar system of reasonable size and cost. Detection by radar of 1 cm. size debris at GEO is a much more difficult task, and one that will not be discussed here. A typical system can guarantee detection of a 1 cm. debris piece at 1000 km. range with a 1 megawatt transmitting power, and an antenna size of 1000 square meters (about 3 meters by 300 meters). Mechanical precision required in constructing such an antenna is about 1 mm., which is an amount that is taxing but not unworkable over such an extent.

## SUMMARY

In summary, use of the concept of an asymmetrical beam radar patterned after the NAVSPASUR system looks not only useful but necessary for the task of space debris cataloging. An X-band redesign will clearly be needed. Although general parameters of such a design have been determined, there is much detailed design work and tradeoff analysis to be performed. This DIFR design will always benefit from coordination with auxiliary tracking radars, but will probably provide useful information if operated alone. Construction of a prototype which would detect 0.1 to 1.0 square meter targets would help greatly to define the design, and could be accomplished at a small fraction of the cost. The remainder of the problem associated with creating the catalog seem easily solvable. However, a minimum-cost prototype system might not be able to 'unconfuse' all objects. It is probably worth while obtaining experimental experience with the severity of this problem. This would clearly mark a significant advance in man's monitoring and control of his near-earth environment, and should be operated on a continuing basis.

**Ref:** R.L. Easton and J.J. Fleming, "The Navy Space Surveillance System", Proc.I.R.E., pp 663-669, Vol. 48, No. 4, April 1960

**Search, Detection and Tracking  
of Micrometeoroids, Orbital Debris,  
Near Earth Objects and Other Satellites**

6 February 1995

**J. A. Hand\*, L. J. Freier\*, D. G. Sargent\* and J. L. Munroe\*\***

*\*Charles Stark Draper Laboratory, Inc.*

*\*\*Los Alamos National Laboratory*

**1.0 BACKGROUND AND INTRODUCTION**

**1.1 Background**

A general set of requirements within precision pointing and tracking is identified. The set is based upon the needs for accurate space-based or ground-based search, detection and tracking of objects in space such as micrometeoroids and orbital debris, Near Earth Objects (NEOs - asteroids and comets), and man-made satellites. The set is characterized by stringent requirements for search, detection and tracking of targets with varying needs for:

- Fast, large-volume search
- Dim image detection
- Optical signal enhancement by artificial light
- High reliability target discrimination in a noisy background
- Precise reference to the inertial frame
- Fast, accurate, quiet, inertially referenced tracking with image stabilization (e.g., base motion isolation and servo jitter removal).

Of course the overall requirement is to determine and project accurate orbital parameters of the objects of concern. Then, where necessary, the active mitigation of unwanted objects such as orbital debris and/or NEOs may be implemented in conjunction with the prerequisite search, detection and tracking functions. These mitigation activities, such as nudging debris out of orbit, or changing the orbit of a NEO (a.k.a. Earth Crossing Asteroids - ECAs) to miss the earth are subjects of current investigation beyond the scope of the present paper.

**1.2 Introduction**

Generally, the purposes of this paper are first to outline the specific problem involving search, detection and tracking of micrometeoroids and orbital debris ("space debris"), then to describe the two optical technologies which address the problem in terms of the requirements listed previously, then followed by conceptualizing a Proximity Warning System incorporating one or both of these technologies, and finally to provide a matrix of the requirements vs. the potential solution components.

Dual-use optical technologies, which were originally developed under military programs, are becoming available from the United States and the Former Soviet Union (FSU) to address non-weapon search, detection and tracking problems. These technologies can help meet key requirements for the pointing and tracking applications of debris, NEOs and other satellites.

## 2.0 Summary

### 2.1 Problem Overview

Several spacecraft have been struck and a few satellites have been destroyed, apparently because of impact by space debris /1/. As of last year, a total of 32 Space Shuttle windows have been replaced due to damage from particle strikes /2/. Estimates of debris population have ranged to roughly 150,000 particles out to about 1000 km altitude. Roughly 7500 particles, greater than 20 cm in diameter, are currently tracked from the ground and have orbits defined such that collisions can be avoided. The probability of a catastrophic strike to the International Space Station Alpha has been estimated to be high enough that augmented shielding will be required and additional debris tracking capabilities will be required /3, 4/.

The problem with space debris is localized to sizes in the range of roughly 1 to 10 cm in diameter with relative velocities above about 8 km/sec. Smaller sizes can be stopped by shielding against spacecraft penetration and larger sizes can be detected by ground radar tracking such that evasive and protective maneuvers can be implemented in a timely manner. Present shielding technology extends only to objects about 2 cm in diameter above the stated relative velocity /5, 6, 7/. Very valuable spacecraft have, or will have, delta velocity capability aboard such that protective maneuvers can be executed if a threat is defined in time. Here, "in time" means 2 to 3 orbits prior to conjunction, thereby allowing time for executing attitude and/or orbit change maneuvers of the spacecraft.

### 2.2 Solutions

Solutions to the debris problem include consideration of procuring a dedicated network of high frequency ground radars, onboard radars, ground-based optical tracking combined with improved shielding, as well as preventive and active mitigation. Solutions to the debris problem, to make several useful orbits safe for various spacecraft, are expected to be expensive, such as providing new dedicated radars (e.g., roughly \$0.5 to 1 B procurement plus operating costs) /8/.

Onboard optical systems for search, detection and tracking are also being considered. Heretofore, the difficulties with space based optics has been the inability to search and detect, then precisely point and track the debris particles at useful ranges (e.g., ~15 km to much greater than 5000 km). The solutions discussed in some detail below address these difficulties in that new techniques for laser illumination of the debris is proposed and newly available precision pointing and tracking capability is proposed.

### 2.3 Optical Solution Component - U.S. - Inertial Pseudo Star Reference Unit

The IPSRU instrumentation was designed and developed by Draper Laboratory for a military program to track non-cooperative missiles. Present plans are for IPSRU to support a High Altitude Balloon Experiment (HABE) /9, 10/. The IPSRU flight unit was tested at Draper and is being integrated into a 60 cm telescope for the HABE. Basically, the IPSRU is a stable inertial platform with a very bright laser star shining from it. Essentially the search, detection and tracking functions are aided by base motion isolation (provided by IPSRU) through an artificial inertially stabilized laser star injected into the tracking telescope. Tracking the artificial star provides image stabilization by a fast steering mirror to better than 40 nanoradians (~0.008 arc second), rms, per axis over the range from 0.4 to 312 Hz., with a base motion isolation of approximately 80 dB on the focal plane. Component tests have shown the capability to achieve 20 nanoradians (~0.004 arc second) per axis jitter stabilization. Essentially, the modes of operation include inflight calibration, image stabilization and telescope-follow mode for slewing.

---

\* References are indicated by boldface /n/ and are listed in Section 4.

Another device in development at Draper is the Optical Reference Gyro (ORG) /11, 12/. Essentially, this instrument is a two degree of freedom inertialized laser star shining from a two-axis gyro and used in the same manner as the IPSRU outlined above. The ORG is smaller, less expensive than IPSRU and has more modest performance capability - approximately 500 nanoradians (0.1 arcsec), rms, per axis to 100 Hz with 32 dB base motion isolation.

#### 2.4 Optical Solution Component - FSU - Optical Phase Conjugation (OPC)

OPC was originally reported by Russia in the early '70s and has been extensively developed by the FSU. The technology is currently being led by the FSU in certain areas such as application to high power lasers /13 through 18/. OPC has important characteristics for illumination, detection, and tracking of dim targets such as space debris. Essentially, the capabilities result from the fact that a Phase Conjugate Mirror (PCM) returns light exactly along the incoming path, unlike a conventional mirror. Therefore, the PCM can support automatic tracking of targets. The PCM also enhances the signal such that a weak incoming signal is returned along the incoming path and is near diffraction limited in quality. This feature enhances signal to noise ratio, by permitting multiple round trips of the light between the target and tracker telescope. A strong return signal (the conjugate) is formed from a weak incoming signal. Importantly, the return beam has its phase reversed. Thus, when the beam is double passed through intervening media, such as a laser and/or a telescope, the intervening errors are canceled. Other characteristics of OPC include capability to operate a laser at higher repetition rates and with lower thermal recovery requirements, and thus operate as a more efficient laser.

Certain agencies of the FSU have proposed use of this OPC technology for devices such as a lidar which can be used for search, detection and tracking orbital debris /Ibid. 15/.

#### 2.5 Optical System Concept

The IPSRU and OPC can be integrated into a space based or ground based optical system for search, detection and tracking space debris. The important features of such a system would include fast, accurate inertial search, detection and tracking with base motion isolation, servo jitter isolation and inflight calibration capabilities. Laser illumination of the debris would be possible, a pivotal issue when considering the deterministic directions from which threatening debris will approach a spacecraft, and when considering the need to track both on the night and day sides of the orbit to maximize efficiencies. Laser illumination substantially narrows the overall problem through capability to search, detect and track debris in the specific danger corridors which potentially threatens the spacecraft.

### 3.0 DISCUSSION

#### 3.1 Present and Future Collision Avoidance

Figure 1 summarizes the present and future collision avoidance approaches, including ground based radar, collision avoidance maneuvers, shielding and mitigation of debris (active and preventive). This figure also illustrates the energy levels of the debris for penetrating and disrupting space vehicles (unzipping a pressurized compartment, or blowing up a fuel tank) /Ibid. 5/. Also shown is the approximate 1 to 10 cm gap in tracking coverage of all potentially dangerous particles. The proposed solutions have included ground based dedicated radar networks costing from about \$0.5 to 1 B, plus annual operating costs, and/or ground or onboard optical tracking and improved shielding. The preventive mitigation solution component is progressing in that space vehicles are being launched less frequently and are being designed for parking in unused orbits upon completion of operational life. Active mitigation, under consideration, includes use of ground based high power lasers to impart delta velocity onto small debris particles such elliptical, decaying orbits are achieved, including the help of increased atmospheric drag in the region of the periapsis to earth.

### 3.2 Utility of Space Based Optical System

The utility of a space based optical subsystem can be illustrated by scaled drawings which indicate observations to several Low Earth Orbits (LEO), to Geosynchronous Transfer Orbits (GTO) and Geosynchronous Orbits (GEO). **Figure 2** illustrates the observation capabilities for viewing space debris in these various orbits (shaded areas in drawings). The utility of a space based system extends, therefore, to use in observing orbits including its own and other satellite orbits or planned orbital slots. For example, the debris situation in a proposed GEO parking orbit slot could be assessed prior to launch of the satellite. The utility of such an optical system permits lasers of modest power which can be used to illuminate and range onto the debris with low interference from atmosphere.

The previously mentioned capability to track threatening debris is an important factor which has been compared to the difference between an environmental sensor and a threat sensor /Ibid. 8/. An environmental sensor might view all debris which was sunlit, even though it never threatened any spacecraft. As noted previously there are a large number, roughly 150,000 particles potentially viewable to 1000 km, and more at very high altitudes, such as in GEO /19/. The large volume and large number of particles, could make an environmental sensor impractical in terms of identifying specific threats to spacecraft in a timely manner. By comparison, a threat sensor (Proximity Warning System) could illuminate and therefore concentrate on tracking just debris in the threat corridors relative to the spacecraft orbital trajectory.

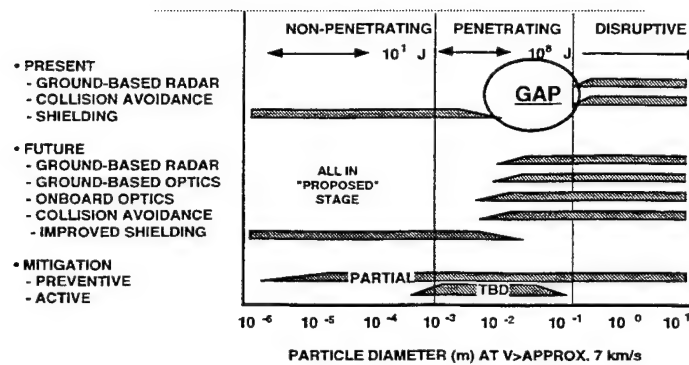
This threat-sensor point is illustrated by **Figure 3** which depicts search, detection and tracking opportunities near nodal crossings between debris and spacecraft orbits. It turns out that the general orbits of the debris are deterministic because the launches are generally eastbound, and from known latitude locations such that the debris is concentrated in corridors which are known. Therefore, the angles of attack relative to the spacecraft orbit are known to a significant extent. The orbital mechanics dictate further that the debris going in the same direction as the spacecraft is not dangerous because of the low to zero relative velocities. The dangerous debris comes only from the crossing orbits at substantial inclination angles between orbits, at roughly 30 to 70° angle of attack /Ibid. 3, page 5/. Also, it has been shown by NASA that the primary threat is from debris in the earth tangent plane relative to the spacecraft /Ibid. 4/. As shown in this figure, and as dictated by mechanics, the concept of tracking with an onboard optical system requires two data points, minimum, before conjunction and then symmetrical verification after closest approach.

**Figure 4** is a side view of the debris encounter for the situation where the threatening debris and spacecraft are at the same altitude (e.g., 400 km altitude). The side view indicates that the opportunity to track the threatening debris at 4500 km, first sighting, and then from inbound to outbound, is brief as it rises over the horizon and then sets in roughly a total of 18 minutes. Moreover, part of the observable trajectory is through the tangent earth limb atmosphere as indicated by the shaded part of the tracking trajectory. Based on these considerations, the onboard tracker will need to be fast, accurate and capable of long range tracking in order to provide protection of a safety box around the spacecraft (e.g., 4 km along the track and 2 km cross track) with uncertainty much less than 2 km along track and 1 km across track /Ibid., 7/.

### 3.3 Inertial Pseudo Star Reference Unit Characteristics

A pivotal step in being able to detect, track and eventually mitigate small, low-albedo debris is the capability to provide ultra-stable image stabilization. The technical benefits of such capability include:

- Inertializing the line of sight such that it is decoupled from base motion vibrations
- Closing a tracking loop around a strong signal - i.e., an inertialized laser signal in the tracking telescope - rather than around a low-strength image signal which would result in noisy tracking



SEE ALSO "NASA DEBRIS COLLISION WARNING SENSORS, PHASE A STUDY", JULY 1989  
AND CRISTENSEN, E. L., "SPACE STATION FREEDOM DEBRIS PROTECTION TECHNIQUES",  
ADVANCED SPACE RESEARCH, VOL 13 NO 8, 1993, AND NASA PRESENTATION BY CRAMER, B.,  
ON SPACE STATION FREEDOM, AND ON ISSA, 22 OCT 93.

Figure 1 Present and future collision avoidance approaches

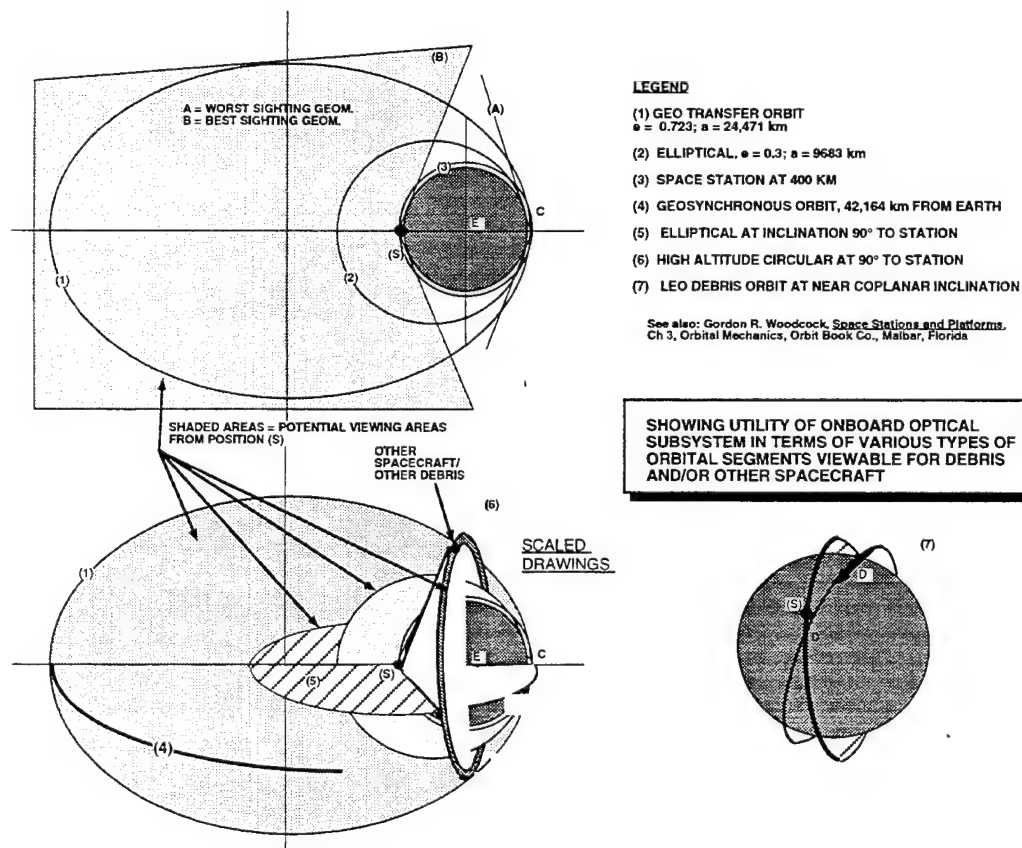


Figure 2 Utility of space based system for search, detection and tracking orbital debris

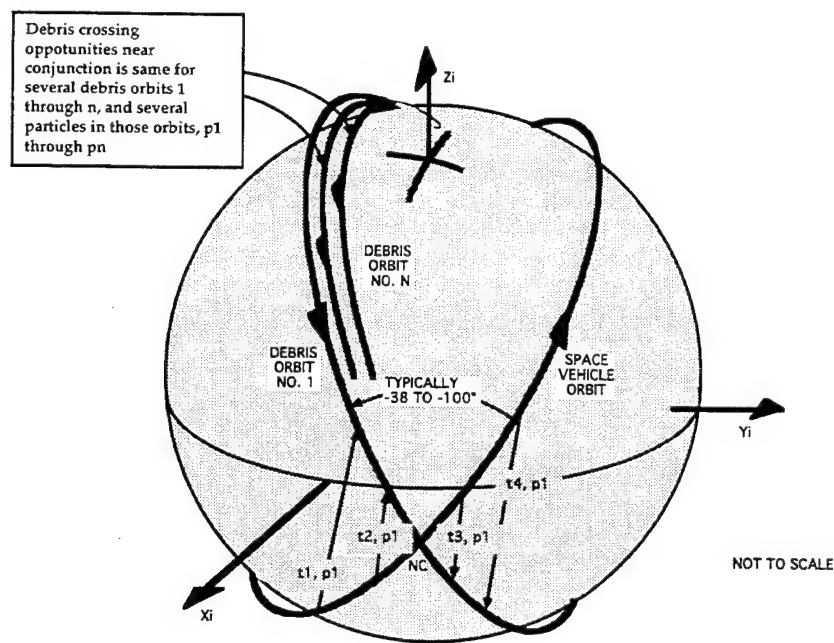


Figure 3 Top view: Search, detection and tracking opportunities near conjunction

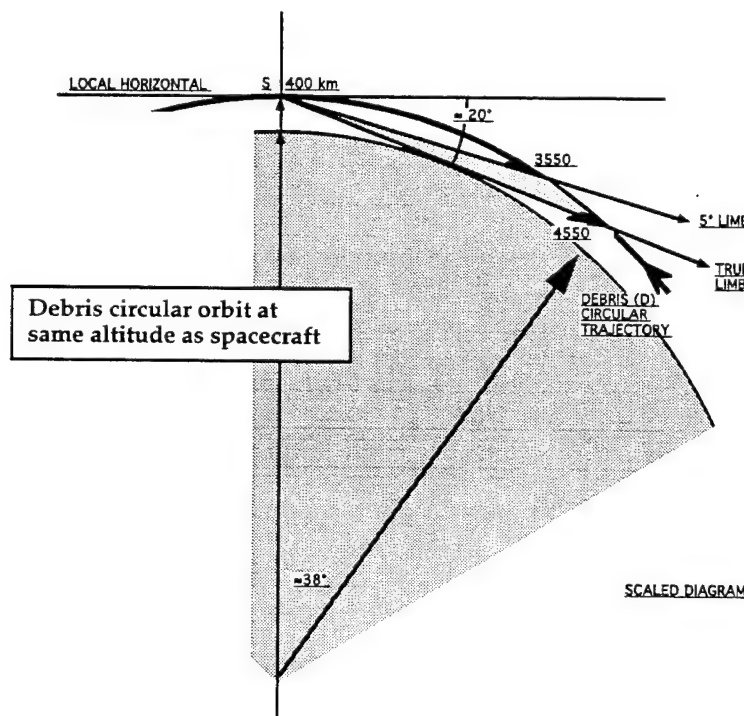


Figure 4 Side view: Observation opportunities at 400 km altitude  
(right half of symmetrical observation is shown)

- Signal to noise ratio enhancement by integration of image signals onto individual single pixels rather than an image sweeping through several pixels
- Support of spatial and temporal resolution of image locations; e.g., locating multiple pieces of debris in the telescope field of view
- Hardware support of smooth optical tracking directly in an inertial reference frame

IPSRU is a pointing reference system which emits an inertially stabilized collimated optical beam. IPSRU stabilizes this emitted beam against host vehicle vibrations and precisely steers the beam via an inertial attitude command, or along an inertial trajectory. The IPSRU beam thus serves as a reference for stabilizing the line of sight of an optical payload - for instance an optical telescope, an illumination laser, or a communications laser.

An IPSRU was built and delivered, by Draper Laboratory, to ARPA/BMDO at a stabilization performance level of 34 nanoradians, rms, with a base disturbance of 366 microradians, rms (0.4 to 312 Hz).

**Figure 5** shows an application concept of IPSRU for a tracking telescope. This general approach is being implemented in the previously mentioned balloon-borne telescope. A reflecting telescope is schematically depicted in the figure. In this example, the telescope is assumed to be in the visible spectrum and the IPSRU beam in the near infrared (e.g., 780 nm, a few nanometers wide). The scene enters the telescope, is magnified, and exits through the primary mirror as in a Cassegrain telescope. The scene is reflected off of a Fast Steering Mirror (FSM), and then through a dichroic beam splitter, as shown. The dichroic beam splitter is selected such that the visible light of the scene passes through and onto the imaging array, while the infrared beam is turned onto the alignment sensor.

Initially assume that the reflecting surface of the FSM is locked to the optical bench (host vehicle) and that the bench is jittering with time varying jitter,  $\phi$ . Under these assumptions, the image from the tracked image will jitter on the image sensor causing image smear. Now consider the IPSRU beam. It is injected into the imaging telescope via an extended corner cube (ECC). The ECC turns the IPSRU beam, but does not corrupt the beam with base motion because the input and output of the ECC always remain parallel. The IPSRU beam also reflects off of the FSM and strikes the dichroic beam splitter. However, because the IPSRU beam is infrared, it is turned by the beam splitter to fall onto the alignment sensor (a quad cell or CCD).

Now, as the optical beam jitters, if the FSM remains locked, the alignment sensor output will indicate the base jitter because the IPSRU beam is inertially stable. Thus, the alignment sensor output provides a measurement that can be used by a stabilizing servo. The servo is closed from the alignment sensor output to the FSM angle drive input such that the alignment sensor will be nulled by the FSM in spite of bench motion. That is, there will be no relative motion between the IPSRU beam and the alignment sensor. Because the IPSRU beam and the scene image follow the same optical path and, in particular, both reflect off of the FSM, the scene image will be simultaneously stabilized on the image sensor, thereby removing image smear. This line of sight stabilizing function is critically important when the tracked image is dim, requiring a relatively long integration time. The IPSRU beam is bright, providing a high SNR for the stabilizing function.

It may be instructive at this point to illustrate the Optical Reference Gyro because it is an instrument which has the same general operational feature of injecting a bright laser star into a tracking telescope. **Figure 6** shows the two degree of freedom gyro with the laser star injected first into the two-axis rotor such that a pinhole is illuminated and then projected onto a collimating lens. Then, the resulting collimated laser light emanating from the instrument is inertially stabilized by virtue of the two-axis gyro rotor on which the lens is mounted. Of course the gyro can be torqued in each degree of freedom for alignment, and it can be inflight calibrated onto a focal plane by common boresighting of the telescope image and ORG image simultaneously relative to a star line of sight. In other words, when the telescope is boresighted to the star, the ORG is also torqued so that it nulls on its detector. At

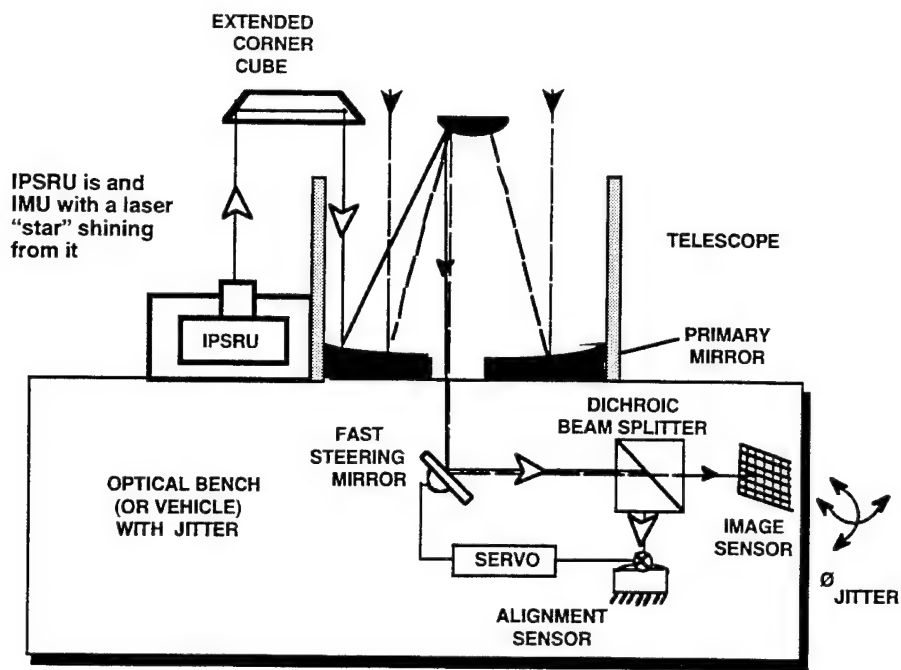


Figure 5 Inertial Pseudo Star Reference Unit (IPSRU)

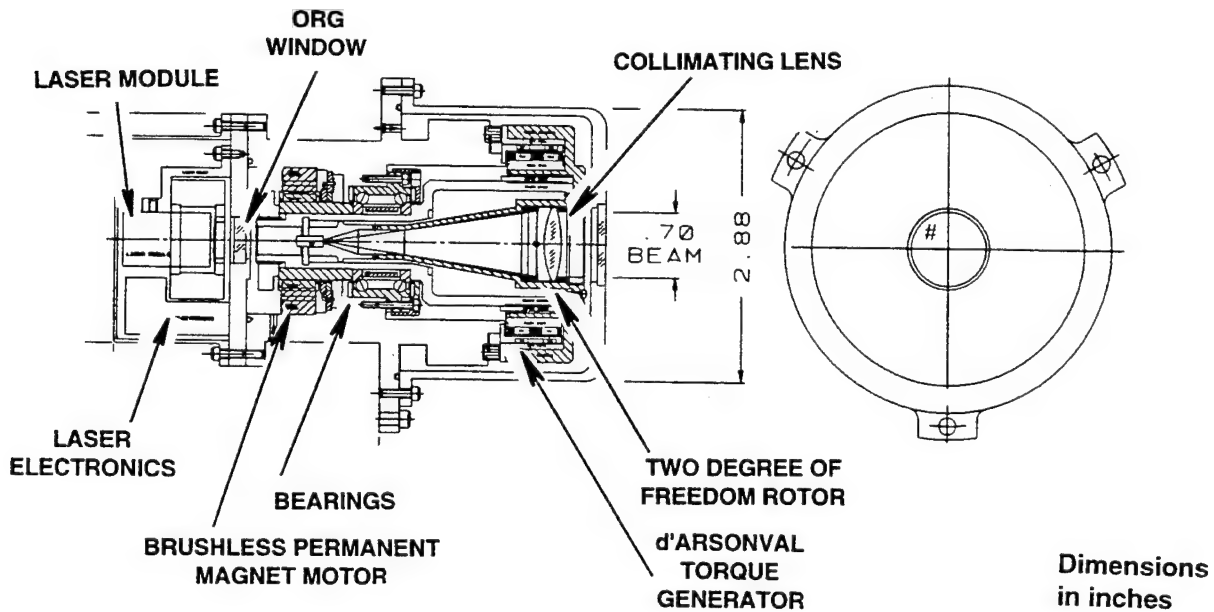


Figure 6 Optical Reference Gyroscope

this calibration point the inertial memory is transferred to optical memory (the detector) and the subsequent operation is subject only to the low residual jitter, not the inertial drift error component.

Returning now to the IPSRU discussion, note that much more detailed design information on IPSRU and test scoring descriptions are available from the referenced material. However, for purposes of this summary paper, we progress immediately to a summary of the test results on IPSRU. Table 1 summarizes the projected IPSRU performance vs. measured performance. As shown, the data are consistent with image stabilization below 40 nanoradians over a 300 Hz. bandwidth and the demonstration was carried out with a superior gyro to 20 nanoradians. (This temporarily consigned gyro was not available for the delivered unit.) Note that the angular accelerations and rates of the line of sight can be approximately 30 degrees/second due to the higher rates achievable with the IPSRU than could be tested in the laboratory and due to the doubling effect of the fast steering mirror. Acceleration capability of the fast steering mirror is more than capable of any foreseeable target acceleration rates. The line of sight acceleration of the fast steering mirror can be as high as 2400 radians/second<sup>2</sup>. In a system application, this would provide the capability for several functions related to modulation of the image on the focal plane.

Figure 7 shows the performance of the IPSRU in terms of the isolation of base motion disturbance. The plot indicates the disturbance input of 366 microradians, rms from 0.4 to 312 Hz and the isolation at 34 nanoradians, rms. The various components of noise are also shown, such as gyro wheel hunt, ground motion, bearing retainer noise and wheel speed.

### 3.4 Optical Phase Conjugation Characteristics

The OPC was described in a presentation and paper given last year at the Space Surveillance Workshop and has been described in several other publications /Ibid. 13 through 18/. Therefore, only the salient features relative to search, detection and tracking are summarized here.

There are three subsets of the OPC technology which may be used for an onboard optical system. The technology subsets are optical phase conjugate mirrors, efficient lasers and large telescope apertures. These subsets are inter-related as to the capabilities which they add to the debris detection/tracking issue. An outline description of these technologies follows, along with the relationships perceived relative to the debris detection/tracking issues.

#### 3.4.1 Phase Conjugate Mirror

Figure 8 shows the return of a strong near diffraction limited signal (the conjugate) from a weak incoming signal which was passed through a gain medium, such as a laser cavity and/or a telescope. Signal  $A_p$  is the incoming signal and  $A_c$  is the outgoing signal. The formation of the enhanced signal is accomplished in the Phase Conjugate Mirror (PCM) by nonlinear mixing of sound and light provided by pumps into the PCM. The areas of nonlinear optics of interest, for those who wish to investigate further, is described in the previously referenced material.

Another very important characteristic of the PCM is that the incoming light is returned precisely along the inbound path (Figure 9). Therefore, the PCM can readily support automatic tracking, unlike a conventional mirror where alignment of the mirrors is of first order importance. This feature is shown in the figure where the conventional mirror returns light along the direction equal to incidence plus reflection angle from the normal whereas the PCM returns light directly along the negative direction of incidence angle. The implications in tracking systems are profound in that light can be passed back and forth between the target being tracked and the optical system, thereby enhancing signal level at each cycle.

Table 1 IPSRU Characteristics

Performance	Units	Projection	Results**
Dynamic Environment (0.4 - 312 Hz)	$\mu\text{R}$ rms	320	366
Jitter (RMS)	nR	40*	
Bandwidth	Hz	0.1 - 300	
Angular Acceleration	$\text{deg}/\text{s}^2$	5	0.4 - 312
Angular Rate	$\text{deg}/\text{s}$	5	$\geq 5$
Base-Motion Rejection			3.15 (measured)
0.1 Hz	dB	$\geq 100$	
1 - 100 Hz	dB	>40	112
Drift Rate Stability (1H, 1 $\sigma$ )	$\text{deg}/\text{h}$	$\leq 0.005$	>55
Gyro Torque Loop BW	Hz	>30	0.004
Optics			
• Wavelength	nm	Phase II 830	Phase III 780
• Wavefront Quality (Peak-to-Valley)	nm	$\lambda/10$	$\lambda/8$
• Power	mW	$\geq 10$	25
Physical Dimensions (Platform Assy) (Phase III)	in	7.7 H x 11 W x 13.5 L	7.1 x 10.6 x 12.8
Platform, Weight (Phase III)	lb	<25	22.75
Electronic Assembly (Phase III)	lb		
• Commercial ATR		70	50.85
• Space Package		18	8.5
Fixed Power on Platform Base Assy (Phase III)	W	<9 W	8.7

\*Jitter was increased from 20 nR (based upon consignment gyro 542E) to 40 nR (based upon flight delivered gyro #266).

\*\* Phase II measured results unless noted otherwise.

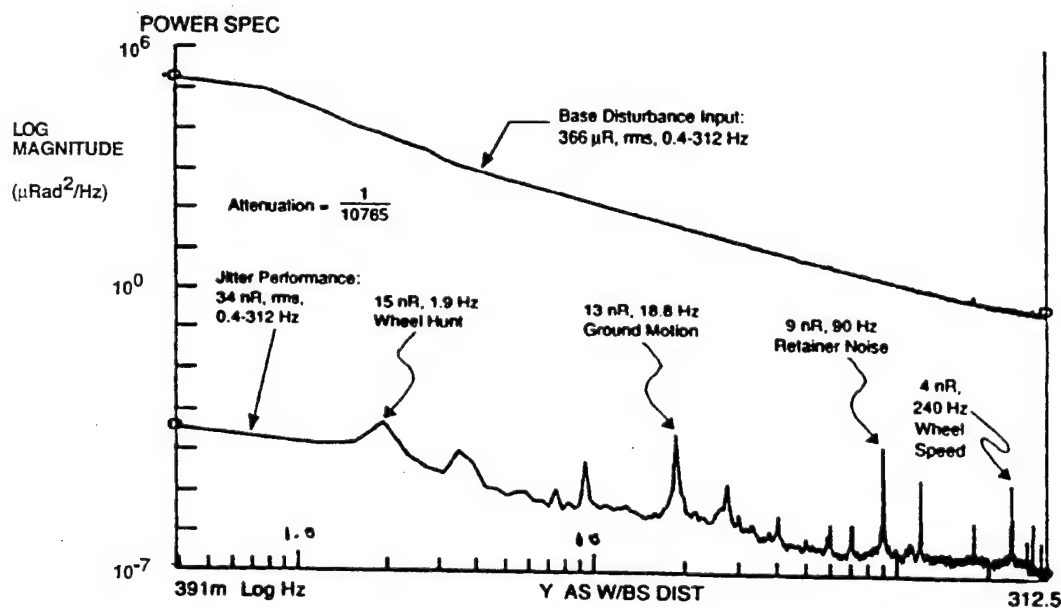


Figure 7 Jitter Performance Measurement

### Optical Phase Conjugation -

Forming a bright near diffraction limited beam from a weak incoming signal

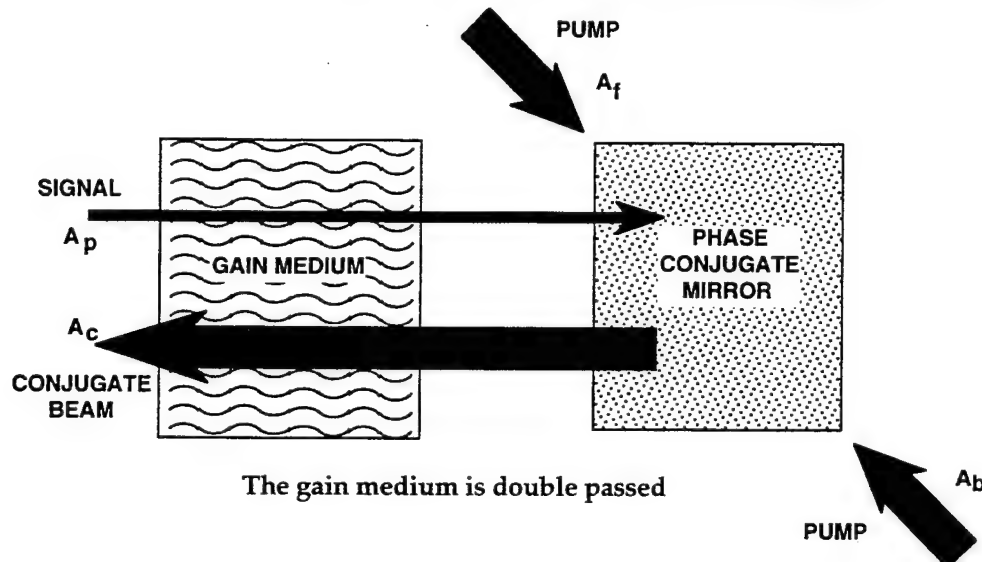


Figure 8 Optical Phase Conjugation

Conventional mirror returns the beam along Return = Incidence +Reflection direction. Phase Conjugate Mirror returns the beam exactly along the incoming direction;  $R = -I$ . Automatic tracking potential is provided.

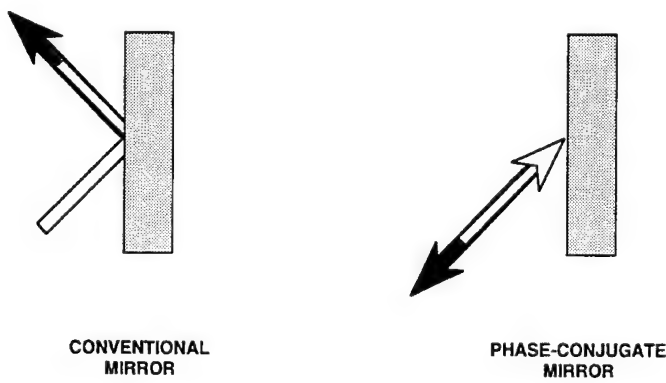


Figure 9 Comparison of reflection from conventional and Phase Conjugate Mirrors

### **3.4.2 Efficient Lasers**

The efficiency of lasers can be improved with OPC by the features that the light is returned along the inbound path. That is, one end of the laser cavity can be the PCM. Thus, the alignment of the laser becomes of no major importance because alignment is automatic with the PCM return path. The nonlinear mixing of sound and light within the PCM also enhances the return signal brightness compared with the incident light. Other aspects of the use of OPCs in lasers include areas such as the capability for higher repetition rates, less susceptibility to vibration effects and to thermal effects.

### **3.4.3 Large Inexpensive Telescopes**

**Figure 10** illustrates the aberration correction properties of optical phase conjugation as compared with a conventional mirror. Essentially, a standard mirror retains the sign of phase error and the phase error is doubled. By comparison, as shown, a PCM reverses the sign of the initial phase error relative to the direction of light travel and the error therefore cancels. The application of this technology could be to relatively large space-based telescopes of relatively light and low optical quality construction. In such a case, the large primary mirror would be the "aberrating medium" in collection of a few photons from the distant debris objects. OPC would then conjugate the received beam relative to the outgoing beam to correct the telescope aberrations and the high order debris signals would then be imaged and processed by a CCD detector.

**Figure 11** illustrates another characteristic of OPC which applies to detection and tracking. That is, the path of light between target and tracker needs to include consideration for the finite speed of light, and this can be accomplished by the non-reciprocal geometry shown. By using polarization splitters, the inbound and outbound light are separated along the two paths shown. The lead angle to the target is developed in the acousto-optic modulator as shown. The point-ahead lead angle correction then passes outbound toward the target. The potential importance of this characteristic is that the telescope does not have to slew to accommodate the small angle correction for light speed and required lead angle.

## **3.5 Concept of Proximity Warning System**

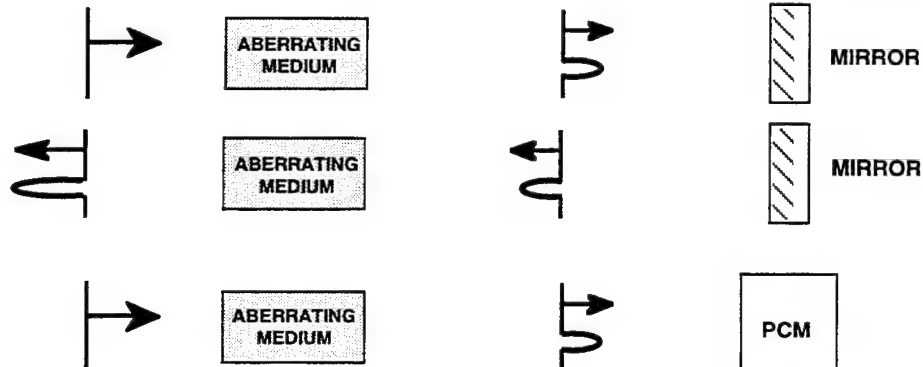
The concept of a space-based optical system for search, detection and tracking of space debris is summarized by **Figure 12**. This system could be stationed aboard a spacecraft such as the Space Station, or could be completely automated for operation aboard a separate satellite. Essential elements of the system include the command and control function, the computer function, the lidar pointer-tracker, and interfaces to other functions such as spacecraft sensors and effectors (attitude control, power systems, etc.) to ground operations and to spacecraft operations for maneuvers.

The IPSRU and PCM are shown schematically in the lidar pointer-tracker. The lidar could be separated into a laser subsystem and a tracker subsystem. The IPSRU can be used with multiple telescopes for such a design. An important system characteristic of the lidar is the ranging capability to the target and the range gating which defines the resolution of target range which can be defined. Range gating to approximately 20 picoseconds (single shot resolution of 3 millimeters) is within the state of the art with an appropriate clock /19/.

The space-based system would be used in cooperation with ground-based operations. For example, if mitigation were being implemented from the ground, the space-based system could provide illumination of the debris to support detection and tracking functions on the ground.

The figure lists some of the computations which would be required for the debris search, detection and tracking functions. These computations would include, but are not limited to, debris Position, Velocity, Time of near conjunction, Irradiance, Range (and range rate), Angles of line of sight, and Size estimates.

A standard mirror returns the sign of the phase error and the error is doubled



A Phase Conjugate Mirror reverses the sign of the phase error and the error cancels



Figure 10 Comparison of phase aberration from conventional and Phase Conjugation Mirrors

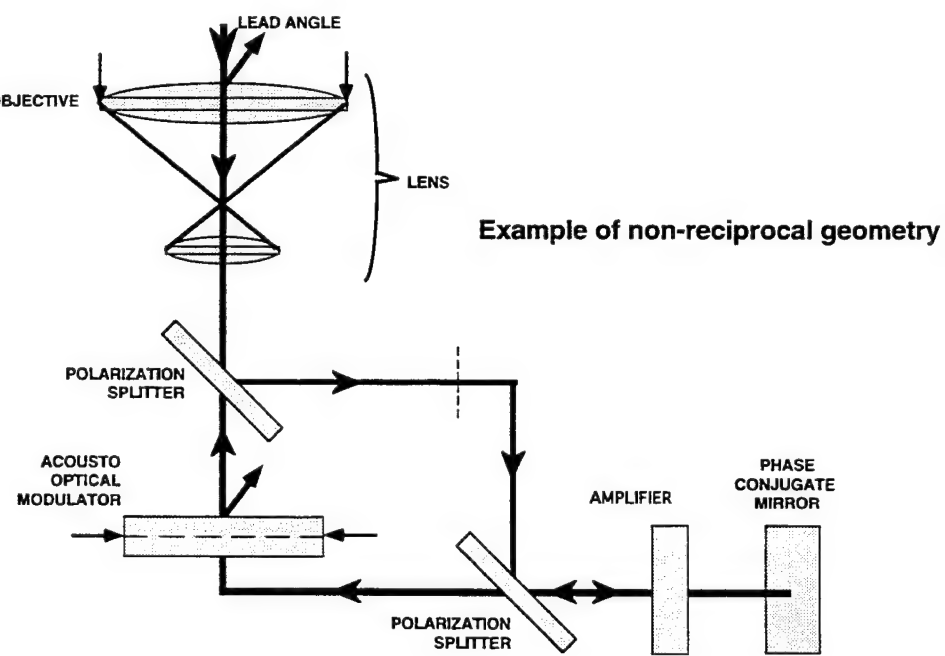
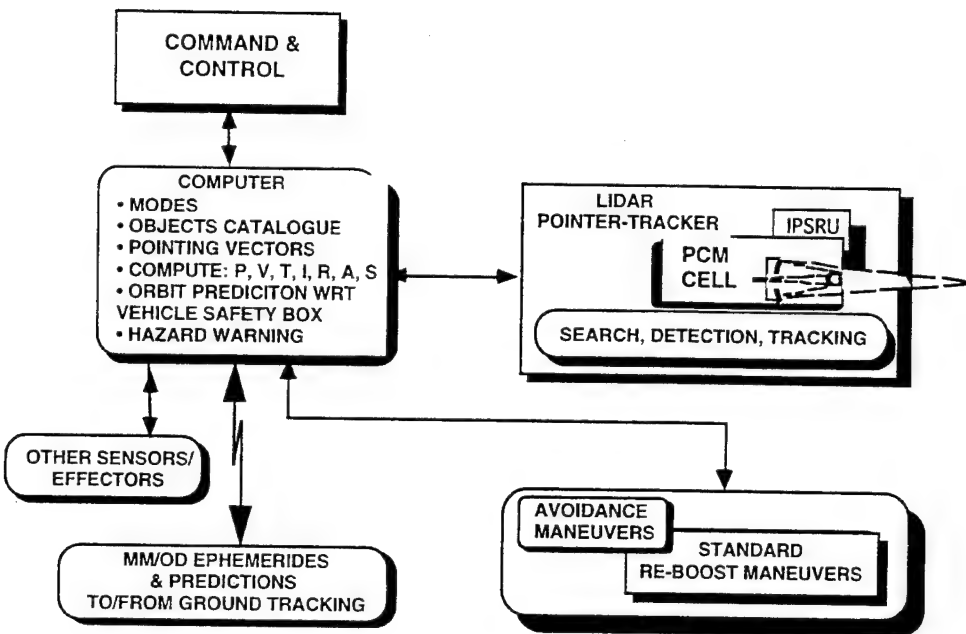


Figure 11 Point-ahead capability in phase conjugated laser system (after G. Pasmanik)



P: position, V: Velocity, T: Time, I: Irradiance, R: Range, A: Angles, S: Size

Figure 12 Proximity Warning System Approach

TECHNOLOGY	SEARCH			DETECTION			TRACKING		
	SPACE DEBRIS	NEAR EARTH OBJECTS	MANMADE SATELLITES	SPACE DEBRIS	NEAR EARTH OBJECTS	MANMADE SATELLITES	SPACE DEBRIS	NEAR EARTH OBJECTS	MANMADE SATELLITES
INERTIAL PSEUDO STAR REFERENCE UNIT (IPSRU)	Fast search & stop image on Focal Plane (FP)	Maintain inertial reference during search. Aid alignment of large segmented telescopes	Fast search with fast steering mirror referred to inertial frame	Stop on FP and support of lidar ranging by modulation on FP	Modulate image on FP, minimize effects of background and gradient	High precision pointing to inertial position	Fast, quiet tracking referred to inertial frame. Used with lidar	Maintain alignment of large segmented telescopes	Image stabilization, base motion isolation, fast track referred to inertial frame. Servo jitter isolation during fast track.
OPTICAL REFERENCE GYRO (ORG)	Same function as IPSRU	Aid portable telescopes with inertial line of sight	Aid portable telescopes with inertial line of sight (e.g., GEODSS,etc)	Stop on FP and support of lidar ranging by modulation on FP	Modulate image on FP, minimize effects of background and gradient - less accurate than IPSRU	Same as IPSRU, less accurate	IPSRU more accurate, ORG smaller, less expensive	Aid small telescopes with smooth inertial tracking	Same as IPSRU, less accurate
OPTICAL PHASE CONJUGATION (OPC)	Illuminate small debris in danger corridors. Lidar ranging	Image intensification in telescope	Lidar ranging & Image intensification in telescope	Single cycle and multi-path signal enhancement	Image intensification in telescope	Signal to noise enhancement in telescope	Negate intervening phase errors of telescopes and lasers	Image intensification in telescope	Multi cycle ranging to target

Figure 13 Matrix of Search, Detection and Tracking Requirements and Applications vs. Technologies

These data, measured and computed relative to the craft from which tracking is implemented, could then be used to compute the required six elements of the debris orbits, and from there compute the protected maneuvers, if required /20 ,page 47/:

Another important potential of the space-based system is that the debris avoidance maneuvers could be combined with the standard re-boost maneuvers which would take place on a craft such as the Space Station. Periodic re-boost maneuvers are required to account for the atmospheric drag on a large craft such as the Station. Combination of re-boost and avoidance maneuvers to stay well clear of harms way could prove fuel efficient.

### 3.6 Summary - Matrix of Search, Detection and Tracking Requirements vs. Technologies and Applications

The application of IPSRU or ORG and OPC technologies to the example of space debris search, detection and tracking has been discussed. Now, we summarize the discussion with a matrix of various search, detection and tracking requirements vs. the precision pointing and tracking technologies and the potential applications, including space debris, NEOs and man-made satellites. Figure 13 shows the search, detection and tracking requirements vs. the IPSRU, ORG and OPC technologies. Within the matrix elements are examples of specific functions which could be supported for each requirement by using these technologies. Of course, much more work in quantitative analysis, specific designs and field tests remains to be done for the example applications.

## 4.0 REFERENCES

1. S. F. Portee and J. P. Loftus, Orbital Debris and Near-Earth Environmental Management: A Chronology, NASA Ref. Publication 1320, December 1993
2. McKnight, D., el al, "Space Shuttle Window Impacts Events Study", Advances in Space Research, Space Debris, v 13, no 8 Aug 93, Pergamon Press, Tarrytown, N. Y.
3. Cramer, C., Bogart, P., NASA Presentation " Status of Micrometeoroid and Orbital Debris Protection for Space Station Freedom", 22 Oct 1993
4. Debris Collision Warning Sensor Reports: Phase A (July 1989) by NASA, including NASA Technical Memorandum by Kessler, D. J. and Reynolds, R. C. and Anz-Meader, P. D. - "Orbital Debris Environment for Spacecraft Designed to Operate in Low Earth Orbit, Phase B Final Report by Ball Aerospace (15 April 1991), and Phase B Final Report by Kaman Sciences (23 April 1991)
5. Christianson, E. L., Robinson, J.H., Crews, J. L., Olsen, G. D., "Space Station Freedom Debris Protection Techniques", P. 191 - 200, Advances in Space Research, Space Debris, v 13, no 8 Aug 93, Pergamon Press, Tarrytown, N. Y.
6. NASA Level II Space Station Control Board Directives, Space Station Requirements, BB003683, SSCN 003683, and BB003213, and 000869, and 003032, Update of Micrometeoroid and Obital Debris Environment Definition
7. Loftus, J. P. Jr., and Stansbery, E. G., "Protection of Space Assets by Collision Avoidance", IAA6.4-93-752, NASA/JSC
8. NASA and Draper and Los Alamos and DOE meeting, at NASA, September 1994
9. USAF, Phillips Laboratory, High Altitude Balloon Experiment, Preliminary Design Review, 18 - 19 May 1992

- 10 Freier, L. J., Inertial Pseudo Star Reference Unit, August 1994, Draper presentation
11. Freier, L. J., Optical Reference Gyro, April 1994, Draper Presentation
12. Gilmore, J. P., Chien, T. T., et al, "Pointing Stabilization System Using the Optical Reference Gyro", Presented at the ION 49th Annual Meeting, 23 June 1993
13. Fisher, R. A., Boyd, R. W., Klein, M. B., Kurnit, N. A., Miloni, P. W., Rockwell, D. A., Yeh, P., Soviet Phase Conjugation Research, Sept 1990, SAIC, Corp.
14. Munroe, J. L. and Peterson D. G., "Non-linear Optics in Remote Sensing *"A Major Opportunity for Mutually Beneficial US - Russian Technical Collaborations"*", LA-UR-93-4212, Nov 93, Los Alamos National Laboratory, NM, and Idaho National Engineering Laboratory.
15. Munroe, J. L., Utilization of Russian Space Technology, Optical Phase Conjugation and Analog Image Processing, An Important Opportunity for Collaboration, 5 Feb 93, Los Alamos, National Laboratory, 93079-1a, Los Alamos, NM
16. Munroe, J. L., "High-Power Nonlinear Optics, *A Major Opportunity for a Mutually Beneficial FSU-US Technology Collaboration*", Presentation by Los Alamos, National Laboratory, to Draper Laboratoty, 93079-1a, Los Alamos, NM
17. Rabins, LTC J. M., "The Quest for Russian Optical Surveillance Technology", Presentation on Trip Report to Former Soviet Union, Vol. 2, Schwan, K. P., Ed., Proceedings of the 1994 Space Surveillance Workshop, 5 April 94 Report STK-221, MIT Lincoln Laboratory, Lexington, MA.
18. Schwan, K. P., Ed., Proceedings of the 1994 Space Surveillance Workshop, 5 April 94 Report STK-221, v 1, MIT Lincoln Laboratory, Lexington, MA. (All in Vol. 1 unless noted otherwise)
19. Degnan, J. J., and Pavlis, E. C., "Laser Ranging to GPS Satellites with Centimeter Accuracy", GPS World, September 1994
20. G. R. Woodcock, Space Stations and Platforms, Orbit Book Co. Malabar, Fla., 1986

# STARE-AND-CHASE AT TRADEX

D. L. Izatt (Lincoln Laboratory, Massachusetts Institute of Technology)<sup>†</sup>

## ABSTRACT

TRADEX has developed a Stare-and-Chase capability for automatically detecting, initiating track, and collecting data on objects in low earth orbit between 300 to 1200 km altitude. This supplements the Staring capability that was used for NASA data collections in 1991 and again in 1994. Stare-and-Chase has been used operationally for a total of 64 hours of observation time. This initial capability allows TRADEX to detect, initiate track, and collect data on a 2.7 cm diameter sphere at a range of 500 km. Approximately one object per hour of observation time is being found in low earth orbit that does not correlate with objects in the Space Surveillance Network Catalog. The focus of this paper is on the current space debris detection, tracking, and data collection capabilities at TRADEX and various proposed improvements to the existing capability.

## INTRODUCTION

TRADEX is a high power L-Band and S-Band instrumentation radar located nine degrees north of the equator. It is one of four Kwajalein Missile Range radars located on the island of Namur, with the others being ALTAIR, ALCOR, and the Millimeter Wave Radar. During early 1994, TRADEX developed a Stare-and-Chase capability. In this mode, the beam is parked. Automatic detection and track initiation occurs when an object between 300 and 1200 km altitude passes through the beam. This capability was first tested in April of 1994, with the first operational use being in support of NASA space debris studies in August 1994. A second period of Stare-and-Chase operations was performed in support of the 1994 Space Debris Search Campaign in October and November.

Stare-and-Chase is the second space debris detection mode that has been used operationally at TRADEX. The other method is "Stare Mode" where the antenna is parked at zenith and no attempt is made to initiate track on detected objects. Objects are detected as they pass through the beam, but data collection is limited to the beam transit time. This capability was used operationally for the first time in July of 1991 when nineteen objects with estimated sizes as small as 3 to 4 cm were found during 4.4 hours of staring<sup>1</sup>. An additional 25 hours of staring was done for NASA in September of 1994.

These two space debris detection modes have relative advantages and disadvantages. The advantages of the Stare-and-Chase Mode over Stare Mode are

- The ability to track and collect several minutes of on-axis data on an object,
- Substantially better characterization of the signature of the object,
- Ability to generate orbital element sets, and
- Much larger range detection window than currently possible in Stare Mode.

The advantages of the Stare Mode over the Stare-and-Chase Mode are

- The wavelength dependence of the scattering cross-section allows smaller objects to be detected using S-Band in Stare Mode than using Stare-and-Chase Mode which requires using L-band.

---

<sup>†</sup> This work was sponsored by the Kwajalein Missile Range, Department of the Army. The views expressed are those of the author and do not necessarily reflect the official policy or position of the U.S. government.

- Initial angle rates needed for Stare-and-Chase acquisitions require two independent detections during a beam transit. This reduces the allowed data integration time to less than half of what is available in Stare Mode, with a corresponding reduction in sensitivity.
- Stare-and-Chase is limited to L-Band detections only. Stare Mode detections can be done at either frequency, though S-Band is normally used.

TRADEX is a very flexible sensor that can be easily adapted to support new tasks. The current debris data collection modes are simple adaptations of existing capabilities, with no hardware modifications having been done and only minor software changes having been made to support these modes of operation. This paper will discuss these capabilities, with a focus on the more complex Stare-and-Chase Mode.

## THE RADAR

This section will briefly discuss various features of the radar that are significant in Stare-and-Chase development. The antenna is an 84 ft diameter parabolic dish with a dual-frequency focal-point feed. The antenna is fully steerable over the entire hemisphere above the horizon. It can move at up to 12.5 deg/sec in azimuth and elevation, and can be accelerated from rest to full speed in under a second. This antenna produces an 11.0 mr L-Band beam and a 5.5 mr S-band beam. Klystrons are used to generate 2 MW peak power at each frequency with up to 240 kW of average power currently being radiated in L-Band and up to 40 kW of average power at S-Band. Upgrades currently under way will allow these average powers to increase to 300 kW in L-Band and 60 kW in S-Band. TRADEX transmits right circular polarization at both frequencies and receives left and right circular polarizations. Today's TRADEX is a dual frequency high power instrumentation radar operating at 1320 MHz in L-Band and 2950 MHz at S-Band, with full monopulse capability at L-Band. These frequencies, powers, and antenna size give TRADEX the sensitivity needed for Stare Mode detections on objects as small as 1.4 cm at a range of 500 km and Stare-and-Chase detections and tracks on objects as small as 2.7 cm at that range<sup>2</sup>.

Pulse-by-pulse data can be recorded on a High Density Recording System (HDR). This is a high speed tape system capable of recording approximately 14 minutes of data per tape. Two HDR tape drives can be ping-ponged, permitting continuous data recording. Ballistic Kalman tracking filters are used to generate target state vectors on exo-atmospheric objects using coherently integrated radar data. The state vector can be passed to the Kwajalein Mission Control Center over a secure ethernet connection where it can be examined for consistency with state vectors from other sources. It can also be passed to other KMR sensors to provide directing sources. One use of this network is to permit TRADEX to function as a space track backup to ALTAIR. In this mode, known as TRADATS mode, TRADEX tracking data is passed to ALTAIR where the TRADEX state vector replaces the normal ALTAIR state vector in creating and updating orbital element sets. This capability permitted ALTAIR to correlate TRADEX Stare-and-Chase detections with the SSN Catalog, generate element sets on uncataloged targets (UCTs), and to forward the element sets to other sensors through the Space Surveillance Network.

Detections are made while the TRADEX beam is parked. At a 70 degree elevation angle, the maximum L-Band beam transit time for an object in circular orbit at an altitude of 300 km is 0.4 seconds. This increases to 2.0 seconds for an object at 1200 km altitude. Though brief, these times are consistent with mechanical abilities of the antenna. These times are too brief, however, to permit operator intervention in the detection and track initiation process.

TRADEX was able to quickly develop a Stare-and-Chase capability because of two existing capabilities. The first was the TRADEX Multi-target Tracking System (MTT) that is able to monitor a large range extent, automatically detect and initiate track on an object, and automatically send the new track file to TRADEX. This system also provides the detections in Stare Mode operations. This is a stand-alone tracking subsystem that operates in parallel with the rest of TRADEX. It can automatically detect and place into track up to 63 targets. The two principal components of MTT are the Multi-target Integrator Box (MIB) and the MTT Computer. The MIB is designed to receive and digitize the L-Band sum and difference channel video returns. The MIB performs non-coherent integration over up to 128,000 range gates. The normal data integration time is 0.1 seconds, but there is an extended range processing mode that allows the MIB to

integrate over multiple 0.1 second intervals. Target detection is accomplished through use of a constant false alarm rate (CFAR) algorithm that estimates the noise level around each range cell and calculates a SNR for that cell. A detection is declared if the SNR exceeds an adjustable detection threshold. Though not designed to process S-Band returns, the L-Band video signal can be replaced by the S-Band signal for Stare Mode detections.

The MTT Computer correlates the MIB detections with existing MTT track files. When a correlation exists, the MTT track file is updated. When there is no correlation, the detection is used to automatically initiate a new track. MTT was designed to allow TRADEX to simultaneously collect data on up to six separate targets without the need to record data on the empty space between the objects. Though the files sent to TRADEX were intended to be used for data collection, these files are used in the Stare-and-Chase Mode for providing the initial directing data needed to begin moving the antenna.

The other existing TRADEX asset that permitted the quick development of a Stare-and-Chase capability is the TRADEX Radar Control Language (RCL). This is essentially a macro language that has been developed to permit the real-time program (RTP) to take any action that is normally controlled through the TRADEX computer, including almost any action that is normally performed by an operator. The RCL is a FORTRAN module within the main program and has access to all variables maintained by the RTP. Any operation under computer control can be easily triggered using any of the RTP variables and the logic can be made arbitrarily complex. Stare-and-Chase development at TRADEX mostly consisted of developing an RCL module to look for the MTT track file, redirect the radar to follow the detected object, and initiate closed loop tracking.

## STARE-AND-CHASE OPERATIONS

Stare-and-chase operations require a close cooperation between the MTT subsystem and the TRADEX computer which controls the radar. When an operator instructs the RCL to initiate Stare-and-Chase, the following RCL activities are initiated:

- The antenna is parked at the designated stare point by directing the radar to a static track file. This file holds the antenna at a fixed azimuth, elevation, and sets the detection region.
- The guard gates which control the MIB integration region are set by the RCL to cover an altitude window from 300 to 1200 Km.
- The RCL looks for the arrival of an MTT track file. TRADEX operates in a basic 10 Hz update rate and the RCL looks for this file every 0.1 seconds. When an MTT file is found, the RCL redirects the radar to the moving MTT file and the antenna begins chasing the object.
- The Catalog Tape that records radar summary and status data at a 10 Hz rate is automatically turned on by the RCL when a detection is received. The RCL also sends a message by ethernet to a Silicon Graphics INDY workstation when the detection occurs. This workstation is used for operator displays. The INDY has been programmed to watch for the detection report and to produce an audible sound when one is received. This "doorbell" is the first indication the operators receive that an object has been found and placed in track.
- The RCL changes the PRF from a fixed 100 Hz used for staring to auto PRF where an algorithm is used to set the PRF as high as possible consistent in keeping the return of the object out of the duplexer blanking zones. This increased PRF allows higher integration gains than are available while staring.
- The RCL begins monitoring the output of the TRADEX Array Processor. This subsystem performs coherent integration over 64 range gates around the target gate. It is the primary source of tracking data used by TRADEX. When the SNR of the largest peak exceeds 15 dB the RCL automatically locks onto the object and initiates closed loop tracking. This process of detecting the presence of an object and initiating track occurs without operator intervention.

- The RCL opens a “snapshot file” on an INDY workstation immediately after closing the tracking loop. A small amount of summary data is written to this file at a 10 Hz rate for the duration of the pass. Among other things, it contains the GMT time and the range, azimuth, and elevation of the track.
- The azimuth of the track is monitored by the RCL and tracking is terminated by the RCL if the antenna is about to move into the mechanically forbidden azimuth region. This is important in Stare-and-Chase operations where the trajectory of the object is not known in advance and the operator cannot pre-position this sector based on the expected trajectory.
- A task running on an INDY workstation uses the snapshot file to correlate the track with objects in the SSN Catalog. Eventually TRADEX will be able to also use this file to generate an element set for the object.

## STARE-AND-CHASE RESULTS

The first demonstrations of actual Stare-and-Chase operations on unknown objects were performed in early April of 1994. The beam was parked at 1000 mr elevation (60 degrees). Detections were performed using a 565  $\mu$ s L-Band chirp waveform. The MTT CFAR threshold was lowered until frequent false alarms were observed, and then increased until the false alarms were infrequent. The Stare-and-Chase software was armed and the Stare-and-Chase experiment begun. The first operational test was conducted on April 8, 1994, with three objects being found and placed in track during the two hour test.

The first operational use of Stare-and-Chase occurred in support of 25 hours of Stare-and-Chase observations for NASA debris studies between August 3 and August 11, 1994. ALTAIR supported these operations in TRADATS mode by performing correlations with the SNN Catalog, generating element sets on the UCTs, and forwarding the element sets to Haystack and Millstone through the Space Surveillance Network. A total of 26 objects that did not correlate with objects in the SSN Catalog were detected and placed in track. Another 27 cataloged objects were also found. A second round of Stare-and-Chase operations occurred between October 12 and November 9 in support of the 1994 Space Debris Surveillance Campaign. A total of 39.5 hours of Stare-and-Chase was conducted with an additional 39 UCTs being found in low earth orbit. Of these objects, ALTAIR was able to generate usable element sets on 23 of the UCTs which were forwarded to Space Command. The combined operations produced tracks on 65 UCTs, with another 65 cataloged objects being found in 64.5 hours of observation time. This demonstrated that TRADEX is able to find and track twice as many objects in low-earth orbit as are currently cataloged, with uncataloged objects being found at a rate of one per hour.

Figure 1 shows the result of the Stare-and-Chase detections. The cross-sections are the first cross-section measurement made after track initiation and are the best currently available indication of the strength of the return at the time of detection which occurred several tenths of a second earlier. The cross-sections are calculated from the L-Band LC channel, using coherently integrated data. The data was integrated for 0.1 second and, depending on the instantaneous PRF, consisted of 10 to 20 PRIs of data. The first usable measurement is plotted instead of a representative cross-section since this plot focuses on detectability. Using the first usable measurement eliminates various biases associated with using maximum, minimum, or average cross sections during the first few seconds of track, but at the expense of greater fluctuations in the plotted cross-sections.

There are three categories of objects shown in the plots. The asterisks are detections on cataloged objects with cross-sections below -15 dBsm. The other two, indicated by the pluses and the squares, are the UCTs. The squares represent UCTs with cross-sections that change by less than 4 dB during the first few seconds of track and are good estimates of the strength of the return at the time of detection. The pluses represent the UCTs with more rapidly varying cross-sections.

Most of the detections occurred in a band from 750 km to 1050 km in range. Another band of detections occurs around 500 km. One concern is the possibility of the system not performing properly outside the main band. The only difference between detections within the densely populated band and the other regions of the plot is the transit

time of the object. The closer the object, the less time it spends in the beam and the more demanding the acquisition becomes. The presence of several UCTs around 500 km indicates that the objects within the 550 to 750 km gap did not exceed system capabilities.

The NASA debris operation conducted between August and October of 1994 also included 25 hours of Stare Mode operations, with 20 hours spent monitoring a 400 km range extent centered at 650 km. Significantly fewer detections were found during these operations than were expected based on the 1991 study<sup>3</sup> when the 400 km swath was centered at 1000 km. The final 4 hours of the 1994 Stare Mode operations were conducted with the coverage centered at 900 km. The rate of detections significantly increased during this final period, with the rate being consistent with the 1991 rate. This supports the conclusion that the bands are not system artifacts.

A second concern is the lack of detections below -32 dBsm. TRADEX sensitivity should allow detection and track initiation on a 2.5 cm sphere at a range of 500 km. Such an object would have an L-Band cross-section of around -42 dBsm, 10 dBsm below the smallest sized object found in that region. Though various possible explanations have been examined, nothing has been found that would indicate a system performance problem. Unidentified problems and system limitations could always account for this lack of detections, but with only nine objects found in the vicinity of 500 km range, it seems more likely that the lack of detections is due to the low population of objects in that region. More observation time is needed to resolve this issue.

Minimum detectability is determined by SNR which, for a single pulse return on an object with a fixed cross-section, varies with the fourth power of the range. Since the MIB integration time is independent of range, the minimum detectable cross-section will exhibit this fourth power of range dependence. This permits use of the objects with slowly varying cross-sections at longer ranges to estimate the current sensitivity at the 500 km reference range. A sensitivity curve is plotted in Figure 1, with the curve fit to the smallest non-fluctuating objects found beyond 800 km. This curve is consistent with a minimum detectability at 500 km range of -40 dBsm. Along the right side of the figure are the diameters of spheres with the indicated cross-sections. Using the Raleigh approximation, a sphere with a -40 dBsm cross-section at L-Band has a diameter of 2.7 cm. Though the curve indicates another 2 dB of sensitivity is needed to detect a 2.5 cm diameter sphere at 500 km, current sensitivity is close to the expected sensitivity. Increased observation time would produce more minimum detectable non-fluctuating objects and would better define the sensitivity curve. Furthermore, proposed waveform and signal processing modifications that will be discussed below are expected to produce another 5 dB in sensitivity at 300 km, and increases to 8 to 10 dB at 1200 km. These improvements would be sufficient to permit Stare-and-Chase detection, tracking, and data collection on a 2.5 cm sized object.

## PROPOSED UPGRADES

Objects of high interest in space debris studies include objects in low-earth orbit that are one to ten centimeters in size. Though TRADEX cannot currently detect a one centimeter object, it can come close. For objects at a standard 500 km reference range, it does have the sensitivity to do Stare Mode detections and data collection on objects as small as  $1.3 \text{ cm}^2$ , with L-Band Stare Mode minimum detectability being around  $2 \text{ cm}^2$ . Stare-and-Chase detections require objects larger than 2.7 cm.

The demonstrated space debris detection and tracking capabilities at TRADEX are initial capabilities that have been developed with only a modest software effort. Significant performance improvements are possible through a series of modifications, with the mods ranging from being simple and inexpensive extensions of existing and planned capabilities to being very expensive. If all upgrades were performed, TRADEX would be able to develop a true 1 cm detection capability at S-Band. The proposed modifications include

- Doubling the Stare Mode range coverage available with the HDR tape recording system.
- Implementing a range dependent real-time data integration algorithm that matches the integration time to the expected beam transit time.

- Implementing simultaneous Stare Mode and Stare-and-Chase capabilities, with Stare Mode detections available at both frequencies.
- Eliminating range smearing losses through the use of pulsed CW waveforms at both frequencies.
- Installing an S-Band monopulse system for S-Band angle information in Stare Mode. This would allow S-Band angle measurements on objects too small to be seen in L-Band and would allow S-Band Stare-and-Chase operations.
- Replacing the S-Band Klystron with a new Klystron capable of 4 MW peak power with 1000  $\mu$ s pulse<sup>2</sup>. This would give a true 1 cm detection capability.

The remainder of this paper will discuss these upgrades in greater detail.

#### DEBRIS RECORDING SYSTEM :

Stare Mode operations currently require the use of the High Density Recorder (HDR) tape system, but the recording bandwidth of this system is too limited to properly support Stare Mode operations. The waveforms currently used have a compressed pulse width of 200 meters and are normally sampled every 75 meters. The HDR recording bandwidth limits the recording of both polarizations of S-Band data to a 400 km range window which is less than half the desired 300 to 1200 km range coverage. In L-Band, where the monopulse channels also need to be recorded, recording over this same 400 km range window requires a reduction in the L-Band sampling rate by a factor of two, with samples spaced every 150 meters. This leaves the L-Band data slightly undersampled.

The need to record data on an object during the entire time that the object is in the beam, including the period before the object was detected, imposes the requirement for the HDR tapes to run continuously. The tapes are expensive and hold only 14 minutes of data per tape. If inordinate tape costs are to be avoided, the number of tapes devoted to Stare Mode needs to be limited and the tapes reused. This severely limits the number of hours that can be devoted to Stare Mode operations in any one day. Also, after the data is recorded, data within a couple of seconds of the detection must be transcribed to 9-track tapes. The playback time is quite high and usually requires more time than the original recording time. These restrictions limit Stare Mode observation time to a maximum of about two hours per day.

Operations would be much more efficient if the data were recorded on a special Debris Recording System that would be sized to coverage of the full 300 to 1200 km swath. High tape costs and tape transcription times would be eliminated through the use of a circular RAM memory buffer that would hold several seconds of data over the entire range coverage while waiting for a decision on the presence of an object. When a detection occurs, the memory would be frozen and a few seconds of data around the detection would be transferred to a hard disk. This would eliminate the playback time entirely, with the observation time being limited only by the size of the hard disk. This Debris Recording System would be a simple extension to the Data Analysis Workstation that is currently under development at TRADEX. The only addition needed is the circular RAM buffer.

#### REAL-TIME DATA INTEGRATION SYSTEM:

The present detection capability relies on the use of the MIB for data integration and target detection. The MIB can perform data integration over 128,000 range gates, which permits coverage over the desired 300 to 1200 km altitude envelope. Though the MIB is a powerful signal processor, the signal processing algorithms are implemented in hardware and are very inflexible. TRADEX is currently developing a Real-time Data Integration System (RDIS) that will be programmable in high level languages. It will be very flexible and will have sufficient processing capability for detection.

One disadvantage of the MIB data integration algorithm is that the integration time is fixed. The MIB cannot take advantage of the increased beam transit time that occurs as the range increases. This loss can be estimated. Beam transit

times are as short as 0.4 seconds. In Stare-and-Chase, two detections are required during the beam transit to build the initial tracking file. This limits the MIB integration time to 100 ms, which is half the desired integration time at 300 km range and a tenth of the desired integration time at 1200 km. Since detectability with non-coherent integration scales roughly with the square root of the number of PRIs integrated, if beam shape losses are ignored, this mismatch produces a loss in detectability of approximately 5 dB at 1200 km. This increases the diameter of the minimally detectable sphere at 1200 km from 4 cm to 5 cm. Though the MIB cannot accommodate range dependent integration times, such algorithms have been proposed for RDIS.

Stare Mode operations have been limited to S-Band. Though S-Band has the wavelength advantage that permits detecting smaller sized objects, the S-Band beam is only half the width of the L-Band beam. Many objects are detectable in L-Band, but since they fall outside the S-Band beam, they currently go undetected. Detection efficiencies would be increased by implementing simultaneous detections at L-Band and S-Band. This requires a second signal processor to cover the other frequency. RDIS will have the necessary processing power to perform the detections over the desired range interval. Other RDIS advantages, like range dependent integration times, make it desirable to expand RDIS to operate at both frequencies.

#### CW WAVEFORMS:

When staring at 70 degrees elevation, an object in circular orbit at 300 km altitude will move up to 1.2 km in range during the L-Band beam transit. This increases to a maximum of 4.2 km at 1200 km. Chirp waveforms are currently used with range resolutions of approximately 200 meters at each frequency. Ignoring beam shape corrections, the L-Band energy that is concentrated within 200 meters on each PRI becomes smeared over 1.2 to 4.2 km during the beam transit.

An ideal integration algorithm would concentrate all received energy into an area comparable to the resolution of the waveform, permitting the loss in detectability to be estimated from the ratio of the range smearing to the waveform resolution. This gives a maximum L-Band Stare Mode loss in detectability of 8 dB at 300 km, increasing to 13 dB at 1200 km. The loss will be 3 dB less for in S-Band due to the smaller beam. It is also 3 dB less for L-Band Stare-and-Chase where two detections are needed during the beam transit. This loss estimate is pessimistic since it does not properly take into account beam shape losses from the change in illumination of the object as it crosses the beam. It also corresponds to a worst case loss. In fact, objects that cross perpendicular to the beam produce no smearing loss. On an average, roughly 3 to 7 dB of loss can be expected with the current waveforms.

The simplest solution to the range smearing problem is to select a waveform with a lower range resolution. A pulsed continuous wave (CW) waveform would have the lowest range resolution and provide the most immunity from range smearing. A 94  $\mu$ sec S-Band CW waveform has a resolution of roughly 14 km, with a 565  $\mu$ s L-Band waveform having an 85 km resolution. These sizes are significantly larger than the expected range smearing during the beam transit and would be insensitive to the smearing.

TRADEX currently generates CW waveforms in L-Band and S-Band, but they are currently available only as recorded waveforms. No operational use can currently be made of these CW waveforms. Operational use requires the development of digital pulse compression systems which can be built with off-the-shelf components. The MIB cannot be used with digitally pulse compressed waveforms, but by developing new radar data buffers, RDIS could easily process the new waveforms.

Another benefit of developing a new waveform for space debris detection is the ability to fit the pulse duration to the duty cycle of the transmitters. Detections are made while operating at a fixed 100 Hz PRF, but the waveforms currently used can be used at up to 220 Hz PRF. If waveforms are developed that are restricted to 100 PRF, a 270  $\mu$ s S-Band CW pulse could be developed that would provide an additional 4.6 dB sensitivity relative to the current 94  $\mu$ sec waveform. TRADEX is also examining the possibility of using a 1000  $\mu$ s CW pulse in L-Band which would provide an additional 2.5 dB of sensitivity.

### NEW S-BAND TUBES AND S-BAND MONOPULSE:

For objects that produce an S-Band detection, but with no usable L-Band signal, no monopulse information is available. Without this angle information the beam loss correction to the cross-section cannot be determined and the cross-section can only be estimated to within a range of values. The object must be small enough to produce no L-Band return, but larger than the minimum sized object that could produce the observed S-Band return. In addition to providing Stare Mode angle measurements, an S-Band monopulse system would also provide the angle information needed for closed loop tracking, and the potential for an S-Band Stare-and-Chase. S-Band monopulse could be developed, but it would be expensive. New receivers would be needed for the monopulse channels and a new feed with S-Band monopulse horns would be required.

Another costly proposal involves replacing the S-Band Klystrons. The current Klystrons are limited to a 3% duty cycle and can support a 2 MW 270  $\mu$ s pulse at 100 Hz. Estimates<sup>2</sup> indicate that new S-Band klystrons could be built that would allow a 4 MW 1000  $\mu$ s pulse at 100 PRF with a duty cycle of around 10%. The increased energy in the pulse would provide an additional 8.6 dB gain over the 270  $\mu$ s pulse and a gain of 13.2 dB over the currently used 94  $\mu$ s waveform. This would allow detection of a 1 cm sized object at a range of 500 km.

### **SUMMARY**

TRADEX currently possesses the capability to detect, track, and collect high quality data on objects in low earth orbit, including objects in equatorial orbit. Two modes of detection have been developed and have been used operationally. One is a Stare Mode that uses S-Band data for detection, with no attempt made to initiate track on the object. Objects as small as 1.3 cm at a range of 500 km can be detected in this mode. The other is the Stare-and-Chase Mode that uses the L-Band return. Stare-and-Chase is capable of detecting and initiating tracks on spheres with diameters as small as 2.7 cm at a range of 500 km. TRADEX is currently able to find and track twice as many objects in low-earth orbit as are currently cataloged, with uncataloged objects being found at a rate of one per hour.

The current space debris capability at TRADEX is based on the existing system without any special modifications having been made to improve the efficiency or sensitivity of the radar for space debris detection, tracking, or data collection. Various modifications have been identified that would significantly increase sensitivity and efficiency. Most of these modifications are fairly simple, with low hardware costs. A true 1 cm capability could be developed, but would cost several million dollars. Though expensive, the cost remains much less than the cost of designing and building a new radar.

### **REFERENCES**

1. D. Morton, S. Vento, A. Larson, N. Orrick, "NASA Multifrequency Space Debris Radar Tests (MSDRT) -- TRADEX Vertical Staring," 20 April 1994, Viewgraph presentation.
2. P. Ingwersen, "KMR Orbital Debris Measurements," 1994, Viewgraph presentation.
3. S. Six, "TRADEX Data Validation Letter for NASA Multi-frequency Space Debris Radar Tests (MSDRT)," 19 July 1991, TRADEX Technical Publication.

### **ACKNOWLEDGMENTS**

Stare-and-Chase development and operations has received broad support from many people at TRADEX and ALTAIR. A complete list of those contributing will not be attempted since it is inevitable that people will be inadvertently omitted. The dominant contributors whose efforts made Stare-and-Chase possible do deserve

recognition. Dominic Balesteri developed the Stare-and-Chase RCL and Shaun Woodburn made required MTT software modifications. Also deserving recognition are Eric Stevens, Gary Duff, and Andrew Gerber at ALTAIR. They assumed responsibility for providing correlations with the SNN Catalog, generating element sets from TRADEX data, and forwarding the element sets to other sensors.

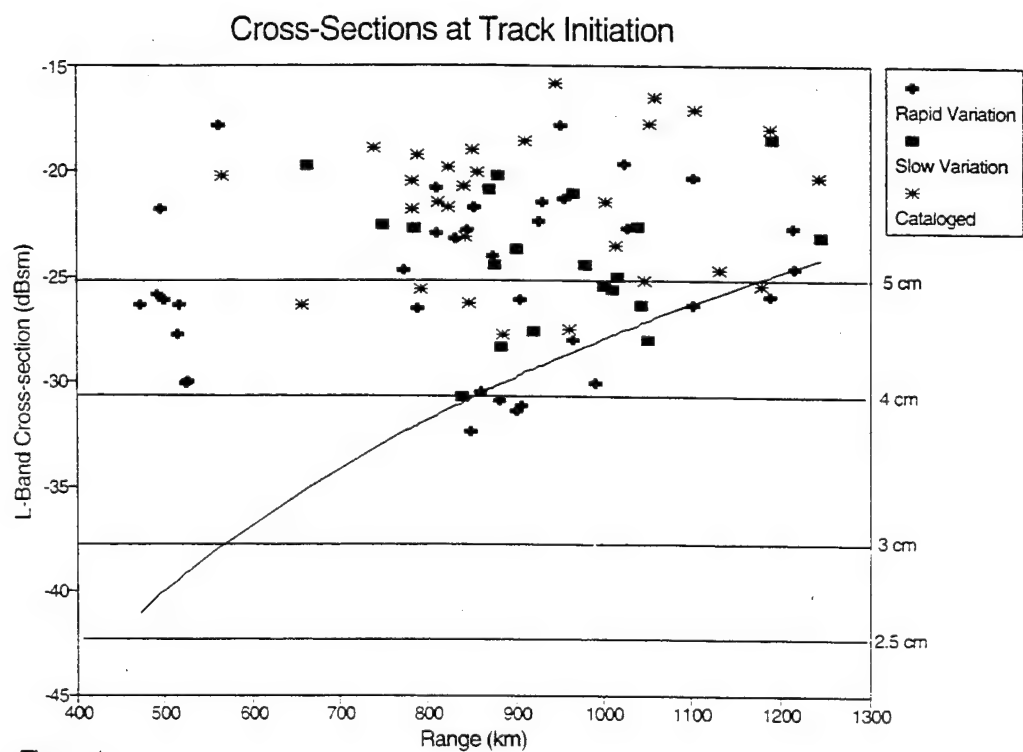


Figure 1

## ALCOR Sensitivity and Detection Enhancements

K. J. Witt, R. K. Avent

(Lincoln Laboratory, Massachusetts Institute of Technology)\*

### **1 Introduction**

The Kwajalein Missile Range (KMR) is operated under the scientific direction of MIT Lincoln Laboratory and host a suite of instrumentation radars located on the island of Roi-Namur in the Republic of the Marshall Islands [1]. This suite of instrumentation radars consist of four highly sophisticated sensors which cover the RF spectrum from VHF to W-band. Two of these radars function as wideband high frequency imaging sensors that provide precision metrics while the other two are high-power acquisition sensors with large search volumes. The ARPA Lincoln C-band Observable Radar (ALCOR) is one of the two high resolution imaging sensors and as such, operates as a broadband all-weather metric and signature system. In its current configuration, ALCOR supports reentry measurement missions, space debris campaigns, and Near Real-time Imaging (NRTI) for the Space Object Identification (SOI) program.

ALCOR was designed to track in either beacon or skin, and during reentry missions, the typical configuration is a combination of both modes. ALCOR's signature waveforms consist of a 6 MHz narrowband and a 512 MHz wideband LFM chirps and the currently advertised single pulse sensitivity is 23 dB SNR on a 0 dBsm target at 1000 km range. With its expanding role in both KMR missions and space debris campaigns, ALCOR has recently been tasked to collect signature data on non-beaconed objects beyond its current skin tracking range. To expand the skin track range, ALCOR's sensitivity and detection capabilities have recently been enhanced with further improvements planned. These enhancements should improve ALCOR's ability to support its SOI and debris study activities. This paper will discuss the sensitivity and detection improvements, and the associated capabilities these improvements can provide for the Space Surveillance Network.

### **2 Coherent Integration**

The ALCOR skin track range has been severely limited, in comparison to the other KMR instrumentation radars, by its inability to integrate radar pulses. Traditional ballistic missile missions utilize ALCOR's dual beacon tracking capability to provide excellent metric coverage on up to two independent targets, from horizon break through reentry. Skin tracks are typically delayed until reentry because the high SNR beacon tracks offer better metric performance; however, the diversifying role of ALCOR has recently dictated the need to track integrated pulses.

Provisions for coherent integration were included in the ALCOR console upgrade [2]. The ALCOR computer system passes display, control and radar data through a reflective memory bus. A Skybolt application accelerator, as seen in Figure 1, resides on this reflective memory bus and has access to all radar data. This application accelerator supports both coherent integration and real-time imaging, and is currently capable of processing 256 pulses. The addition of both noncoherent integration and postsumming is currently being developed. The application accelerator consist of two processors: an Input Output Processor (IOP) and Arithmetic Processor (AP). The IOP performs all task synchronization and data transfers, the AP performs the actual processing. The first step in processing is the phase correction of each return. Cross-range FFTs are then implemented

---

\* This work is supported by the Army's Kwajalein Missile Range (KMR). The views expressed in this article are those of the authors and do not necessarily reflect the official policy or position of the U.S. government.

to compute a range-Doppler image, and the image is collapsed into an A-scope range return. Multiple phase correction techniques and A-scope generation algorithms are supported. Computation and display of integrated pulses, along with real-time imaging, have been operational for sometime; however, modifying the radar's Real-Time Program (RTP) to track integrated pulses has been the thrust of the recent effort.

To this end, the ALCOR tracker has been modified to track integrated pulses and coherent integration is now a fully operational mode. The Kalman filter, track file handling and pulse scheduling software have been modified to accommodate the Coherent Processing Intervals (CPI's). ALCOR recently set a range track record of 5400 km on Lincoln Calibration Sphere 1 (LCS1) by performing 128 pulse integration. The coherent processing system was able to realize a 19 dB integration gain while maintaining a stable track with a track update rate of only 2.3 Hz. ALCOR's relatively low Pulse Repetition Frequency (PRF) limits the track rate for a given integration level.

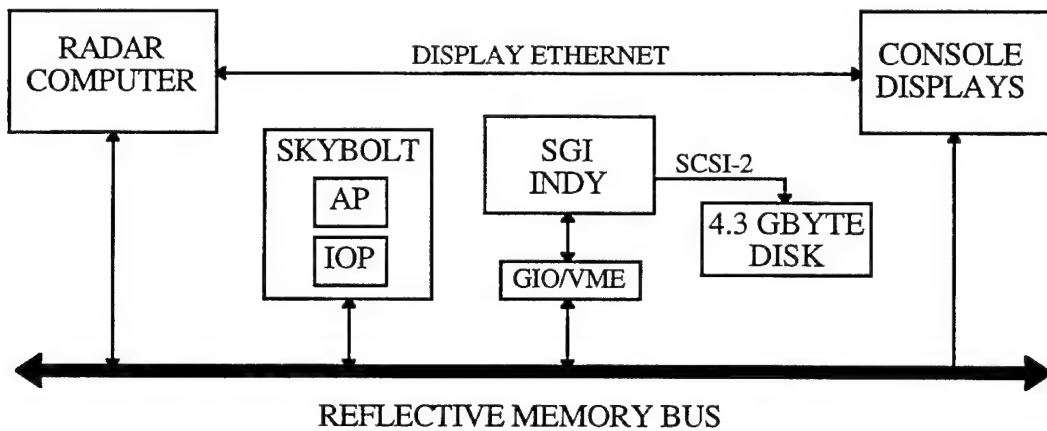


Figure 1. A Generalized Schematic of ALCOR Computer System

### 3 Final Power Amplifier Replacement

The maximum PRF at ALCOR was recently increased from 203 to 323 Hz while maintaining the same peak power across the pulse. Although this increase has provided many advantages, it was originally desired to increase the PRF to 400 Hz or higher. Increasing the PRF offers three distinct advantages: (1) it decreases the chance of Doppler aliasing on tumbling objects, (2) it increases the number of pulses available to integrate on low SNR targets, and (3) it increases the tracker update rate for a desired integration level. Due to the diminishing number of spare Final Power Amplifiers (FPA), the effort to increase PRF was postponed until a suitable replacement could be identified and procured.

ALCOR currently utilizes a Varian 146N Twystron tube as the Final Power Amplifier (FPA). Because this tube is no longer supported by the manufacturer, a candidate replacement tube, a Varian VKC-8313 Extended Interaction Klystron (EIK), is being evaluated and validation tests are under way with a loaner EIK tube to insure the EIK is compatible with ALCOR's transmitter subsystems. Initial test results have been positive and indicate that the EIK is nearly a drop-in replacement for the 146N and its peak wideband range sidelobes after equalization should be at least 30 dB below the main return.

The EIK offers the potential to operate at higher peak power levels and PRFs. Thus, not only will the previously mentioned benefits of a higher PRF be realized, but ALCOR's single pulse sensitivity can also improve. The EIK can operate at 4 MW peak power across the band, which is 1 MW (1.25 dB) higher than the 146N. An investigation is underway to determine what transmitter subsystems modifications are required to support higher peak power levels. The current 146N is being restricted to an RF duty factor of 0.00323 to enhance filament life expectancy. The EIK will support a 0.004 RF duty factor, which results in a single waveform PRF of 400 Hz; furthermore, with proper cooling, Varian considers 0.006 duty (600 PRF) achievable.

#### **4 Direct Disk Recording**

Increasing the system PRF requires off-loading the recording system from ALCOR's real-time computer. This will reduce the RTP's processing requirements and creates the opportunity to increase the recording bandwidth. The current system uses a bank of nine-track tape drives which are high maintenance and near their maximum recording capability. The system under development, illustrated in Figure 1, is a disk-drive based recording system which will access data through the reflective memory bus. This direct-disk recording system will read radar data from the reflective memory bus over a GIO-VME adapter to a SGI Indy workstation hosting a Seagate Barracuda drive. This single drive has a 4.3 GByte capacity and is rated at sustained recording rates of 7 MBytes/sec. The data path from reflective memory onto this disk drive has been established and has demonstrated sustained recording rates of 5 MBytes/sec. This recording bandwidth will support a 500 Hz system PRF.

#### **5 Noise Figure Reduction**

ALCOR's most recent opportunity to improve sensitivity was created by replacing the parametric preamplifiers (LNAs) with low noise Amplica GaAs FET amplifiers. These GaAs FET amplifiers have a built-in input overload protection. Because they are self-protected, a 32 dB attenuator could be moved from in front of the LNA and combined with the post-LNA AGC attenuator. The 32 dB attenuator has measurable loss even in the "0dB" attenuation state; therefore, a noise figure reduction is achieved by moving the attenuator down-stream of the LNA. A sensitivity increase of 0.9 dB was realized with this modification. The current sensitivity figure of ALCOR is 23.9 dB single pulse SNR on a 0 dBsm target at 1000 km.

A second sensitivity enhancement under investigation is to replace the Amplica LNAs with a newer lower noise figure design. Satellink offers a replacement unit that has a noise figure of 0.99 dB, which is 0.75 dB lower than the current units, while providing the necessary input overload protection. This amplifier replacement would result in an additional sensitivity increase of 0.8 dB, resulting in a single pulse sensitivity of 24.7 dB.

#### **6 Implications for the Space Surveillance Network**

The recently completed and ongoing sensitivity and detection enhancements improve ALCOR's ability to meet its changing mission roles; furthermore, these enhancements enable ALCOR to better serve the space surveillance network. Although MMW is the primary imaging radar at KREMS because of its twofold advantage in range and cross-range resolution, ALCOR provides additional capabilities. Because ALCOR is nearly all-weather, substantially less sensitive to atmospheric effects than MMW, and can search a

larger volume, it is better suited to responding to new launch alerts and collecting images on passes with a non-favorable (low elevation) geometry. Coherent integration increases the SOI imaging range to higher altitude satellites and thus creates the opportunity expand the type of objects ALCOR can support.

These enhancements also enable ALCOR to better support other activities such as ODERACS, PMG, and the space debris campaigns. ALCOR's metric performance, beamwidth, dual range tracker, and now coherent integration provide exceptional coverage of small objects and closely spaced objects without the previous constraint of single pulse sensitivity on small targets.

## 7 Summary

To expand its skin track range, ALCOR's sensitivity and detection capabilities have recently been enhanced with further improvements planned. Real-time coherent integration of up to 256 pulses has been implemented on a Skybolt application accelerator and is fully operational. A usable integration gain of 19 dB has been demonstrated on a spherical satellite tracks. The system's sensitivity has been improved by reducing the receiver's noise figure. A pre-LNA attenuator was incorporated into the post-LNA automatic gain control attenuator and a 0.9 dB sensitivity improvement was realized; furthermore, replacement LNAs with a lower noise figure have been identified. These new LNAs will result in a further sensitivity improvement of 0.8 dB. A replacement HPA has been identified for ALCOR's Varian 146N Twystron. This candidate tube is a Varian VKC-8313 Extended-Interaction Klystron (EIK). With appropriate modifications to the transmitter subsystems a 1.25 dB sensitivity improvement could be realized by operating at 4 MW. Additionally, the EIK will support increasing the system PRF to 400 Hz, with the potential of going as high as 600 Hz.

## References

- [1] Roth, K., M. Austin, D. Frediani, G. Knittel and A. Mrstik, "The Kiernan Reentry Measurements System on Kwajalein Atoll," Lincoln Laboratory Journal 2:2, pg. 247 (1989)
- [2] Rejto, S. B., Personal Communication

# **95 GHz Sensitivity Improvements at the Kwajalein Missile Range<sup>1</sup>**

**J. C. McHarg and R. F. Lucey Jr.**  
**MIT Lincoln Laboratory**  
**Lexington, MA**

## **INTRODUCTION**

The Millimeter Wave Radar (MMW) is a Kwajalein Missile Range high resolution instrumentation radar located on the Kwajalein Atoll in the Republic of the Marshall Islands. It is operated under the scientific direction of MIT Lincoln Laboratory in support of the US Army Kwajalein Atoll. It was originally built in the early 1980's and was designed for two-frequency operation, full monopulse at 35 GHz and range-only at 95 GHz. These frequencies complemented existing radars on the site and provided data to support two major mission areas. The first, reentry vehicle tracking and signature data collection, is a long-standing mission area for most of the site instruments. The second, detection and imaging of orbital objects, has increased in importance over recent years.

As a part of its original suite of capabilities, MMW collected 95 GHz data in both principal and orthogonal polarizations. (MMW radiates a right-hand circular polarized signal.) This data is available on a pulse-by-pulse basis and can be used to track a target's range. The 95 GHz portion of the radar has its own signal upconverter, driver amplifier, final power amplifier and millimeter-wave receivers. However, due to limitations of the IF hardware and the digital signal processing, either 35 GHz or 95 GHz data, but not both, can be collected on each pulse. The original design relied upon conventional rectangular waveguide for the feed structure and high-power transmit paths. Because of the relatively high loss in these paths, with its resultant impact on noise figure, there was little incentive to use cooled receiver components. The original design for the 35 GHz system was implemented in rectangular waveguide as well, but the smaller waveguide loss at this frequency allowed cryogenics to be used effectively to reduce the receiver noise figure still further.

As a result the early sensitivity values at the two frequencies showed a wide disparity. The sensitivity of the 35 GHz system originally was about 17 dB. (Sensitivity is defined as the single pulse signal-to-noise ratio on a target of 1 square meter cross section at a range of 1000 km and an elevation of 30° through a clear weather atmosphere.) This was sufficient to allow tracking and signature requirements to be met on targets of interest significantly before and throughout reentry and it also allowed data collection on a variety of near-earth orbit space objects. In contrast, the 95 GHz system displayed a system sensitivity almost 20 dB lower, yielding usable data for only a portion of reentry and preventing data collection on any orbiting space object.

Since MMW was first declared operational, several upgrades have been installed to improve the functioning of the 35 GHz system. Some of these upgrades provided benefits for the 95 GHz system as well, but by the late 1980's, the gap between the sensitivity figures had widened

---

1. This work was sponsored by the Kwajalein Missile Range, U.S. Army Kwajalein Atoll, Department of the Army under Air Force Contract F19628-95-C-0002.

and it was clear that few data users would ever be willing to forego 35 GHz data in order to collect even a small amount of 95 GHz data, unless the 95 GHz performance could be radically improved.

A presentation before the 1994 Space Surveillance Workshop [1] detailed a project to improve the 95 GHz sensitivity, including its justification, goals and early development. At that time the system was soon to be installed at MMW. This paper details additional work that was not available as of the first paper. After a brief summary of the project, the topics covered here are cryogenic system reliability and performance, extensions to the quasi-optic design used at 35 GHz and current operational characteristics.

## THE 95 GHZ SENSITIVITY UPGRADE

As detailed in [1], the 95 GHz sensitivity upgrade was based on a successful sensitivity upgrade at 35 GHz. In that project, the 35 GHz rectangular waveguide feed was replaced by quasi-optical components which were designed to allow free-space propagation, using curved mirrors to periodically compensate for the effects of diffraction. Along with the reduced feed loss, this upgrade showed improved power handling and excellent antenna sidelobe performance. The 95 GHz sensitivity upgrade, shown in the block diagram of Figure 1, was designed to bring these benefits to the 95 GHz system.

The reduced loss of the beam waveguide was crucial to the 95 GHz sensitivity upgrade. Not only did it directly improve the system sensitivity, it made improvements in the receiver noise figure more effective. Thus the project replaced the original room-temperature receivers with cryogenic counterparts. Two factors argued in favor of this approach. First, the experience gained in the operational use of the original 35 GHz cryogenic system could be used to improve the design of the 95 GHz cryogenics. And secondly, the very low loss of the quasi-optical feed allows larger noise figure gains to be realized by the introduction of cryogenic components.

One additional improvement to the 95 GHz system rounds out the sensitivity upgrade project. The original system design specified the peak transmitter output power at 6 kW. This was never achieved, especially for the wider bandwidth radar waveforms, mostly due to inadequate drive levels to the final power amplifier. So the current project has solved this problem by replacing the old intermediate power amplifier with a more modern design. The new design relies on Gunn diode technology to provide unconditionally stable operation at higher power levels, while improving the reliability and eliminating water cooling.

Shown also in Figure 1 is the 95 GHz upconverter, a subsystem which was non-functional at the start of the project and was to be restored. However, it was found that defective components could not be economically returned to the required specifications, so the entire subsystem will be replaced in the near future.

## CRYOGENIC SYSTEM

One major concern with the plan proposed in 1991 was the reliability and maintainability

of cryogenically cooled receiver components. To this end, several design specifications were made to improve on the experience gained with the 35 GHz radar system.

Foremost among these addressed cryogenic system failure in the middle of a mission. Failure of the cryogenic receivers must not be allowed to prevent radar operation. For this reason, the procured 95 GHz system was required to operate at room temperature, even without cooling. This was achieved, though the noise figure degrades considerably. This can be attributed to two factors. First, the majority of the receiver noise contribution is due to the resistive loss of the front-end mixers, the magnitude of which is relatively independent of temperature. The noise added by this loss, though, is directly proportional to the temperature of the mixer diodes. This effect is expected to increase the receiver noise figure by 2.4 dB at room temperature (total cryogenic failure). The second important noise contribution is due to the noise temperature of the IF amplifiers that follow the receiver mixers. The noise figure of these units have been experimentally determined to be 0.5 - 1.0 dB worse at room temperature than at 20° K.

Degraded but stable room temperature operation is only one aspect of reliability designed into the new 95 GHz system. Also important is the ability of the cryogenics to recover from a power outage. This multi-faceted problem was addressed by using a power conditioner to regulate the AC line voltage and a reset timer to ensure the system does not toggle on and off too rapidly. Together these units provide reasonable protection from damage for expected line conditions at Kwajalein.

Though these steps mitigate the effects of a power outage, they are only effective in extreme cases, namely extended power outages or intermittent line conditions. The key reliability factor, however, is the thermal response of the system to disturbances. Longer response times correspond to more stable operation and more immunity to disturbances. The strongest determinant of this thermal response time and also of the achievable final temperature, has been found to be the leakage rate of the vacuum vessel. Great care was taken to make the leakage of external gases into the container as low as possible. This included rewelding of weak joints, careful attention to gaskets and mating surfaces and selection of a proper waveguide seal that would be flexible enough to form a good seal, but strong enough to hold back the pressure differential between the inside and the outside of the vessel. In addition, this seal had to display low loss at millimeter-wave frequencies. The best material found to date is 0.005" polyethylene. Through these careful efforts, very low leakage rates have been attained. In addition to achieving the best cooling performance and the slowest warming rates, these efforts have made possible prolonged operation (several months) between maintenance periods. This is shown in the plot of cryogenic system temperatures taken from the maintenance log for this system in Figure 2. In fact, the current system has demonstrated an ability to operate without maintenance except during scheduled maintenance periods which occur three times each year.

## QUASI-OPTIC DESIGN

An artist's concept of the final beam waveguide configuration is shown in Figure 3. Unlike the design of the current 35 GHz quasi-optic feed structure, where the support structure could be built to accommodate the feed, the 95 GHz system had to be adapted to the existing feed structure.

This led to a design for the transmit beam path that incorporated otherwise unnecessary beam redirections and unusual beam reflection angles in order to preserve the excellent PP-OP isolation of the medium. It also meant that the receive paths must incorporate transmissive focussing elements, i.e. lenses. Lenses are not permitted in the transmit path because their loss, while small, is sufficient to cause most materials to overheat and melt. In the receive path, however, vastly reduced power levels are encountered and so lenses are permissible. Calculations indicate the dielectric lenses cause additional loss of about 0.1 dB and a 0.02 dB increase in the system noise figure. This will have a negligible effect on the radar data quality.

The quasi-optic beam waveguide was assembled in a special test frame to undergo antenna range testing prior to shipment last year. The results of these tests are shown in Figure 4. It can be seen that there is good agreement with the predicted far-field beam pattern and the design value which was based on the existing Cassegrain antenna and an edge illumination at the subreflector of -10.6 dB. In addition, the individual receive and transmit beams have been collimated to within one tenth of the beamwidth and the beamshapes of all beams are similar. Sidelobes measured on the test range were 22 dB down, showing that the launching horns and the optic elements introduced insignificant truncation effects.

Antenna range testing has validated the design procedure which was used to specify the reflective elements. The new design procedure was extended from the original method described in [2] to include a more accurate initial approximation. This reduces the time required to reach an optimum design, eliminating some iterative adjustments of the surface parameters. Also validated were design changes that were introduced to improve the performance of the individual components. This includes the designing in of non-normal incident angles to reduce or eliminate unwanted reflections, the use of relatively thick wires and vanes made necessary by the increase in center frequency and the elimination of distinct laser alignment mirrors in favor of polishing the aluminum reflector surface.

## SYSTEM TESTING RESULTS

Although the new hardware has been installed for several months, full system testing has been hampered by the lack of a final power amplifier tube. Though the project makes no changes to the final power amplifier, the existing tubes are not in operational order. Recent efforts by the tube manufacturer are not yet completed. Thus the initial installation of the 95 GHz upgrade hardware bypasses the final power amplifier. This bypass allows the radar to be operated on driver power only. The resulting output power, much reduced over the design levels, should still be sufficient to gather returns from existing test and calibration targets. This has yet to be accomplished, but results from a test target, injected into the 95 GHz receivers are very encouraging.

Other tests confirm initial results that the current output power from the 95 GHz upconverter is not sufficient to drive the receiver mixers at their recommended level. This is due to lower than specified output power from repaired multipliers and higher than anticipated losses in the distribution of that LO signal. For this reason, a new upconverter has been designed and built and is due to be installed in the near future. Bench testing indicates that LO drive levels will be significantly increased which should lead to more efficient mixer operation and better system sensitivity.

Though the current receiver noise temperature has yet to be measured, meaningful results will also depend on the installation of the new upconverter.

## SUMMARY

The 95 GHz Sensitivity Upgrade reported last year at the Space Surveillance Workshop has been successfully installed and will enter operational status once the high power amplifier is brought on-line. Cryogenic system reliability has been demonstrated and bandwidth specifications are being met. These improvements can be traced to achievement of an extremely low vacuum envelope leak rate and success in extending the 35 GHz quasi-optic design principles. Early results from the installed system show expected levels of driver amplifier output power and verify the need for an improved upconverter.

Future work is pointed towards installation of the improved upconverter, high power operation and finally system testing leading to operational status. It is hoped that these goals will be accomplished in the current year and that processed results will be available in time for next year's workshop.

- [1] McHarg, J.C., and W. D. Fitzgerald, "A Sensitivity Upgrade for the Millimeter Wave Radar at Kwajalein", Lincoln Laboratory Project Report, STK-221, Volume 1.
- [2] Fitzgerald, W.D., "A 35-GHz Beam Waveguide System for the Millimeter-Wave Radar", *Lincoln Laboratory Journal* 5, 245 (1992)

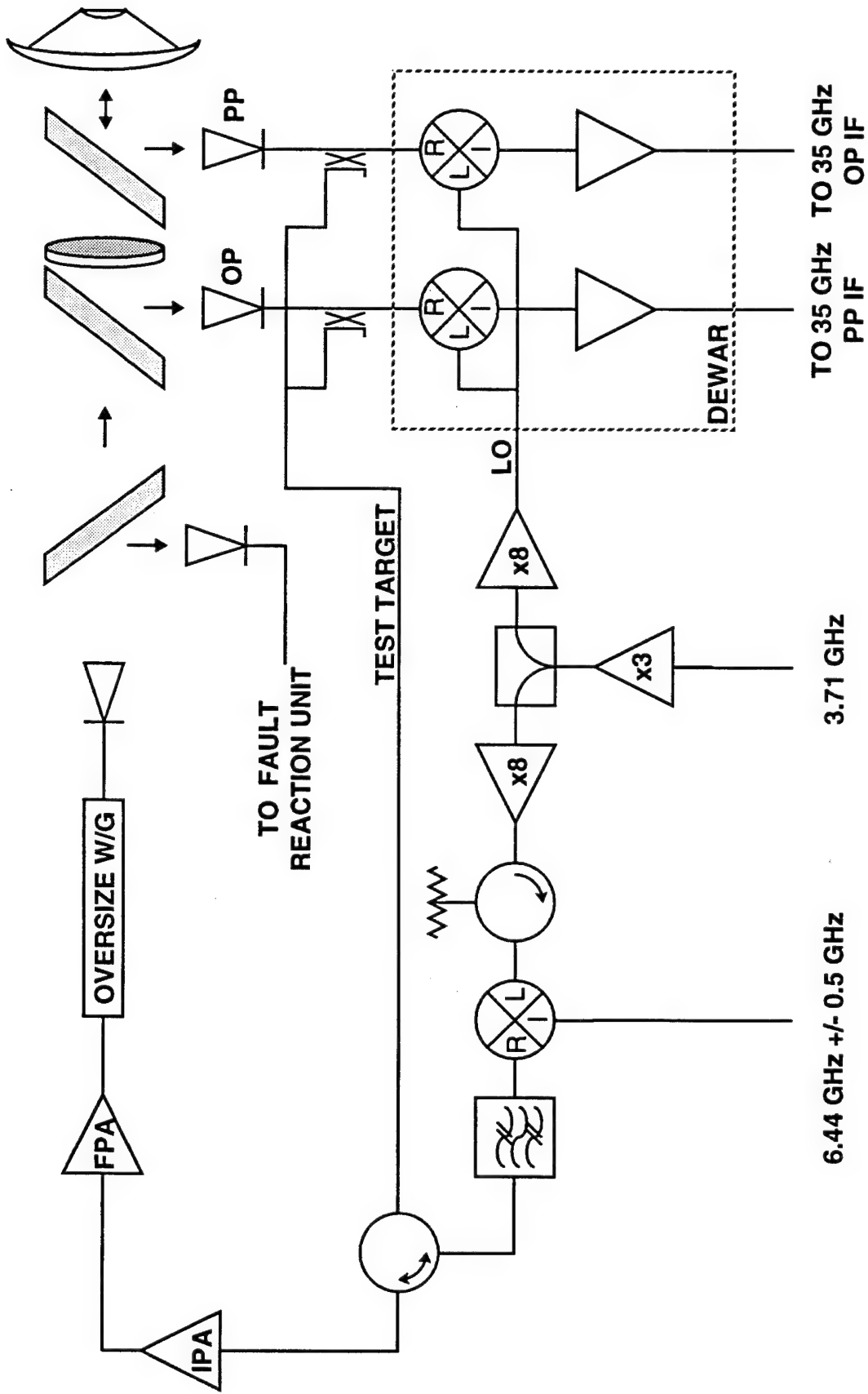


**Figure 1. MMW 95 GHz Sensitivity Upgrade Block Diagram**

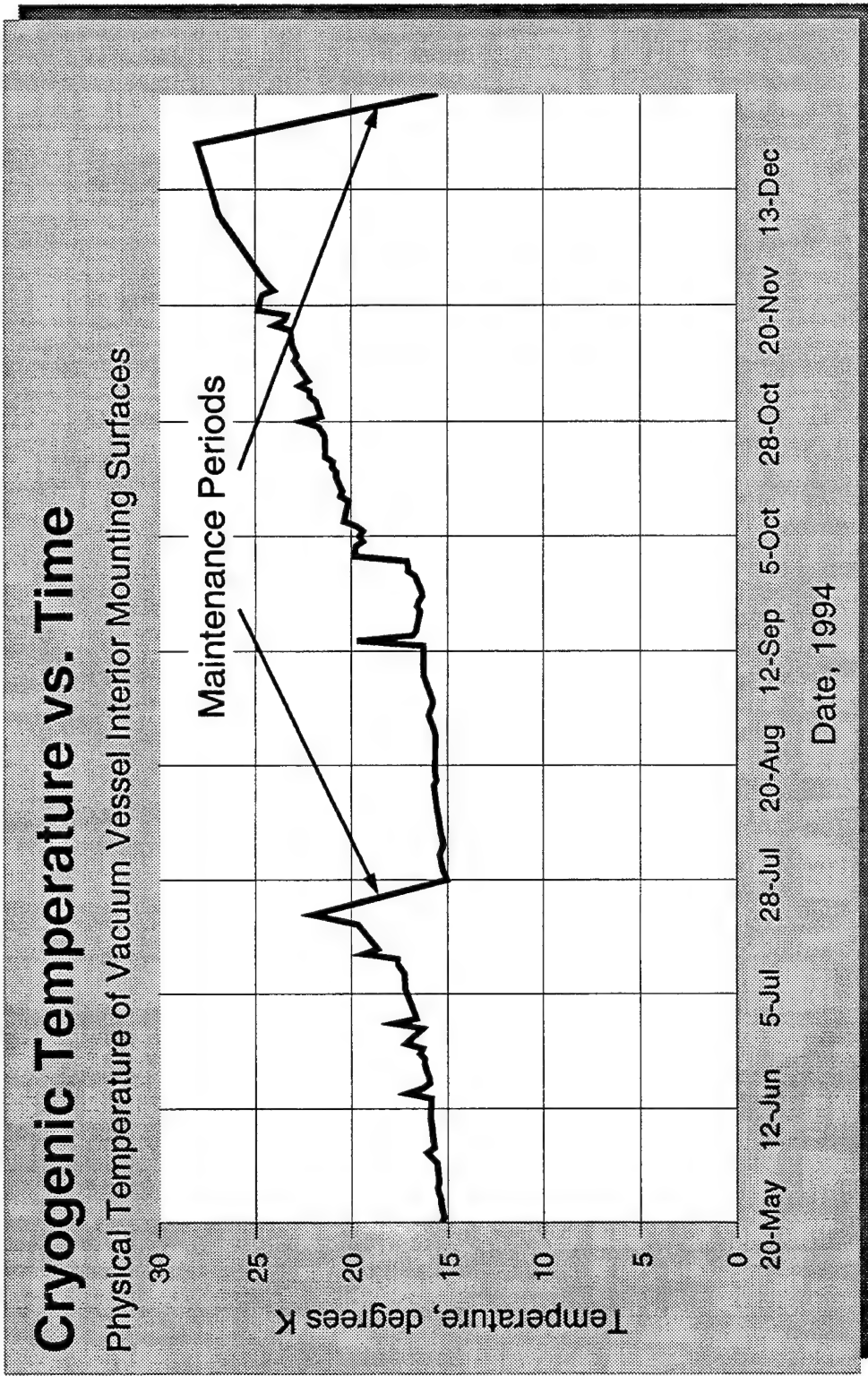


FIGURE 2. Cryogenic Receiver Physical Temperature vs. Time

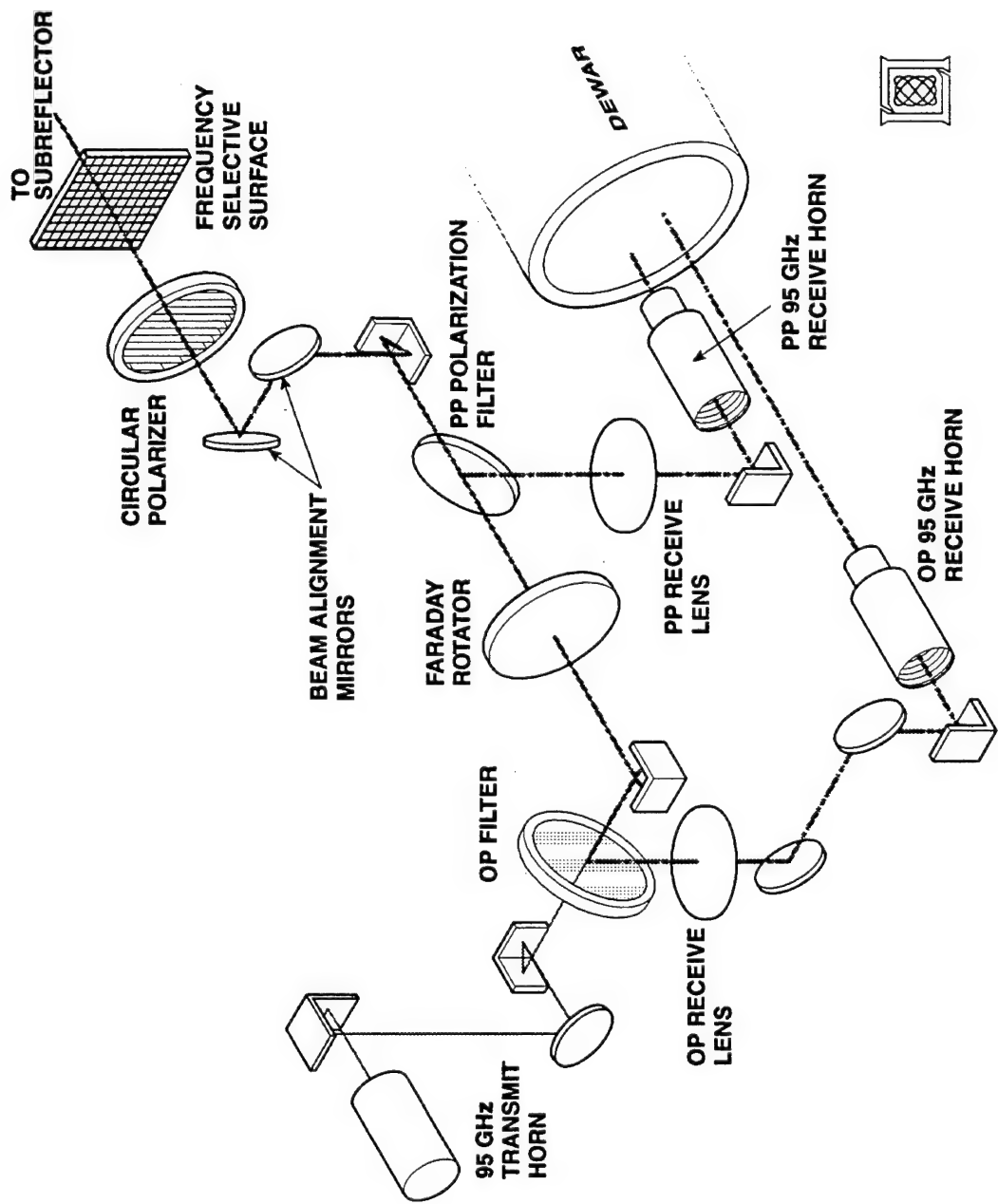


FIGURE 3. Artist's Concept of 95 GHz Beam Waveguide Layout

## 95 GHz TEST RANGE BEAM PATTERNS

Horizontal Polarization, Amplitude vs. Angle from Boresight

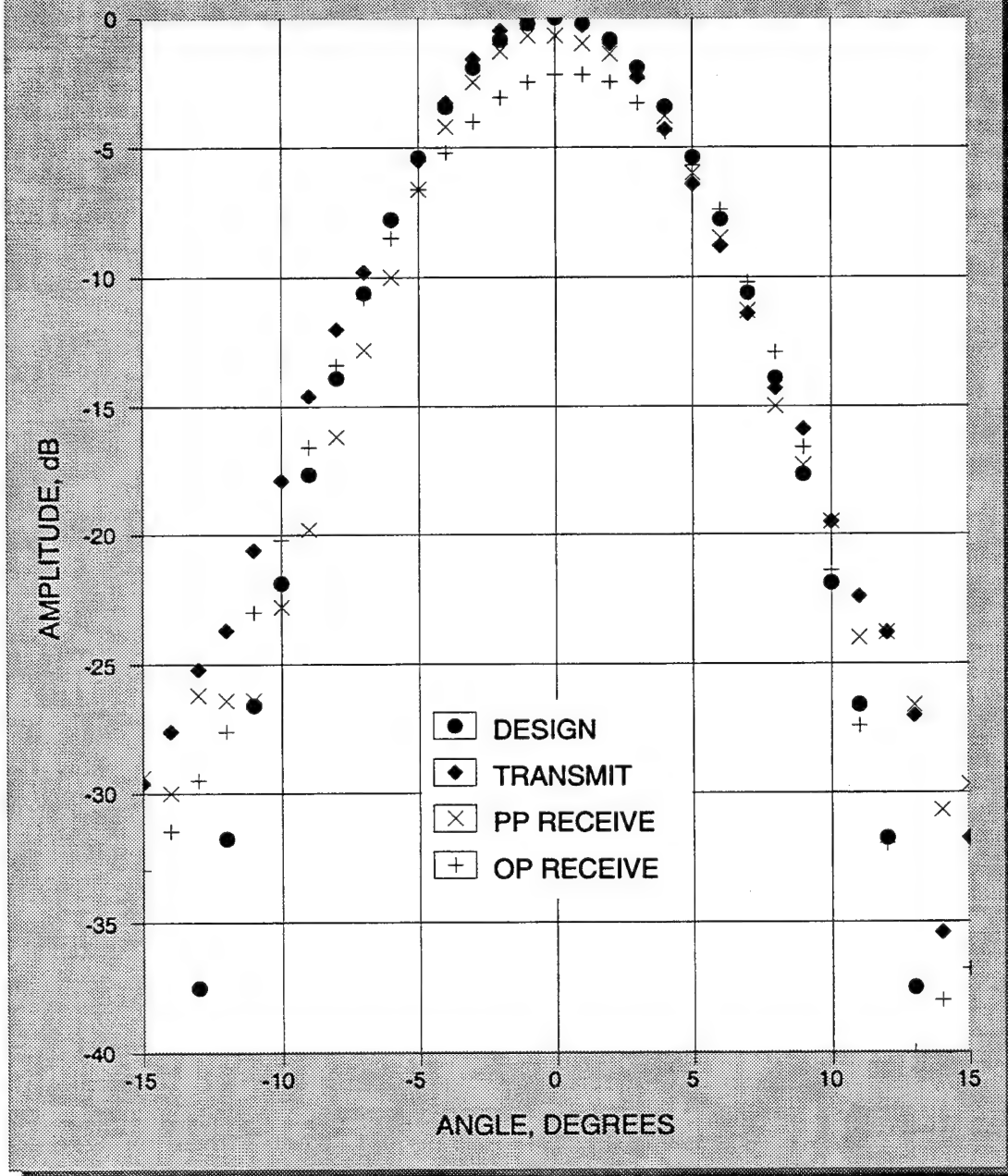


FIGURE 4. Measured 95 GHz Feed Beam Patterns

Remote Sensing of LAGEOS I/II Rotational Motion. Scientific Exploitation of Space Surveillance Techniques

D.G. Currie, K.E. Kissell, P. Avizonis, D. Wellnitz (University of Maryland)

ABSTRACT

The magnitude and the orientation of the spin vectors of the geodetic satellites LAGEOS I/II have been measured to high accuracy by the University of Maryland. These measurements exploit two different optical SOI techniques in conjunction with the 48-inch telescope at the Goddard Optical Research Facility. These measurements are performed by observing the Fresnel sun glints from the external faces of the corner reflectors which are mounted at the surface of the satellite. Repeated measurements, spread over one and one-half years, allow a critical comparison of the actual motion with dynamical models for the gyroscopic motion of the near-spherical satellite.

This behavior is due to the magnetic and gravitation torques acting upon the complex internal structure of the conducting bodies of these satellites. By comparison with computer-based simulations of the dynamical history of the rotation vector, one may address questions of the internal thermal and electrical properties of the primary components of the assembled satellites.

This measurement program is in scientific support of the LAGEOS III experiment, a joint NASA/ISA/USAF project to determine the gravo-magnetic vector coupling constant as predicted by the theory of General Relativity.

EXECUTIVE SUMMARY

A series of ground-based measurements to precisely determine the spin orientation of the LAGEOS satellite are described. This explanation is in the context of our scientific objectives. However, the approach is of direct application in Space Object Identification, to determine the health of a satellite, and to quantify changes in state or in operational characteristics of a satellite.

We will address the science background, the scientific objective, and the science requirements of the LAGEOS III Lens-Thirring Experiment (LIII-LTE) which forms the context of our Photometric Rotation Vector Measurements (PRVM). Thus the PRV measurement has been accomplished by the method of collecting "glint" photometric data and the analysis of the solar satellite glints in an appropriate geometric structure. The analysis of these data yields a determination of the spin axis of the satellite. The data collection is accomplished primarily by the University of Maryland Photometric Automatic Guider System (PAGS), a high-speed, auto-tracking, photon-counting photometer developed at the University of Maryland. This system has been used on a variety of telescopes for such diverse applications as Interferometer auto-guiding, balloon telescope auto-tracking, target stabilization, spacecraft signatures and to obtain telescope tracking parameters for input to a Kalman filter. Time-tagged video recording of the glints are sometimes used to supplement the PAGS.

SCIENTIFIC OBJECTIVE AND BACKGROUND

The overall science objective of the current project is to measure the magnitude of the Lens-Thirring effect. This is a predicted General Relativity effect describing a "gravo-magnetic" effect, that is, the vector part of the gravity field of a massive rotating body. This is also referred to as the "frame-dragging" effect. To date, this very difficult measurement has not been made, and it has been the subject of a twenty-year project at Stanford University (currently denoted Gravity Probe B). We describe briefly a new experiment, using the LAGEOS geodetic satellite in a concept due to Ignazio Ciufolini, working in conjunction with the Italian Space Agency, NASA, and the USAF. Its actual conduct is not yet approved, but its feasibility is enhanced

by the SOI application described in this paper.

#### SCIENTIFIC APPROACH TO THE LIII-LT EXPERIMENT

In essence one needs a gyroscope which interacts with the gravitational field of a rotating body to sense the LT effect. Either a physical gyroscope in a satellite (the GPB experiment) or the gyroscope formed by the orbit of a spacecraft (the LIII experiment) could suffice. For LIII, there are many challenges but two main challenges which we shall discuss.

The LT effect causes the spacecraft orbit to precess in the inertial frame by a few thousandths of an arc second per year, over and above any other secular orbital perturbations. The current regular observations by the NASA Laser Ranging Network measures such motions with a very good signal-to-noise ratio. For a perfectly spherical earth, one could consider the direct measurement of this orbital motion. However, for a nonspherical earth, such that the  $J_2$  term plus higher moments have significant value, there will be an additional classical precession of this orbit which is almost three orders of magnitude larger than the general relativistic effect. To address this problem, the LAGEOS III Lens-Thirring experiment proposes the launch of the new LAGEOS satellite (LIII) to be placed in a congruent but supplementary inclination orbit as compared to LAGEOS I. The effects of the LT precession and the classical ( $J_2$ ) precessions are then opposite in sign. Thus the two effects may be independently evaluated and numerically subtracted to arrive differentially at the LT effect.

The second effect which will degrade the accuracy of the measurement is the "photon thrust" or momentum imparted to the satellite due to emitted thermal photons. A deviation from spherical symmetry is caused by asymmetrical heating of the spherical LAGEOS satellite. This known non-gravitational force affects the orbit at the level of many thousands of kilometers over the lifetime of LAGEOS. It thus significantly compromises the accuracy of the measurement of the Lens-Thirring coefficient. This photon thrust is caused by the heating effects of the visible radiation from the sun and the infrared radiation from the earth. This asymmetrical heating of the satellite is in a manner which depends upon the orientation of the satellite with respect to the direction of the sun and with respect to the direction to the center of the earth. It results in asymmetric re-radiation of the scattered or absorbed photons. The motion of the satellite thus depends upon the orientation of the spin axis of the satellite, and we must measure this orientation and understand its dynamics to control this error.

#### TECHNICAL OBJECTIVE OF LAGEOS SPIN MEASUREMENT

In order to satisfy the above objectives, one must measure the spin rate, indeed the rotation vector, as a function of time. We also must determine the appropriate dynamical model which may be used for the interpolation or prediction the motion of the axis between the direct measurements of the orientation of the spin axis. The parameters of this theoretical model may then be optimized to best describe the motion of the axis. With an appropriate model for the description, we may then define the optimal future observation program to achieve the desired accuracy for the LIII-LTE. This work is being performed in advance of the launch of LIII, using both the LI, launched in 1976, and then LII (launched in 1992) spacecraft.

Thus we seek additional data for a better evaluation of the physical basis of the dynamical model, of the parameters which describes the physical structure of the satellite and the proper initial conditions of the motion of the spin axis. This will allow us to establish the time interval over which the predictions of the model may be considered sufficiently accurate for the Lens-Thirring measurement and for operational use in the measurements to extract new predictions.

## TECHNICAL APPROACH OF LAGEOS SPIN MEASUREMENT

The analysis of the laser ranging data from the GSFC network can give only indirect knowledge of the orientation of the spin vector [Rubincam, 1990], i.e. about  $\pm 20^\circ$ . This result is highly dependent upon a complete theoretical knowledge of the dynamical behavior and has an uncertainty which is too large to be useful in the LIII-LT experiment. Indeed, by design choice, the laser ranging data is indifferent to both the magnitude and direction of the spin.

The photometric glint measurement by the University of Maryland is achieved by the detection and timing of the Fresnel reflection of the sun from the faces of the corner retro-reflectors on the rotating spacecraft. This is followed by a detailed analysis of high speed photometric data record and the geometry of observation.

## DESCRIPTION OF LAGEOS SATELLITE

The LAGEOS is a dense spherical satellite. It has numerous prismatic corner retro-reflectors, arranged in twenty bands about the axis of symmetry, which is the nominal spin axis. In general there are a different number of reflectors in each of the different rows or bands. The moments of inertia were chosen so that the band configuration is symmetric about the preferred spin axis. They are also mirror symmetric north and south of the spacecraft rotational equator. Uncertainties exist in the moments of inertia, the details of the surface reflectivity and absorbtivity and of the internal thermal and electrical conductivity (i.e. connectivity) of the external body of the satellite leads to difficulty in the models. The nominal locations for all the prisms in body latitude (Table 1) and longitude are known, but the precision of prism alignment is not. Overall the spacecraft seems smooth and more-or-less uniform, difficult to study without help from telemetry, which of course it has none.

## OBSERVATIONAL PROCEDURE

The challenge to measure the spacecraft rotational dynamics by passive optical remote sensing is not without precedent, however, since the dynamics of earlier artificial satellites and even asteroids have been studied by both radar and by photoelectric photometry [Bent, 1967], [Kissell, 1968], [Binzel, et al., 1989].

In the case of asteroids one depends upon asymmetry of shape and non-uniformity of surface albedo (optical reflectivity) to yield a distinct scattering function which rotates with such irregular kilometer-size objects. Manmade spacecraft in rotation are much easier since they often have geometrically regular surface elements (windows, solar panels, antenna booms) which will yield regular reflections of short duration when a normal (vector) to the surface element is coincident to the bisector of the angle formed at the spacecraft by the line to the sun and the line to the observer. This is illustrated in Figure 1 for the case of LAGEOS where the spacecraft is shown in a simplistic fashion with some of the belts of corner prisms (426 prisms in all).

The compact size of the LAGEOS spacecraft makes exceedingly difficult the use of established radar techniques. The many regular recesses in the surface do provide scattering centers for incident microwave energy, but the corner reflector recesses are only some 4 cm in diameter and perhaps 3 cm in depth. The Millstone UHF and Haystack X-band space surveillance radars can infer spin rates, at least in the early days of high spin, due to subtle signal periodicities or to Doppler broadening in the backscattered energy. It proves to be easier to use optical photometry when the spinrate becomes low. This is in part due to the relative ease of +7 to +8 stellar magnitude glints produced by Fresnel reflections from the optically flat outer surfaces of the 3.8-cm

diameter fused silica prisms.

Armed with a map of the corner-prism locations, particularly the number of reflectors in each of the latitude belts, the identification of a belt can be made by recording lightcurves of long-arc transits. Four to eight belts can be detected. Photoelectric observations of LAGEOS I by the Canadians at the St Margarets site in 1976, some months after launch, showed that individual prism belts exhibited characteristic patterns of glint brightness so that the latitude could be identified by simple numbering of the glints between anomalies. This has worked on a number of other spacecraft with reflective structure, e.g., the early PRC spacecraft, two of the UK cosmic ray satellites, and two Canadian ionospheric sounders. The progression of the glint source from belt to belt is easily followed. How then do we infer the spin axis as well as the spin rate? The spin period, except for a small synodic correction, comes directly from the data. The spin axis can only be obtained from the observation of multiple bands on a single transit or, better still, observations on successive transits so that the observation geometry is quite different.

The reflected beams from the prism array can be thought analogous to those from a heliotrope onto a wall in a ballroom, tracing out multiple pencils of sunlight onto the surface of the earth. At a typical range of 6000 km the diameter of the circular to elliptical beam at the earth-based observer is some 53 km in diameter. The duration of the glint is mostly determined by the LAGEOS rotation rate and will be about 1/1000 of the rotational period.

At the instant the observer finds oneself in the center of a glint pencil (or a burst of glint pencils), and if one knows which prism belt (latitude) produces the glint, it is straight-forward that the pole of the spacecraft rotation lies on the small circle on the celestial sphere which lies at the co-latitudinal distance from the spot on the celestial sphere which corresponds to the sun-to-satellite-to-observer angle bisector at that instant. This small circle represents the locus of all possible spin-axis locations. Only if a second burst of glints is observed on the same satellite pass, also of an identifiable belt latitude, can we construct a second locus of pole positions, one which will intersect the first locus at two equally possible spin-axis positions. If a third or fourth belt can be evidenced, and the measurement errors are small, only one of these poles will prove unambiguous. Such loci are shown (in a Mercator-like projection) in Figure 2A and where three glint bursts were seen on each of two successive passes. The correct choice for a solution is seen to lie near RA-90 and Decl. -75. Figure 2B shows a fitted solution at RA-88.7, Decl. -76.8. The solutions will be improved by the greater number of glint trains observed, by new and independent observations on the next satellite pass, and by observations on succeeding days.

Since it is known and expected that the spin axis will precess with time, it is desirable that new measurements be made every few days or weeks to map out the trajectory of the spin momentum vector. When this was done for other spacecraft, it was sometimes surprising to find that the spacecraft were spinning in a slightly unbalanced mode, i.e., there was a slight wobble (0.3 to 1.2 degrees) due to manufacture or deployment anomalies not considered in testing. Too little data exist on the L I and L II spacecraft to see if the spin is precisely on the dynamic figure axis. This axis is an internal one, due to a brass cylindrical core, not an external one. We shall have to see the data, but there is no reason to expect a spin anomaly if all of the corner prisms remain intact and in place.

#### MARYLAND MEASUREMENTS OF LAGEOS I

Over the sixteen years between the LAGEOS I launch and a set of data collected over 158 days in 1992, the spin rate dropped from about 100 rpm to 0.5 rpm.

At present, the spin rate is so low that there will be no certainty that even one prism face will be seen in a belt as the sun-observer geometry moves the phase-angle bisector over a belt. The spin rate has been dropping by a factor of two every 2.5 years. If this applies to LAGEOS II, its rotational period should now be longer than one second.

#### HOW WERE THE MEASUREMENTS MADE?

##### Method I

The University of Maryland Photometric Automatic Guider System, a photon-counting quadrant detector using an electron bombarded silicon array, is mounted at one of the Coude ports of the 48-inch Telescope located at the Goddard Geophysical and Astronomic Observatory, associated with the Goddard Space Flight Center. Using tracking data from the Goddard network, we convert to pointing vectors and use the telescope to track the satellite, keeping the target within the 70 arc-second field-of-view at the PAGS, detecting the changes in brightness or glints due to solar reflection. In principle, one will see many flashes for each band. One then has a blank period in passing from one band to the next and then another family of flashes, at a slightly different rate due to a different number of corners which present during a given rotation. Time resolution of this system can be up to 0.1 msec.

##### Method II

Brightness data are collected and recorded at standard video frame rates (RS-170) using an intensified SIT camera (Xybion Model 750) located atop the tracking telescope with its own 30-cm telescope. Time resolution cannot be better than about 30 msec and sensitivity improves when the flash duration exceeds about 5-10 msec.

#### Analysis

Six data sets are presented here, in detail, collected from early April to September 1992, along with preliminary but very interesting data extending to mid-1993. The use of a combination of graphical and analytical was required, and spline fits of the data collected at irregular intervals. It is important to note that a unique solution is not always found for the spin axis. To resolve this, some a-priori knowledge of the satellite's motion is used. Namely, solutions are limited to the southern declination because LAGEOS-I was launched with a southern-hemisphere orientation of its axis (Slabinsky, University of Maryland Workshop), and all theoretical models [Bertotti and Iess, 1991], [Habib, et al., 1995] indicate that it should stay in or near the southern hemisphere.

Data taken on the night of April 6, 1992 provide unique confirmation of the earlier stated assumptions. From pass 1 (Figure 2A) it is clear that two possible solutions exist, as is the case with pass 2. Since the two passes were consecutive and occurred within hours of one another, we could safely assume that the orientation of the spin axis would not change dramatically. Co-plotting the light curves from the two passes shows that there is only one such stable solution. The results of the pole position measurements are provided in Table 2.

Since consecutive passes generate constraint curves that are highly parallel, special care is taken in the analysis of the intersections as well as a new definition of the error. The highly parallel curves often do not offer any new information as to the pole position due to their highly variable intersection (a more detailed analysis is offered later in this paper), and thus are de-selected as data points. On the other hand, bursts that are well separated in the pass (i.e., first and fourth) tend to have large intersection angles and generate less divergent spin axis positions. Once the proper data

points are selected, the pole position is found by the average position, and the error is found as on-track and cross-track error. It is expected that the intersection will occur along the constraint curve, so it is more reasonable to expect the points to intersect in some volume that is distorted along the constraint curve. This is done by assuming, to first order, that the intersections all occur along a line (on-track). To find the on-track and cross-track errors, the points are first fit to a line, then de-rotated by the angle defined by the slope, then the spread is found by calculating the standard deviation of the mean in the de-rotated coordinates, then rotated back. The result is an error lying on an average light curve and an error perpendicular to the curve. This error may also then be projected to the RA and DEC axis (Figure 2B).

Analyses of data from June 10, 1992 plus June 13, 1992, were treated in a similar manner as that of April 6. That is, that we believe the pole to be stable over a period of a few days. By superimposing data from the two passes sets, it is clear which of the solutions should be chosen as stable. Once this information is discerned, the points were dealt with independently.

July 29, 1992 and September 1, 1992 provided very strong data points, in that many (eight and nine respectively) sets of flashes were observed, thus providing a good base of constraint curve intersections to work with. This resulted in firm solutions, since all of the curves for a given pass only intersected in one region.

Figure 3 shows the solution area for each data set in greater detail.

#### PHOTOMETRIC DETECTION SYSTEM (PAGS)

The PAGS is a four quadrant photon-counting detector system. It has a maximum count rate of 10,000 counts/sec. For the current observations, it has been used with 500 and 1,000 counts/sec. Its capability will be discussed shortly under the examples.

#### INTERFACE BETWEEN PAGS AND THE TELESCOPE

In tracking various satellites in general, in order to control the telescope pointing, the PAGS creates a telescope pointing error signal. This signal is used by the telescope control computer to correct the orbital elements. This is entered into a Kalman filter in order to provide the most stable pointing information.

#### METHOD OF ANALYSIS

The method by which the spin axis may be determined may be considered first in an ideal fashion. Thus let us consider a satellite with only the single equatorial row of corner reflectors. Thus when we receive the light from this set of corner reflectors, whose spaces are normal to the spin axis, and we know the direction to the satellite and the direction to the sun, we have established a direction which must be normal to the spin axis. Thus we have a constraint on the spin axis but no actual direction.

Now consider the measurements on successive bands. As the satellite progresses across the sky, the family of normals constrains the spin axis to be in a specific direction. However one portion of this constraint is obviously much stronger than the other. Thus we shall have an error ellipse rather than an error circle.

Finally, the identification of the bands is more subtle since there are four bands near the equator with the same number of reflectors. Thus it requires passage over a number of bands to make a concrete determination. For a pass from low elevation to low elevation through a high elevation we may get eight

bands which performs an effective determination. Smaller number of bands result in more ambiguity, or data which must be combined with a pass taken on a nearby night.

#### CURRENT RESULTS FOR ROTATION VECTOR MOTION

We now present the results of the 1992 measurements. In Table 2 we list the date, the coordinates and the errors for these observations. Thus, in Figure 4A the actual observations, described in Table 2, are shown with a spline fit connecting the observations. The individual errors, in the form of error ellipses from Table 2 are also included, although they are too small to be seen clearly on this scale.

In Figure 4B, a different presentation of our data shows more clearly the motion or kinematics of the rotation vector. In particular, we wish to illustrate the velocity at which the spin axis is moving. Thus we indicate, with square boxes, the positions that the spin axis would occupy every tenth of a year. The spline fits to the RA and Dec as a function of time are used to develop the representation of the direction of the spin axis every 36 days. In order to illustrate the complex dynamical behavior, we have included additional observations made during the following year. These data have not yet been completely reduced to establish proper error bars. However this curve generally shows the very interesting behavior in which the motion of the spin axis continues to move smoothly for several months, then essentially stops and then starts up again in roughly the same directions.

The position and evolution of the spin axis are roughly consistent with Bertotti's and Reis' theoretical statements that the spin-axis should move around the pole with a period of a couple of years, though there is disagreement with their models as to the amplitude of that motion. Clearly, more data would add greater detail to our picture of the polar motion and assist the improvement of the theoretical models.

#### CONCLUSIONS

We have exercised a method of directly measuring with high accuracy the spin-axis orientation of the LAGEOS-I satellite using solar glints from the front surfaces of the corner cube reflectors. This same analysis may be applied to other LAGEOS-like satellites. The present results should be combined with an analysis of older data from archival observations. Such additional data points may then be used to refine theoretical models being developed for future relativity-testing satellites. These models should then be tested on data collected from LAGEOS-II, in orbit since late 1992, since it now has a reduced spin rate which may be measured.

#### ACKNOWLEDGEMENTS

We wish to thank the Optical Systems Branch of the Goddard Space Flight Center for use of the 48-inch telescope at the Goddard Optical Research Facility, and direct support during the early phases of the development of the PAGS, used for satellite tracking, and integrated into the telescope control system. The University of Maryland has supported the taking of these observations, the reduction of the data and supplied the required computer facilities in supporting an analysis of the data. The Los Alamos National Laboratory provided support for P. V. Avizonis as a Graduate Research Assistant for some of the observations and their analysis under 9-XG2-V4034-1.

#### REFERENCES

- Bent, R. B. Attitude Determination of the Ariel III Satellite, *Nature*, 216, 45, 1967.

Binzel, R. P., Gerbils, T. and Matthews, M. S. Asteroids II. University of Arizona Press, 1989.

Bertotti, B. and Iess, L. The Rotation of Lageos. Journal of Geophysical Research, 96(B2), 2431-2440, 1991.

Habib, et al. Phys Rev. D 50, 6068, 1995.

Kissell, K. E. Diagnosis of Spacecraft Surface Properties and Dynamical Motions by Optical Photometry, Space Research IX - North-Holland Publishing Company, Amsterdam, pg. 53-75, 1969.

Rubincam, D. The Lageos Along-Track Acceleration: A Review. Presented at the First William Fairbank meeting on Relativistic Gravitational Experiments in Space, Rome, Italy, September 10, 1990.

Table I. Corner Cube Reflector Placement on LAGEOS-I

Band Number	Lattitude (Degrees)	Number of Corner Cube Reflectors
1	90.00	1
2	79.88	6
3	70.15	12
4	60.42	18
5	50.69	23
6	40.96	27
7	31.23	31
8	22.98	31
9	13.25	32
10	4.86	32
11	-4.87	32
12	-13.25	32
13	-22.98	31
14	-31.23	31
15	-40.96	27
16	-50.69	23
17	-60.42	18
18	-70.15	12
19	-79.88	6
20	-90.00	1

Table II. LAGEOS-I Spin Axis Solutions

Date	Days From April 6, 1992	Spin Axis RA (Deg.)	Spin Axis DEC (Deg.)	On-Track Error (Deg.)	Cross-Track Error (Deg.)
April 6, 1992	0	-88.68	-77.76	0.94	0.14
June 10, 1992	85	-53.41	-77.28	1.47	0.12
June 13, 1992	88	-51.76	-77.57	0.41	0.04
July 29, 1992	114	-23.64	-80.14	0.60	0.03
September 1, 1992	148	0.17	-80.43	0.60	0.07

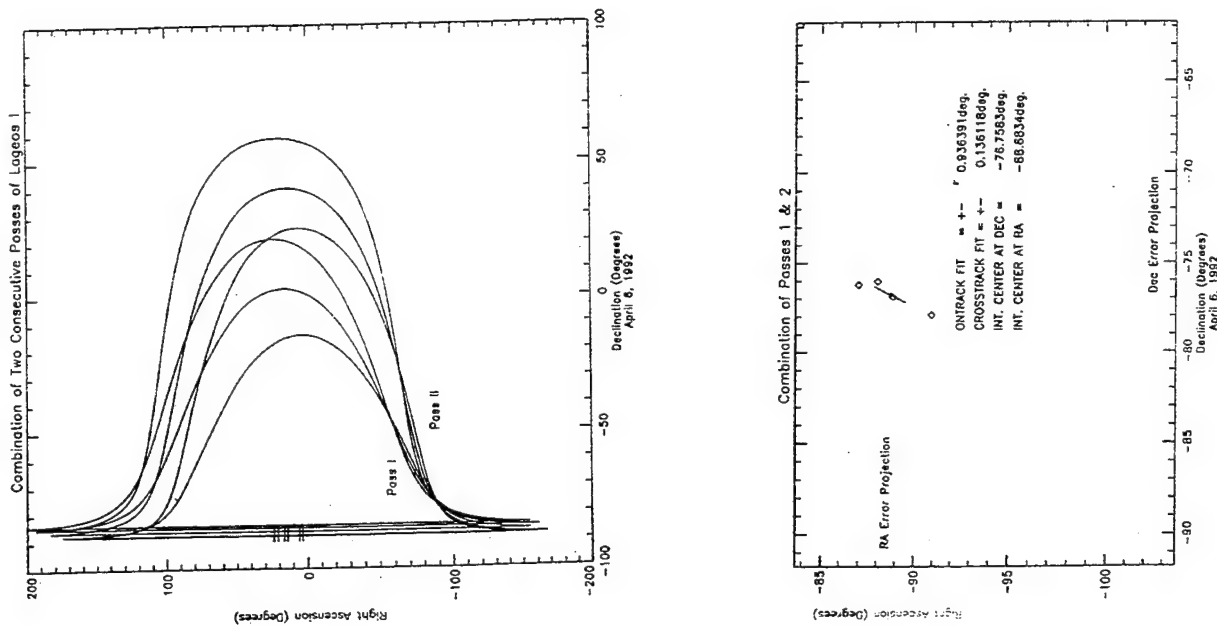


Figure 2. Combined locus curves from pass 1 and pass 2 on 6 April 1992 demonstrate the elimination of ambiguity. There is only one possible solution that satisfies this condition over few hours.

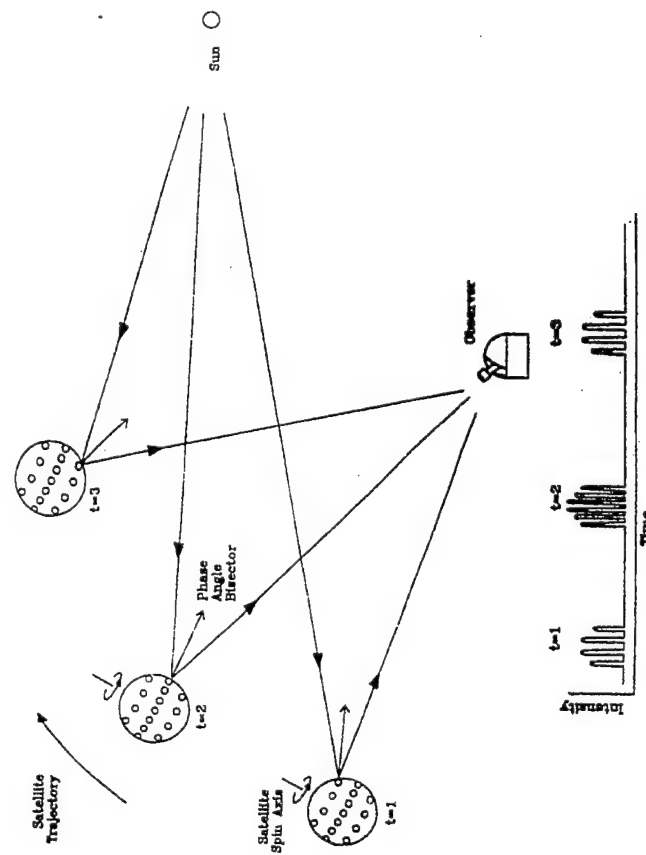


Figure 1. Illustration of spinning satellite observation. When the Fresnel condition is met, observer witness reflections from the front surfaces of the Corner Cube Reflectors. These reflections appear to be "bursts" on the light curve (bottom of figure). Ratio of frequencies of flashes within each burst identify which band of CCR's the burst is coming from.

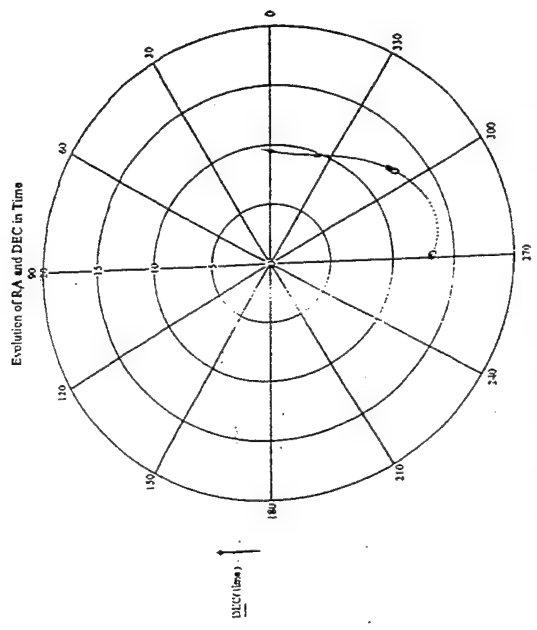


Figure 4A. Successive measured orientations of the rotation vector expressed in inertial celestial coordinates from February 1992 to September 1992

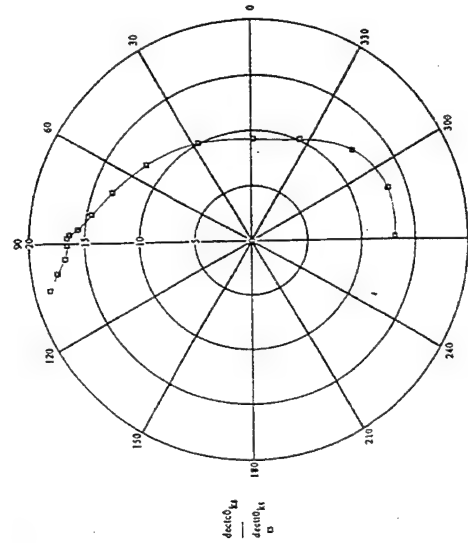


Figure 4B. Interpolated orientations of the rotation vector for every 0.1 year from February 1992 to July 1993  
 $\text{RA} = \frac{1}{160} \cdot \text{RA}_{\text{ME}} + \frac{5}{160}$   
 $\text{dec} = \frac{1}{160} \cdot \text{dec}_{\text{ME}} + 10$

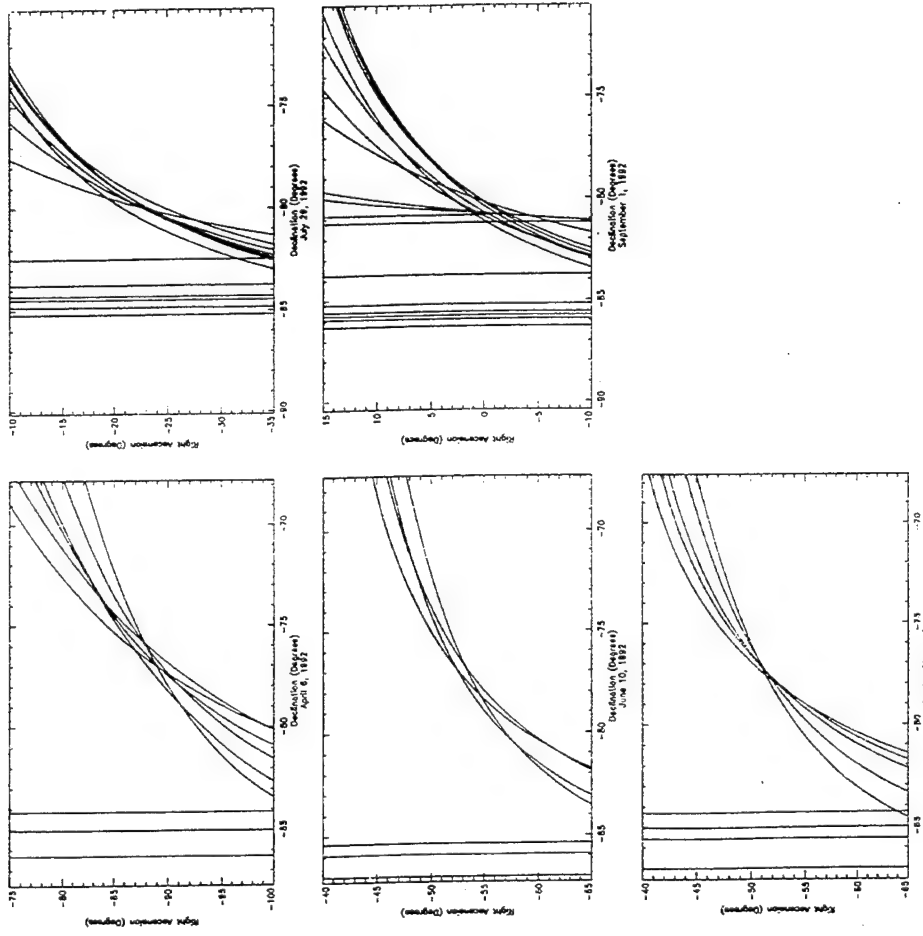


Figure 3. Expanded regions of constraint curves for all six passes  
(April 6 passes were combined to generate a single solution)

## **The Small Expendable Deployer System (SEDS)**

G. Gorski-Popiel (MIT Lincoln Labs P.O. Box 73, Lexington, Ma. 02173),  
J.J. DeLong (Raytheon RSE 200 Sparkman Drive, Huntsville, Al. 35806 )

### **Overview**

In March of 1994, NASA placed the SEDS experimental package into orbit using a Delta rocket. The SEDS experiment consisted of an electronics package, referred to as the End Mass, connected to the second stage of the Delta rocket by a 20 km synthetic fabric tether 0.5 mm in diameter. The system was initially expected to stay aloft 30 - 45 days.

In conjunction with other, globally distributed sensors, the radar assets of the Kwajalein Missile Range (KMR) were tasked to track both the second stage and the End Mass for up to 21 passes. Initial deployment of the experiment was nominal and KMR sensors achieved all mission objectives during the first four passes. On the fifth and subsequent passes the KMR sensors were unable to locate the End Mass. By then, the orbital elements of the deployed complex had undergone a significant change. Eventually a concerted search, undertaken by the KMR radars and co-located highly sensitive optical sensors, verified conclusively that the End Mass was missing. As a result NASA was able to terminate the experiment after the 10-th pass, reducing the expenses associated with planned coverage of additional passes and resulting in considerable savings.

This presentation will provide background on the SEDS experiment and review the sequence of events leading up to the determination that the End Mass had prematurely separated from the tether attached to the Delta rocket second stage. A video of the severed tether, taken by the KMR optics sensors, will also be shown.

### **Background**

SEDS was a NASA mission sponsored by the Space Science Branch of the Solar System Division at NASA's Johnson Space Center. SEDS was to study the behavior of tethered objects in earth orbit. Such systems may be used on Space Station Freedom (SSF) to precisely de-orbit

short-lived experiments or hazardous waste. The technology may also be used to isolate, outside the SSF, hazardous substances when not in use.

The SEDS experiment was carried aboard the second stage of a Delta II Launch Vehicle which was launched from Cape Canaveral on 10 March 1994. A world wide network of radars and telescopes was to participate in the data gathering. Major objectives were the determination of time-dependent profiles of altitude, position and velocity, the identification of tether aerodynamic effects, second order trajectory deviation dynamics influenced by a trailing tether and the establishment of impact coordinates.

### **Experiment Description**

Slightly over one hour after launch, the second stage of the Delta rocket reached its tether deployment position. The SEDS "Spinning Reel" deployment system was activated and the End Mass was released downwards, directly towards the center of the earth. The tether was a non-conductive, synthetic fabric less than .5 mm in diameter and 20 km long. At its midpoint a 100 element set of C-band dipoles was to be embedded. The elements, each 2.5 cm long, were spaced at about 10 cm intervals. The peak C-band cross section of the dipoles was expected to be between -5 and -10 dBsm.

The End Mass package measured approximately 20 \* 40 \* 33 cm, with a 50 cm corner reflector on its bottom. It had an aluminum exterior and contained sensors as well as telemetry and a C-band beacon. Average C-band cross sections were predicted by NASA to be +20 and -10 dBsm, for the Delta second stage and the End Mass respectively. Peak End Mass cross section was expected to reach +10 dBsm.

NASA initially requested the support of ALCOR, a 2.25 MW of peak power, 40 ft dish C-band radar with beacon tracking capability to provide 30 seconds of precision metric data on each object (the Delta second stage and the End Mass) on each pass covered. It was further requested that both objects be tracked simultaneously whenever possible. Up to 21 passes were expected to be supported. In addition four selected passes required mandatory participation by Beal, Eldorado, Robbins, Eglin as well as KMR to collect data on the same orbit.

After a detailed examination of experiment specifications, KMR expressed some concerns to NASA about its ability to satisfy all objectives with ALCOR alone. With its 5.2 milliradian beamwidth and the geometry of the deployed complex, ALCOR's ability to track both objects simultaneously, was restricted to very limited periods, at elevation angles in excess of 85°. Passes of this kind were unlikely. Further, such high elevation angle trajectories would require azimuth rates at or beyond the limit of ALCOR's capabilities. Also, the expected nominal cross section of the End Mass, meant that ALCOR would have difficulties tracking it in skin mode, if the Point of Closest Approach (PCA) was 1000 km or more (a likely trajectory). Provisions had to be made for such tracking in case the End Mass C-band beacon became disabled.

Due to these considerations, NASA and KMR agreed to utilize TRADEX (L-band and S-band) also. With its wider beamwidth (10 milli radians) and higher gain, TRADEX would provide better search capability and the ability to skin track the End Mass at ranges up to 3000 km. This would cover all possible orbits of the complex. In addition TRADEX would be able to simultaneously track both objects for a number of likely trajectories. Consequently, TRADEX was to act as a complex evaluator and provide directing data for ALCOR if needed.

### Mission Preparations

Pre-mission planning covered both nominal deployment and various contingency scenarios. There were good reasons to believe that the mission might pose data collection difficulties. It was unclear how the objects would behave once deployed. The End Mass was 20 km closer to earth than the Delta second stage and it was possible that it's slightly larger drag would make it lag and perhaps induce a rotation. No data were available on the likelihood, or the degree, of this possibility. The longevity of a stable orbit for the complex was also uncertain. Pre-mission predictions gave estimates of 21 to 45 days.

To prepare for the possibility of incomplete deployment of the End Mass, a modification was added to the Real Time Program (RTP), used by the KMR mission control center (KMCC) to control sensor pointing. This modification made it possible to perform rapid searches for the End Mass along its expected deployment path. To deal with the orbit uncertainty, procedures were set up to provide latest ephemeris data as soon as it became available from Space Command. This data was transferred electronically to both the

KMCC and ALCOR. After each track, all available tracking files were to be examined for possible metric deviations and trends in orbital elements.

## The Mission

KMR's coverage was to start with the fifth revolution of the complex. By then it became known that the C-band beacon was unavailable. As a consequence, TRADEX's role as complex evaluator became crucial.

**Pass #1 (Rev #5, Rise Time 11:18:16Z, 10 March):** By this time the tether was to have been fully deployed. The objective was to verify correct deployment of the complex. Only TRADEX was to participate. The trajectory was low elevation, only 19°. Using an element set just transmitted from Space Command's Cheyenne Mountain complex, TRADEX acquired and tracked the Delta second stage. Shortly thereafter, using the offset search modification of the RTP, TRADEX acquire and tracked the End Mass. This verified that both objects were deployed nominally. However, all attempts to locate the dipoles at the tether mid-point were unsuccessful.

**Pass #2 (Rev #6, Rise Time 12:54:33Z, 10 March):** The objective of this pass was to further verify correct deployment. TRADEX again readily acquired both objects and found them to be in nominally predicted positions. Another attempt to locate the dipoles met with no success. It was later confirmed by NASA that the dipoles had not been deployed.

**Pass #3 (Rev #15, Rise Time 01:57:51Z, 11 March):** This was the first mandatory data collection track for ALCOR. It was a high elevation pass, with target elevations reaching a maximum of 80°, however PCA was less than 500 km and ALCOR easily acquired the Delta second stage. Immediately following PCA it acquired and tracked the End Mass as well. The KMR 35 Ghz millimeter wave radar (MMW) participated on this pass also, collecting high precision metric data which was transferred to Space Command via ALTAIR. Its use would enhance the accuracy of the available element sets.

**Pass #4 (Rev #18, Rise Time 11:41:51Z, 11 March):** At this point it started to become apparent that things were departing from the nominal. The most recent element set (few hours old) received by ALTAIR, showed this to be Rev # 18 even though it had the rise time and geometry which the pre-mission data associated with Rev # 21. After an initially unsuccessful search, both TRADEX and ALCOR were able to acquire and track both objects satisfying all requirements. The objects were within 450 m and 2.5 milli radians (mRs) of their predicted positions, as seen from ALCOR.

Prior to the next coverage, TRADEX received a Space Surveillance Network (SSN) tasking to track the objects. However the latest available element sets proved of such poor quality that TRADEX was unable to acquire and track the objects. As a result, using other data at their disposal, Space Command generated a new element and assigned a new catalog number to the object (referred to as the Analyst's object).

**Pass #5 (Rev #88, Rise Time 23:00:49Z, 15 March):** The fifth data collection track represented a critical pass, requiring same orbit participation of Beal, Eldorado, Robbins, Eglin and ALCOR. It was to have a nominal maximum elevation of 41°, a PCA of 496 km and be visible from KMR for 9 minutes and 35 seconds. Scans were performed around both the positions of the nominal complex and the Analyst's object with no success. Eventually, shortly after PCA, TRADEX did acquire the Delta second stage as a result of a systematic spiral scan search around the nominal position. This was a remarkable feat considering that the TRADEX beam is only 10 mR wide and the object was found 198 mR off in azimuth and 80 mR off in elevation from its predicted position. ALCOR immediately began its mandatory data collection while TRADEX engaged in an unsuccessful search for the End Mass.

The next two passes covered by KMR produced similar results. In both cases the second stage was acquired, with some difficulty, but the End Mass was never detected.

Although Beale, Bermuda, El Dorado and Robbins were reporting that the End Mass was still attached, some doubts were beginning to appear. As a result it was decided, at KMR, to make every effort to determine whether the End Mass was present. Preparations were made to systematically scan the volume of space contained in a sphere with a 20 km radius centered on the track of the Delta second stage. The next two passes

covered, concentrated on this strategy. Despite all efforts however, KMR sensors never saw the End Mass again.

In the meantime, several optical sightings of the second stage and the tether were reported. An optical observatory in Chile reported observing the Delta second stage and glinting from the end of the tether. However it could not be determined whether or not the glint was due to the End Mass. By then, most mission participants were agreeing that the End Mass was very unlikely to be still attached, but conclusive evidence was needed. On March 19, NASA ordered an all out effort to resolve the issue once and for all.

**Pass #10 (Rev, #136, Rise time: 0815:52Z, on 19 March):** At KMR, ALCOR, TRADEX, the Millimeter Wave Radar - MMW and five optical tracking telescopes (called Super RADOTS) were assigned to the task. The horizon to horizon time of the pass was 9 minutes 20 seconds. However, the available sun illumination time of the objects was only 3 minutes and 10 seconds. TRADEX was the first to acquire the Delta second stage. It transmitted directing data to the Super RADOTS. Within seconds, Optics had the Delta and the tether in sight. A systematic search downwards, by the Super Radot, along the tether located a distinctly brighter object at its end. Using the known viewing angle of the Super RADOT and its angular offset from the Delta second stage it was determined that both the Delta and the observed tether ending were well within TRADEX's beam. TRADEX's sensitivity is such that an object much smaller than the End Mass should have been easily seen. No returns were detected other than that of the Delta second stage. Therefore, it was concluded that the End Mass was indeed no longer attached. The optically bright object was attributed to light pipe effects of the terminated tether. This allowed NASA to cancel the rest of the mission and to save the cost of continued support.

## **Spectral Signatures Predicted From Detailed Satellite Models**

A. E. Prochko (W. J. Schafer Associates, Inc.), M. Culpepper, S. Durham, J. O'Hair (USAF Phillips Laboratory)

### **Abstract**

The Phillips Laboratory (PL) spectral imaging team is developing methods to extract information from hyperspectral satellite signatures to uniquely identify space objects and verify their status. These methods use the principle that the spectral signature of an object is representative of the surface materials which reflect solar light into the observer's field of view. For space object identification (SOI), PL has been conducting ground-based experiments since 1993. To enhance experimental efforts and results, PL is using computer simulations to study signature variation due to orientation, illumination conditions, and satellite configuration and materials. The simulations use codes developed by the Phillips Laboratory Satellite Assessment Center.

### **Introduction**

The Phillips Laboratory program has typically been a visible spectral sensing program for space object identification.<sup>1</sup> Although wavelength regions in the ultraviolet and infrared are being considered in more detail, only the wavelength region from 0.3 to 1.4  $\mu\text{m}$  at 10 nm resolution will be the subject of this paper. Satellite materials reflecting solar light into the observer's field of view contribute to an object's signature. Material reflectivity is a function of incident and reflected directions, wavelength, temperature, and surface roughness.<sup>2</sup> The exoatmospheric satellite signature varies with object configuration, materials, and orientation as well as illumination conditions and dynamic behavior. Illumination conditions depend on the sun-satellite-observer angle or solar phase angle and the geometry of the spacecraft, and dynamic behavior refers to anything that moves on the spacecraft such as solar panels, antennae, louvers, etc.

The PL SATellite SIGnature (SATSIG) code is used for the simulations. SATSIG generates radiometrically accurate pristine (exoatmospheric) satellite images and spatially unresolved spectral signatures. Other codes are available to account for atmospheric and sensor degradation. The satellite models are constructed using combinatorial solid geometry. Spectral reflectivity data for over 90 satellite materials can be applied to the model surfaces; many of the materials have measured bidirectional reflectivity (BDR) data (not degraded by the effects of space). Some of the SATSIG input parameters are sun and observer directions relative to the satellite (corresponding to illumination conditions and satellite orientation relative to the observer), wavelength and wavelength interval, and BDR model (Lambertian, Phong or Maxwell-Beard).<sup>3</sup> Options include earthglow, thermal blanket wrinkling, telescope gimbal method, and stabilized or rotational motion. The code may be used with an orbit generator to simulate passes over the observer or independently to take a snapshot of a particular case.

Two satellite models, DMSP and Seasat, are used in this paper. Spectral signatures are presented for various orientations and illumination conditions.

Two approaches to study the simulated satellite signatures are in progress. One is to simulate signatures of typical overhead passes, and the second is to simulate possible signal variations due to other normal and abnormal satellite operations. Simulating a variety of passes at different times of the year is used to represent typical orientations and illumination conditions. The orbital and stabilization characteristics are taken into account as seen by a ground-based observer. Actual pass scenarios for which there are photometric data will be reconstructed to verify simulated photometric values. Quantifying the signature variability will take many simulations. Other signatures than those observed during a typical overhead pass may be viewed when the satellite is maneuvering, from a space-based observer, or if the satellite is unstable. To represent these conditions, a more systematic approach to orientation and illumination conditions will be used. The systematic approach will serve to spectrally characterize the object; the variability and number of simulations needed will depend on the symmetry of the satellite.

In the field, photometry has typically been used to characterize the magnitude and color of satellites.<sup>4,5,6</sup> Plotting visual magnitude and color against solar phase angle are some of the photometric analysis techniques used to study satellite behavior. To establish the correlation between spectrometry and photometry, visual magnitudes and colors are calculated from the simulated spectral signatures. Follow-on work will determine the information content in photometric, multispectral, and hyperspectral approaches to studying space objects.

### Photometric Analyses

Equation 1 is used to calculate the satellite total radiant intensity through a filter at the range in meters between the observer and the satellite with no atmosphere.

$$E \left[ \frac{W}{m^2} \right] = \frac{1}{range^2} \int [Sat(\lambda) \bullet f(\lambda)] d\lambda \quad (1)$$

where  $Sat(\lambda)$  is the reflected intensity from the satellite in  $W/sr/10\text{ nm}$  and  $f(\lambda)$  is a standard filter transmission such as U, B or V (ultraviolet, blue or visible). To convert to traditional magnitude units, equation 2 is used to calculate magnitudes,  $m_U$ ,  $m_B$  and  $m_V$ , in a particular band.

$$\log_{10} \left[ \frac{E_i}{E_j} \right] = 0.4 \bullet (j - i) \quad (2)$$

where for  $i=0$ ,  $E_0$  is given in Table 1 for different photometric filters for a zero magnitude star above the atmosphere. Using the transmission data for each filter,<sup>7</sup> the magnitude values were calculated for the sun used in the SATSIG simulation and are listed in the table.

Table 1. UBV intensities for a zero magnitude star<sup>7</sup> and  $m_U$ ,  $m_B$  and  $m_V$  for the sun used in SATSIG.

Filter Band	$\lambda_0$ ( $\mu\text{m}$ )	Spectral Intensity ( $\text{W}/\text{m}^2$ )	SATSIG Sun Magnitudes
U	0.3534	2.87 E-9, $m_U = 0$	$m_U = -26.00$
B	0.4439	6.42 E-9, $m_B = 0$	$m_B = -26.10$
V	0.5538	3.08 E-9, $m_V = 0$	$m_V = -26.73$

For a star with  $m_V=0$ ,  $E_0 = 3.08 \text{ E-9 W/m}^2$  in the visible filter band. To find  $m_V$  for a satellite with total radiant intensity,  $E_j = 4.30 \text{ E-12 W/m}^2$ , using the visible filter at a range of 1957 km, the resulting magnitude,  $j$  or  $m_V$ , is 7.1. This is an apparent magnitude because the actual range of the satellite was used. Normalizing the magnitude to 1000 km,  $M_V$  is 5.6. The difference in magnitudes (e.g. B-V), called color, is related to the ratio of intensities  $E_V/E_B$ , so a more positive difference means that an object is redder.

## Results

Figure 1 illustrates three exoatmospheric spectra corresponding to three different orientations of Seasat. The intensities are in  $\text{W}/\text{sr}/10 \text{ nm}$ , so no range effects are reflected in the spectra. The Lambertian material reflectivity model was used to generate these spectra. Orientation 1 peaks in the blue. Orientations 2 and 3 peak in the yellow due to the Kapton on the synthetic aperture radar antenna in the model. In orientation 3, the stronger peak corresponds to the larger portion of the synthetic aperture in view. The image in Figure 2a corresponds to the spectrum of orientation 1. This is most similar to the orientation as seen from the ground

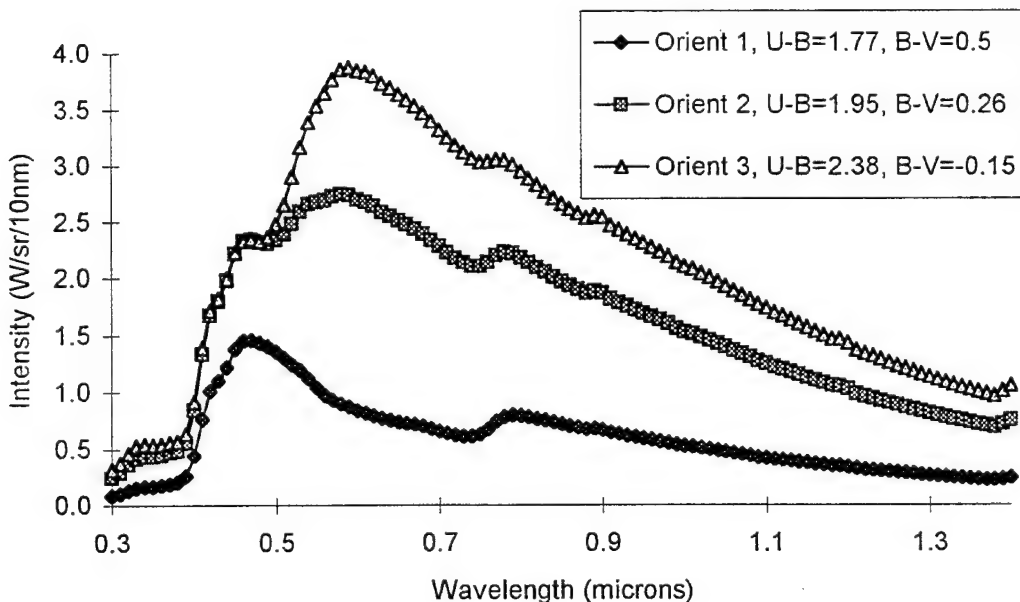
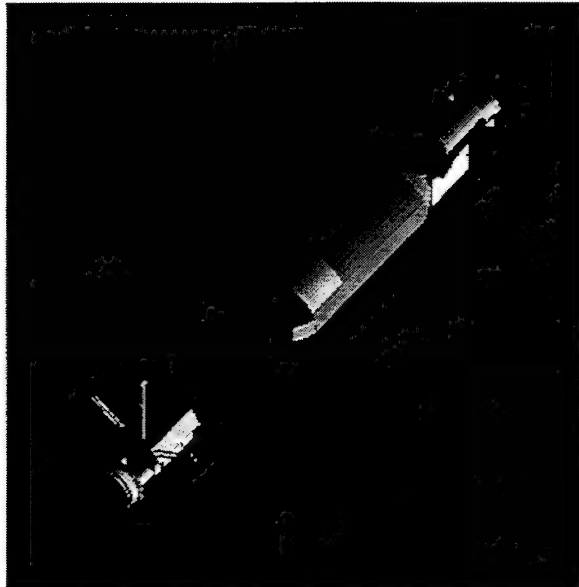
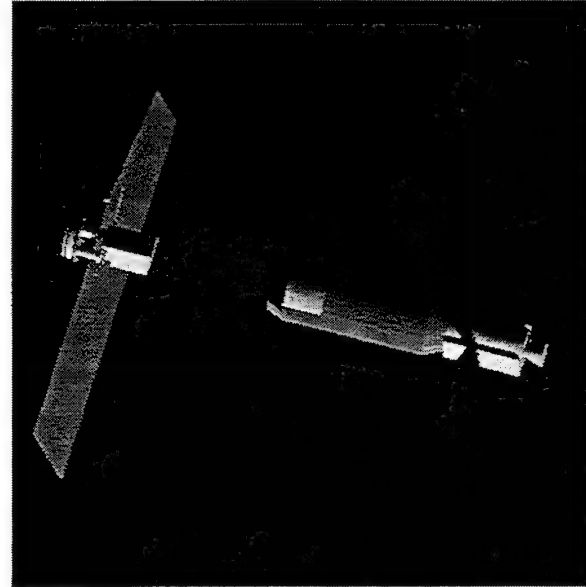


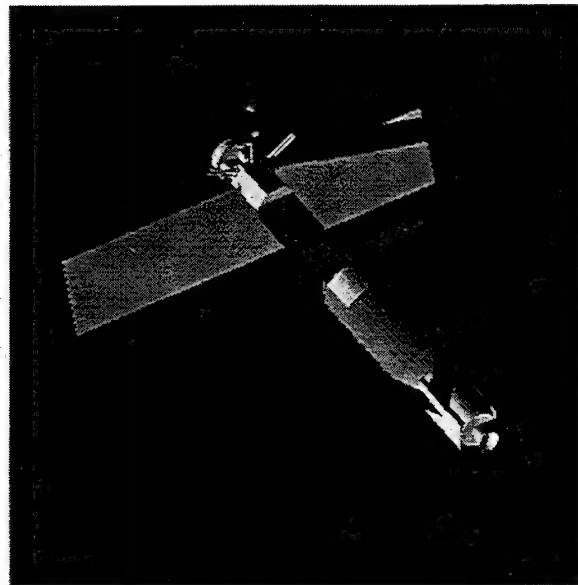
Figure 1. Spectra associated with three different orientations of Seasat.



(a)



(b)



(c)

Figure 2. Seasat in three different orientations.

because it is a nadir-stabilized satellite. Figure 2b corresponds to orientation 2, and Figure 2c corresponds to orientation 3.

For the satellite pass simulations, the Maxwell-Beard reflectivity model was used and the solar panels are static with respect to the body of the spacecraft (i.e. not tracking the sun). Figure 3 shows a series of spectra predicted for a Seasat pass at intervals of 90 seconds. Each spectrum is labeled with a time (min:sec), zenith angle (ZA), and solar phase angle (SPA). The visual magnitude normalized to a range of 1000 km varies from 4.5 to 7 for the Seasat pass, and the average color values are  $U-B = 2.54$  and  $B-V = -0.29$ . For reference, the color values for the sun in these simulations are  $U-B_{\text{sun}} = 0.10$  and  $B-V_{\text{sun}} = 0.63$ .

DMSP is three-axis stabilized and is in a near-polar orbit. Figure 4 shows a set of spectra for a DMSP pass. The visual magnitude normalized to a range of 1000 km varies from 5.5 to 7.5 for this set of spectra. The color is fairly constant over the DMSP pass with  $U-B = 1.16$  and  $B-V = -0.06$ . The spectra for DMSP are distinctly different than for Seasat. In Figure 5, a DMSP spectrum and a Seasat spectrum are compared. They are normalized at  $\lambda = 0.46 \mu\text{m}$ . The most marked spectral differences between DMSP and Seasat are in the ultraviolet and yellow-red.

The solar panel in the Seasat model has primarily silicon solar cells on one side and black chemglaze on the back side to radiate away heat. For a near-earth satellite pass on a particular day, the sun remains in a stationary position throughout the pass. As the satellite moves across the sky, the solar phase angle changes and the solar panels move to track the sun. Code development to simulate solar panel tracking is underway. Figure 6 shows two spectra for Seasat -- in one case, there is solar panel tracking, and in the other case, the solar panels are fixed. The solar panel spectral reflectivity is overlaid on these two spectra. The solar panel contribution to the upper spectrum is seen where its reflectivity is high, especially in the ultraviolet and near-infrared. The difference in  $U-B$  values for these two spectra is on the order of 0.4 magnitude. However, the solar panel area of Seasat is fairly small, so the effect of larger tracking solar panels may be more dramatic. It is anticipated that this dynamic behavior will be detected in the spectra over the course of a pass if the conditions are right. The time scale of variation of the solar panel tracking behavior will depend on the orbit and the satellite. For instance, satellites in geosynchronous, sun-synchronous, polar, low-inclination circular, and elliptical orbits have different requirements for tracking the sun and will thus have different time-dependent photometric signatures associated with this dynamic behavior. Some satellites have fixed solar panels, so this behavior is not representative of all satellites.

## Issues

There are limitations in comparing simulated to observed signatures. Satellites of the same type are not identical. In addition to design changes, there may be slight variations due to the quality of a material and how different parts are manufactured or secured. In space, material degradation will affect the spectra over time. For example, radiation degrades the spectral

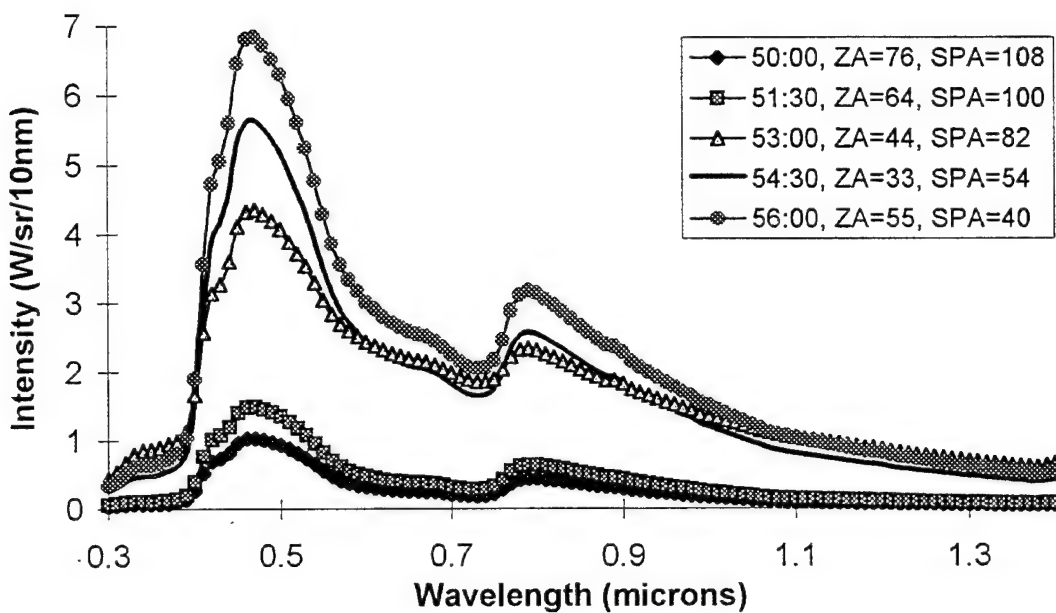


Figure 3. Spectral series from a Seasat pass.

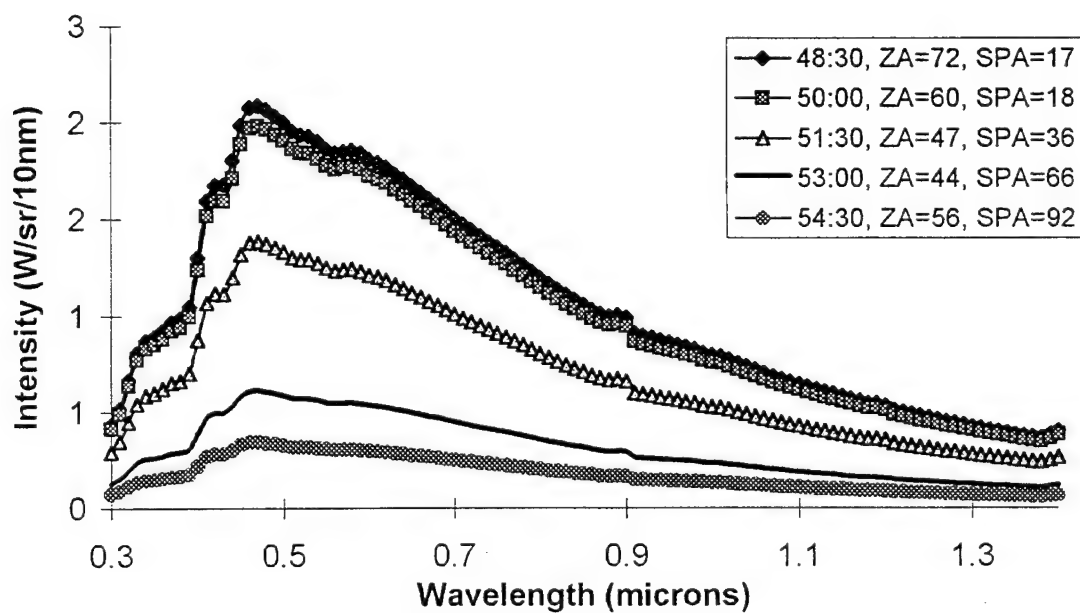


Figure 4. Spectral series from a DMSP pass.

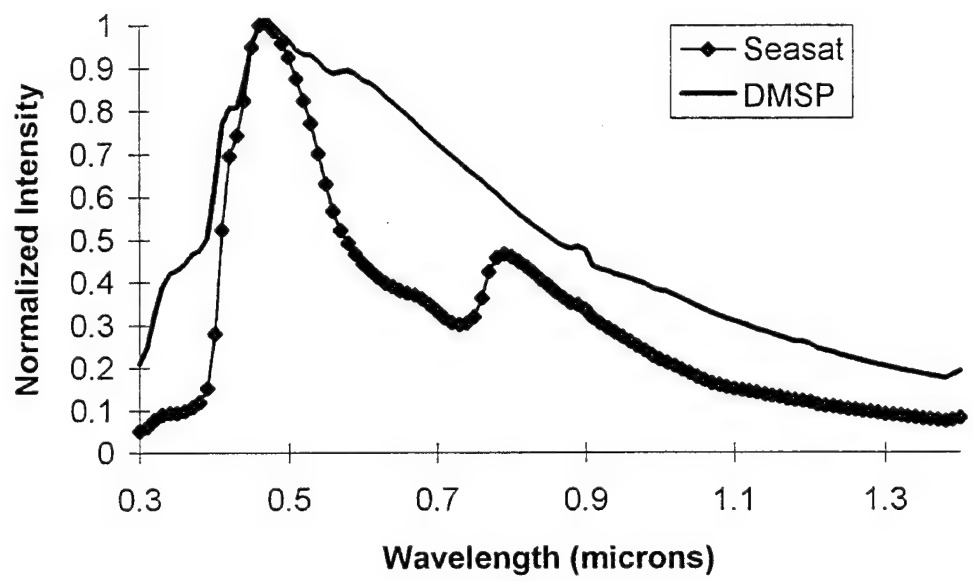


Figure 5. Comparison of a DMSP spectrum to a Seasat spectrum.

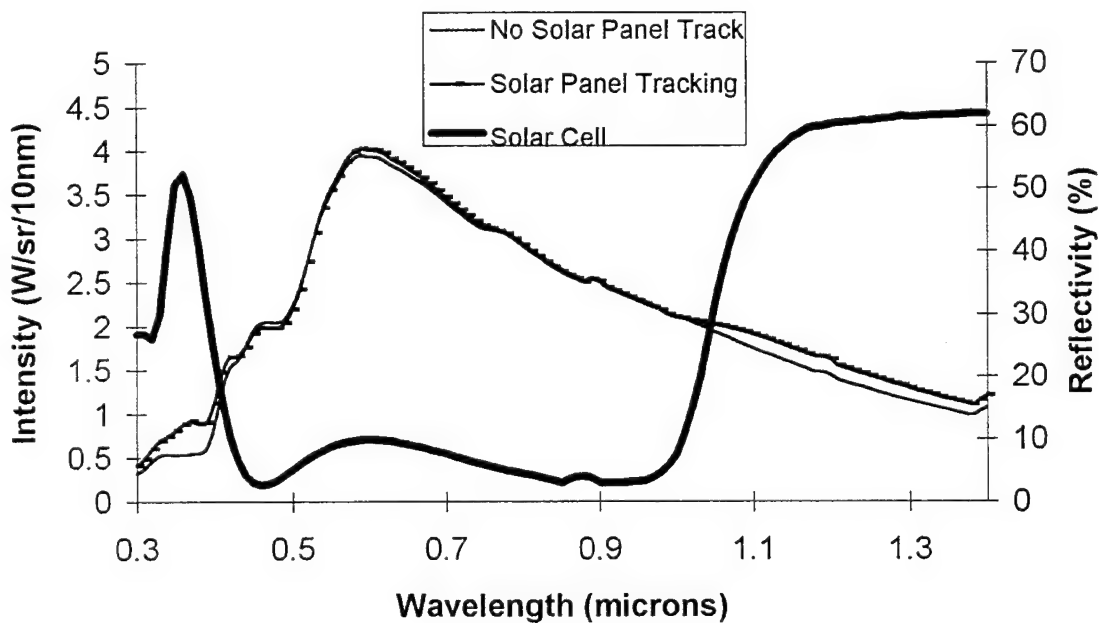


Figure 6. Differences in spectra from tracking and non-tracking solar panels.

response of silicon solar cells towards the blue part of the spectrum. This may redden the reflected signature. Thermal paints also degrade with radiation (e.g. white chemglaze will have a reduced reflectivity); this may result in a reduced magnitude as well as color change. In addition to radiation, other natural and man-made environmental factors degrade spacecraft materials such as atomic oxygen, ionized and neutral species, micrometeoroids, and man-made debris. The effect of surface roughness can be modeled, but the actual surface roughnesses on a satellite depend on the environment of its orbit and its duration of exposure. There also may be some influence on the spectrum due to material temperature. These are just some of the real effects that will influence observed spectra that are not presently modeled in the simulations.

## Conclusions

These initial results show that there is potential for spectral signatures to be used to identify spacecraft types. The spectra for DMSP and Seasat are very different for the passes modeled. As the satellite orientation and illumination conditions change with respect to the observer, different materials influence the observed spectrum.

Future work will include spectral utility (what is the value added to other SOI techniques) studies for deep space objects, more detailed analysis of the simulated spectra, including developing advanced feature extraction techniques, and benchmarking with lab and eventually field data.

Spectral data combined with other SOI data may be a valuable identification and status assessment tool. The materials database, satellite models, and the simulation software are continually evolving and are valuable tools to understanding how best to sense space objects.

## Acknowledgements

This work was sponsored by the Strategic Defense Initiative Organization, Phillips Laboratory, Kirtland AFB under Contract No. SDIO84-C-92-0008. Acknowledgements are deserved by the other members of the team who have worked hard on the program this year. They include Mike Hawks, Steve Gregory, Eirik Holbert, Dave Tyler, Helix Fairweather, Tamara Payne, Ted Turner, and Dennis Duneman. Thanks also to Rett Benedict, Bill Burckel, Terry Gray, Tamara Payne, and Rhonda Peyton for their helpful input in preparing this work.

## References

1. Prochko, A. E., Holbert, E., Gregory, S. A., Rafert, J. B., Payne, T., Durham, S., Horton, R., "Hyperspectral Imaging of Near-Earth Space Objects at the Phillips Laboratory," Proceedings of the 1994 Space Surveillance Workshop, Lincoln Laboratory, ESC-TR-94-083, pp. 163-172.
2. Gilbert, John, "Review of Optical Predictive Reflectance Models," WGRC 75-3916, March 1975.

3. Culpepper, Mark A., "Empirical Bidirectional Reflectance Model," to be published in the Proceedings of the SPIE Aerosense '95 Symposium in Tactical Photonics, April, 1995.
4. John Lambert, private communication, 1994-1995.
5. Beavers, W. I., Angione, R., Alten, V., Yanow, K., Lane, M., "Cylindrical Satellite Specular Season Photometry," Proceedings of the 1993 Space Surveillance Workshop, Lincoln Laboratory, ESC-TR-93-249, pp. 9-18.
6. W.I. Beavers, *et al.*, private communication, 1994.
7. Budding, Edwin, An Introduction to Astronomical Photometry, Cambridge University Press, New York, NY, 1993.

## **Initial results from the new sensor system on the UK SOI facility at Herstmonceux**

*Dick, J., Sinclair, A., (Royal Greenwich Observatory, Cambridge, UK)  
Greenaway, A., and Liddell, P., (Defence Research Agency, UK)*

### **1. Introduction**

In support of the UK's SOI programme, a new sensor system has been installed on the 0.5 m satellite-tracking telescope at Herstmonceux. The new system, known by the acronym FOX, is used principally for acquiring photometric SOI data and also provides a general-purpose optical bench for enhanced-resolution imaging experiments. FOX has been in use since mid-1994. This paper describes both the system and some of the observations taken.

### **2. The FOX system**

The FOX system has five main components:

- i) a camera assembly that holds two scientific-grade charge-coupled device (CCD) cameras and their associated optics. Within this assembly, there is a beam-director to direct the light from the telescope to one or both cameras, to the optical bench, or to the bench and one camera. In front of each camera is a carousel that holds up to eight filters. At present, each carousel is fitted with a range of neutral density filters. Immediately prior to each camera is another holder that can be used to hold other optical components (*e.g.* colour filters).
- ii) a telescope-resident microcomputer system that controls the positioning of the optics within the camera assembly. The beam-director and the two neutral density carousel wheels are controlled by this microcomputer. The microcomputer is, in turn, controlled remotely by the FOX's main computer system via a serial link.
- iii) the camera controller units. There are two camera controllers that are housed near the telescope, provide drive signals to the cameras, and process the low-level analogue output signals from the cameras.
- iv) the main computer system that controls the experiment, acquires and processes data. This is sited in the telescope control room. It contains interface cards that enable it both to control and to receive image data from the cameras.
- v) a platform structure which can host optics experiments. This is mounted on the telescope and has a matrix of tapped holes for standard optical bench components.

The general layout of FOX is shown in Figures 1 and 2. The camera system is driven from application-specific software that was written in-house. The software allows images to be taken with the cameras and recorded to disk; quite sophisticated image processing can be carried out *post hoc*.

For photometry, the software measures the positions and integrated intensity of any objects that are detected within each and every frame taken by the cameras.

Results from photometric observations are in the form of a dictionary that has one entry for each object detected during a given observing session.

Each entry in the dictionary contains positional information about the object it describes as well photometry.

The photometry is stored as a list of {time, intensity} pairs for one-camera operation or {time, red intensity, blue intensity} triplets for two-camera operation. From one frame to the next, nearness in position is used as the criterion for same-object identification. If, possibly due to tracking error, an object strays far enough between frames so that it fails the nearness test then the system does not lose that object (because all objects are tracked and measured) but merely identifies it as a new object (*i.e.* a different entry in the dictionary). In practice, such discontinuities in the

**Fig. 1 General layout of FOX**

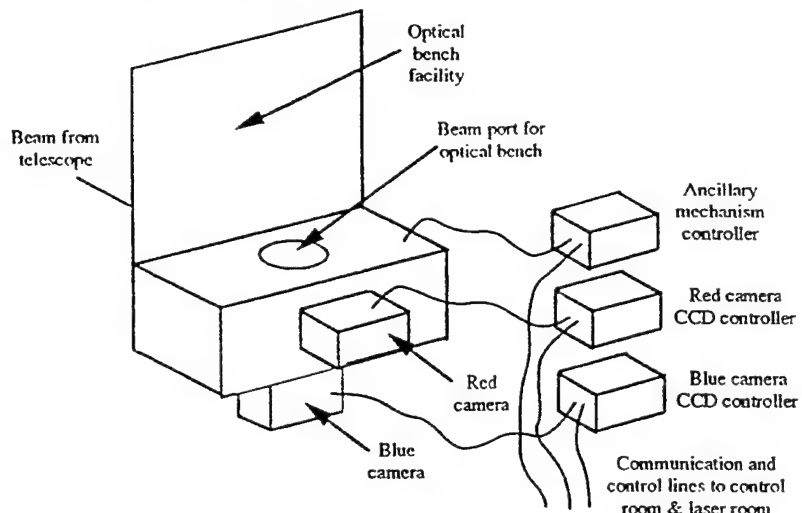
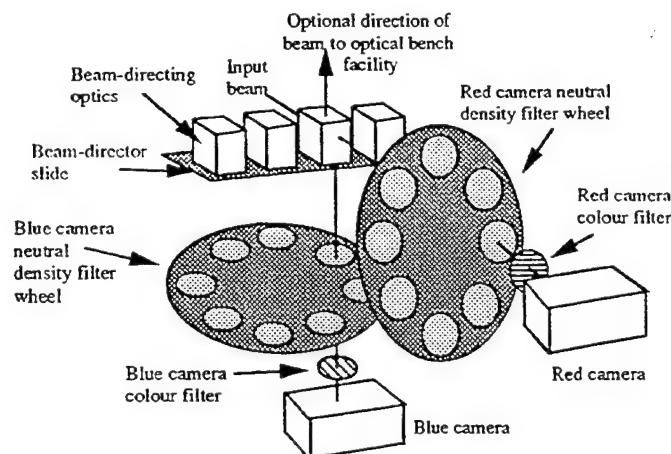


**Fig 2. Optical components within FOX**



dictionary can be rectified during off-line data analysis and so continuous data collection is possible. Occasionally, because another object (*e.g.* a star) passes the nearness test, it is possible within one frame for two objects to be identified with the same dictionary entry. In such a case, photometry for both objects is logged.

### 3. Commissioning results

Since installation, FOX has been used for both photometry and imaging, although the imaging work was done without the system being configured for such work.

A variety of photometric and astrometric tests have been carried out to characterize FOX. The photometric sensitivity of the FOX cameras has been tested both in the laboratory and on stars of known irradiance; astrometric tests have been carried out using star clusters.

#### 3.1. Imaging

Shortly after FOX was installed on the telescope, the space station MIR was observed during a high-elevation pass. During this pass, a short exposure image of MIR was taken and this is shown in Figure 3.

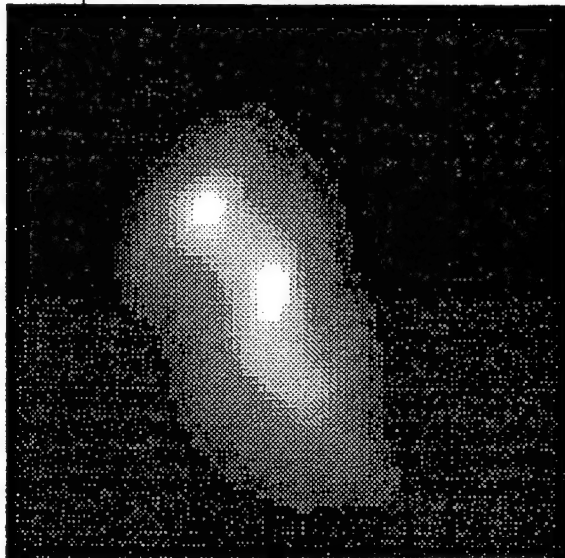
Although blurred, the shape of MIR can be seen clearly. (This image was taken with one of FOX's photometry cameras, which is *not* designed for high-resolution imaging work.)

At the range of MIR, one pixel is roughly 1 m; the total size of the image is therefore about 35 to 40 m.

In the near future, it is hoped to commission a fully-sampled imaging facility that will be located on the optical bench. After initial observations have been taken to characterize the guiding accuracy of the system, a fast image stabilization system using a tip-tilt mirror will be designed. Later, low-order corrections for wavefront curvature will be introduced.

It is possible for one of the FOX cameras to be installed on the SLR's 20 cm wide-angle telescope (co-mounted with the main telescope). FOX has been used in this mode for a European debris-watch campaign. Figure 4 shows a short exposure of the open star cluster NGC752 used for astrometric characterization tests; on-line

**Fig. 3** MIR imaged with one of FOX's photometric cameras



star catalogues are used to establish field identification and positional data for satellites within the observed field.

### 3.2. Photometry

FOX has been used for photometry of satellites in low-, high-, and geostationary Earth orbit. In summary, the system has proved to be more sensitive than its predecessors and has much better signal-to-noise even in bright-sky conditions; typically, the sky background *noise* in an observation is about 20 times smaller with FOX than with the previous photometer.

Figure 5a shows the red-only signal from the TOPEX satellite (92-052-01, 22076).

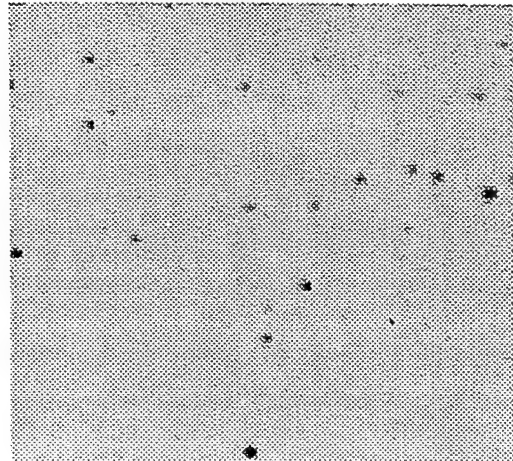
Observation starts at 02:16 on 18th October 1994 and shows the satellite coming out of shadow, a plateau of near-constant brightness, and a bright long-lived flash.

Figure 5b shows the blueness of the satellite during the same period of time: the satellite emerges from the Earth's umbra red, becomes bluer as it passes through the penumbra into direct sunlight, and then gives a bright blue flash.

Figure 6 shows a rich-featured photometric observation of one of the Glonass series.

Geostationary satellites have also been observed successfully. Figure 7 shows the apparent visual magnitude of Intelsat 6 F-1 (1991-075-01) during a night. This observation was taken during a joint US-UK observation campaign called JOVIAN. Observations of three geostationary satellites were taken simultaneously by the

**Fig. 4** Star cluster NGC752 used for astrometric tests



**Fig. 5a** Red-light irradiance from TOPEX

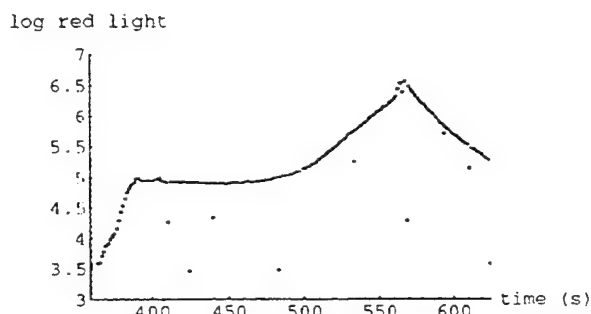


**Fig. 5b** Blueness analysis for TOPEX

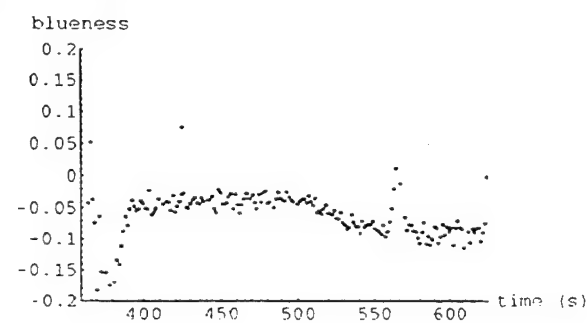
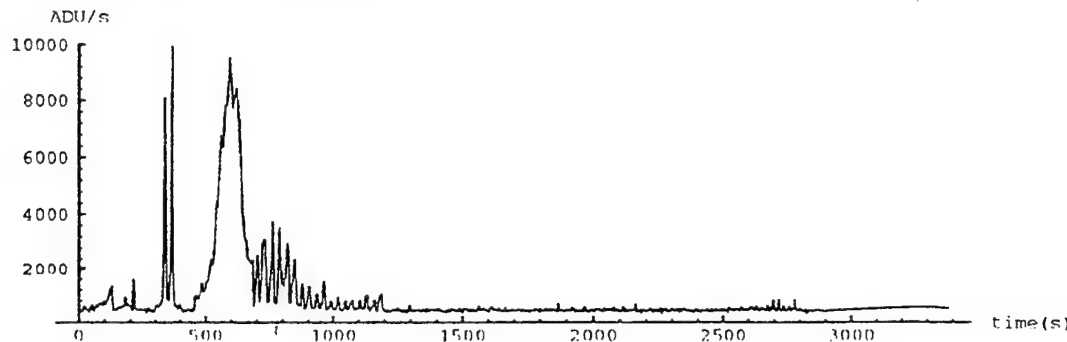


**Fig. 6** Photometry of 92-005-03



Phillips Laboratory Malabar telescope facility and by the SLR at Herstmonceux. The JOVIAN program showed that the two sites could work together, acquiring bistatic photometric SOI information.

### 3.3. Spectral information

To extend the colour capability of the system, a transmissive diffraction grating can be placed in the optical path.

Figure 8 shows a typical image obtained with FOX configured with the grating. The image shows both the "white light" image of the object (which acts as an in-image calibrator), and, to the left, the first-order spectrum of the object.

**Fig. 8** FOX spectral data



### 4. Summary

FOX has been successfully commissioned on the SLR at Herstmonceux. FOX has extended the SLR's optical SOI capability by enabling colour information to be acquired on objects in all orbital regimes, including geostationary. During its first year, as well as carrying out routine SOI work, FOX has been used for joint UK/US geostationary observations and in a European debris campaign. The authors would like to thank the SLR Group staff for their contributions to the work reported in this paper, and the UK MoD for funding support.

## IOTA: Operational Status and Measurements

W.A. Traub, N.P. Carleton, M.G. Lacasse, P. Nisenson,  
M.R. Pearlman, R.D. Reasenberg, X. Xu, C.M. Coldwell, A. Panasyuk  
(Smithsonian Astrophysical Observatory),  
H.M. Dyck (Univ. of Wyoming),  
J.A. Benson, C. Papaliolios (Harvard University),  
R. Predmore, F.P. Schloerb (Univ. of Massachusetts at Amherst),

### Abstract

The first two telescopes of the Infrared-Optical Telescope Array (IOTA) -- a Michelson interferometer with space surveillance potential -- are now yielding results. Constructed by a five-institution consortium at the Smithsonian Institution's F. L. Whipple Observatory on Mt. Hopkins, south of Tucson, IOTA achieved first fringes on December 3, 1993.

IOTA uses a number of technical innovations to image objects with an angular resolution of 7 nano-radians in the visible (0.5 micron) to 29 nano-radian in the infrared (2.2 micron). The 45 cm collectors, each consisting of a siderostat and an afocal telescope, can be moved to any of 17 stations along an L-shaped track. The maximum baseline is 38 m. The compressed light beams are directed in vacuum to a beam combination area to eliminate unwanted spectral dispersion. A two-part path-compensating "trombone" delay is inserted using dihedral reflectors. One is mounted on a slew-and-clamp carriage and the other is mounted on an air-bearing positioning table capable of fringe tracking. After exiting the vacuum chamber, the visible and infrared beams are dichroically split. Active stabilization of the beams, a necessity for pupil-plane beam combination, is achieved by directing all or part of each visible beam onto 32x32 fast-framing CCDs. Offset errors are determined by a Quadra 950 which sends corrections to a fast-steering turning mirror located close to each telescope.

Beam combination takes place on beam splitters. Because a 45-cm collector is about an  $r_0$  in size at K-band (2.2 micron), the combined infrared beams can be fed directly to two cooled InSb detectors. The outputs of the visible beams are directed onto a four-lenslet array, where each lenslet is matched to the visible  $r_0$ , and then into four optical fibers that feed a grism spectrometer. The output, a spectrally modulated fringe pattern, is detected by a PAPA photon-counting detector. System control is provided by a distributed network of MacIntosh II computers. Infrared data acquisition and quick-look processing are handled by a PC.

Currently, size estimates of giant stars are being determined from fringe visibilities at different baseline lengths. Binary star measurements are being made using a novel technique dubbed "freckle interferometry". Future plans involve the addition of a third telescope, making phase closure measurements, and mapping more complex objects.

### Instrument Description

The Infrared-Optical Telescope Array (IOTA) project now has its first two collectors operational and yielding useful interferometric data at the Smithsonian Institution's F. L. Whipple Observatory on Mt. Hopkins, near Tucson, Arizona. The IOTA project is a collaborative effort between Harvard University, the University of Massachusetts, the Smithsonian Astrophysical Observatory, and the University of Wyoming. This array will consist of three 0.45-m collectors on baselines extending to 38 m, the third telescope to be added as soon as funding permits.

We present below a general description of the array, including the rationale for some of our choices of configuration. Then we return to give some of the details of obtaining and interpreting interferometric data from IOTA. Finally, we give more rationales of choice and some of the details of performance of our various sub-systems, in hope that these may be useful to others engaged in similar work.

The site, just below the MMT installation at the summit of Mt. Hopkins, was tested and found to be good at the time of the MMT construction. Its size and shape (unalterable because of a precipitous boundary) determined the geometry of the array. The collectors may be located at one or another of 17 stations on an L-shaped layout, giving an assortment of baselines with some redundancy. From these station locations the beams are relayed to the corner of the array in an evacuated envelope, folded back along the long arm for path equalization, and then delivered out of the vacuum within the enclosed area, where separate infrared and optical beam-combination and detection systems are located on optical tables.

The stations of the layout extend along each arm in two modular systems, one at multiples of 5.00 m, and one at multiples of 7.04 m. The redundancy involved here provides that three collectors may be moved to successive configurations in which there is always a baseline vector in common between one configuration and the next. This permits phase-closure information to be continued as we build up U-V-plane coverage.

The individual collector assemblies consist of a siderostat, an afocal Cassegrain telescope, and an active relay mirror. These components are mounted on a massive and stiff steel pedestal so that the telescope looks down at the siderostat at an angle of 30 degrees to the horizontal. The telescope produces a 10-x-reduced parallel beam that is directed vertically downward by the active mirror, which receives its commands from a detector system in the beam-combination area, and acts so as to stabilize the image position there. The collector assemblies are housed in shelter-transporter units that provide a well-insulated enclosure with a sectioned roll-off roof and hinged end-wall that open for observing. Each shelter may move on rollers along steel I-beam tracks on the arm on which it is located, and the shelter frame supports a hydraulic mechanism that can lift the collector assembly so as to transport it from station to station.

We chose the combination of siderostat and stationary telescope in order to make it easier to maintain good primary- secondary alignment, which is critical for interferometric- quality imaging. This geometry, like that of any coude telescope, entails certain compromises. Suppose, for instance, that we might try to provide good steep angles of incidence on the siderostat, and hence mount the telescope directly above it, looking vertically downward. The telescope structure would then make an intolerable cone of obscuration around the zenith. If we move the telescope away from the zenith in some direction, then when we look in the opposite direction, the angle of incidence on the siderostat will at some point become too flat. Our placement of the telescope at 60° from the zenith gives a compromise between these two effects that allows a sweep of 40° on either side of the zenith in the plane of the siderostat- telescope axis. We oriented this axis in the E-W direction in order to take this limitation in hour angle. Then in declination we have no fundamental limit near the meridian. The shelter walls allow us to view down to 63° from the zenith, so that at our latitude of 31.7° we can nominally see from Polaris to the Galactic center,

Our beam-relay path after the active mirror is arranged so that the beams undergo identical sequences of reflections, thus ensuring that they arrive at the combination point in identical states of polarisation (Traub, 1988). To save money, we are only providing two active delay lines for three telescopes. For a given observing configuration, the beam that needs no delay is directed into a stationary "stub" delay path by moving (on remotely controlled stages) two of the mirrors that

direct the beams around the corner of the array. The other beams are sent down the long arm to reflectors on simple carriages that are operated in slew-and-clamp mode. The beams are then returned back near to the corner, where they encounter reflectors mounted on air-bearing carriages running on a precisely-finished 2.4-m granite track under laser-interferometer control (all obtained from the Anorad Corp.). These carriages provide fine-positioning and tracking capability, with such smoothness that they introduce less phase jitter into the beams than does

Our reflectors in the delay path are "dihedral" or "roof" mirrors, which are not true retro-reflectors, but which have one less reflection than do cat's-eyes or cube-corners, and which also are relatively inexpensive. After the delay, the beams travel once more down the long arm to where they are directed out into the beam-combination area. They exit (as they entered, just below the guide mirrors) through IR-grade fused silica windows.

Once out into the room, the beams pass across the end of the "IR table", where the infrared radiation is diverted by dichroic reflectors and directed to an IR beam splitter and thence to two cooled InSb detectors. This is a simple scheme, adequate for the present operation with two telescopes, but which will grow in a way depending on the state of the art of IR detectors when the third telescope is added. At present, the IR interference pattern is displayed by programming the fine delay line to sweep back and forth across the point of zero path-difference, at such a rate that interference fringes are generated in the detector outputs at around 200Hz. Radiation from an entire IR transmission band (e.g., the K band at 2.0-2.4 microns) is being modulated, so that we can derive the fringe contrast as a function of wavelength across the band.

Visible radiation is transmitted onto the "visible table", where for IR operation it is all directed to be focussed onto the guider detectors, which are small (32 x 32) CCDs with fast readout circuitry. For visible-light operation only a portion (initially the central part) of the beams goes to the guiders; the rest is conveyed to a beam splitter, and the outputs of this (two for now; ultimately six) are focussed by arrays of four-lenslets onto multimode optical fibers. Each lenslet (full aperture 15 cm, referred to the primary) is intended to collect light from a  $1-r_0$  patch of wavefront. The optical fibers are led to the slit of a grism spectrometer designed to give constant dispersion in frequency space (Traub, 1990), and the spectra are focussed onto the cathode of a PAPA photon-counting detector (Papaliolios, et al., 1985), spanning the range 0.45-0.80 micron. In this case the interference pattern is displayed by running the delay line consistently at several wavelengths away from the zero-path position. This will provide several cycles of modulation across the spectrum, again giving fringe contrast as a function of wavelength. The possibilities and limitations of multi- $r_0$  recording will be an important area of learning.

Control and data recording for our system are distributed to several small machines. The siderostats, delay lines, and guiding mirrors are run by Macintosh II computers; the IR and visible data-recording operations, with quick-look display capability, are handled, respectively, by a 286 PC and a Quadra 950. A conscious decision led us to distribute these functions to small machines; the actual present configuration of machinery is essentially the result of historical accident.

### Measurements

IOTA went into operation in December, 1993, and has yielded a number of astronomical observations. We have measured apparent diameters of cool giant stars in the 2.2-micron band, noticing the effect of the variation of opacity with wavelength. In a demonstration measurement on a close binary star we have shown that the direction of sweep of the delay line gives a reference for determining phase in the spatial spectrum of an object, even with a two-telescope interferometer. We will be continuing these observations and also entering into a program of observations of dust distributions around young stellar objects and around evolved stars with strong stellar winds

We can also test the ability of IOTA to map complex objects by making "ground-truth" observations of man-made objects in space. The tracking capabilities of both siderostats and delay lines have been designed with this in mind, but not all satellites and rocket bodies are suitable, since there will be instrumental limitations on the brightness, apparent size, angular velocity, and the apparent structural complexity of the observed object. We have identified more than 200 objects with the requisite characteristics. The GPS satellites, in particular, offer some interesting possibilities for instrumental testing (Gibson, 1990).

### Subsystem performance

Siderostat mechanisms -- The primary criteria for our siderostat design were smoothness in tracking and low cost, with less weight given to accuracy and speed of pointing. The design (mechanical detailing by P. R. Lichtman) has a simple yoke-mounted cell for the flat mirror, with air pads supplementing three defining points for back support. The drive systems each use a Compumotor microstepper with a Harmonic Drive 200:1 reduction-gear unit turning a 25-mm diameter capstan. This is connected to a 15-times-larger drum on the siderostat axis by 16 plastic-jacketed wire cables of about 2 mm diameter. Each cable is anchored at one end on the drum, passes along the surface of the drum to the capstan, makes two turns around the capstan, and then passes on around the drum to a spring-tensioned anchoring point. The cables are wound in a figure-eight pattern so that they can always lie tight against one surface or the other. There are eight cables with fixed ends pulling one way around the drum, interleaved pairwise with eight pulling the other way. The capstan surface has a smooth-bottom helical groove (essentially a screw thread with a pitch equal to the cable diameter) to accommodate the pattern of the figure-eight winding. As the capstan turns, the cables move up and down the capstan, by +5mm for +60° axis travel, which is about our full range. The anchor points on the drum are located so as to lay out the cables in a matching helix, but the drum surface is smooth. We received engineering advice on this drive system from Sagebrush Technologies, Inc. We also found that essentially the same drive had been developed in 1855 by Alvan Clark as an improvement to the original drive of Harvard's 15-inch refractor (then the world's largest telescope), in response to the demands of the then-brand-new application of photography to astronomy.

The microsteppers for the siderostats are driven by pulse trains at commandable quasi-regular repetition rates, generated by so-called rate-multiplier circuits. The rates are updated by the computer at 0.1 sec intervals. Typical rates, using 25 000 microsteps per revolution, are a few hundred Hz or less. There are no encoders in the system other than the microsteppers; the reference for absolute position is a "home" location defined by a flag that interrupts a light signal to a photodiode. This position is inherently repeatable (for small offsets and returns) to about 0.02 mm, or 3 arcsec.

The performance of the siderostats satisfies very well our basic requirements: there are no tracking errors that are more difficult for the guide mirrors to correct than are atmospheric effects, and the pointing is accurate enough so that it is easy to find objects. For tracking trials we have viewed the images at high magnification on a TV monitor at standard framing rates, and cannot detect any high-frequency image motion beyond what seems appropriate for the seeing conditions being displayed, even at good (sub-arcsecond) seeing. We do see periodic errors (period 1/3000 of a revolution) of up to 10-12 arcsec peak-to-peak from the Harmonic Drive units, but these are easy for the guiders to correct. To point accurately we work with a model that includes various possible alignment corrections, as well as the axis orientation. Using this, we can develop from observations of 15-20 stars a set of pointing-correction parameters that allows us to direct the siderostats to a desired position within 20 arcsec or better. We believe that these residual errors are due to slippage in the cable drive system, since the axes sometimes fail to return to their "home" positions by errors on this scale.

We acquire objects by sending the siderostats to the nominal position and then instituting a spiral search until the object is detected on the guider CCDs, whereupon the guider computer tells the siderostat computer to stop the search, and gives it appropriate offsets so as to center the object in the CCD field.

Main collector optics -- These optics consist of the siderostat flat mirrors, 46 x 69 cm and 75 mm thick of an octagonal shape approximating an ellipse, and the primaries and secondaries of the beam-compression telescopes. The primary is an f/2.5 paraboloid, 46 cm in diameter and 75 mm thick. The Cassegrain secondary, also paraboloidal and 6 cm in diameter, produces a 10- x reduced parallel beam. All these components are made of Zerodur. Our specifications are that neither the flat nor the primary-secondary combination should introduce wavefront errors of more than one-tenth wave into the beam. This specification holds over 90% of the area of the large elements (allowing a poor-quality edge) and for this we take the wavelength to be 2 microns. For visible-light operation we make the specification hold for a wavelength of one-half micron, but only over any 15-cm sub-aperture located roughly on the center of the radius of the primary. Working to these tolerances Zygo Corp. produced two flats for us, and Fair Optical Co. produced the beam-compression optics. The latter have an additional condition to meet, which is that their magnification factors must match to good accuracy. We specified a match to 2%, and Fair was able easily to hold it to 1%. These optics, like other elements in the system, have a protected silver coating (Denton Vacuum, Inc.) that has 98-99% reflectance longward of one-half micron. All of these elements underwent interferometric acceptance tests against calibrated flats, conducted by their manufacturers. The primaries were tested in auto-collimation by themselves, and then the primary-secondary combinations were also tested in auto-collimation, using a parallel-beam input to the system.

Relay optics -- Our relay mirrors for the compressed beams are sized so as to give at least 70 x 100 mm of reflecting area for 46-mm beams incident at 45°, to give a little latitude in placement without getting too near the edge, where quality may degrade. Where possible we used stock mirrors that conform to the specification of surface errors being less than 1/20 wave, peak- to-peak. Where our configuration demands it, for the fast-guider mirror and the dihedral reflectors, we had mirrors made to the above specification. All are of Zerodur or of fused silica. We made up the dihedrals from two rectangular mirror elements, holding them in a jig that could bring them to an accurate right angle, under optical monitoring. The two elements were then cemented to each other and to a light strut on one side, using small-area (1 x 5-mm) bonds of UV-setting epoxy. These assemblies have survived transportation without any failures and appear to be doing their job well. The guide mirrors are of minimal size, 60 x 70 mm, octagonal in shape and beveled on the back side to reduce weight, all so as to permit high-bandwidth tracking. Their lowest mechanical resonance when mounted on a piezo-electric driver assembly (obtained from Physik Instrument) is about 500 Hz. All of our custom-made small flats were fabricated by Planar Optics.

System optical performance -- We have made visual interferometric tests of our entire system, sending laser light out via the visible-light beam splitter to both systems, setting both siderostats normal to their beams, and comparing the return beams, first separately against a test flat and then to each other. These are very severe tests, since there are 13 reflections in each beam, used in double pass. To reduce the effects of thermal turbulence we ran with the relay path evacuated. We used the unequal-path tests to collimate the telescope optics to a point within our specifications. Operating the system as an equal-path interferometer we could use the laser beam to examine the actual interferometric path that we use in observations, and could make the judgement that it was good enough for observations (i.e., of the order of a half-wave rms error between the wavefronts in the double-pass mode, in visible light). In the equal-path mode we also operated the delay line

so as to find the point of exact path equality, defined by white-light fringes. To speed up the search for these fringes we first found the point of maximum contrast of fringes from a low-pressure Hg lamp, and then of those from an Osram commercial fluorescent lamp with several spectral lines, which located the point of equal path to an uncertainty of 1 mm. The final measurement in white light, together with careful surveying with tape measure and theodolite that we had employed in laying out the system, allowed us to predict a priori the delay-line position for interferometric stellar observations.

Telescope structure -- The telescope primary and secondary mirrors are supported from a heavy, perforated plate that is in turn rigidly connected to the upper platform of our pedestal, with its normal pointed down toward the siderostat at an angle of 30°. The primary is drawn up against three defining points on this plate by six springs, two on either side of each point. Radial support is defined by two contacts near the bottom of the periphery, and a spring pulling radially outward at the top that bears part of the weight. The secondary assembly is supported by a heavy perforated tube cantilevered out from the primary plate. This tube, and all parts of the telescope structure, except where noted, are of stainless steel. The secondary assembly consists of three spider vanes connected to a hub that supports a compact three-axis stage to which the secondary mirror is mounted, by silicone-adhesive pads that draw it against three defining points. The outer ends of the spider are not fastened directly to the support tube, but are connected to it by flexures that permit movement along the optical axis, but give stiff radial support. The ends of the spider proper are spring-loaded axially against rods of low-thermal-expansion material (Neoceram, made by Nippon Electric Co.) whose other ends are supported at the primary plate. These rods, which have a small negative coefficient of thermal expansion, are combined with metal parts (both stainless steel and aluminum) to make a very-low-expansion axial path between primary and secondary, such that their separation remains constant to a tolerance of several micrometers over a temperature range of at least 15 C. The combination of this with rigid, nearly-symmetrical radial support allows the telescopes to remain in collimation without attention and to be resistant to wind buffeting. The three-axis stage (range 1 mm) makes precision translation of the secondary quite easy. Secondary tilt adjustment is performed via threaded fittings incorporated in the spider-to-Neoceram contact.

Star-guider detectors -- We have described above the active guide mirrors that serve to keep images stabilized on our interferometric detectors. The signals to drive these are derived from small thermoelectrically-cooled CCD detectors that were designed by Dr. John Geary for this type of application. These have a 32 x 64-pixel format, with one half of the area blocked from receiving light. After a short integration (<0.01 sec during actual guiding) the charge from the active area is rapidly shifted into the blocked area, whence it may be read out during the next integration. The whole 32 x 32 area may be read out during acquisition, but to maximize bandwidth for guiding, the readout may be chosen to skip to a central 8 x 8 area. The centroids of the two images are found by the computer, and after suitable filtering and conditioning, drive signals are sent to the piezoelectric actuators of the guide mirrors. The parameters of the system may be varied in order to adapt to different signal levels, conditions of seeing, etc.

For infrared observations the IR beams are directed into their combination and detection optics by dichroic mirrors, and all the light of wavelength less than 1 micron is relayed to the guider CCDs (which have their greatest sensitivity in the range 0.6-0.8 m). For operation in visible light, where we can only use four sub-apertures, small spider-mounted mirrors direct the central parts of the beams onto the CCDs. In the IR mode we have tracked stars down to V = 6 with a 100-Hz bandwidth, giving stabilization to a few tenths of an arcsecond.

**Delay lines** -- Our coarse-motion delay lines extend down along the long arm of the array for 30 m, giving us our full sky coverage at maximum baseline. The mechanism for this part of the delay line is a carriage moving on nylon sliders over a track that is simply constructed from well-aligned cold-rolled steel bars, supported on lengths of steel I-beam. The carriage is used in a slew-and-clamp mode, positioned by a taut-cable stepping-motor drive, with the position determined by laser metrology. After positioning, the yaw angle of the dihedral can be refined by a remotely-controlled battery-operated mechanism on the carriage.

The fine-motion part of the delay, as cited above, is an air-bearing carriage on a polished granite beam, with 2.4 m of travel (made by the Anorad Corp). The carriage is driven by a brushless linear induction motor under interferometric laser-beam control. Because of the lack of mechanical contact, this system can be driven smoothly enough so that the phase jitter, measured by the laser beam, is appreciably less at all frequencies than that introduced by the atmosphere (Carleton, 1990). Like the siderostats, the delay line is essentially driven by a pulse train whose rate is updated every 0.1 sec. In this case the command-pulse train is compared with a pulse train being generated by the Hewlett-Packard laser-detector electronics at a rate of one pulse per 1/60 wavelength of carriage motion. A counter is counted up by one train and down by the other, and the running sum in this counter provides an error signal for the servo electronics that drive the linear motor (and provides us also a diagnostic signal). This delay-line arrangement allows us about 1/2 hour of observation in any part of the sky at maximum baseline, before having to re-position the coarse-delay carriage. At present we have only one carriage for each function. When we add the third telescope, a second coarse-delay carriage will run on a second track, beside the first, and a second fine-delay carriage will operate on the granite beam under separate interferometric control. The dihedral on this will be offset laterally from that on the first, but the carriages themselves will run end-to-end. We have shown that, for the range of possible locations for the third telescope, the two carriages need never conflict in position on their track, and the time between re-positionings in the worst case will be about 25 min.

**Vacuum system** -- The largest-diameter segment of our vacuum system houses the fine-delay line and all the components associated with relaying the beams into and out of the delay path. It consists of three sections of tank, about 0.8 m in diameter and 9 m in overall length, all of which were obtained as surplus equipment. A 1.8-m section at the corner end rolls away to give access to one end of the Anorad track and to the relay mirrors at the corner. Large ports are located so as to give access to the inner end of the coarse-delay line, which protrudes into the large tanks. These ports also permit access to the beam-exit mirrors and to the mirrors that receive the down-coming beam when a telescope is located in the corner or the first two (5.00-m and 7.04-m) stations on the long arm. Ports are provided for these beams and for the horizontal beams from the two arms. A 10-cm-diameter tube suffices for the short-arm beam, but the long arm requires a 40-cm tube to contain the coarse-delay paths as well as the incoming beams. At each station outside the building there is a junction box that houses the relay mirror that receives the telescope beam, which comes down through a chimney at the top of which is an Infrasil infrared-transmitting fused-silica window (Heraeus-Amersil). When we move a collector we must break the vacuum and move the relay mirror, chimney, and window along to the next station (in order to save the substantial cost of duplicating these components). In order to allow for thermal expansion, all sections of tube between junction boxes are supported separately and joined to stub sections on the boxes by simple neoprene-band seals. These require no machining of the tubing beyond hand-smoothing to give a slight radius to the outer edge of the tube. The band is clamped to the outside diameters of the tubes on either side of the joint, but the actual seal is made when the band is sucked a little way into the gap between tube ends and is thereby pulled tight over each edge. The gap is arranged to be about three times the thickness of the band material, which is 3 mm for the small tubes and 5 mm for the large. The system is evacuated by a Leybold Sogevac SV280 rotary-vane forepump and a Leybold Ruvac WA501 Roots blower, which together can maintain a vacuum better than 1 torr, even in the presence of the input of gas from the air-bearing carriages, which is 15 liters/min at

STP for each. These pumps are located in a shed on a separate 3 x 4-m concrete slab that is several meters from the nearest location of optics. The slab (30-cm thick) is poured on top of a foam material to improve vibration isolation, and the pumps are in turn supported on another spring-suspended slab with a 1-Hz resonant frequency.

Shelter-transporter units -- These units are based on a simple square frame of steel I-beams, 5 m on a side, that rests on rollers running on steel tracks, with one unit on each arm of the array. Either unit may go to the corner position; the third unit will reside on the long arm, always nearer to the corner than the present one. Each unit has two steel frames erected on the base, providing overhead lifting points for the ends of the collector pedestals, which are oriented along the diagonals of the shelters. The pedestals are lifted by steel cables that pass over sheaves to hydraulic cylinders. For shelter, there is additional steel framing that supports a three-section hemi-cylindrical roof, also oriented along the diagonal. At the high end of the pedestal, where the telescope is mounted, there is a fixed roof section. The other two, of successively larger diameter, roll back over this section to open up for observing. In addition, the vertical end wall against which the moving sections close is hinged at the bottom and folds down. The shelter is completed around the sides by wooden walls that, together with the roof sections, have fiberglass insulation. As well as a door on either side, the walls have large adjustable louver openings in each end, and in the vertical section of the fixed-end roof. These allow a large flow of air, in order to assist all structures to come to equilibrium with the ambient air temperature. If wind velocities become high enough to make wind-buffeting a problem, then we can close the louvers appropriately. Since in good weather our winds nearly always have a westerly component, we oriented the pedestals and shelters with their high ends (and fixed-end roofs) toward the west, to give the best shielding.

#### Acknowledgements

We acknowledge the support of a NASA Innovative Research Project grant (NSG-7176) to Harvard Univ., which helped get the project under way, and an NSF grant (AST-9021181) to the Univ. of Wyoming, which helped in beginning an observational program.

#### References

- Carleton, N. P. 1990, in "Amplitude and Intensity Spatial Interferometry", ed. J. Breckenridge, SPIE 1237, 138.
- Gibson, D. M. 1990, *ibid.*, p.166.
- Papaliolios, C., Nisenson, P., and Ebstein, S., 1985, *Appl. Opt.* 24, 287.
- Traub, W. A., 1988, in "High Resolution Imaging by Interferometry", ed. F. Merkle, ESO Conf. Proc. No. 29, 1029.
- Traub, W. A., 1990, *J. Opt. Soc. Amer. A*, 7, 1779.

## The Accuracy of General Perturbations and Semianalytic Satellite Ephemeris Theories

R. N. Wallner, S. J. Casali, W. N. Barker (Kaman Sciences Corporation)

### **Abstract**

Several general perturbations and semianalytic satellite ephemeris theories have been evaluated from the points of view of accuracy, computational efficiency, and operational utility. The theories have been evaluated for both orbit determination and orbit prediction, and over a wide range of orbit types and time, using Space Surveillance Center (SSC) and Space Defense Operations Center (SPADOC) techniques and algorithms. In this phase of the study, all of the theories have been evaluated using the highest level of sensor tasking available; therefore, the results of this phase may not be representative of the accuracies achieved when normal tasking levels are used. The theories that have been evaluated are Simplified General Perturbations (SGP), Simplified General Perturbations 4 (SGP4) / Deep Space Perturbations 4 (DP4), the Hoots Analytic Dynamic Ephemeris (HANDE) theory, the Semianalytic Liu Theory (SALT), and the Draper Semianalytic Satellite Theory (DSST). For comparison, we have also evaluated a high-accuracy Special Perturbations (SP) model.

To date, only near-Earth satellites have been analyzed. In addition, we have not yet evaluated Position Partials as a function of Time 2 (PPT2), as originally planned. The purpose of this paper is to describe the methodology used in the study; numerical results will be presented at the workshop.

### **1. Introduction**

The ultimate purpose of this study is to perform a comprehensive evaluation of various general perturbations (GP) and semianalytic satellite ephemeris theories from the points of view of accuracy, computational efficiency, and operational utility. This paper describes our methodology; the results to date will be presented at the workshop.

The following ephemeris theories have been evaluated: Simplified General Perturbations (SGP)<sup>1</sup>, Simplified General Perturbations 4 (SGP4)/Deep Space Perturbations 4 (DP4)<sup>2</sup>, the Hoots Analytic Dynamic Ephemeris (HANDE) theory, the Semianalytic Liu Theory (SALT)<sup>3</sup>, and the Draper Semianalytic Satellite Theory (DSST). For comparison, we have also evaluated a high-accuracy Special Perturbations (SP) model in the same context as the other theories. The SP model we evaluated used a 12<sup>th</sup> order summed Cowell/Adams Predict-Partial Correct integrator, and modeled perturbative accelerations as follows: the Goddard Earth Model (GEM) 10B 21<sup>st</sup> degree and order geopotential; drag, using the Jacchia 70 dynamic atmosphere; lunar and solar gravity; and solar radiation pressure. In addition, we will be evaluating Position Partials as a function of Time 2 (PPT2)<sup>4</sup> later this year.

The theories have been evaluated for both orbit determination and orbit prediction, and will be evaluated over a wide range of orbit types, although up to this point we have analyzed only near-Earth satellites. The theories have been evaluated as they are used in the currently operational space surveillance systems; i.e. real observational data (as opposed to simulated observations) as well as

<sup>1</sup> SGP is operational in the Space Defense Operations Center (SPADOC) and at several of the Space Surveillance Network (SSN) sensor sites.

<sup>2</sup> SGP4/DP4 is operational in the Space Surveillance Center (SSC), the SPADOC, and at several SSN sites.

<sup>3</sup> SALT and HANDE are operational in the SPADOC.

<sup>4</sup> PPT2 is operational in the Naval Space Operations Center (NAVSPOC).

Space Surveillance Center (SSC) and Space Defense Operations Center (SPADOC) techniques and algorithms have been used. The evaluation has been performed using the highest available level of Space Surveillance Network (SSN) observations in order to give an idea of the best accuracy achievable with current data and techniques. Because these results may not be representative of the accuracies achieved when normal levels of observations are used, in a future phase of the study we will use routine observation levels to determine the "routine operations" results.

The end result of this effort will be a relational database of the study data and results, and software to automate the retrieval of results for any combination of object type, orbit type, etc., so that timely information concerning statistical accuracy of a specific situation can be provided to agencies such as USSPACECOM, the Satellite Control Facility (SCF), and NASA. This database, the astrodynamics code, and the software that we have developed to run many orbit determinations (ODs) and predictions automatically will together comprise a new astrodynamics tool which can be used to either perform further analysis on one of the study theories, or rapidly evaluate a new astrodynamics theory.

## **2. Study Software, Hardware and Data**

### **2.1 Study Testbed**

The software used to conduct the study was the Research and Development (R&D) version of the Goddard Trajectory Determination System (GTDS), which was supplied by the Charles Stark Draper Laboratory. The hardware used was a Silicon Graphics workstation, model IRIS 4D/310GTX, running the operating system IRIX, version 4.0.5.

Because different implementations of the theories may vary in their results, it was necessary to choose a "baseline" implementation. For SGP, SGP4, HANDE, and SALT, we implemented the operational SPADOC 4C Version 1 code for the theories and their associated partial derivatives into GTDS in place of the pre-existing SPADOC 4B code. For DSST and SP, the versions supplied with GTDS were used.

### **2.2 Study Data**

Because the objective of this study is to provide a comprehensive evaluation of the theories' performance, we needed to use satellites in many different orbits. However, because different perturbations dominate in different orbits, it was necessary to subdivide the satellite catalog to distinguish between these effects. In order to create meaningful groups of satellites to study, we chose seven categories of orbits that we believe are representative of the satellite catalog. These categories were chosen to distinguish regions in which different perturbative effects are dominant, while keeping the number of categories small. The orbit categories are described in Table 1. As can be seen, our seven categories represent nearly 93% of the satellite catalog, and contain most common orbits. Note that we have adopted the SSC/SPADOC definition of "deep space" (period greater than 225 minutes).

**Table 1 -- Kaman Orbit Categories**

Category Number	Name	Eccentricity	Mean Altitude <sup>5</sup> (km)	Number in Catalog <sup>6</sup>	% of Catalog <sup>6</sup>
1	Low Near Earth Circular	$0.0 < e < 0.05$	$0 < \bar{h} < 575$	166	2.45
2	Medium Near Earth Circular	$0.0 < e < 0.05$	$575 < \bar{h} < 1000$	2460	36.36
3	High Near Earth Circular	$0.0 < e < 0.05$	$1000 < \bar{h} < 2500$	2014	29.77
4	Near Earth Eccentric	$0.05 < e < 1.0$	$0 < \bar{h} < 2500$	652	9.64
5	Low Deep Space Circular	$0.0 < e < 0.05$	$5700 < \bar{h} < 22000$	115	1.70
6	Molniya/ Geosynchronous Transfer	$0.05 < e < 1.0$	$18000 < \bar{h} < 22000$	403	5.96
7	Geosynchronous	$0.0 < e < 0.05$	$33000 < \bar{h} < 39000$	480	7.09
TOTAL				6290	92.96

In addition, several satellites in each category must be studied in order to be able to make a mathematically valid assessment of a theory's performance within an orbit category. Within each category, a minimum of five satellites are necessary to statistically analyze a group of satellites<sup>7</sup>. For this study, we chose seven representative payloads or large rocket bodies from each orbit category.

Generally, the observational data that is available from the SSC/SPADOC corresponds to a "routine catalog maintenance" level of sensor tasking. This level of sensor tasking (from 1-10 observations<sup>8</sup> per day) was not adequate for this study, because a large number of observations were needed to generate reliable reference ("truth") orbits. Therefore, we arranged for increased sensor tasking on the 49 study satellites. The data collection began on 14 Oct 93 and ended on 30 June 94. The solar activity during this time period is shown in Figure 1. On the chart, F10 is the 10.7 cm solar flux, F10Bar is the 90-day average of F10, and A<sub>p</sub> Max is the maximum value of the geomagnetic index. As can be seen, solar activity was moderate during the period of the study, with the exception of the A<sub>p</sub> spike in mid-April. However, this spike did not affect the study, because we only analyzed deep space satellites (which are

<sup>5</sup> We defined mean altitude as the semi-major axis minus the Earth's mean radius.

<sup>6</sup> As of August 31, 1993.

<sup>7</sup> Platt, T. D. and Herder, L. E., Ranking Satellite Propagators: A Statistical Approach. Proceedings of the 1995 Space Surveillance Workshop, MIT Lincoln Laboratory.

<sup>8</sup> For near-earth satellites, an SSN observation consists of Azimuth, Elevation, Range, and usually Range Rate. For deep space satellites, an observation consists of Azimuth and Elevation (or Right Ascension and Declination), and sometimes Range and Range Rate.

not affected by solar activity) during this time period.

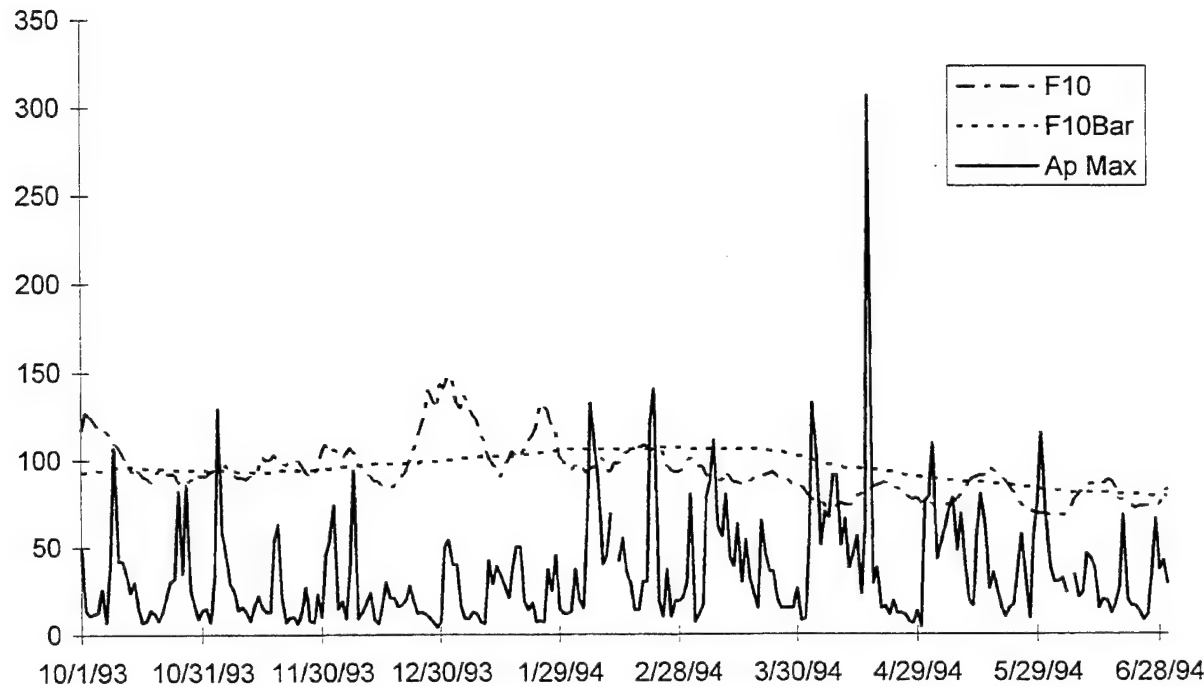


**Figure 1 -- Solar Flux for study period**

On the near-Earth satellites (orbit categories 1-4), we received approximately 150-200 observations per day. However, because of the limited resources of the deep space network, only 10-20 observations per day were generally available on the deep space satellites (orbit categories 5-7). This lack of observations on deep space satellites, coupled with some large data gaps, precluded the creation of reliable reference orbits for deep space satellites. Therefore, we are looking to outside sources for deep space reference orbits. To date, we have acquired precision orbits on the Global Positioning System (GPS) constellation, LAGEOS, and LAGEOS II (orbit category 5). In addition, work is currently proceeding to get precision orbits on the Defense Support Program (DSP) constellation (orbit category 7) from the 1<sup>st</sup> Space Operations Squadron, and we are in contact with authorities in Russia (through Lt. Col. John Rabins, USSPACECOM/ J5S) in order to obtain precision ephemerides on non-military Molniya satellites (orbit category 6).

### **3. Methodology**

We used the following basic methodology in this study: For each satellite and theory, we solved for a state vector using actual SSN observations at many different times, used the theory to predict the satellite's position into the future, and compared the predictions to a "truth" orbit obtained by an independent process. The details of this methodology are given below.

### 3.1 Analysis Intervals

The fundamental span of time used in the study is the Analysis Interval (AI). As shown in Figure 2, each AI consists of one Orbit Determination Interval (ODI), three Prediction Intervals (PIs), and a Reference (“truth”) Orbit (RO) covering the entire span. In order to standardize the OD and prediction time spans, and in keeping with our goal of emulating operational procedures, the SSC algorithm was used to compute the Length of Update Interval<sup>9</sup> (LUPI), which was then used as the length of the ODI and the PIs. The ODIs were between 3 and 14 days for the near-earth satellites studied to date.

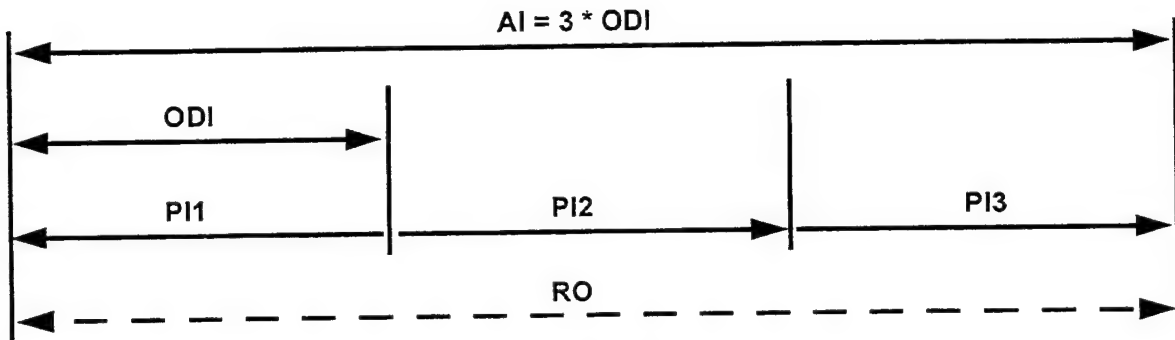


Figure 2 -- Analysis Interval

After the runs for one AI were completed, the AI “slid” forward in time by 3 days, and the process was repeated, using the output theory elements of the previous AI as inputs to the next AI. For example, if for a given satellite, the ODI was 7 days and the AI started on day 100 and ended on day 121, the next AI would span from day 103 to day 124. In this manner, we used the same satellite for many different trials, allowing many different orbital perturbations and geometries to be sampled.

In order to satisfy statistical Central Limit Theorem constraints (reference Platt and Herder), it was necessary to run 36 AIs for each satellite. In addition, a “dummy” AI was performed prior to the test AIs in order to get a good set of theory elements that could be used to start the test AIs.

### 3.2 Theory Evaluation

The theories were evaluated as follows: for each satellite and study theory, an OD was done using one ODI of observations. Next, an orbit prediction was done with each theory over a time span of three ODIs (one over the OD span, and two forward, as shown in Figure 2). Each PI was subdivided into many output intervals; at each of these output times, the predicted orbit was compared to the reference (“truth”) orbit by calculating vector magnitude residuals. This process was repeated for all 36 test AIs.

All theory ODs were run with sensor weights and biases, which were supplied by the 1<sup>st</sup> Command and Control Squadron (1CACS) of Air Force Space Command (AFSPC). The ODs solved for all six orbital elements and the model parameters listed in Table 2, where  $B$ ,  $B^*$  and  $\dot{v}_2$  are the theory drag parameters, and  $C_R$  is the coefficient of reflectivity in the solar radiation pressure model.

<sup>9</sup> The SSC LUPI algorithm is a function of perigee altitude and eccentricity.

**Table 2 -- OD Solution Parameters**

Theory	Category 1	Category 2	Category 3	Category 4
SGP	$\dot{i}/2$	$\dot{i}/2$	-	$\dot{i}/2$
SGP4	B*	B*	-	B*
HANDE	B	B	-	B
SALT	B	B	-	B
DSST	B	B	$C_R^{10}$	B
SP	B	B	$C_R^{10}$	B

DSST differs from the other four GP and semianalytic theories in that it contains many parameters that can be customized for a particular orbit. In order to ensure that our DSST parameter settings were consistent with the way DSST is set up by its users, we asked 1Lt. Dan Fonte of the U.S. Air Force Phillips Laboratory, Astrodynamics Division (PL/VTA) to examine our orbit categories and provide us with parameter settings for each orbit category that balanced accuracy and computational efficiency. Based on his recommendations, we used the settings given in Table 3.

**Table 3 -- DSST Parameter Settings**

Parameter	Category 1	Category 2	Category 3	Category 4
Geopotential (GEM 10B) (AOG <sup>11</sup> )	12x12	8x8	8x8, plus 13 <sup>th</sup> , 14 <sup>th</sup> order resonance	8x8, plus 12 <sup>th</sup> , 13 <sup>th</sup> order resonance
Degree of Zonals (SPG <sup>12</sup> )	12	8	8	8
Max Power of Ecc., Zonal SPG	11	2	2	7
Max freq. in true long., Zonal SPG	25	11	11	17
Degree, order of m-daily (SPG)	12	8	8	8
Tesseral high-frequency terms (SPG)	8x8	OFF	OFF	OFF
$J_2$ squared	AOG & SPG	AOG	AOG	AOG & SPG
$J_2$ - secular tesseral m-daily coupling (SPG)	OFF	OFF	OFF	OFF
Drag (AOG)	ON	ON	OFF	ON
Drag Short Periodics	ON	OFF	OFF	OFF
3 <sup>rd</sup> body effect (AOG)	OFF	ON	ON	ON
3 <sup>rd</sup> body short periodics	OFF	OFF	OFF	OFF
Solar radiation pressure (AOG)	OFF	OFF	ON	ON
Solar radiation pressure (SPG)	OFF	OFF	OFF	OFF

For each AI, the following data was captured: the start and end times of the ODs, the solved-for theory parameters and their respective epochs, all relevant information about the quality of the OD fits, all prediction points (position and velocity), and all CPU execution times.

<sup>10</sup>  $C_R$  was only solved for on four of the seven satellites.

<sup>11</sup> AOG is the DSST Averaged Orbit Generator.

<sup>12</sup> SPG is the DSST Short Periodic Generator.

To ensure adequate orbit coverage during orbit prediction while keeping the data volume down to a manageable level, we have defined a set of prediction output intervals. The intervals for each orbit category, which were defined to ensure a point approximately every 20 degrees of true anomaly, are 5 minutes for orbit categories 1, 2 and 4, and 6 minutes for orbit category 3.

### 3.3 Reference Orbit Generation

In order to generate ROs ("truth" orbits) against which to compare the predicted orbits generated by the study theories, we fitted the SSN observations with the best SP model in our version of GTDS. We consider these fits to be the "truth"; all "errors" are measured relative to them. The perturbations modeled in the ROs were geopotential, using the GEM 10B 21<sup>st</sup> degree and order model; atmospheric drag, using the Jacchia 70 density model with dynamic solar flux; lunar and solar gravity; and solar radiation pressure. All RO fits were run with the sensor weights and biases provided by ICACS.

The ROs were generated by performing successive 3- to 4-day fits, each overlapping the previous fit by 1/2 the span, as shown in Figure 3. The 3- to 4-day span was chosen in order to balance three considerations: 1) The interval must be short enough that drag modeling error is small, 2) Enough observations must be sampled so that the resulting fit is highly accurate, and 3) The span must be long enough to lessen the impact of occasional data gaps in the SSN data. The fits were overlapped so that each fit used many of the same observations as the previous fit, in order to increase the consistency between successive fits.

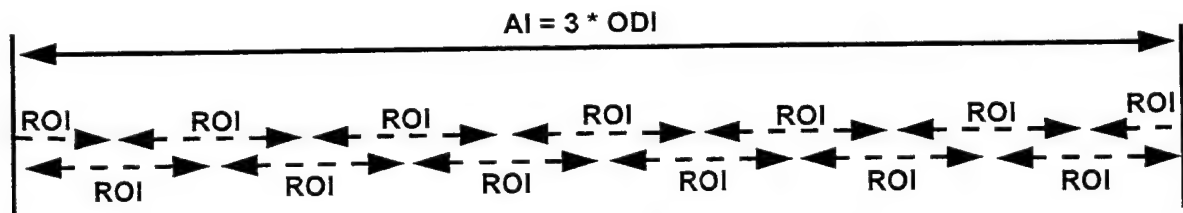


Figure 3 – Reference Orbit Intervals (ROIs)

Additionally, "external" precision ephemerides have been obtained for several satellites for the purpose of calibrating our ROs. The satellites for which we obtained high-precision orbits are ERS-1 (orbit category 2) and TOPEX (orbit category 3)<sup>13</sup>. Since these satellites' positions are routinely known to within centimeters, they make ideal candidates for the calibration.

#### 3.3.1 Reference Orbit Validation

The results of this study are highly dependent upon the quality of the ROs used. Therefore, we have spent a considerable amount of effort to determine the quality of the ROs, and to improve them whenever possible. Four measures of the quality of the ROs were available. These measures were:

- 1) the (unweighted) position Root Mean Square (RMS) of the fits that constituted a single RO;
- 2) the state error covariance matrix associated with each fit;

<sup>13</sup> The ERS-1 and TOPEX orbits were obtained from Dr. Byron Tapley of the University of Texas at Austin.

estimate of overall accuracy. We believe these estimates to be conservative because the fits tended to be less accurate near the ends (especially when the occasional data gaps happened to fall near an end), and because our analysis of the external precision orbits showed that the actual trajectory would in many cases fall somewhere in-between the discontinuity, producing a somewhat lower error than indicated by the abutment. An analysis of the approximately 75 abutments present in the ROs of each satellite showed the following:

- 1) For orbit category 1, the RMSs of the abutments ranged from 45 to 75 meters, with the exception of two satellites for which the RMSs of the abutments were 175 meters and 94 meters. We believe that these relatively large errors are due to unusually high drag on these two satellites. We will be investigate this further in the future.
- 2) For orbit category 2, the RMSs of the abutments ranged from 26 to 52 meters, with one exception for which the RMS was 87 meters.
- 3) For orbit category 3, the RMSs of the abutments ranged from 30 to 55 meters, with one exception for which the RMS was 81 meters.
- 4) For orbit category 4, the RMSs of the abutments ranged from 70 to 124 meters, with one exception for which the RMS was only 27 meters.

Not surprisingly, orbit categories 2 and 3, which are relatively high and circular, gave better results than orbit categories 1 and 4, in which the satellites experience significant drag and, in the case of orbit category 4, significant eccentricity.

Finally, the surest measure of the quality of the ROs was achieved by examining the level of agreement between the ROs and the precise, externally provided ephemerides. The TOPEX and ERS-1 satellites were available for this purpose. In the case of TOPEX, four days of high sensor tasking (over 200 observations per day) was available for analysis, while for ERS-1, 40 days of medium sensor tasking (40-50 observations per day) was available.

Upon performing the four-day fit to SSN observations for TOPEX, we achieved a 39 meter RMS level of agreement with the external ephemeris, with a maximum error of 89 meters. Our analysis of the 40 days of ERS-1 data showed that our RO agreed with the external ephemeris to a 42 meter RMS level, with a maximum error of 141 meters. The agreements with the external ephemerides were achieved despite position RMSs of over 1000 meters, which underscores our previous assertions regarding the insufficiency of the position RMS as a measure of merit. In addition, the fact that the RMS of the abutment errors for ERS-1 was 51 meters indicates that the abutment errors are a reliable measure of RO quality.

The above analysis of the abutment errors in the ROs indicates that overall, our ROs are good to 50-100 meters for orbit categories 1, 2 and 3, and 100-150 meters for orbit category 4. Because these errors are much smaller than the anticipated prediction errors in the theories (particularly for the GP theories), we believe that they are sufficient for the purposes of this study.

### **3.4 Progress to date**

The runs that have been done to date consist of over 11,000 ODs and predictions, and took over 50 days of CPU time to complete, as shown in Table 4. The resulting data consists of over 3.0 GB of ephemerides and OD information, not including the residuals or the externally provided ephemerides.

**Table 4 -- Synopsis of runs performed to date**

Run type	# ODs and Predictions	CPU Time (days)
Theories	7252	27
Reference Orbits	4200	24

## 4. Results

In general, our preliminary results have shown that the theories have performed as would be expected from an examination of the algorithms and force models used: the theories that contain the most complete models (DSST and SP) have performed better, but they take longer to run. At the workshop, we will present charts and graphs depicting the absolute and relative performance of SGP, SGP4, HANDE, SALT, DSST and SP for orbit categories 1-4. The only results available at present are the rankings of the six theories for orbit categories 1-4, which are described in the referenced paper by Platt and Herder. However, note that run time is not a factor in those rankings; prediction accuracy is the only factor considered.

## Acknowledgments

This work was done in response to Contract Support Request (CSR) 95-15-C-ASTR-001, in support of paragraph 3.9.7.3 b.(h) of the statement of work for contract F05603-91-C-0011. The task monitor is Dr. Kitt C. Carlton-Wippern of the Electronic Systems Center of Air Force Materiel Command (AFMC/ESC/SRSS). We are grateful to Dr. Wippern for supporting the study and providing his guidance throughout.

The authors would like to acknowledge the contributions of Dr. Thomas J. Eller and Mr. Kenneth D. Kopke, whose guidance and comments are greatly appreciated.

## Bibliography

Mathematical Foundation for Astrodynamics Theory. NORAD Technical Publication for the Space Surveillance Center Number 008 (TP SSC 008).

A.C. Long, et al, editors. Goddard Trajectory Determination System (GTDS) Mathematical Theory, Revision 1. NASA Goddard Space Flight Center Publication #FDD/552-89/0001 and CSC/TR-89/6001, July 1989.

Platt, T. D. and Herder, L. E., Ranking Satellite Propagators: A Statistical Approach. Proceedings of the 1995 Space Surveillance Workshop, MIT Lincoln Laboratory.

## **Air Force Space Command Space Surveillance Requirements Task**

Maj B. Pimentel (AFSPC/XPX), LtCol S. Willis (AFSPC/DOY), and Mrs. L. Crawford (GTE Government Systems)

### **Abstract**

This paper provides the methodology, completed activities, and initial results for the revalidation and update of the space surveillance requirements in support of the Space Surveillance and Space Control missions. Air Force Space Command (AFSPC) initiated this task in October 1994, since the last major definition and justification of such requirements were completed in the mid 1980's. At that time the emphasis was on specific systems and during a threat environment that has now changed.

### **Introduction**

The AFSPC Space Surveillance Requirements Task, initiated in October 1994, has the following objectives:

- a. Support the Space Surveillance Mission Area Assessment (MAA) by updating user requirements and developing a Space Surveillance Mission Area Concept of Operations (CONOPS).
- b. Support the Mission Need Analysis (MNA) by establishing space surveillance models, performing sensor utility assessments, and supporting the development of an United States Space Command (USSPACECOM) capstone requirements document.
- c. Support future Space Surveillance Network (SSN) architecture decisions.

This task was initiated because of a long-overdue need to update the requirements, as well as an USSPACECOM tasking to revisit requirements and sensor utility assessments as presented in a 1994 USSPACECOM Space Surveillance Study<sup>1</sup>.

### **Study Methodology**

The first phase of this task, the MAA, established a Space Surveillance Mission Area Team (SS-MAT). The SS-MAT, led by AFSPC/XPX (Plans), has members from AFSPC, 1 Command and Control Squadron (1CACS), Space Warfare Center (SWC), 14 Air Force (14 AF), 73 Space Group (73 SG), and USSPACECOM.

The first activity compiled information on the space surveillance requirements documents and studies from prior efforts. The purpose of this compendium was to determine existing requirements documents and their contents, to assess which

requirements might still be valid, and to evaluate prior methodologies and categorization of requirements.

To obtain current space surveillance requirements from the current users, the SS-MAT distributed a survey to over 150 Department of Defense (DoD) and civil organizations. These organizations included users getting space products from 1CACS, satellite owner/operators, acquisition agencies, research and development (R&D) laboratories, intelligence community, and sensor sites. The survey requested the requirements in terms of data type, frequency, accuracy, and the justifications for these requirements. The responses were then incorporated into the Space Surveillance Requirements document.

To support the sensor utility assessments during the MNA phase, a survey was also sent to 50 military, civil, and defense organizations to determine the availability and capabilities of existing SSN models and analysis tools.

AFSPC/IN provided an updated threat environment assessment that included for example, world-wide launch facilities, and types, numbers, and sizes of satellites.

The SS-MAT formulated a space surveillance validation structure and process that categorized requirements by tasks, conflict spectrum, users, and time period. Requirements were reviewed to ensure that they were quantified (e.g., timeliness, frequency of information, and data accuracy), as well as documented with the justification and source for the requirement.

With this information, AFSPC provided an initial draft requirements document to support the development of a capstone USSPACECOM surveillance requirements document. Additional updates are anticipated with a coordinated document by April 1995. Additionally, a plan would be presented to request the retirement of obsolete requirements documents.

The SS-MAT will develop a Space Surveillance Mission Area CONOPS that will be consistent with the tasks and activities in the Space Control Mission Area Plan (MAP) and requirements document. Since the establishment of space surveillance in the mid 1950s, a Space Surveillance Mission Area CONOPS has not existed.

The SS-MAT also will be completing an initial MNA using existing analytical tools to identify and prioritize deficiencies, given the new set of requirements and the current SSN baseline capabilities.

The task schedule and completed activities to date are shown in Figure 1.

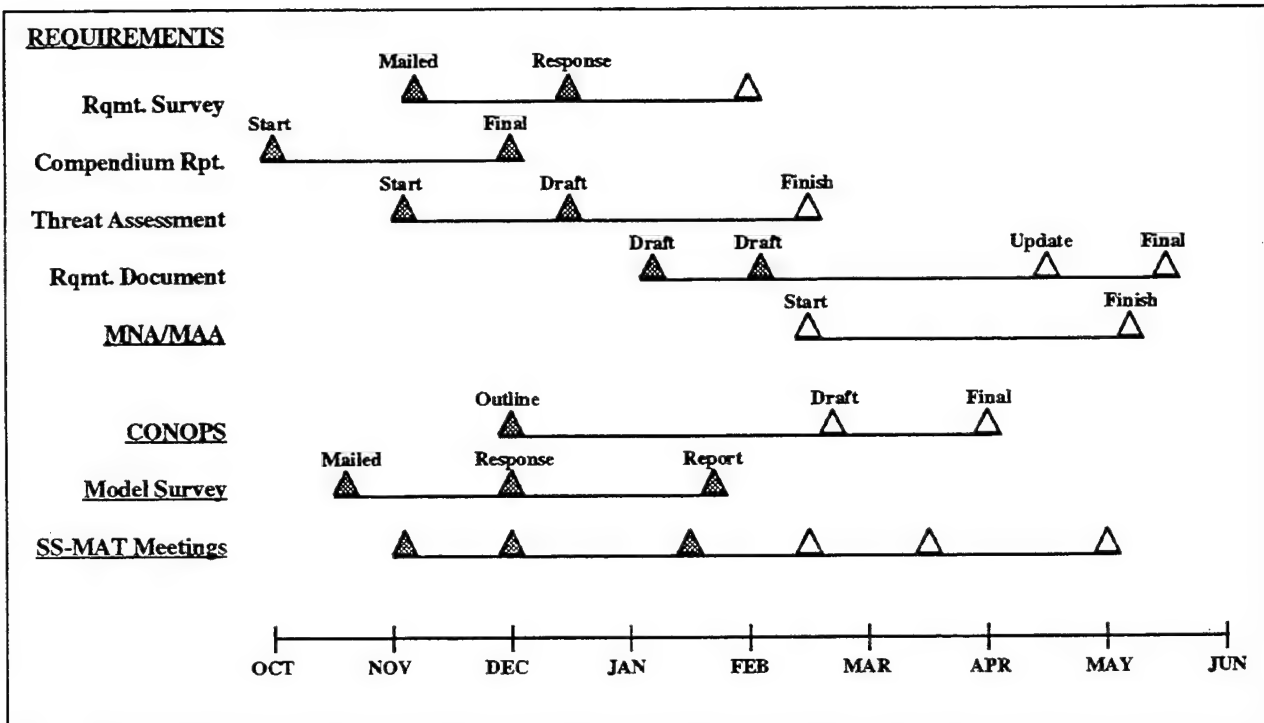


**Figure 1. Space Surveillance Requirements Task Schedule**

#### Results - Prior Efforts Compendium

There are over 70 surveillance requirements documents, dated between 1957 and 1994, and ranging from international treaties to architectures. The early foundation requirements documents included the 1979 ADCOM 03-79 Statement of Operational Need (SON) for Space Defense, the 1981 Surveillance Mission Element Need Statement, the 1985 Refined Space Surveillance Requirements (RSSR) in Support of Space Defense, and the 1988 USSPACECOM Required Operational Capability 88-01 for Space Surveillance. These documents usually followed the activation of a major or unified command assigned with a space surveillance or space defense mission. The space surveillance requirements have not been reassessed for the surveillance mission area or the SSN as a whole since the 1985 RSSR. Emphasis on the requirements at that time was to support the Air-Launched Anti-Satellite system.

In 1993 with decreasing funding and support for the Kinetic Energy Anti-Satellite (KE ASAT) and Space Defense Initiative (SDI) programs, AFSPC started activities to review the current SSN and requirements. This followed the realization that the SSN had been developed without a master plan, that most of its assets were acquired from other agencies and originally developed for other missions, that the last set of validated surveillance requirements were from the mid-1980's time period, and that budget cuts required more stringent sensor utility analysis.

Shortfalls of many of these prior efforts<sup>2</sup> to revalidate the surveillance requirements and provide a SSN architecture included:

- a. Requirements were geared towards specific systems (e.g., KE ASAT).
- b. Requirements were not quantified or validated in the current environment (such as resulting from Desert Storm and the termination of the Cold War).
- c. Changing threat descriptions have not been documented, especially to represent the rest of world country launch and satellite capabilities.
- d. Limited user involvement, concurrence, and endorsement precluded community-wide acceptance.
- e. Requirements revisit activities were hampered by shortened schedules, limited agency participation, and lower task priority.
- f. Recent requirements efforts were bogged by the legacy of the over 70 already validated requirements documents.
- g. The requirements and acquisition processes were not well understood for the SSN's "system of systems".

#### Results - Surveillance Model Survey Results

The results of the Surveillance Model Survey<sup>3</sup> included a 62 percent response. Several software tools were found which performed either part of the SSN functions or can be used to build a SSN model, but there is no comprehensive model available. Before additional efforts can be made in this area, the high level model requirements used to assess the responses need to be reviewed and validated.

#### Results - Surveillance Requirements

The surveillance requirements were categorized by time period, conflict spectrum, user, task, and function. The categorization provides insight on which requirements must be supported for the Space Control mission and which ones may be considered goals. The time period was defined as current (through the year 2003 and corresponding to the budget cycle) and future (after the year 2003). Conflict spectrum was separated into peacetime, regional/global conflict, and global war.

User has been defined as follows:

- a. DoD Operations - All military services to include AFSPC, USSPACECOM, Naval Space Command, U.S. Army Space Command, and national security-related agencies such as DIA and NAIC.
- b. DoD R&D - Laboratories, such as Phillips, Los Alamos, and Lawrence Livermore, associated with space-related experiments.
- c. Civil - Primarily includes NASA and NOAA.
- d. Commercial - All commercial space-related companies, including those associated with launch facilities and those having on-orbit satellites.
- e. United Nations (UN)/Foreign - All foreign space organizations, such as the European Space Agency.

The space surveillance mission tasks have been defined as follows:

- a. Maintain Resident Space Object (RSO) Catalog - Routine monitoring and update of the position and status of detectable earth orbiting objects. Includes sensor tasking, sensor observations, C4 capabilities and connectivity throughout the SSN, orbit determination/other products processing at the C2 centers.
- b. Maintain Space Order of Battle (SOB) - Detect, track, identify, and report on activities associated with SOB satellites. SOB satellites are those of particular concern to military and other national security-related organizations.
- c. Support Launch and On-Orbit Operations - Compute and report on windows of safe passage, early orbit determination, and piece discrimination, and payload deployment for announced space launches. Compute and report on positional data for analyzing space system or geophysical anomalies, orbital conjunctions, collision avoidance, rendezvous, payload deployments, and deep space probes. Both manned and unmanned activities are supported.
- d. Support Counterspace - Includes both offensive and defensive counterspace. Compute and report on data for target sets and processing of data for post-mission strike assessments. Detect and warn satellite owner/operators of possible hostile space acts. After such acts, collect data for damage assessment. Provide overflight warning to military forces worldwide.
- e. Support Intelligence Needs - Collect data for intelligence agencies who are conducting Scientific and Technical (S&T) and other intelligence evaluations.
- f. Monitor Non-Hostile Objects/Events - Detect, track, identify, process, and report data on decays (normal and TIP), debris, and breakups of space objects. Detect, track, identify, process, and report meteorite and asteroids entries (support to planetary defense).

The surveillance functions have been defined as follows:

- a. Surveil - Detect and track in a timely fashion orbital or newly launched objects. Once detected, objects must be tracked by coordinating sensor assets, using coverages, revisit schedules, and sensor measurement accuracies to adequately support the space track and space intelligence databases.
- b. Identify/Characterize - Determine the status of orbital or newly launched objects; assess the mission and intention, ownership, capabilities, and vulnerabilities of payloads; determine the object's size, shape, motion, configuration, etc.
- c. Maintain Databases - Create or update entries in the space track and space intelligence databases, to include continuous receipt, processing, and analysis of satellite positional or intelligence data.

- d. Disseminate Information/Products - Disseminate information from the databases, for example, space event notifications and reports (e.g., maneuvers, decays, collision avoidance) and updated element sets.

Figure 2 shows the matrix of space surveillance task versus function. In allocating the requirements to this matrix, there are some instances where there are no entries.

Task	Function			
	Surveil (Detect/Track)	Identify/ Characterize	Maintain Databases	Disseminate Info/Products
Maintain RSO Catalog				
Maintain SOB				
Support Launch and On-Orbit Operations				
Support Counterspace				
Support Intelligence Needs				
Monitor Non-Hostile Objects/Events				

**Figure 2. Surveillance Task/Function Matrix**

#### Results - CONOPS

The CONOPS is currently in draft outline format. This effort has been on hold waiting for the tasks derived from the Mission Area Assessment process supporting the Space Control MAP.

#### Conclusions

The surveillance requirements as documented<sup>4</sup> address the space surveillance mission area and the SSN as a “system of systems”, rather than sensor-specific. The requirements have been updated to reflect the current threat and space environment, as provided by AFSPC/IN. The updated threat environment describes the increased worldwide launch capabilities, and the changing emphasis to deep space satellites. Also to be considered in the space environment is the impact of certain non-DoD users, such as commercial constellations containing hundreds of payloads.

Current efforts focus on documenting the driving requirements for the SSN, the key attributes necessary for requirement satisfaction, and the justification for the requirements. These requirements then form the basis for future analysis of the Space Surveillance force structure to determine sensor utility and future upgrades.

Follow-on actions from this task will include developing comprehensive analysis tools (such as a SSN model and requirements traceability database), completing detailed MNAs and sensor utility assessments, updating the deficiencies and their

prioritizations, developing concepts and solutions, and evaluating applicable technologies. After these activities, and in conjunction with other agencies, surveillance modernization roadmaps, cost and operational effectiveness analysis, and operational requirements documents can be developed.

#### References

- 1) USSPACECOM/J5S, Space Surveillance Study (U), June 1994, SECRET.
- 2) AFSPC/DOY (GTE Government Systems), Space Surveillance Prior Efforts Compendium Report, 1 December 1994, UNCLASSIFIED.
- 3) AFSPC/DOY (GTE Government Systems), Space Surveillance Models Survey Results, 13 January 1995, UNCLASSIFIED.
- 4) AFSPC, Air Force Space Command Space Surveillance Requirements (U), draft, 6 February 1995, SECRET/NOFORN/WNINTEL.

## **Ranking Satellite Propagators: A Statistical Approach**

T. D. Platt, Dr. L. E. Herder (Kaman Sciences Corporation)

### **ABSTRACT**

This paper describes the statistical approach needed to transform sets of orbital propagator residuals into discrete rankings of propagators for an individual satellite and for groupings of five or more satellites. Discussion includes the basis for the data used in the study, constraints imposed by the data used, and an explanation of how valid the results are from a rigorous statistical reference.

Statistical algorithms used to calculate the propagator rankings and their validity include: Bonferroni method, Central Limit Theorem, Shapiro-Wilks Chi-Square Test for Normality, Wilcoxon T Non-Parametric median comparisons, Hartley's test for Homogeneity of Variance, Hypothesis Testing for Homoscedasticity, Hypothesis Testing for Equality of Means, Orthogonal matrix manipulation for transformation of ratio variables to an ordinal reference basis, Fisher-Behrens Adjusted Degrees of Freedom, Kruskal-Wallis H Tests for Non-Parametric grouping of discrete propagator rankings and groups of satellite results and the Fisher's Least Significant Difference (LSD) test.

We can use the described statistical process to find a ranking for a set of orbital propagators such that can be sure that the ranking is correct, and that the better propagator will show evidence of smaller position residual values over time than for a worse propagator. This process can be used to compare and contrast orbital propagation techniques in terms of their efficacy of expected residual position error.

### **INTRODUCTION**

The ultimate purpose of the study<sup>1</sup> of which this statistical analysis is a part, is to perform a comprehensive evaluation of various general perturbations (GP) and semianalytic satellite ephemeris theories from the points of view of accuracy, computational efficiency, and operational utility. This paper describes the methods used to determine when statistically significant differences existed in the prediction accuracies (as measured by the position residuals) of the propagators, and to create rankings showing the relative quality of the theories. This paper does not address the issues of computational efficiency or operational utility.

The following ephemeris theories have been evaluated: Simplified General Perturbations (SGP)<sup>2</sup>, Simplified General Perturbations 4 (SGP4)/Deep Space Perturbations 4 (DP4)<sup>3</sup>, the Hoots Analytic Dynamic Ephemeris (HANDE) theory, the Semianalytic Liu Theory (SALT)<sup>4</sup>, and the Draper Semianalytic Satellite Theory (DSST). For comparison, we have also evaluated a high-accuracy Special Perturbations (SP) model in the same context as the other theories. The SP model we evaluated used a 12<sup>th</sup> order summed Cowell/Adams Predict-Partial Correct integrator, and modeled

<sup>1</sup> Wallner, R., Casali, S., and Barker, W., "The Accuracy of General Perturbations and Semianalytic Satellite Ephemeris Theories," MIT/LL 13th Space Surveillance Workshop Proceedings.

<sup>2</sup> SGP is operational in the Space Defense Operations Center (SPADOC) and at several of the Space Surveillance Network (SSN) sensor sites.

<sup>3</sup> SGP4/DP4 is operational in the Space Surveillance Center (SSC), the SPADOC, and at several SSN sites.

<sup>4</sup> SALT and HANDE are operational in the SPADOC.

perturbative accelerations as follows: the Goddard Earth Model (GEM) 10B 21<sup>st</sup> degree and order geopotential; drag, using the Jacchia 70 dynamic atmosphere; lunar and solar gravity; and solar radiation pressure. In addition, we will be evaluating Position Partials as a function of Time 2 (PPT2)<sup>5</sup> later this year.

This paper will not describe the methodology used to generate the position residuals used to create the rankings. That methodology can be found in the related paper by Wallner, Casali and Barker<sup>1</sup>.

## DATA SAMPLING

As can be seen in the related paper<sup>1</sup>, thirty-six different starting time points were used for each satellite. The value of 36 starting points reflected our desire to have as near a random configuration as possible, given the constraints of the time required to generate all the reference orbits on our hardware platform, and accounting for the Central Limit Theorem minimum value of 30+ degrees of freedom.

The Central Limit Theorem for statistics states that : If  $Y(1) \dots Y(N)$  are independent and identically distributed random variables such that the expected value of  $Y(i)$  is the mean and the expected value of the variance of  $i$  is  $\sigma^{**2} < \infty$ , then the distribution function  $U$  of sample size  $n$  , represented as

$$U_n = \left( \frac{\bar{y} - \mu}{\sigma / \sqrt{n}} \right) \quad (1)$$

where

$$\bar{y} = \frac{1}{n} \sum_{i=1}^n y_i, \quad (2)$$

then the distribution function converges to a standard normal distribution as  $n$  goes to infinity, in other words,

$$P(a \leq U_n \leq b) \rightarrow \int_a^b \left( \frac{1}{\sqrt{2\pi}} \right) e^{-u^2/2} du \quad (3)$$

as  $n$  goes to infinity. Usually, a value larger than 30 for  $n$  will ensure that  $U$  can be approximated as a normal distribution<sup>6</sup>.

---

<sup>5</sup> PPT2 is operational in the Naval Space Operations Center (NAVSPOC).

<sup>6</sup> Mendenhall, W., et al., "Mathematical Statistics with Applications," Boston: PWS-Kent, 1990: p. 319-320.

The 36 reference points equated to 35 degrees of freedom, which was useful for table lookup values for the statistics while minimally satisfying the Theorem constraint.

The propagators began at these starting points and created position residuals over two Orbit Determination Intervals (ODIs) in time, that is, from about 6-50 days in the future depending on orbit type. Twenty time points spaced evenly across these Prediction Intervals (PIs) were selected as input points to the process. This spread gave us about three sample points per day for near-earth orbits (one point per 2 orbital revolutions or revs), and one point per 2 1/2 days for deep-space objects (one point per two to five revs). Thus, we sampled 36 intervals \* 20 time points \* 7 propagators, or 5040 points per satellite within the study.

Because the objective of this study is to provide a comprehensive evaluation of the theories' performance, we needed to use satellites in many different orbits. However, because different perturbations dominate in different orbits, it was necessary to subdivide the satellite catalog to distinguish between these effects. Within each orbit category, 7 satellites were studied. The orbit categories are defined as follows:

Kaman Orbit Categories					
Category Number	Name	Eccentricity	Mean Altitude (km)	Number in Catalog*	% of Catalog*
1	Low Near Earth Circular	$0.0 < e < 0.05$	$0 < \bar{h} < 575$	166	2.45
2	Medium Near Earth Circular	$0.0 < e < 0.05$	$575 < \bar{h} < 1000$	2460	36.36
3	High Near Earth Circular	$0.0 < e < 0.05$	$1000 < \bar{h} < 2500$	2014	29.77
4	Near Earth Eccentric	$0.05 < e < 1.0$	$0 < \bar{h} < 2500$	652	9.64
5	Low Deep Space Circular	$0.0 < e < 0.05$	$5700 < \bar{h} < 22000$	115	1.70
6	Molniya/Geo-synchronous Transfer	$0.05 < e < 1.0$	$18000 < \bar{h} < 22000$	403	5.96
7	Geosynchronous	$0.0 < e < 0.05$	$33000 < \bar{h} < 39000$	480	7.09
TOTAL				6290	92.96

\* As of August 31, 1993

Please note that, at this time, only near-earth satellites (orbit categories 1-4) have been studied.

### STATISTICAL APPROACH

Before applying any Hypothesis tests, we had to determine the means by which we would create the ordinal rank of the propagators as we tested the 21 pairs ( $7!/ (2!5!)$ ) or 7 items combined 2 at a time) of propagator *A* vs propagator *B* (assuming 7 propagators). We also had to concern

ourselves with the Bonferroni method error compounding that would naturally occur. Bonferroni states a standard principle of probability theory in a different light<sup>7</sup>. If the probability of an event is  $A$ , then the probability of  $n$  independent events occurring is  $A^{**n}$ . As  $n$  increases, the chance of all events being true decreases, and decreases exponentially, although not quite as rapidly if  $A$  is very close to 1.0 to begin with. Since we wanted to find statistically significant results, and yet many tests must be made to determine our results, a major question we have to resolve is what level of alpha significance can we choose that will still allow us to see significant results, and yet will not be so low as to have the implications of Bonferroni invalidate our results. For a typical satellite, we will have to make 21 tests times 20 time points, or 420 tests. If, as we shall see, we made 42 additional Hypothesis tests for this satellite, then we need to make 462 assumptions that in each case, all of our Hypothesis tests are true for there to be no error. It can be shown that the chance of 7 Hypothesis errors (using alpha level of 0.975) or less across these tests is .9973+. In other words, we are 3 sigma sure that at least .9848 or 455/462 of all of our Hypothesis tests are correct for a given satellite. This gave us a good chance of finding statistically significant differences among the propagators while limiting the amount of expected testing error due to the alpha level setting of 0.975.

This brings us to an interesting point in our study. Whether comparing medians or means, how can we rank the differences into ordinal form? We have ratio-style results for mean testing, and non-parametric testing to no less than the ordinal level for median testing. This implies that only an ordinal rank can be statistically correct for comparing propagator ranks. Educated insight to the problem reveals an elegant answer to ranking the propagators.

Assume we have  $n$  propagators to rank. The rank sum of these propagators is the sum of  $1$  to  $n$ , or  $(n)(n+1)/2$ . The beginning rank of the propagators must be the median rank possible for them, or  $(n+1)/2$ . Since this rank value can range as a number delineated by values of 1/2, adjust the ranks of the propagators from equality by 1/2 up or down as appropriate, depending on whether the propagator's mean or median was statistically larger, or smaller respectively as a result of the Hypothesis test used.

Thus, if there are 7 propagators, then the initial rank of the propagators is 4, and if a propagator has a better mean/median by Hypothesis testing for all of its comparisons to the other 6 propagators, then its final ranking will be  $4 + (-0.5 * 6)$ , or 1. Likewise, a propagator whose mean/median comparisons are worse than all other 6 propagators will receive a rank of  $4 + (+0.5 * 6)$  or 7. Thus we can achieve ordinal rankings for the propagators at a time point  $i$ .

We have 36 residual values at time point  $i$  for each propagator under study. If we form distributions of these values, we can perform the standard Hypothesis Tests for Equality of Means given the following constraints:

- a. The distributions are Normal, and

<sup>7</sup>

Byrkit, Donald R., "Statistics Today: A Comprehensive Introduction," Menlo Park: Benjamin/Cummings, 1987: p. 448-450, 475, 552-556, 613, 621, 623-627.

b. The variances between any two propagators are equal<sup>8</sup>.

To test constraint a), we used a tailored Chi-square goodness of fit test for small samples, specifically the Shapiro-Wilk's Chi-Square Test for Normality ( $N < 50$ ). We did not use the standard Chi-Square test because it is not suited for small sample sizes. Shapiro-Wilk's test is well documented as supporting small sample sizes<sup>8</sup>. The null Hypothesis was that the residuals formed a normal distribution. We tested at the 0.975 alpha level of significance, that is, for each propagator, there was a 2.5% chance that if we said that a distribution was normal, it was in fact, not. Shapiro-Wilks uses the test value  $W$  where

$$W = b^2 / S^2,$$

$$S^2 = \sum_{i=1}^n (y_{(i)} - \bar{y})^2 \quad (4)$$

and

$$b = \sum_{i=1}^k a_{n-i+1} (y_{(n-i+1)} - y_{(i)}). \quad (5)$$

The quantity  $k$  in the last equation is table defined as  $n = 2k$ . The  $a$  coefficients are table-oriented for the sample size  $n$ . The  $W$  generated is then compared to another table value for the alpha level desired<sup>8</sup>. If  $W$  is less than the table value, then we can reject the null Hypothesis and claim that the propagator's distribution formed by the set of 36 residuals has evidence to suggest that it is not normal.

The condition for b) is less concerning, but still a necessary condition for evaluating the data. We can perform a simple test of variance, the Hartley's Test for Homogeneity of Sample Variance, to determine quickly if there are any combinations of sets of propagator variance that are unequal<sup>7</sup>. Again at the 0.975 alpha-level of significance, all propagators can be assumed to have equal variance when  $F_{\max} \leq F(p, 35)$  where<sup>7</sup>

$$F_{\max} = s^2(\max) / s^2(\min) \text{ across all propagators and } p = \# \text{ of propagators, and } F(p, 35) \text{ is a table value at } \alpha = 0.975. \quad (6)$$

If the Hartley's test fails, we still have a normal distribution, but we must perform individual Hypothesis Tests for Homoscedasticity<sup>7</sup>. This is performed using standard methods as shown:

<sup>8</sup>

Dunn, Olive J. and Clark, Virginia C., "Applied Statistics: Analysis of Variance and Regression, 2nd Ed.", New York: John Wiley & Sons, 1987: p. 396-398, 435-437.

Reject null hypothesis of  $H_0: \sigma_1^2 = \sigma_2^2$  if where

$$F^* = \frac{s_1^2}{s_2^2} \quad (7)$$

$$F^* > F_{\alpha} \{n_1 - 1, n_2 - 1\}.$$

When the above test fails, the two propagators can still be compared despite their unequal variances, but the number of shared degrees of freedom is something less than the standard  $n_1 + n_2 - 2$  degrees of freedom<sup>7</sup>. Instead, we must perform the calculation to determine the Fisher-Behren's new T-value:

$$t' = t_{\alpha/2} \{v\} \text{ where}$$

$$v = INT \left[ \frac{\left( \frac{s_1^2 + s_2^2}{n} \right)^2}{\left[ \frac{s_1^4 + s_2^4}{(n^2)(n-1)} \right]} \right] \text{ and } n = n_1 = n_2 \quad (8)$$

In our case where  $n_1$  and  $n_2$  are both equal to 36, the shared degrees of freedom will be an integer of something less than 70. This new T-value will be used in a look-up table for adjusting the test statistic when performing the Hypothesis Test for Equal Means.

We have reached the point in the process where we either have a normal distribution of data across all of the propagators, or, at least one set of propagator residuals are non-normal. For the normal case, we may proceed with the more robust Parametric test of Hypothesis Testing for Equality of Means adjusted as necessary for degrees of freedom using Fisher-Behren. If we have a non-normal case, we can proceed with the most powerful Non-Parametric Hypothesis test for equality of medians available, the Wilcoxon T-Test.

Given that we could test at the 0.975 alpha level of significance, the Non-Parametric median comparison for the Wilcoxon T-Test proceeds as follows<sup>7</sup>:

For the case of 36 orbit starting points,  $n > 25$ , therefore

Calculate

$$Z^* = (T_+^* - \mu_T) / \sigma_T$$

$$\mu_T = n(n+1)/4,$$

$$\sigma_T = \sqrt{n(n+1)(2n+1)/24} \quad , \text{and}$$

$T_+^*$  is the positive sum of the ranks of residual differences such that  $[y_i(A) - y_i(B)] > 0$  are the only contributing factors where propagator A is vs propagator B.

Test the null hypothesis  $H_0: Md_A = Md_B$  that the median value of propagator A equals B.

Reject  $H_0$  where:  $|Z^*| > Z_{\alpha/2}$

This can give us statistically significant results of evidence when two propagators have unequal medians.

If all propagators are normal, then the Hypothesis Test for Equal Means<sup>7</sup> is used for the normal distribution time points as follows:

$$H_0: \mu_1 = \mu_2$$

Reject  $H_0$  if  $|t^*| > t_{\alpha/2}$

$$\text{where } v = n_1 + n_2 - 2$$

or

$$v = t' \text{ if } \sigma_1^2 \neq \sigma_2^2 \text{ and } t^* = \frac{\bar{x}_1 - \bar{x}_2}{\sqrt{\frac{s_1^2 + s_2^2}{n}}} \text{ where } n = n_1 = n_2.$$

In either the normal or non-normal case, rejection of  $H_0$  implies that the pairs of propagators being compared have statistically unequal values. We then adjust the rank of the propagators appropriately. After 21  $H_0$  tests, we will have an ordinal rank set denoting the propagator results for one time point.

After testing the 20 time points, we will have 20 time point's worth of ordinal rank sets denoting how the propagators perform as a result of 420 Hypothesis tests. In order to combine these into an overall ranking for the satellite in question, we turn to the robust Non-Parametric Kruskal-Wallis H test for median comparisons. Note that we do not use what might be considered by some to be viable tests of Analysis of Variance. This is because we cannot assume that the data involved will be normally distributed<sup>7</sup>. The H test will determine if the null Hypothesis that all median ranks of the propagators are equal is viable. The H Test proceeds in the following manner<sup>7</sup>:

Suppose we obtain  $k$  independent random samples

(of size  $n_1, n_2, \dots, n_k$ ) from populations

of median  $Md_1, Md_2, \dots, Md_k$

Test  $H_0: Md_1 = Md_2 = \dots = Md_k$  by:

if  $\left( N = \sum_i n_i \right)$  then (11)

$$H^* = \frac{12}{N(N+1)} \left( \frac{R_1^2}{n_1} + \frac{R_2^2}{n_2} + \dots + \frac{R_k^2}{n_k} \right) - 3(N+1)$$

where  $R_i$  is the rank sum of the observations

and  $H_0$  is rejected when

$$H^* > \chi_{\alpha}^2 \{k-1\}.$$

If the H test finds no evidence to suggest that there is not even a single pair of median ranks that are unequal, the ranking for the satellite will show all propagator ordinal ranks as equal.

If the H test finds evidence to suggest that there is at least one pair of median ranks that are unequal, then we will proceed to the Fisher's Least Significant Difference (LSD) test to determine which propagators have differing medians of rank. The mechanism for the Fisher's LSD test is shown below<sup>7</sup>:

$$LSD = Z_{\alpha/2s} \sqrt{\frac{N(N+1)}{6n}} \text{ where } s = k(k-1)/2 \text{ where}$$

$k = \# \text{ of treatments and two propagators are}$

$\text{significantly different when } |\bar{R}_i - \bar{R}_j| > LSD \text{ where}$  (12)

$\bar{R}_x$  is the Kruskal-Wallis rank sum of propagator

$i$  or  $j$  as appropriate, divided by the sample size.  $N$  is

$\text{defined as above in the Krusal-Wallis H test.}$

We start again with our assumption that all ranks are equal by the same definitions shown previously. This again means that we start with ranks of 4 when using 7 propagators, and adjust the ordinal ranking as previously shown by +/- 0.5 when the Fisher's LSD test finds differences in median ranks. Again, this will require 21 Hypothesis tests.

We will now have sets of orbital propagator rankings for each satellite. If the satellites belong to similar orbit category classes, we can combine these sets of ordinal rankings to get a class ranking of the propagators using the above Kruskal-Wallis H test and the Fisher's LSD test and a further 21 Hypothesis tests. Any differences from the nominal rank that the propagator is given

for its comparison testing are directly and statistically a result of differences in the data obtained from the orbit propagation for that category.

## RESULTS

Our results show that the theories perform as would be expected by examining the algorithms and force models used: the theories that contain the most complete models (DSST and SP) have performed better, although they take longer to run. When interpreting the following results, it is important to note that only the position residuals are statistically accounted for, not run time or any other operational factor. For this reason, when run time and other factors are taken into account, the operational desirability of the theories will likely be different than these rankings.

When interpreting rank data, remember that a rank of 1.0 indicates that the propagator is statistically better than all other propagators. Two propagators tied at a particular rank are also statistically “tied” in position residuals. Any difference in rank between two propagators for the same prediction span, even a 0.5 difference, is enough to claim that significant statistical differences were observed between the two propagators. However, the magnitude of the differences are not indicated by these results.

Given the data from the related study<sup>1</sup>, the following charts were obtained using the statistical approach outlined above. Because the PPT2 theory has not yet been studied, the rankings generated by the methodology described above were adjusted manually to reflect the proper ranks for only six theories.

Category 1 Orbit Propagator Rankings						
Predict Span	SP	DSST	SALT	HANDE	SGP4	SGP
1 day	1.0	2.0	3.0	4.5	4.5	6.0
2 day	1.0	2.5	2.5	4.5	4.5	6.0
7 day	1.0	3.0	2.5	4.0	4.5	6.0
1 ODI	1.0	3.0	2.5	4.0	4.5	6.0
2 ODI	1.0	3.0	2.5	4.0	4.5	6.0

Category 2 Orbit Propagator Rankings						
Predict Span	SP	DSST	SALT	HANDE	SGP4	SGP
1 day	1.0	2.0	3.5	5.5	3.5	5.5
2 day	1.0	2.0	3.5	5.5	3.5	5.5
7 day	1.0	2.0	3.0	5.0	5.0	5.0
1 ODI	1.0	2.0	3.0	5.0	5.0	5.0
2 ODI	1.0	2.0	3.0	4.0	5.0	6.0

Category 3 Orbit Propagator Rankings						
Predict Span	SP	DSST	SALT	HANDE	SGP4	SGP
1 day	1.0	2.0	3.0	5.5	5.5	4.0
2 day	1.0	2.0	3.0	5.5	5.0	4.5
7 day	1.0	2.0	3.5	6.0	5.0	3.5
1 ODI	1.0	2.0	3.5	6.0	5.0	3.5
2 ODI	1.5	1.5	3.5	6.0	5.0	3.5

Category 4 Orbit Propagator Rankings						
Predict Span	SP	DSST	SALT	HANDE	SGP4	SGP
1 day	1.0	2.0	3.0	4.0	5.0	6.0
2 day	1.0	2.0	3.0	4.0	5.0	6.0
7 day	1.0	2.5	2.5	4.0	5.0	6.0
1 ODI	1.0	2.5	2.5	4.0	5.0	6.0
2 ODI	1.0	2.0	3.0	4.0	5.0	6.0

## SUMMARY

We can create statistically significant rankings of orbital propagators, by class or by satellite, given position residual information. The rigorous statistical procedure followed ensures that the conclusions that may be drawn upon the data are biased only as a result of either sampling or collection methods, which are of merit for debate and study within the astronomical community. Every effort was made to reduce the instance of error as a result of error compounding in Hypothesis testing. There are no more than 7 Hypothesis errors across 462 required Hypothesis tests for each satellite's data at a 3 sigma level of confidence. We can therefore conclude that the answers given by using this method are viable for use in scientific research.

## ACKNOWLEDGMENTS

The authors are grateful to Dr. Samuel Houston, Chairman Emeritus of The University Of Northern Colorado's Statistics department for his appraisal and insight into the concepts of this paper.

The authors are grateful to our customer, ESC, for funding the research of this paper. The authors are further indebted to Dr. Kitt Carlton-Wipperfurth, AFMC/ESC/SRSS, for his sponsorship, contributions and review of the contents of this paper and the overall project.

The authors are also grateful to Dr. Thomas J. Eller, AIAA Fellow, for help in balancing statistical rigor with practical utility to help communicate our concepts to a variety of audiences.

# REPORT DOCUMENTATION PAGE

*Form Approved  
OMB No. 0704-0188*

Public reporting burden for this collection of information is estimated to average 1 hour per response, including the time for reviewing instructions, searching existing data sources, gathering and maintaining the data needed, and completing and reviewing the collection of information. Send comments regarding this burden estimate or any other aspect of this collection of information, including suggestions for reducing this burden, to Washington Headquarters Services, Directorate for Information Operations and Reports, 1215 Jefferson Davis Highway, Suite 1204, Arlington, VA 22202-4302, and to the Office of Management and Budget, Paperwork Reduction Project (0704-0188), Washington, DC 20503.

1. AGENCY USE ONLY (Leave blank)	2. REPORT DATE 20 March 1995	3. REPORT TYPE AND DATES COVERED Project Report	
4. TITLE AND SUBTITLE  Proceedings of the 1995 Space Surveillance Workshop			5. FUNDING NUMBERS  C — F19628-95-C-0002
6. AUTHOR(S)  Kurt P. Schwan (Editor)			
7. PERFORMING ORGANIZATION NAME(S) AND ADDRESS(ES)  Lincoln Laboratory, MIT P.O. Box 73 Lexington, MA 02173-9108		8. PERFORMING ORGANIZATION REPORT NUMBER  STK-235 Volume I	
9. SPONSORING/MONITORING AGENCY NAME(S) AND ADDRESS(ES)  ESC Hanscom Air Force Base Bedford, MA 01730		10. SPONSORING/MONITORING AGENCY REPORT NUMBER  ESC-TR-95-022	
11. SUPPLEMENTARY NOTES  None			
12a. DISTRIBUTION/AVAILABILITY STATEMENT  Approved for public release; distribution is unlimited.		12b. DISTRIBUTION CODE	
13. ABSTRACT (Maximum 200 words)  The thirteenth Annual Space Surveillance Workshop hosted by MIT Lincoln Laboratory was held 28-30 March 1995. The purpose of this series of workshops is to provide a forum for the presentation and discussion of space surveillance issues.  This <i>Proceedings</i> documents most of the presentations from this workshop. The papers contained were reproduced directly from copies supplied by their authors (with minor mechanical changes where necessary). It is hoped that this publication will enhance the utility of the workshop.			
14. SUBJECT TERMS			15. NUMBER OF PAGES 244
			16. PRICE CODE
17. SECURITY CLASSIFICATION OF REPORT Unclassified	18. SECURITY CLASSIFICATION OF THIS PAGE Unclassified	19. SECURITY CLASSIFICATION OF ABSTRACT Unclassified	20. LIMITATION OF ABSTRACT Same as report